

LEVEL

III
B037169

12



RADC-TR-78-279, Vol I (of two)
Interim Report
March 1979

HOLOGRAPHIC GRATING STUDY

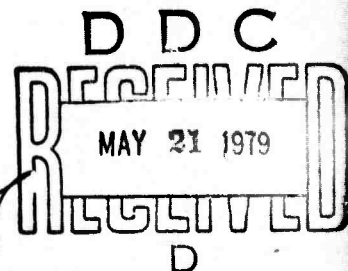
Hughes Aircraft Company

Sponsored by
Defense Advanced Research Projects Agency (DoD)
ARPA Order No. 1279

APPROVED FOR PUBLIC RELEASE; DISTRIBUTION UNLIMITED

The views and conclusions contained in this document are those of the authors and should not be interpreted as necessarily representing the official policies, either expressed or implied, of the Defense Advanced Research Projects Agency or the U.S. Government.

ROME AIR DEVELOPMENT CENTER
Air Force Systems Command
Griffiss Air Force Base, New York 13441



AD A068811

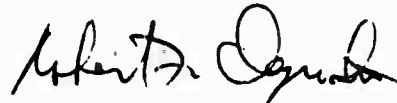
DDC FILE COPY

**BEST
AVAILABLE COPY**

This report has been reviewed by the RADC Information Office (OI) and is releasable to the National Technical Information Service (NTIS). At NTIS it will be releasable to the general public, including foreign nations.

RADC-TR-78-279, Vol I (of two) has been reviewed and is approved for publication.

APPROVED:



ROBERT F. OGRODNIK
Project Engineer

If your address has changed or if you wish to be removed from the RADC mailing list, or if the addressee is no longer employed by your organization, please notify RADC (OCTM) Griffiss AFB NY 13441. This will assist us in maintaining a current mailing list.

Do not return this copy. Retain or destroy.

LEVEL II

12

HOLOGRAPHIC GRATING STUDY

J. O. Garvey, et al

Contractor: Hughes Aircraft Company
Contract Number: F30602-76-C-0402
Effective Date of Contract: 2 August 1976
Contract Expiration Date: 30 December 1978
Short Title of Work: Holographic Grating Study
Program Code Number: 9E20
Period of Work Covered: Aug 76 - Feb 78

Principal Investigator: John Garvey
Phone: (213) 391-0711, x21389

Project Engineer: Robert Ogradnik
Phone: (315) 330-4431

Approved for public release; distribution unlimited.

This research was supported by the Defense Advanced Research Projects Agency of the Department of Defense and was monitored by Robert F. Ogradnik (OCTM) Griffiss AFB NY 13441 under Contract F30602-76-C-0402.

ACCESSION for	
DTIC	White Section <input checked="" type="checkbox"/>
DDC	DDC Section <input type="checkbox"/>
UNANNOUNCED	<input type="checkbox"/>
JUSTIFICATION	
BY	
DISTRIBUTION/AVAILABILITY CODES	
Dist.	Avail. and/or SPECIAL
A	

DDC
RECEIVED
MAY 21 1979
D

UNCLASSIFIED

SECURITY CLASSIFICATION OF THIS PAGE (When Data Entered)

REPORT DOCUMENTATION PAGE		READ INSTRUCTIONS BEFORE COMPLETING FORM	
1. REPORT NUMBER	2. GPOV ACCESSION NO.	3. RECIPIENT'S CATALOG NUMBER	
18. RADC-TR-78-279			
4. TITLE (and Subtitle)		5. TYPE OF REPORT & PERIOD COVERED	
6. HOLOGRAPHIC GRATING STUDY. Volume 1.		Interim (Phase 1) rept. Aug 76 - Feb 78 on phase 1	
7. AUTHOR(s)		8. PERFORMING ORG. REPORT NUMBER	
J. O. Garvey, et al		14. HAC-DR-105-VOL-1	
9. PERFORMING ORGANIZATION NAME AND ADDRESS		10. PROGRAM ELEMENT PROJECT, TASK AREA & WORK UNIT NUMBERS	
Hughes Aircraft Company Aerospace Groups Culver City CA 90230		F30602-76-C-0402, ✓ ARPA Order-1279	
11. CONTROLLING OFFICE NAME AND ADDRESS		12. REPORT DATE	
Defense Advanced Research Projects Agency 1400 Wilson Blvd Arlington VA 22209		62301E 12790024	
14. MONITORING AGENCY NAME & ADDRESS (if different from Controlling Office)		13. NUMBER OF PAGES	
Rome Air Development Center (OCTM) Griffiss AFB NY 13441		220	
16. DISTRIBUTION STATEMENT (of this Report)		15. SECURITY CLASS. (of this report)	
Approved for public release; distribution unlimited.		UNCLASSIFIED	
17. DISTRIBUTION STATEMENT (of the abstract)		15a. DECLASSIFICATION/DOWNGRADING SCHEDULE	
Same		N/A	
18. SUPPLEMENTARY NOTES		12. 226p.	
RADC Project Engineer: Robert F. Ogrodnik (OCTM)			
19. KEY WORDS (Continue on reverse side if necessary and identify by block number)			
Diffraction Limited Grating Holographic Grating Techniques Ion Etching Beam Sampling High Power Laser Componentry			
20. ABSTRACT (Continue on reverse side if necessary and identify by block number)			
<p>The two primary goals of the study were to demonstrate the feasibility of fabricating low and high-efficiency ion-machined holographic gratings and, by means of optical analysis, to establish their suitability for use in practical high-energy laser systems. Both of these goals were achieved. The principal results of the study are summarized below:</p> <p>1. Fabrication techniques for both low-efficiency and high-efficiency nonlinear holographic gratings were successfully demonstrated.</p>			

DD FORM 1473

1 JAN 73

UNCLASSIFIED

SECURITY CLASSIFICATION OF THIS PAGE (When Data Entered)

172 310

UNCLASSIFIED

SECURITY CLASSIFICATION OF THIS PAGE(When Data Entered)

2. The feasibility of producing high-efficiency holographic gratings, with respect to both design and fabrication, was established.

3. The feasibility of designing aberration-corrected holographic gratings was demonstrated.

4. Several important optical configurations utilizing holographic gratings were analyzed in terms of their aberrations, as a function of various distortions and component tolerances. *and*

5. Two major HEL system applications of holographic gratings were investigated in depth:

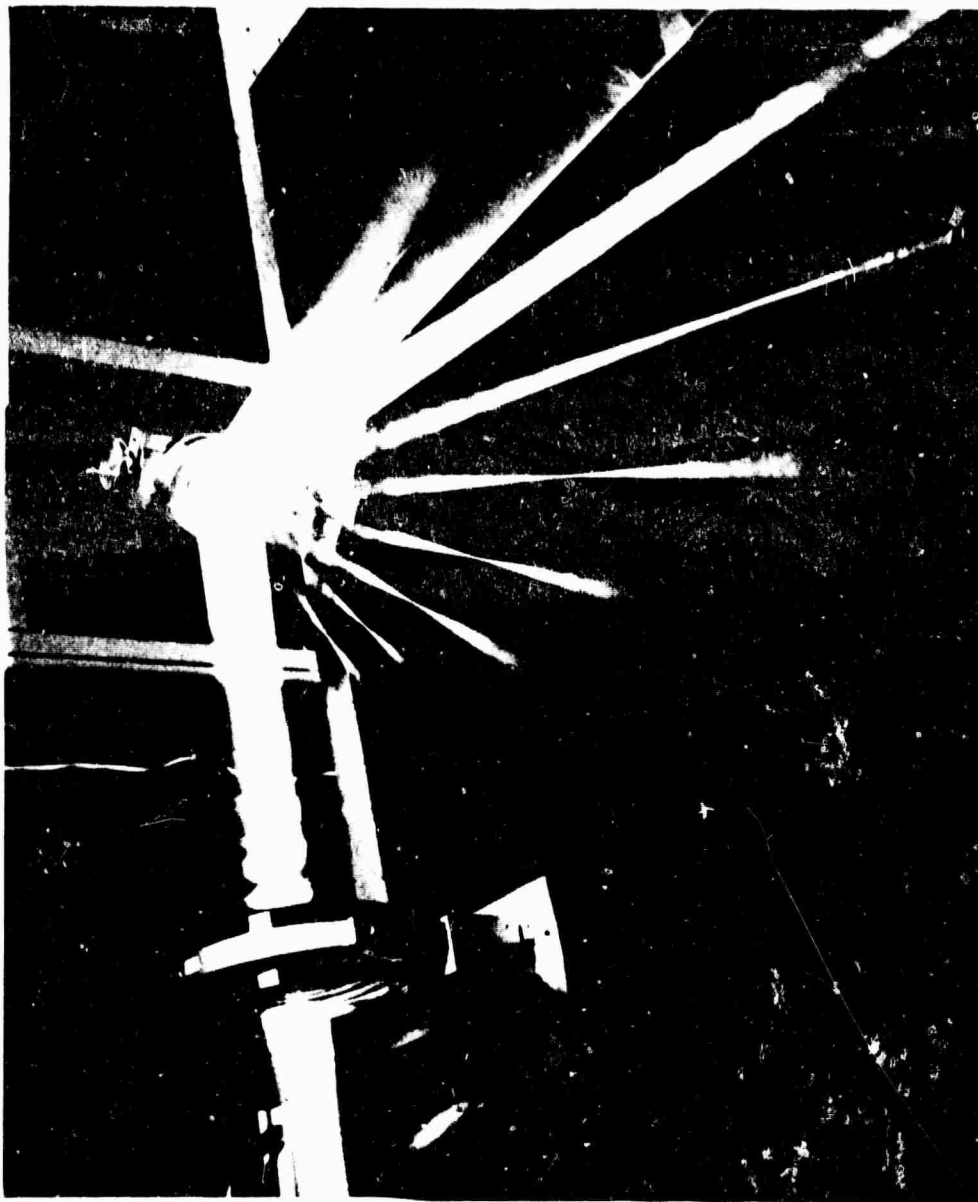
(a.) A primary mirror holographic grating beam sampler for LOS or wavefront control. *and*

(b.) A holographic grating axicon for use as a mode-control device in an annular resonator.

UNCLASSIFIED

SECURITY CLASSIFICATION OF THIS PAGE(When Data Entered)

A collimated helium-neon laser beam ($0.6328\text{ }\mu\text{m}$) is incident on a focusing holographic diffraction grating from the left hand side of the photograph: The various diffracted orders can be seen to have different focal lengths in accordance with theory. The zeroth order and one diverging order are seen at the right hand side. The grating was designed for use at $3.39\text{ }\mu\text{m}$ for which it would have only one aberration-corrected diffracted order.



PREFACE

This report documents the work performed for the Holographic Grating Study from its inception in August 1976 until February 1978, covering the original scope of effort defined in the RFP. An additional effort to investigate the properties of holographic grating axicons is continuing under a contract modification and will be reported on when completed in early 1979.

The study is being conducted by Hughes Aircraft Company, Laser Systems Division, Electro-Optical and Data Systems Group, for Rome Air Development Center, Griffiss Air Force Base, under Contract Number F30602-76-C-0402. Mr. Robert Ogradnik is the technical monitor for RADC.

Technical direction for Hughes during the report period was provided by Dr. John M. Fitts, who also served as Program Manager for the first six months of the study. The other Hughes contributors to the contract were:

Program Management:	J. O. Garvey
Optical Analysis:	R. J. Withrington and O. G. Ramer
Grating Fabrication:	A. Au and A. C. Livanos
High-Efficiency Gratings:	M. Minden and G. M. Janney

The report is divided into two volumes. Volume I, which comprises all but a small fraction of the report material, is issued with unlimited rights. Volume II, containing descriptions of certain proprietary concepts and techniques, is issued with limited rights.

CONTENTS

1.0	INTRODUCTION	1
1.1	Background	1
1.2	Summary of Program Tasks	3
1.3	Principal Accomplishments	4
1.4	Organization of the Report	5
2.0	HOLOGRAPHIC GRATING CONCEPTS	7
2.1	Basic Properties of Holographic Gratings	7
2.1.1	What is a Holographic Grating?	7
2.1.2	Fundamental Properties	9
2.2	Description of Holographic Grating Concepts	15
2.2.1	Low-efficiency Grating Concepts	16
2.2.2	High-Efficiency Grating Concepts	21
2.3	Optical Design Analysis	27
2.3.1	Optical Design Issues	28
2.3.2	Primary Mirror Beam Sampler	31
2.3.3	Wavefront Errors Due to Surface Distortions	50
2.3.4	Holographic Grating Axicon	66
2.3.5	Off-Axis Virtual Mirror	83
3.0	FABRICATION INVESTIGATION	87
3.1	Fabrication Overview	87
3.1.1	Fabrication Techniques	87
3.1.2	Implementation Techniques	90
3.2	Fabrication Issues	93
3.2.1	General Issues	95
3.2.2	High-Efficiency Grating Issues	101
3.2.3	Large-Area Grating Issues	106
3.3	Fabrication Procedures	108
3.3.1	Discussion of the Method	108
3.3.2	Grating Exposure	111
3.3.3	Development of Photoresist Gratings	115
3.4	Experimental Results	117
3.4.1	Investigation of Photoresist Properties	119
3.4.2	Evaluation of Techniques	120
3.4.3	Results of the Coating Technique Evaluation	135

CONTENTS (Continued)

3.4.4	Evaluation of Sample Gratings	136
3.4.5	Standing Waves	143
4.0	HIGH-EFFICIENCY GRATING ANALYSIS AND MEASUREMENT	167
4.1	High-Efficiency Holographic Grating Design Issues	167
4.2	Computer Modeling of High-Efficiency Gratings	170
4.2.1	Description of the Berkeley Code	170
4.2.2	The Need for a Complex Model	175
4.2.3	Verification of the Code	177
4.3	High-Efficiency Holographic Grating Measurement	179
5.0	ABERRATION-CORRECTED HOLOGRAPHIC GRATINGS	181
5.1	Objective and Design Issues	181
5.2	Aberration-Corrected Beam Sampler Design	186
5.3	Evaluation of Demonstration Grating Design	191
5.3.1	Focal Spot Profile Measurement	191
5.3.2	Diffraction-Efficiency Measurements	198
6.0	CONCLUSIONS OF THE STUDY	203
6.1	Summary of Results	203
6.2	Implications for Future Development	204

LIST OF ILLUSTRATIONS

Figure		Page
1	Illustrative Beam Sampling Applications	10
2	Illustrative High-Efficiency HG Concepts	11
3	Plane Diffraction Grating	12
4	Formation of Planar and Converging Wavefronts by a) Linear and b) Nonlinear Gratings	14
5	Illustrative Use of HG Beam Sample for Wavefront and LOS Control	18
6	Aberration-Corrected 45-Degree Beam Sampler	20
7	Holographic Grating Axicon	22
8	Type of Axicons	24
9	Dual Grating Rhomb	27
10	Principal Sources of Error for Beam Steering Control	30
11	Hologram Construction Point Source Locations	34
12	Construction Conjugates and Spherical Aberration in the Sample Beam	34
13	Residual Spherical Aberration at Design Point	35
14	Coma in Sample Beam as a Function of Primary f/Number and Beam Steering Angle	36
15	Variation of Coma with Primary Mirror Conic Constant	37
16	Two Integrated Design Concepts	38
17	The Maximum Decentration of the Primary Which can be Allowed while Maintaining a Diffraction- Limited System (10 μ rad) Versus f/Number	42
18	The Maximum Tilt of the Error Sensing Optics Which can be Allowed While Maintaining a Diffraction- Limited System (10 μ rad degradation)	42
19	Off-Axis System with Axi-symmetric Beam Sampling	43
20	The On-Axis Aberrations of the Parent Telescope	44
21	On-Axis System with Off-Axis Beam Sampling	45
22	Hologram Construction Point Source Locations	46
23	Hologram Aberrations Versus the Angle α and Conjugate Distances	48
24	Hologram Construction Optics at the Chosen Design Point	48

LIST OF ILLUSTRATIONS (Continued)

Figure		Page
25	The Resultant On-Axis Aberrations at the Focal Point of the Hologram	49
26	Off-Axis Aberrations and Tolerance Sensitivity for Asymmetric Beam Sampling	49
27	In Certain Classes of Systems, Good Optical Performance Can be Obtained with a Poor Primary Mirror Figure by Correcting the Sample Wavefront Obtained via an Ideal HG on the Primary	51
28	OPD Error Caused by Out-of-Plane Distortion	53
29	Effect of Out-of-Plane Distortion Prior to Hologram Fabrication	55
30	Playback with Deformed Construction	57
31	Deformed Primary on Playback	58
32	Aberrations Due to Curvature Change	59
33	Aberration Versus Power Due to Distortion of Cooled Metal Mirror	63
34	Geometry for Photoresist Variation Calculation	64
35	Illustrative Holographic Axicon Playback Geometries	66
36	Illustrative Holographic Axicon Construction Geometries	68
37	Configuration Used in Holographic Axicon Aberration Examination	71
38	A Fan of Rays is a Group of Rays Starting at an Object Point and Incident on the Entrance Pupil in a Line as Illustrated.	72
39	Maximum Angular Aberration Due to Misalignment of Inner or Outer Grating	73
40	XFAN Aberrations Introduced by a 2-mm Decentration of Either Grating	74
41	XFAN Aberrations Introduced by 1-mrad tilt on Inner Grating	75
42	Aberrations Introduced by Tilting Axicon	76
43	Behavior of Grating Vector, \bar{q} , for 2-mm Decentration of the Inner Element	78
44	Contours of Zero Intensity in Output	82

LIST OF ILLUSTRATIONS (Continued)

Figure		Page
45	Virtual Primary Mirror: Geometry Used in Efficiency Analysis	84
46	Virtual Primary Mirror Design: Efficiency Guidelines for TM (E_{\perp}) Polarization	84
47	Ruled Grating	89
48	Holographic Grating	90
49	Holographic Grating Recording Setup	94
50	Exposure Apparatus for Exposing Aberration-Corrected Holographic Gratings	96
51	Single Collimated-Beam Exposure System	98
52	Near-Field Diffraction of 1-cm diameter Aperture Recorded in Shipley 1350B Photoresist Layer on Gold	99
53	Intensity Scans of Beam Uniformity Across a 1-cm Diameter Aperture	100
54	Groove Shape Dependence on Photoresist Thickness Uniformity	103
55	Standing Waves in the Photoresist Layer Due to Interference of Incident and Reflected Wavefronts	105
56	Etching Depth Versus Exposure for AZ1350B Photoresist Developed for One Minute in 1:1 AZ Developer	106
57	Exposure Apparatus for Recording Linear Grating	111
58	(a) Linear Grating Recorded in AZ1350B Photoresist Over Gold on 2" x 3" Microscope Slide. (b) Extraneous Diffraction Caused by the Extraneous Grating Structure	113
59	(a) Quasi-Linear Grating Recorded in AZ1350B Photoresist Over Gold on 2" x 3" Microscope Slide. (b) First and Second Diffracted Orders	114
60	Summary of Experimental Data Reported by Various Workers Using AZ1350 Photoresist	116
61	Experimental Data of Etch Depth Versus Development Time at Various Dilutions of AZ303A and AZ1350 Developers	118
62	Resist Thickness Versus Spin Speed	125

LIST OF ILLUSTRATIONS (Continued)

Figure		Page
63	Thickness Variations	133
64	Ion-Etched Gratings	137
65	Ion-Etched Gratings	138
66	Ion-Etched Gratings	139
67	Ion-Etched Gratings	140
68	Ion-Etched Gratings (Sputtered)	141
69	Ion-Etched Gratings	142
70	Photoresist-to-Gold Transfer Characteristics.	143
71	Interference Intensity Distribution of Construction and Reflected Fields	145
72	Intensity Distribution Within Unit Cell in Bulk of Photoresist with 1:1 Construction Beam Ratio.	147
73	Intensity Distribution Within Unit Cell in Bulk of the Photoresist with 20:1 Construction Beam Ratio	148
74	Exposures of AZ1350B Photoresist on Gold	149
75	SEM Photograph of 3000 Å Ion-Beam Machined Grating in Gold.	151
76	Dry Gold Substrate - 1350B Resist/1350 Developer, Beam Ratio 0.72, Developing Time - 1 Minute, Dilution 1:1.	153
77	Dry Gold Substrate - 1350B Resist/1350 Developer, Beam Ratio 0.80, Developing Time - 1 Minute, Dilution 1:1.	154
78	Dry CrO on Gold Substrate - 1350 Resist/1350 Developer, Beam Ratio 0.79, Developing Time - 1 Minute, Dilution 1:1.	156
79	Dry CrO on Gold Substrate - 1350B Resist/1350 Developer, Beam Ratio 0.78, Developing Time - 1 Minute, Dilution 1:1.	157
80	Dry/Non-Reflecting Substrate - 1350J Resist/1350 Developer, Beam Ratio 0.63, Developing Time - 2 Minutes, Dilution 1:1.	158
81	Dry/Non-Reflecting Substrate - 1375 Resist/1350 Developer, Beam Ratio 0.64, Developing Time - 2 Minutes, Dilution 1:1.	159
82	SED Non-Reflecting Substrates - 1375 Resist/3500 Developer, Beam Ratio 0.63, Developer Dilution 5:1	161

LIST OF ILLUSTRATIONS (Continued)

Figure		Page
83	SEM Photographs of Holographic Gratings in Photoresist on Gold with AR Coatings of Varying Reflectivity	162
84	High-Magnification SEM of Typical Grating Profile on Gold with AR Coating Showing Minimal Standing Wave Structure . .	163
85	SEM Photographs of Holographic Gratings in Photoresist on Gold with Minimal Standing Wave Structure	164
86	SEM Photographs of Holographic Gratings on Gold Using 1.4 μm Thick Resist	165
87	High-Efficiency 1- μm Deep Grating Ion Machined in Gold Using Photoresist Grating Mask with 2.6 μm Relief Height . .	165
88	2- μm Deep Grating Ion Machined in Gold Using Photoresist Grating Mask with 2.5 μm Relief Height	166
89	Efficiency Versus Groove Depth	168
90	Efficiency Versus Groove Period	169
91	Construction Geometry for the Hologram	171
92	Fringe Pattern of a Holographic Lens	173
93	Diffraction Efficiency Design Curves: Beam Sampler or Mixing Axicon	176
94	Code Verification: Bausch and Lomb Blazed Gratings	178
95	Code Verification: Hughes Ion-Etched Grating. Reflectivity in Unpolarized Light	179
96	Ten High-Efficiency Samples: Calculations for TM (E_{\perp}) Polarization	180
97	Ten High-Efficiency Samples: Calculations for TE (E_{\parallel}) Polarization	180
98	45-Degree Mirror Beam Sampler	183
99	Interferogram of GFE Mirror	185
100	Construction Optics for Aberration-Corrected 45-Degree Mirror Beam Sampler	187
101	Departure of the Rays from a Perfect Geometrical Focus Versus the Relative Aperture	189
102	Geometrical Spot Diagram and Knife Edge Trace for Nominal Design of the Aberration-Corrected 45-Degree Beam Sampler	190

LIST OF ILLUSTRATIONS (Continued)

Fig. re		Page
103	Lens, Cylinder IA	192
104	Lens, IB	193
105	Focal Spot Profile Measurement	194
106	Interferograms of Collimated Incident Beam at 6328 Å	196
107	Focal Spot Profile of Aberration-Corrected Beam Sample: High Efficiency Sampler	197
108	Focal Spot Profile of Aberration-Corrected Beam Sampler on Water-Cooled Mirror	198
109	Diffraction Efficiency Measurements	199
110	Diffraction Efficiency Uniformity	201

LIST OF TABLES

Table		Page
1	Holographic Beam Sampling Trade-Off Ranges	32
2	Performance for a Typical Linear Obscuration Less Than 40 Percent	40
3	Holographic Axicon Design Example	70
4	Examples of Photoresist and Substrate Layers used in Experiments	109
5	Photoresist Thickness Data	110
6	Summary of Air and Vacuum Baking	121
7	External Environment Variations	122
8	Summary of Acetone Measurements	123
9	Resist Type, Waiting Time, and Spin Speed	124
10	Resist Thickness as a Function of Acetone Concentration and Waiting Time	126
11	Acetone Concentration, Waiting Time and Spin Duration . . .	127
12	Acetone Concentration, Waiting Time and Spin Duration for Reduced Waiting and Spin Times	128
13	Waiting and Spin Time Variables	129
14	Waiting Time, Spin Duration and Spin Speed Variables	130
15	Reduced Spin and Waiting Times	131
16	Thickness Variations for Dynamic Deposition	132
17	Construction Optics Tolerances Assuming Adjustment of the Incident Beam and Focus on Playback	191

PHASE I SUMMARY

Project No: 1279
Contract No: F30602-76-C-0402
Effort Title: Holographic Grating Study - Phase I
Contractor: Hughes Aircraft Co., Culver City, CA


The objectives of this program are to develop and assess a technology which produces diffraction limited beam samplers which are suitable for high energy laser applications and lend themselves to large aperture optical systems, of the several meter range, in their performance of uniformity and distortion.

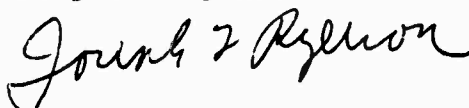
The developed technology is based on holographic exposure methods for grating construction with exposure being made directly on a photoresist layer which is deposited (with controlled uniformity) on the optical surface of the candidate mirror substrate. Ion etch methods are used for permanently etching the grating into the substrate, with the developed photoresist serving as a direct contact mask during the etching process. The combination of controlled ion etching and holographic tailored masks permits grating groove geometry control which insures high quality performance not achievable by conventional grating fabrication methods. Further, the

ion etch approach removes all photoresist after the grating has been imprinted and provides a light optical quality polish to enhance mirror properties.

The overall approach is fully applicable to heat-exchanger mirror faceplates and thus supports high power laser component development. The demonstration of this constitutes the Phase I of this effort.

Since grating design is holographically implemented, the grating generated sampled beam can be made to either focus with a preselected radius of curvature, or to feature any preferred wavefront phase distribution which aids in wavefront monitoring or other beam sampling operations. A significant consequence of this is that the substrate itself can feature differing apparent optical prescriptions for differing wavelengths, thus serving the role as wavelength selective optical control, or, as having a virtual aspheric optical form when the true physical form of the substrate is a simple, easily fabricatable shape. This feature will be fully explored in the Phase II effort where a virtual axicon concept will be studied, fabricated and analyzed for intracavity laser mode control purposes.


ROBERT F. OGRODNIK
Project Engineer


JOSEPH J. RYERSON
Technical Director
Surveillance Division

1.0 INTRODUCTION

1.1 BACKGROUND

This report documents the accomplishments of the Holographic Grating Study from its inception in August 1976 until February 1978, covering the scope of effort defined in the proposal.¹ The overall objective of the program was to establish the feasibility of holographic grating (HG) technology for high-energy laser applications. In the course of the study, the original scope was broadened to include a subsequent investigation of holographic grating axicons for annular ring resonators.² This axicon work, which is a direct outgrowth of the original Holographic Grating Study, is continuing under additional funding and will be documented upon completion of that effort in early 1979.

Although the focusing properties of nonlinear gratings have long been recognized, the possibility of developing them for use on large reflective optics has been seriously investigated only during the last few years, mainly because traditional fabrication methods were ill-suited to such applications. An early study by the Keuffel and Esser Company in 1972 examined the feasibility of producing a low-efficiency holographic beam sampling grating on the primary mirror of a 30-cm astronomical telescope.³ More recently, the Perkin-Elmer Corporation investigated the properties and potential methods of fabricating linear infrared reflection gratings to be used as wave-front samplers for high-energy laser (HEL) beams.⁴ Focusing holographic gratings on mirror surfaces were also investigated by Arizona University.⁵

-
1. "Technical and Management Proposal for a Holographic Grating Study," Hughes Aircraft Company, 10 March 1976.
 2. "Technical and Management Proposal, Holographic Axicon/Annular Resonator Feasibility Demonstration," Hughes Aircraft Company, Report No. TP77-147 (1 August 1977).
 3. K. E. Erickson, "Fabrication and Evaluation of a Weak Zone Plate for Monitoring Performance of a Large Orbiting Telescopes," Keuffel and Esser Company, Report No. NAS1-10564 (July 15, 1972).
 4. J. S. Harris, et al., "Diffraction Grating Development," Perkin-Elmer Corporation Report No. 11991 (AD-A008 199), (July 1974).
 5. "Large Diameter Active Mirror with Holographic Figure Sensing," Arizona University Optical Sciences Center, SAMSO TR 75-17 (Oct 1974)

The Hughes Holographic Grating Study differs from, and goes beyond these earlier investigations in several important respects. First, the study is concerned with only a single type of grating, consisting of nonlinear reflection gratings produced by ion machining through holographically-exposed photoresist masks. Linear (non-focusing) gratings were not considered, although they can also be fabricated using these techniques. The combination of holographic exposure and ion machining techniques was chosen as being the most suitable for producing nonlinear gratings on high-power metal mirrors such as those used in HEL systems.

A second distinguishing feature of the Holographic Grating Study is the detailed optical analysis that was performed to evaluate a number of holographic grating concepts applicable to HEL systems. Among these concepts, originally conceived prior to the study, were several realizations of focusing HG beam samplers for a primary mirror; this analysis led directly to one of the major practical results of the study - a conceptual holographic grating sampling scheme for implementing line-of-sight (LOS) or wavefront control of an HEL beam. Other concepts examined included a holographic grating axicon, a holographic grating rhomb, and a "virtual mirror," all based on the properties of nonlinear high-efficiency gratings.

The inclusion of both analytical and experimental investigations of high-efficiency holographic gratings represents another noteworthy aspect of the Hughes study. As mentioned above, several high-efficiency grating concepts were analyzed, while the feasibility of fabricating high-efficiency HGs was demonstrated in connection with the experimental task. The HG axicon work currently in progress was brought about by the success of these efforts.

Finally, an aberration-corrected 45-degree beam sampler was designed, and this design was then used to fabricate both low-efficiency and high-efficiency sample gratings. Focal spot measurements of these samples revealed nearly diffraction-limited performance, thus demonstrating that the correction of grating aberrations is feasible using straightforward design practices, and is compatible with the fabrication techniques employed.

1.2 SUMMARY OF PROGRAM TASKS

The Holographic Grating Study was structured into the following six technical tasks:

- Task I. Holographic Grating Conceptual Designs
- Task II. Analytical Investigations of Conceptual Designs
- Task III. Nonlinear Holographic Beam Sampler Development
- Task IV. High-Efficiency Holographic Grating Feasibility Demonstration
- Task V. Evaluation of Holographic Grating Applications
- Task VI. Demonstration of "Aberration-Free" Holographic Gratings

Although Tasks I and II were originally conceived as separate tasks, they were, in effect, merged throughout the study. This effort was concerned with identifying and evaluating various conceptual uses of low-efficiency and high-efficiency holographic gratings in HEL systems. Extensive computer analyses were employed to assess the aberrations associated with each concept, including the effects of misalignments and distortions. Concepts investigated in varying levels of detail included two types of HG beam samplers, a holographic axicon, a "virtual mirror," and an HG rhomb.

Task III comprised the experimental investigation of fabrication techniques for both low and high-efficiency holographic gratings. Topics covered under this task included the preparation and coating of substrates with photoresist, holographic exposure and development of photoresist gratings, and ion-machining of the final grating into the substrate. A significant portion of this investigation was devoted to methods of depositing highly uniform photoresist coatings, and of eliminating the standing waves that tend to occur when holographic gratings are fabricated on reflective substrates; solutions of these problems are essential to the successful development of high-efficiency HGs.

Task IV was directed toward acquiring improved theoretical understanding of the relationship between grating diffraction efficiency and various design parameters such as the groove shape and depth, and the angle of incidence and polarization of the incident radiation. A key element in this investigation was a set of computer codes, originally developed at the

University of California, which was used to calculate the grating efficiency as a function of these parameters, and to guide the design of the high-efficiency grating samples fabricated in Task III. The work in Task IV also included efficiency analyses of the beam sampler and "virtual mirror" concepts and laboratory measurements of the efficiency and efficiency uniformity of the sample gratings produced under Task III.

The most promising HG concepts examined in Tasks I and II were subjected to more intensive analysis under Task V. One low-efficiency grating concept (Primary Mirror HG Beam Sampler) and one high-efficiency concept (HG Axicon) were chosen for this purpose. An in-depth investigation of the latter concept is continuing under this task.

Task VI was conceived independently of the other tasks and was funded separately as the "Government Option" during the study. It consisted of the design, fabrication and laboratory evaluation of an aberration-corrected holographic grating beam sampler for a 45-degree folding mirror. This task was included to demonstrate the feasibility of producing such "aberration-free" gratings using the fabrication techniques developed during the program.*

1.3 PRINCIPAL ACCOMPLISHMENTS

The most significant results of the Holographic Grating Study are enumerated below and are discussed in detail in following sections of the report:

1. Fabrication techniques for both low-efficiency and high-efficiency nonlinear holographic gratings have been successfully developed.
2. The feasibility of producing high-efficiency holographic gratings, with respect to both design and fabrication, has been established.
3. The feasibility of designing aberration-corrected holographic gratings has been demonstrated.
4. Several important optical configurations utilizing holographic gratings have been analyzed in terms of their aberrations, as a function of various distortions and component tolerances.

*The term "aberration free" was used initially in place of the more accurate designation "aberration corrected." The two terms are used synonymously in this report.

5. Two major HEL system applications of holographic gratings have been or are currently being investigated in depth:
 - a. A primary-mirror holographic grating beam sampler for LOS or wavefront control,
 - b. A holographic grating axicon for use as a mode-control device in an annular resonator.

1.4 ORGANIZATION OF THE REPORT

The following sections of the report present detailed descriptions and results of the various analytical and experimental investigations that were carried out during the study. Section 2 contains the non-proprietary results of Tasks I, II and V, covering the analysis of holographic grating concepts and applications. (Detailed descriptions of two proprietary concepts are given in Volume II, Section 2.) This section also includes an introductory tutorial discussion of the most relevant properties of holographic reflection gratings. Section 3 documents the results of the fabrication investigation performed under Task 3, except for a proprietary discussion of anti-reflection coatings, which appears in Volume II, Section 3. The section begins with a general discussion of grating fabrication methods that is intended to clarify the reasons for selecting the approach that was adopted.

Sections 4 and 5 are devoted to more specialized topics. The high-efficiency grating investigation (Task IV) is described in Section 4, while the results of the "Government Option" (Task VI) are presented in Section 5. The conclusions of the study are set forth in Section 6, which includes a summary of the principal results and a discussion of their implication for the continued development of HG technology.

2.0 HOLOGRAPHIC GRATING CONCEPTS

This section of the report contains descriptions and optical analyses of the various holographic grating concepts that were investigated under Tasks I, II, and V of the study. Concepts employing both low-efficiency and high-efficiency gratings are discussed. The feasibility of designing and fabricating such gratings is taken up in Sections 3 and 4.

The presentation begins in Section 2.1 by examining certain fundamental properties of holographic gratings that are exploited subsequently in defining the concepts. In Section 2.2, the low-efficiency and high-efficiency concepts are introduced and discussed separately in qualitative fashion. Section 2.3 contains the detailed optical analyses that were performed to assess the viability of the concepts. Proprietary descriptions of two high-energy-laser systems applications are presented in Section 2 of Volume II.

2.1 BASIC PROPERTIES OF HOLOGRAPHIC GRATINGS

2.1.1 What is a Holographic Grating?

The type of grating considered in this report consists of a series of non-intersecting shallow grooves etched into the surface of a flat or curved metallic substrate such as a high-power mirror. The groove locations are defined by the maxima or minima of an interference pattern produced by two mutually coherent wavefronts. In general, the grooves follow curved lines and their spacing (period) varies with position. Such gratings are

called "thin phase reflection holograms" or simply holographic gratings (HGs). They are also sometimes referred to as "nonlinear" gratings to distinguish them from conventional "linear" gratings in which the grooves are straight, parallel and equally spaced. Strictly speaking, linear gratings can also be made by holographic methods, so the adjectives "holographic" and "non-linear" are not quite synonymous. In the context of the Holographic Grating Study, however, this distinction is unimportant, since only true nonlinear holographic gratings were investigated.

When a holographic grating is illuminated with a coherent wavefront from a laser (or other coherent source), part of the incident beam is unaffected by the grating and is reflected from the substrate as the zeroth order of diffraction. The remaining energy* is diffracted by the grating into the various non-zero orders that can exist according to the grating equation. The fraction of the incident energy diffracted into a single specified order is given by the diffraction efficiency for that order. Diffraction efficiency is a function of several parameters including the depth, shape and period of the grooves, and the wavelength, angle of incidence, and polarization of the incident beam. Although multiple orders are of interest in some grating applications, the holographic grating concepts investigated in the present study employ either the zeroth and first orders together (low-efficiency gratings) or the first order alone (high-efficiency gratings).

While the separation of a monochromatic beam into a number of orders is the hallmark of any diffraction grating, the primary distinguishing feature of a holographic grating is its ability to focus such a beam to a point. In other words, an HG can be designed to have

*A small fraction of the incident energy is also lost to absorption and random scattering in the grating.

optical power, while a conventional linear grating cannot. This unique capability is made possible through the use of nonlinear groove patterns, which are practicable only with the holographic method.

Optical power is just one of several holographic grating properties upon which the various concepts were based. Because of their fundamental importance, they are identified and briefly discussed below.

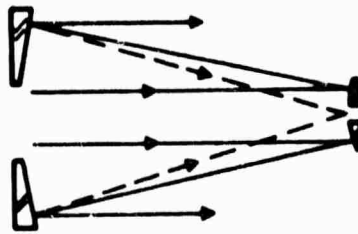
2.1.2 Fundamental Properties

The following five properties of holographic gratings play a central role in the concepts examined in this section:

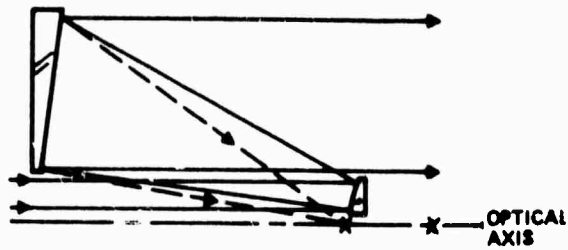
1. Holographic gratings utilize the first or higher orders of diffraction. This, of course, is an essential feature of all diffraction gratings, but in conjunction with Property 2 below, it provides the basis for the unique flexibility that marks the holographic grating optical configurations to be described. The significance of this statement is best appreciated by examining the conceptual designs shown in Figures 1 and 2. It should be evident that the use of holographic gratings opens up a range of design options that would otherwise be impracticable or impossible with conventional optics.

The number and angular positions of the diffracted beams are governed by the grating equation, which is applicable to both conventional gratings and to any small region of a holographic grating. If the grating lines are perpendicular to the plane of incidence, as shown in Figure 3, the incident and diffracted angles ϕ and θ , respectively, are related by the grating equation:

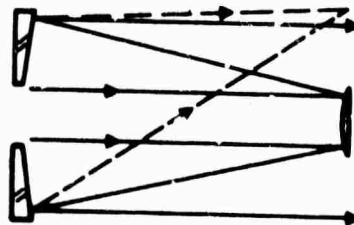
$$\sin\phi + \sin\theta_m = m\lambda/d \quad (1)$$



a. On-axis system



b. Off-axis system with axi-symmetric sampling



c. On-axis system with asymmetric sampling

—— MAIN BEAM OPTICAL PATH
 ---- SAMPLE BEAM OPTICAL PATH

• HOLOGRAM IS A LOW DIFFRACTION EFFICIENCY NON-LINEAR GRATING ON THE PRIMARY MIRROR

Figure 1. Illustrative beam sampling applications.

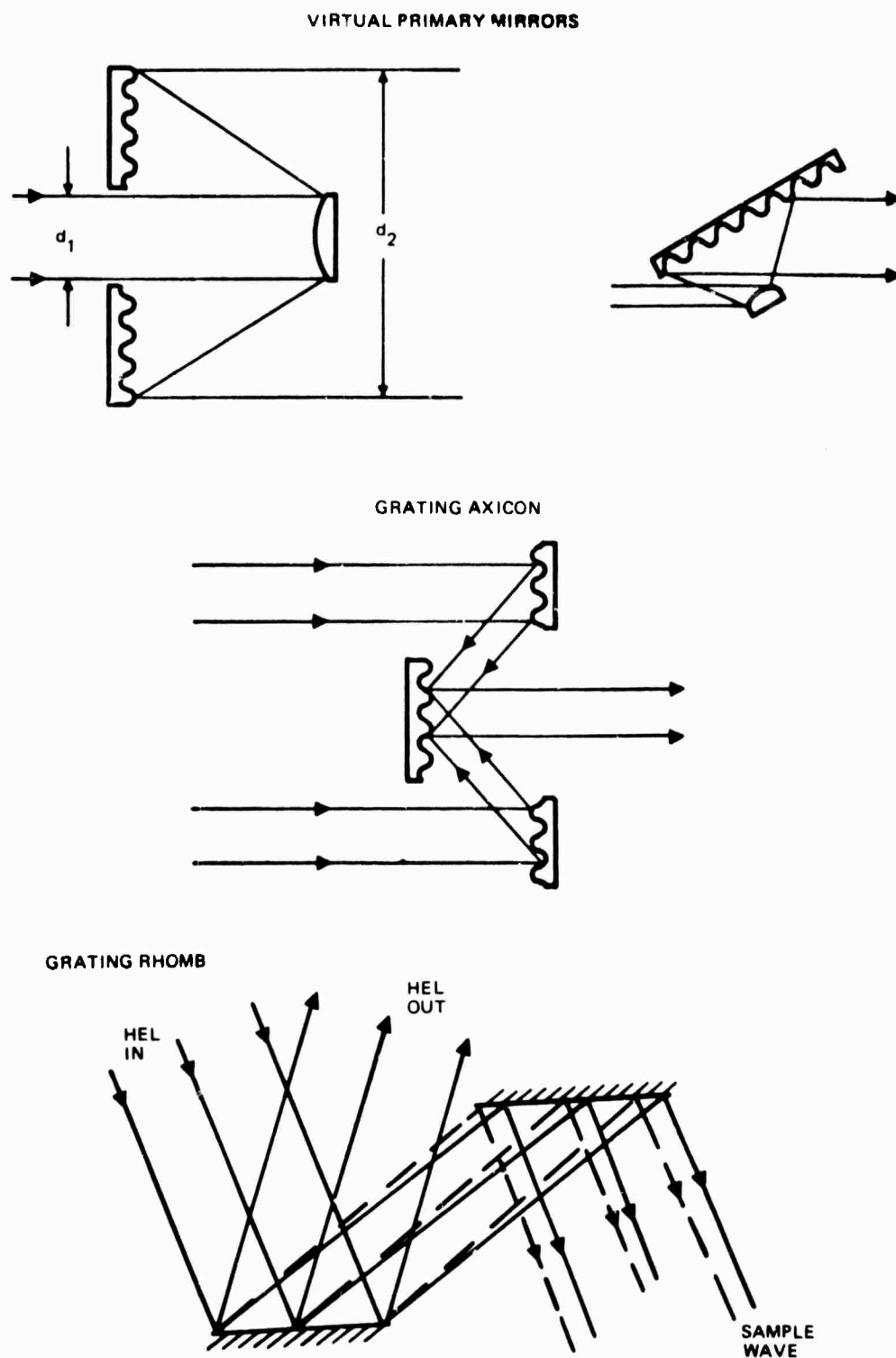


Figure 2. Illustrative High-Efficiency HG Concepts

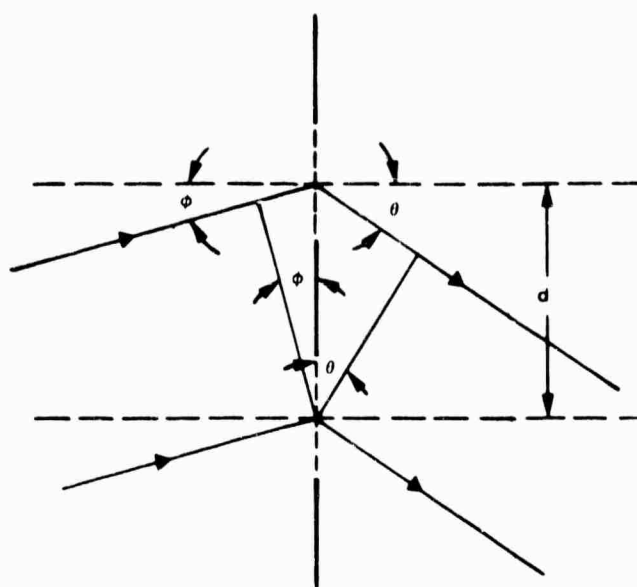


Figure 3. Plane diffraction grating.

where λ is the wavelength of the incident beam, d is the groove spacing or period, and m is an integer (positive or negative) that defines the diffraction order. If the grating lines are not perpendicular to the plane of incidence, the relationship between ϕ and θ_m is more complicated. The diffracted angle is positive when the diffracted beam is on the same side of the grating normal as the incident beam, negative if on the opposite side. (These conventions apply to reflection gratings, which are the only type discussed here.)

The values of ϕ and λ/d determine the number of diffracted orders (the number of secondary beams into which the incident beam is split). In particular, if $\lambda/d > 2$, only $m = 0$ is possible; i. e., there are no diffracted beams, only the zeroth-order or specular beam ($\theta_0 = \phi$). Similarly, if $1 < \lambda/d < 2$, the orders corresponding to $m = 0$ and $m = \pm 1$ are possible for normal incidence, but no others. These two cases are of particular importance in applications where gratings are used as beam splitters and samplers.

If the incident beam is polychromatic, a set of diffracted beams will be produced for each component wavelength. This property provides the

basis for one important method of separating two beams of different wavelengths. (The other primary method is to exploit the long wavelength cutoff $\lambda/d > 2$ to separate the beams.)

2. Holographic gratings have optical power. Because holographic gratings can be made to have almost any desired nonlinear groove pattern, they can be designed to focus a monochromatic wave to a point. (Linear holographic gratings represent a limiting case for which the focal length is infinite.) The formation of planar wavefronts by a linear grating (uniformly spaced grooves) and converging wavefronts by a nonlinear grating is illustrated in Figures 4a and 4b, respectively. Since the focusing property of a nonlinear grating is optically equivalent to the action of an ordinary lens, an HG is sometimes described as a "holographic lens", and this term is used occasionally in the report.* The lens analogy is also suggested by the expression for the power P_{HG} of the diffracted beam from an HG:

$$P_{HG} = \frac{1}{F_{HG}} = m\mu \left(\frac{1}{R_1} - \frac{1}{R_2} \right) \quad (2)$$

where

F_{HG} = Focal length of the grating

R_1, R_2 = Construction point-source distances

μ = Ratio of playback wavelength to construction wavelength

m = Order of diffraction

Comparing Equation 2 with the formula for the power of a thin lens shows that the holographic grating is optically equivalent to a lens having radii of curvature R_1 and R_2 and a refractive index of $m\mu + 1$.

*A "lens" in this context, is to be understood in the sense of a curved mirror with power, since only reflective gratings are considered.

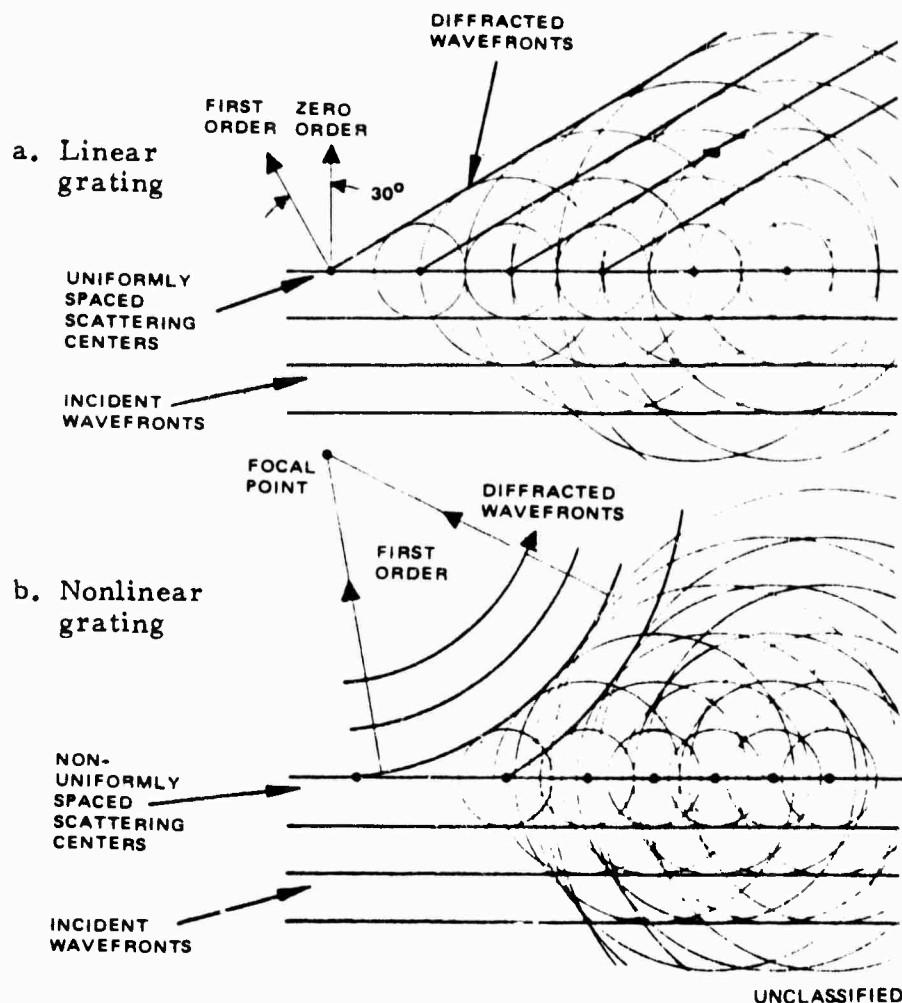


Figure 4. Formation of planar and converging wavefronts by a) linear and b) nonlinear gratings.

3. The optical powers of a holographic grating and its substrate are additive. This property is expressed simply as

$$P_{\text{Tot}} = P_{\text{HG}} + P_{\text{S}} \quad (3)$$

where P_{HG} and P_{S} denote the powers of the grating and the substrate, respectively, and P_{Tot} is the combined power of both. When $m = 0$, P_{HG} is zero according to Equation 2; hence, the zeroth order, when present, is affected only by the substrate power, P_{S} , and therefore represents the

ordinary reflected beam. This property is particularly useful for separating the main beam from the diffracted beam in sampling applications.

4. The diffracted beam from a "perfect" holographic grating is a true phase replica of the incident wavefront.

5. The zeroth-order beam from an HG is unaffected (i.e., undistorted) by the presence of the grating.

Property 4 is important in high-efficiency grating concepts which employ only one diffracted order (other than the zeroth order), while Properties 4 and 5 are both relevant to the beam sampling concepts. The term "perfect holographic grating," as used above, refers to a hologram that is free of aberrations, and is entirely analogous to the notion of a "perfect lens". Although idealized, it is a highly useful concept for analyzing the optical characteristics of holographic gratings.

2.2 DESCRIPTION OF HOLOGRAPHIC GRATING CONCEPTS

During the course of the study, a number of concepts utilizing holographic gratings, based on the fundamental properties described in Section 2.1, were identified and analyzed in varying levels of detail. These concepts are introduced and discussed briefly in this subsection, while the detailed analyses are presented in Section 2.3. For convenience in presentation, the low-efficiency and high-efficiency grating concepts are taken up separately. This distinction is maintained throughout the report since it also provides a natural basis for assessing the fabrication issues, which differ significantly for low- and high-efficiency holographic gratings (See Sections 3 and 4.)

2.2.1 Low-efficiency Grating Concepts

The designation "low-efficiency" is used here in a qualitative, rather than a strictly quantitative sense to denote holographic gratings that have been designed for less than the maximum possible efficiency in a specified order of diffraction. Such gratings ordinarily utilize the zeroth order at high efficiency for the main HEL beam (typically greater than 99. + percent) and the first or higher order(s) at relatively low efficiency (typically less than 0.1 percent). The precise value of the efficiency in a particular application depends upon a number of design considerations, including the power level required in the low-efficiency beam. Thus, the efficiency of holographic grating used to sample a high-energy laser beam could be as small as 0.02 percent, while a sampling grating for a low-power laser might require an efficiency of 20 percent or more.

Although several functional uses for low-efficiency holographic gratings can be envisioned, only one basic concept applicable to HEL systems was identified — the holographic grating beam sampler. Two types of sampling gratings were investigated in detail: (1) A beam sampler on the primary mirror of an HEL telescope and (2) a beam sampler on a flat mirror oriented at 45 degrees to the incident beam. The first of these was regarded as a highly promising candidate for achieving improved LOS and wavefront control in HEL systems and was therefore investigated extensively. The 45-degree beam sampler, on the other hand, was selected for analysis principally to demonstrate the feasibility of designing and fabricating aberration-corrected gratings, as described in Section 5.

Primary Mirror Beam Sampler

In this concept, a low-efficiency holographic grating is etched onto the primary mirror of a beam expander and is used to provide a low-power wavefront sample of the main beam. Ideally, according to

Fundamental Properties 4 and 5 (Section 2.1.2), the holographic sample accurately maps the phase and relative amplitude distributions of the main beam. Therefore, the sample can be used to record its instantaneous wavefront profile. (Deviations from this ideal situation in real systems are considered later.) By making use of Properties 1 through 3, the sample beam is optically separated from the main beam and brought to a focus at a convenient location where it can be measured by a suitable sensor.

Three representative design configurations were illustrated in Figure 1, in which the dashed lines indicate the paths of the sample beams. In the coaxial configuration (Figure 1a), the focal points for both the main and sample beams lie on the telescope axis, at different distances from the vertex of the primary mirror. An off-axis telescope with a holographic grating beam sampler that focuses on the axis is shown in Figure 1b, while Figure 1c represents an on-axis telescope in which the grating focuses the sample beam at a convenient off-axis point. These configurations are analyzed in Section 2.3.

As suggested earlier, the impetus for development of a primary mirror beam sampler stems from the need for improved LOS control and the emergence of adaptive optics technology for local-loop wavefront control of the outgoing HEL beam. In both applications, the full potential of the control system can be achieved only if the wavefront is sampled after the last component of the optical train, i. e., at the exit aperture. This permits the control loop to correct for spurious wavefront tilts or deformation caused by all phase distorting mechanisms up to and including those associated with the primary mirror. Placing a holographic grating on the primary itself therefore represents the closest physically realizable approach to ideal sampling for local-loop control of an outgoing HEL beam.

The two principal control applications of a primary mirror beam sampler are illustrated in Figure 5 for a co-axial system. In this configuration, a full-aperture wavefront sample of the main beam is diffracted

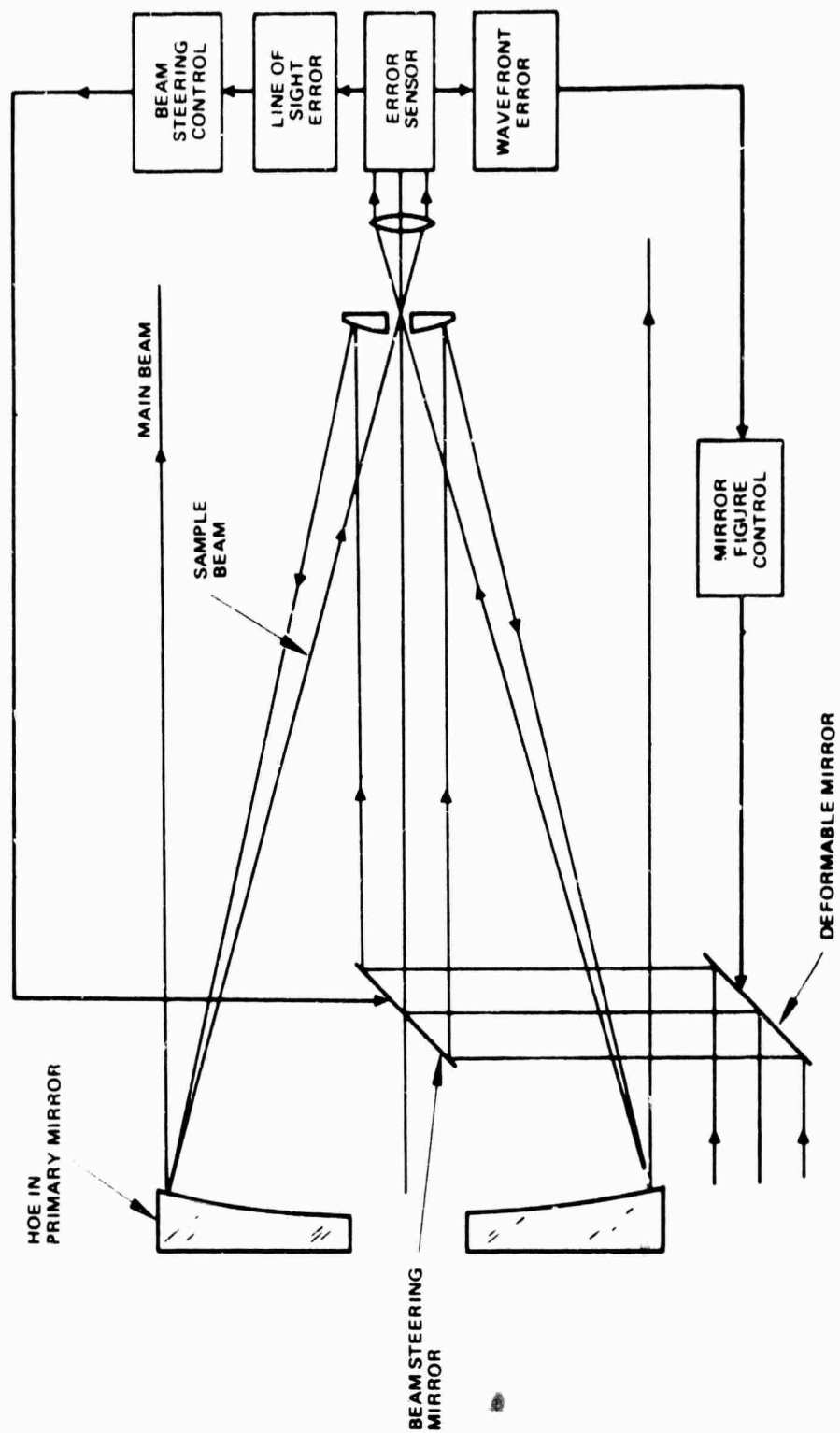


Figure 5. Illustrative use of HG beam sample for wavefront and LOS control.

from a holographic grating on the primary through a hole in the secondary to an error sensor situated behind it. As indicated by the two feedback loops in the figure, the holographic sample can be used, via appropriate servo subsystems, for either (or both) LOS or wavefront control of the main beam.

Beam steering control is accomplished by tilting one or more steering mirrors in accordance with directional (i.e. wavefront tilt) information obtained from the sample beam. Wavefront control is effected in the other loop by means of a different error sensor plus a figure control unit, and an active (deformable) mirror. Phase errors measured by this sensor provide inputs to the figure control which generates the signals that drive the deformable mirror to correct the phase profile of the output beam.

In each loop, the control system operates on the main beam in response to signals derived from the sample beam. The viability of this approach therefore requires that the aberrations in the main beam be mapped directly and unambiguously into the sample beam over the expected range of beam steering angles. For a "perfect" hologram, this property is assured by the wavefront theory of holography. A real holographic grating, on the other hand, introduces additional aberrations of its own into the sample, but not equally into the main beam.

These spurious aberrations originating in the HG itself can be corrected in the grating design, but the correction can be made exact only if the geometry of the two beams and the distortions of the primary mirror are precisely specified and do not change with time. Since the geometry will shift somewhat because of beam steering and various unavoidable misalignments of the telescope and sensor elements, some grating aberrations will remain. To ensure that these residual aberrations do not become excessive, a thorough optical design and tolerance analysis is required. Similarly, aberrations caused by primary mirror distortions can only be assessed by means of a detailed analysis. Such an analysis was performed and is described in Section 2.3.2.

Beam Sampler on a 45-Degree Mirror

An example of the second type of beam sampler investigated during the study is illustrated in Figure 6. This beam sampler consists of a low-efficiency holographic grating on a flat mirror oriented at 45 degrees to a collimated laser beam, as shown. The grating is designed to focus the first-order sample beam to a point on the normal to the center of the mirror, the zeroth order being diffracted (reflected) at 45 degrees. This configuration is representative of a folding mirror such as those used to relay the laser beam from an HEL to the beam expander. In this case, the sample beam might be utilized for laser diagnostic purposes.

Because it employs a flat substrate and an off-axis design, the 45-degree beam sampler involves design and fabrication considerations differing from those pertaining to the on-axis primary mirror beam sampler of Figure 4. In particular, aberrations in both the main and sample beams tend to be larger, while the flat substrate is more easily coated with a

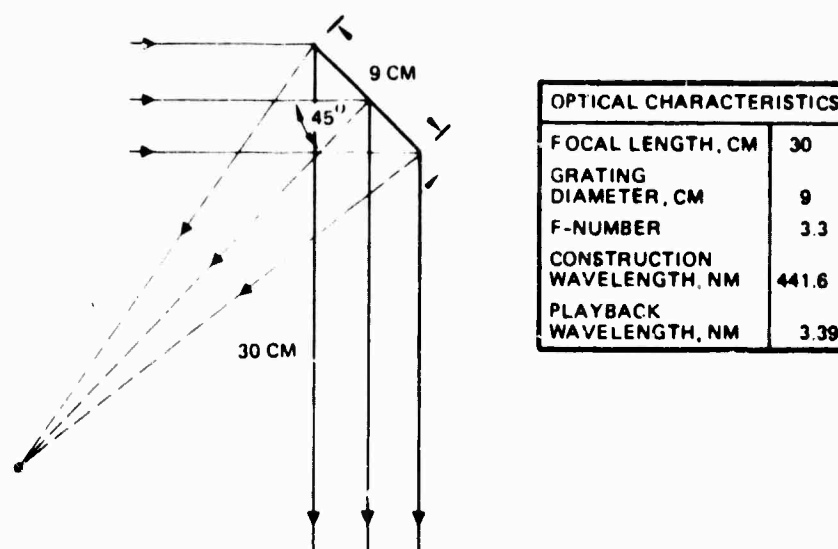


Figure 6. Aberration-corrected 45-degree beam sampler.

uniform layer of photoresist than is a curved primary. For these reasons, this configuration was selected to demonstrate the aberration-corrected grating design described in Section 5.

2.2.2 High-Efficiency Grating Concepts

As in the case of the low-efficiency gratings described above, "high efficiency" holographic gratings are defined in accordance with their usage, rather than by some arbitrary range of diffraction efficiencies. The essential defining characteristics of these gratings is that the zeroth order is intentionally suppressed while the efficiency of one or more higher orders is maximized. This distinguishes them from low-efficiency gratings which utilize the zeroth order at high efficiency along with one or more higher orders at relatively low efficiency.

The foregoing definition of high-efficiency gratings encompasses a wide range of efficiency values, including the special (and idealized) case of 100 percent in a single order. In practice, these gratings usually have efficiencies exceeding 10 percent in all orders of interest. However, the converse is not necessarily true, i. e., an efficiency greater than 10 percent does not necessarily signify a high-efficiency grating. This distinction is also important from the fabrication standpoint since achieving maximum efficiency requires relatively deep grooves with good control of the groove shape and duty cycle; in comparison, the requirements for producing low-efficiency gratings are much less critical. (When efficiency uniformity is important, some degree of groove shape control may still be necessary for low-efficiency gratings, but the difficulties are significantly lessened because of the shallower grooves required.)

The feasibility of designing and fabricating high-efficiency holographic gratings was demonstrated in connection with Tasks III and IV of the study, which are documented in Sections 3 and 4, respectively. The present section is concerned with three conceptual applications of such

gratings in HEL systems: the holographic grating axicon, the virtual mirror, and the holographic grating rhomb. These concepts were illustrated in Figure 2. They are described briefly below and are analyzed in more detail in later subsections.

Holographic Grating Axicon

The holographic grating axicon (HGA), shown in Figure 7, is of interest as a potential high-power optical component in the resonator of a high-energy laser. It consists of equally spaced concentric circles etched onto a flat substrate. The diffracted beam from an HGA has properties very similar to those of a beam reflected or refracted from a conical optical element, i.e., from an axicon. For example, a matched pair of these gratings will split a collimated beam axially into an annular

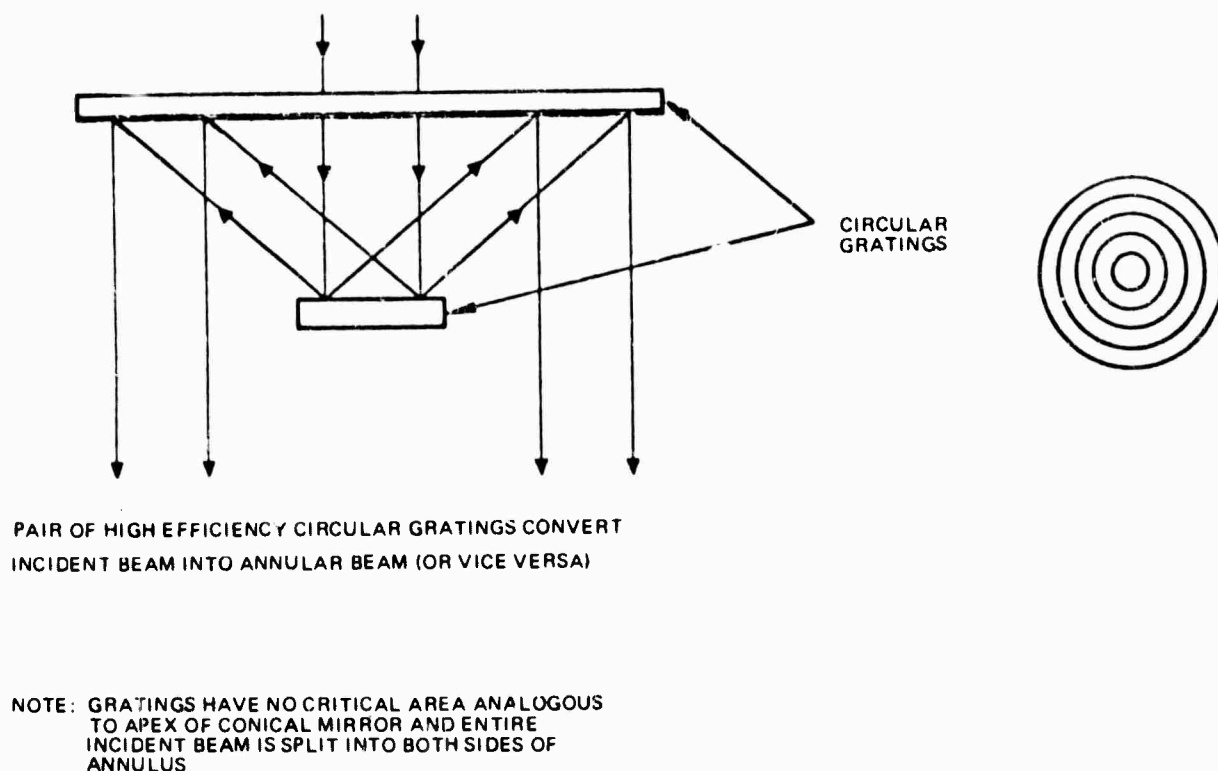


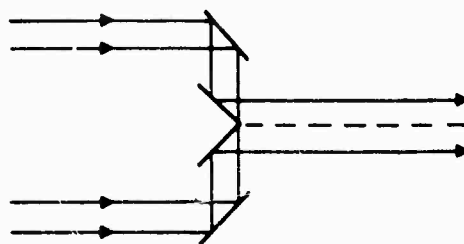
Figure 7. Holographic grating axicon.

beam, or conversely, will convert an annular beam into a compacted or solid beam. These two cases are illustrated in Figures 7 and 8c, respectively; a conventional axicon, constructed from two axial cones, is also shown for comparison in Figure 8a.

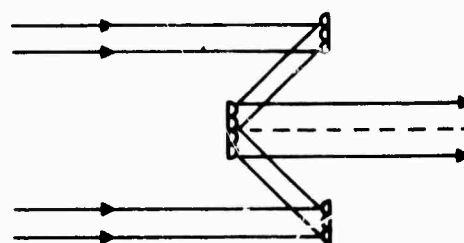
Holographic grating axicons offer several potentially significant advantages over conventional axicons for use as intra-cavity HEL components. First, because the HGA can be fabricated on a flat substrate, it eliminates a major problem associated with the design of conventional high power axicons — that of providing an adequate flow of coolant in the vicinity of the tip. In addition, flat elements are generally easier and less costly to manufacture than conical elements of comparable quality. Finally, when used in the combining mode (Figure 8c), the holographic grating axicon produces a compacted beam containing a complete overlap of the annular beam, whereas with a conventional axicon, only limited mixing occurs, the result of diffractive coupling from the tip. This property of the "mixing" HGA produces much greater communication among all parts of the annular beam, leading, potentially, to improved mode control.

As an intra-cavity device, the holographic grating axicon also suffers certain drawbacks, including: (1) wavelength dispersion (potentially troublesome for multi-wavelength lasers), (2) variation in diffraction efficiency as the groove orientation changes with respect to the polarization vector of the incident HEL beam, and (3) the phase sensitive nature of the mixing HGA when used in the combining mode.

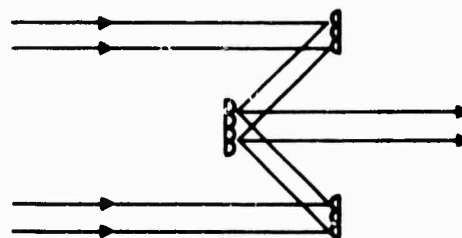
Mixing holographic grating axicons are examined quantitatively in Section 2.3. Another type of HGA, called the "non-mixing" axicon is shown in Figure 8b. Since this device is optically equivalent to a conventional axicon, it does not provide the desired mixing action and hence was not investigated in detail.



a. Conventional axicon



b. "Non-mixing" grating axicon



c. "Mixing" grating axicon

Note: 1. Mixing
2. Beam size change
3. Interference

Figure 8. Types of axicons.

Virtual Mirror

According to Fundamental Property 3 of Section 2.1.2, the optical powers of a nonlinear holographic grating and its substrate are additive. When a high-efficiency grating is used to concentrate the diffracted energy into the first (or higher) order, the grating/substrate combination is called a "virtual mirror". A case of particular interest consists of a high-efficiency holographic grating on a flat substrate, the total optical power being provided by the grating. A device of this type might serve, for example, as a virtual primary mirror. This design would offer a potential cost savings to be realized by using a flat substrate in place of a large figured primary.

Since the optical properties of a holographic grating depend primarily on the groove spacing and are independent of the grating efficiency, the analysis of the primary mirror beam sampler also applies in large measure to the virtual mirror. A key technical question relating to the viability of this concept is whether the requisite high efficiency can be achieved in useful geometrical configurations. From the discussion in Section 2.3.3, the virtual mirror appears to be viable, from an efficiency standpoint, in an off-axis configuration. However the efficiency with on-axis designs is limited to about 40 percent because of the presence of strong multiple orders. On the other hand, off-axis systems have relatively large aberrations and are also highly dispersive.

Holographic Grating Rhomb

In high-energy laser systems, a conventional plane grating is often placed in the path of the HEL beam where the beam diameter is small. The grating may be used to perform one or both of two functions: (1) obtaining a low-efficiency sample of the HEL beam, and (2) permitting the aperture of the main HEL telescope optics to be shared

with infrared target radiation used for target-loop tracking and phase-conjugate adaptive optics systems. However, in systems employing multi-line lasers or a broad-band target return, the high wavelength dispersion of the grating must be corrected before performing wavefront tilt and aberration measurements. This angular dispersion may be corrected by using a grating rhomb, but the angular dispersion at the first grating in conjunction with the separation between the two gratings results in a wavelength dependent aperture shear (or wander) on the second grating. To correct both the angular dispersion and aperture shearing effects, dual grating rhomb configurations may be used. A typical example is shown in Figure 9. Such configurations contain four gratings which are larger than the beam diameter and hence lead to large optical assemblies between the beam sampling (or aperture sharing) grating and the error sensing devices.

In principle, the size of the required optical assembly can be substantially reduced by substituting holographic gratings for the linear gratings in the rhomb. A tentative configuration for such a device was conceived during the study, and preliminary investigation determined that it has sufficient potential to justify a more thorough optical analysis. The holographic grating rhomb concept (which is proprietary) is described in Section 2.4.3.

BACK-TO-BACK RHOMB
CONFIGURATION: FOUR
LARGE GRATINGS, NO
WANDER

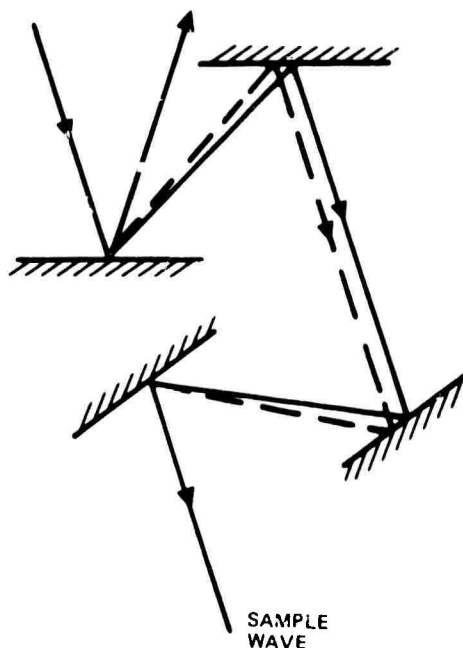


Figure 9. Dual grating rhomb.

2.3 OPTICAL DESIGN ANALYSIS

In this section, the optical analyses performed under Task I (Holographic Grating Conceptual Designs) and Task II (Analytical Investigations of Conceptual Designs) are described. These investigations included one low-efficiency concept (holographic grating beam sampler) and three high-efficiency concepts (holographic grating axicon, virtual mirror, and HG rhomb). A brief discussion of the major design issues precedes the detailed analyses.

2.3.1 Optical Design Issues

Each holographic grating concept described in Section 2.2 was examined analytically to determine the conditions under which it would be practicable in the appropriate HEL system configuration. For this purpose, the grating performance was evaluated principally in terms of the aberrations present in the diffracted beams, computed for a representative range of design parameters. The results were then utilized in various ways to assess the feasibility of each concept.

For HG beam samplers, the appropriate criterion of feasibility depends on whether the sample beam is to be used for wavefront control, LOS control, or both. For wavefront control, the appropriate criterion is the degree to which the aberrations in the sample beam match those in the main beam. The major design issue in this case is the correction of aberrations in the sample caused by the holographic grating itself. Depending on their nature and cause, these aberrations may or may not have counterparts in the main beam. There are three principal sources of aberration, which are discussed in Section 2.3.2:

1. Aberration dependence on field angle
2. Optical alignment errors
3. Distortions of the holographic grating on the primary mirror

In designs having a very small field of view, such as the 45-degree beam sampler, the aberrations in the HG itself can be fully corrected, and this was demonstrated under Task VI of the study. However, in applications such as beam sampling from the primary mirror, the aberrations in the grating can change by a large amount over the field of view of interest (generally a few milliradians). As will be shown in Section 2.3.2, this can be overcome through integrated design of the holographic grating together with other optical elements in the sample beam.

Aberration differences between the main and sample beams can also arise because of misalignments of optical elements relative to one another. Alignment tolerances have therefore been estimated; they indicate that, for purposes of wavefront control, reasonable tolerances can be established for the correction of third and higher order aberrations. This is a valid conclusion since wavefront tilt (or LOS control) is independent of wavefront control, and range (or focus) information is inherently independent of any local error-sensing systems.

Lastly, heating of the primary mirror caused by the typically non-uniform HEL beam intensity profile can cause non-linear distortions of the holographic grating, which, in turn, give rise to wavefront differences between the main and sample beams. Both surface warping and in-plane surface expansions which affect the local grating spacings are of interest. The effects of surface warping are dependent on the geometry. Analytical results show that there is an important class of systems in which the sample beam is diffracted in, or close to, the condition for retro-diffraction. For this class, surface warping of the mirror either before or after the grating is applied causes nearly equal aberrations in the main and sample beams. Hence, correction of the sample wavefront is commensurate with correction of the main beam, as required for wavefront control. This is an important conclusion because it implies that wavefront errors caused by surface warping in all elements up to and including the primary mirror itself can be corrected by correcting the sample beam. However, this advantage does not accrue to highly asymmetric systems in which the magnitude of the angle of diffraction is considerably different from the angle of reflection (or incidence).

For LOS control, a very different situation exists. Here, the basic requirement is that the centroid, or average direction, of the sample beam must coincide with the direction of the outgoing main beam to within a

microradian or less for all beam steering angles (i.e., throughout the field of view). Two basic problems are then immediately apparent in the beam sampling concept as depicted in Figure 5, Section 2.2. First, there is an afocal magnification ratio between the main and sample beams, which implies the absence of a one-to-one correspondence between the two beams as a function of the beam steering angle. Second, a small decentration of the error sensing optics relative to the primary mirror causes a tilt error in the sample beam which is not present in the main beam, as shown in Figure 10. The magnitude of this error, referred to target (i.e., main beam) space, is the decentration divided by the hologram focal length. Thus, a $1\text{-}\mu\text{m}$ decentration error in a system having a 1-meter hologram focal length causes a $1\text{-}\mu\text{rad}$ angular error. This exceedingly tight positional requirement cannot be tolerated for LOS control, particularly in view of the high vibration environment in which the HEL systems of interest must generally operate. Solutions to the foregoing two issues involve questions of systems implementation rather than properties of the holographic grating itself. Several approaches to solving these problems were investigated and are discussed in Section 2.1 of Volume II, following the main proprietary concept for LOS control. In other respects, the design issues and effects of HG distortions tend to be less critical than those for wavefront control since only tilt information is needed for LOS control.

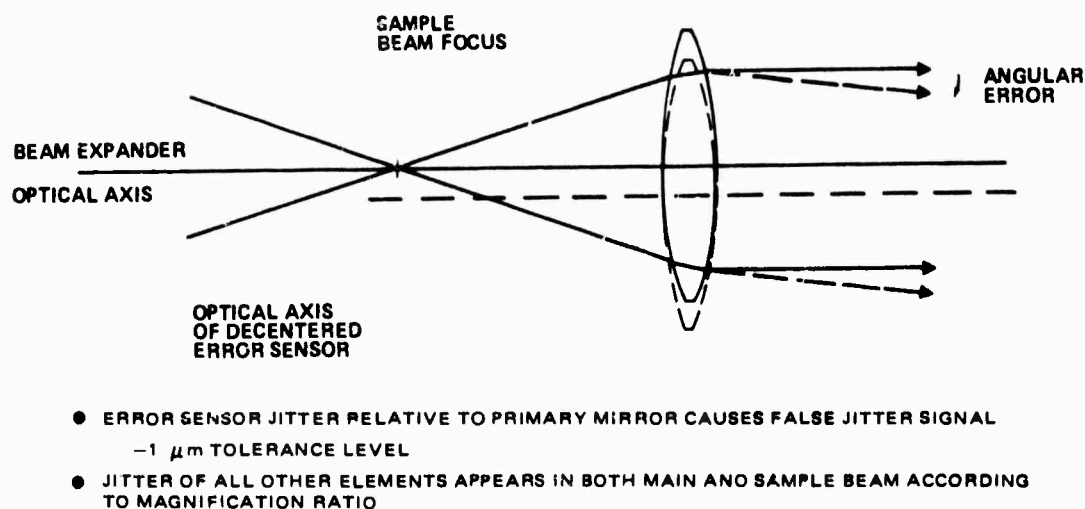


Figure 10. Principal sources of error for beam steering control.

In the case of the holographic grating axicon, the aberrations in the diffracted beams were computed as a function of the tilts and mutual decentration of the two holographic elements. These results were then used to assess the sensitivity of the axicon to such misalignments. An issue of special importance for the mixing HGA was to evaluate the effects of combining two coherent, possibly aberrated wavefronts into a single compacted beam. This issue was analyzed by means of the wavefront theory of holography, which showed that small errors in the incident wavefronts result in an intensity mapping of the aberrations, caused by coherent interference. Another holographic grating axicon issue concerned the question of limiting the possible number of diffracted orders to aid in achieving high efficiency; this was found to be feasible through appropriate design of the grating period.

For the holographic grating rhomb, the major design issues involve correction of aberrations, alignment sensitivity, and wavelength dispersion for multi-line lasers. These questions were not investigated in detail, however.

2.3.2 Primary Mirror Beam Sampler

The analyses that were performed to resolve the issues pertaining to beam sampling from the primary mirror for wavefront control are discussed in this section. As noted in Section 2.3.1, these issues are: (1) aberration differences between the main and sample beams resulting from field-of-view requirements, (2) element misalignments (tolerances), and (3) primary mirror distortions. The magnitudes of the aberrations and tolerances depend on the primary mirror f /number, beam steering angle, beam expander afocal magnification, and telescope type. A general tradeoff range for these parameters was established early in the program and is shown in Table 1, with the added assumption that the beam expander is designed to have no spherical aberration. This means that the primary mirror conic constant is an additional variable, the secondary mirror always

TABLE 1. HOLOGRAPHIC BEAM SAMPLING TRADE-OFF RANGES

Parameter	Values
Primary Mirror f/Number	0.8 to 4
Beam Steering Angle, mrad	0.5 to 4
Beam Expander Magnification	5 and 10
Outgoing Beam Diameter, m	1.0
Holographic Grating Construction Wavelength, μm	0.4416
Main Beam Wavelength, μm	3.8
Telescope Types	Elliptical Primary Spherical Secondary Two Cofocal Parabolas

being figured for perfect on-axis imagery in the outgoing wavefront.* For a nominal starting point, the outgoing beam was assumed to be one meter in diameter and the laser wavelength $3.8\mu\text{m}$, yielding a diffraction-limited beam expander performance of slightly less than $10\mu\text{rad}$. The construction wavelength for the holographic grating lies in the blue region of the spectrum and is therefore suitable for exposing photoresist.

The optical configurations investigated fall into the following three categories: (1) on-axis systems, (2) off-axis systems with axi-symmetric beam sampling, and (3) systems with asymmetric beam sampling (see Figure 1). Most of the optical design work was performed for on-axis systems, which are probably the most applicable to HEL systems, being the least complex and least sensitive to alignment errors. Off-axis, axi-symmetric beam sampling systems are essentially an extension of the on-axis case to low parent f/number systems used with a decentered aperture stop. Asymmetric systems present a difficult and lengthy optical design problem that was addressed only to the extent necessary to gain an

*The conic constant is a parameter related to the eccentricity, it has a different value for each of the conic sections (sphere, paraboloid, etc.)

understanding of the problems involved and the relative magnitude of the tolerances that must be held.

Optical Design of On-Axis Systems

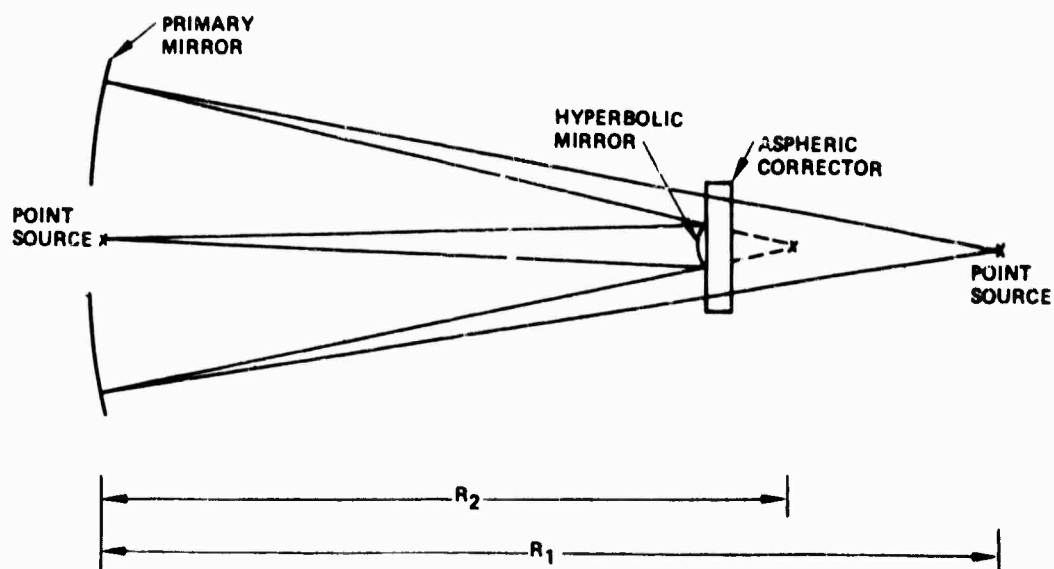
The following discussions cover (1) the aberrations present in the holographic grating itself, (2) correction of these aberrations by integrated design of the HG and error sensing optics, and (3) alignment tolerances for wavefront control.

Aberrations in the Holographic Grating. The first stage in the optical design of on-axis systems is to investigate the aberrations of the holographic grating itself, assuming that the sample beam is brought to a focus in the vicinity of the secondary mirror. The HG can always be designed to have no spherical aberrations. One way to accomplish this is to assume identical construction and playback optics. However, this condition cannot be realized in practice because of the wavelength difference between construction and playback, and also because both construction beams must lie on the same side of the mirror. The desired HG focal length, F_H , can be obtained provided the distances R_1 and R_2 , of the construction point sources from the grating satisfy the equation:

$$\frac{1}{F_H} = \mu \left(\frac{1}{R_1} - \frac{1}{R_2} \right)$$

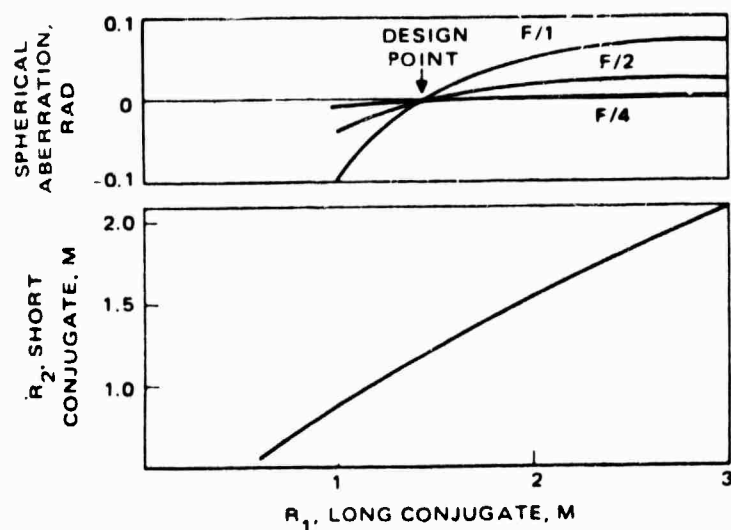
where μ is the ratio of the HG playback to construction wavelengths (refer to Figure 11).

The relation between R_1 and R_2 for a 1-meter aperture, $f/1$ parabolic primary, is shown in the lower curve of Figure 12. The spherical aberration in the sample beam is also a function of R_1 and R_2 , but the third order aberration goes through a zero which presents a natural design starting point. However, it is not possible for both



• ASPHERIC ELEMENT CORRECTS RESIDUAL SPHERICAL ABERRATION

Figure 11. Hologram construction point source locations.



• SPHERICAL HOE CONSTRUCTION WAVEFRONTS
• SPHERICAL SECONDARY MIRROR

Figure 12. Construction conjugates and spherical aberration in the sample beam.

third and higher order spherical aberration terms to be zero simultaneously for any one pair of construction optics conjugates; hence, there is always some residual spherical aberration at the starting point of a holographic grating design. For an $f/1$ primary mirror, this on-axis aberration amounts to about 0.5 mrad. (Figure 13). As the f /number is increased, the residual aberration decreases rapidly, since the third and fifth order spherical aberration terms depend on the third and fifth powers of the aperture, respectively. This spherical aberration is readily corrected by introducing compensating aberrations into one or both of the HG construction wavefronts, using an aspheric corrector as illustrated in Figure 11.

Next, assuming an HG designed to have no spherical aberration, it is of interest to investigate the aberrations off the axis. The most dominant aberration by far is coma, which is a strong function of the shape of the primary mirror (i.e., spherical, parabolic, elliptical,

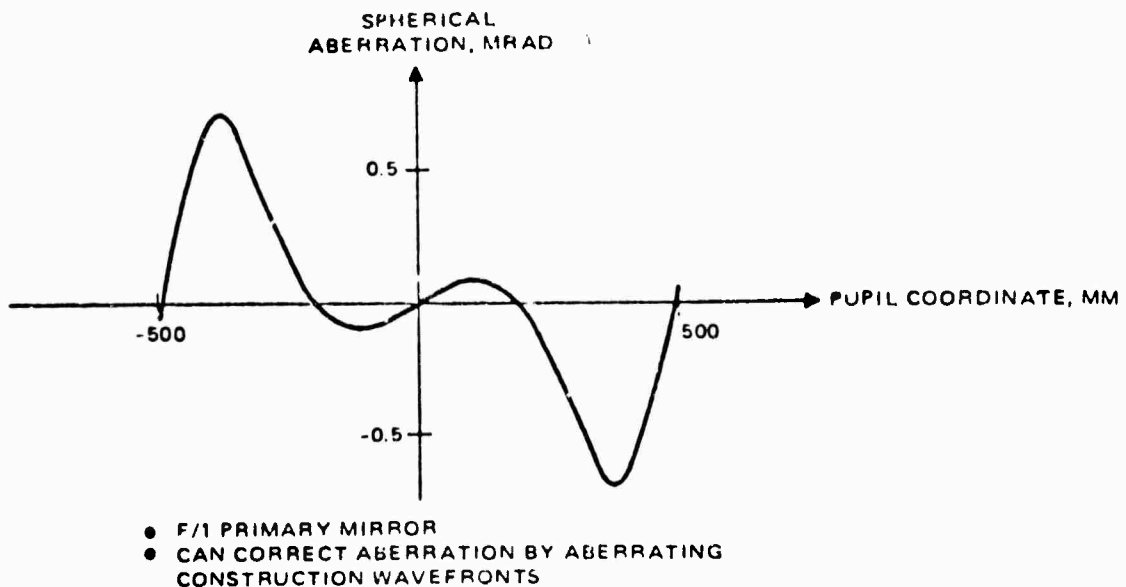


Figure 13. Residual spherical aberration at design point.

etc.). The coma in the sample beam is shown in Figure 14 for a beam expander comprised of (a) two cofocal parabolas, and (b) a spherical primary mirror plus a secondary mirror figured for no spherical aberration in the main beam. There is much less coma in the sample beam with a spherical primary than is present with a parabolic primary. However, the reverse situation exists in the main beam, for which two cofocal parabolas are free of the third-order aberrations coma and astigmatism.

An equal amount of coma in both beams is desirable, so that the aberrations match and wavefront errors can be sensed unambiguously in the sample beam for all beam steering angles. The possibility of matching the coma in both beams by judicious choice of the primary mirror conic constant was therefore investigated. The results, shown in Figure 15, established that such a compromise does not exist; there is an approximately equal difference between the comas in the two beams for all primary mirror conic constants. Such a large aberration difference between the two beams is unacceptable from the point of view of wavefront control as the

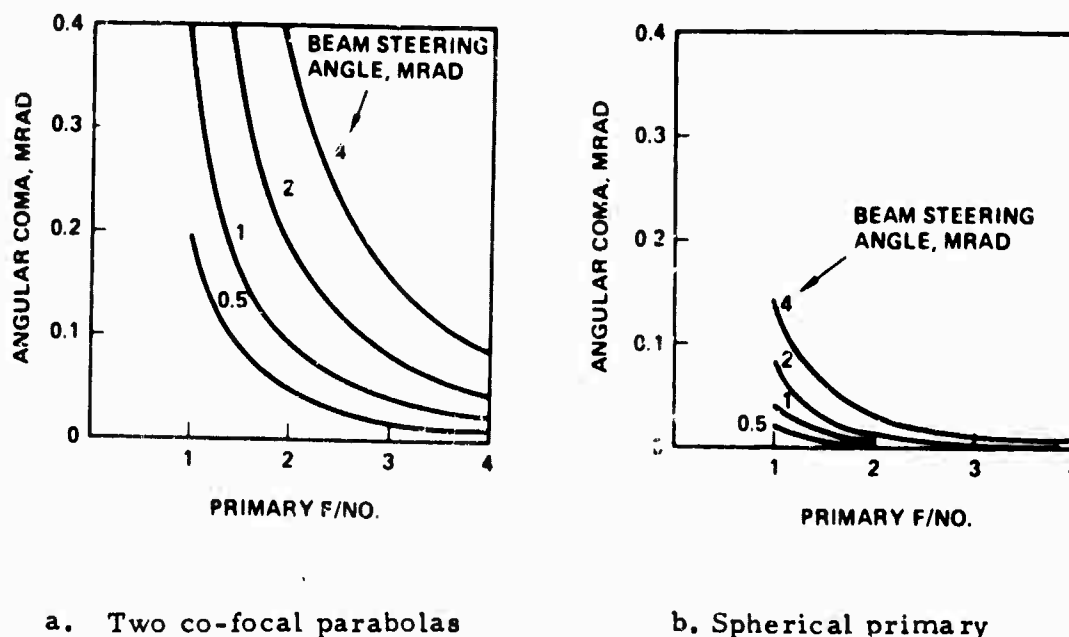


Figure 14. Coma in sample beam as a function of primary f/number and beam steering angle.

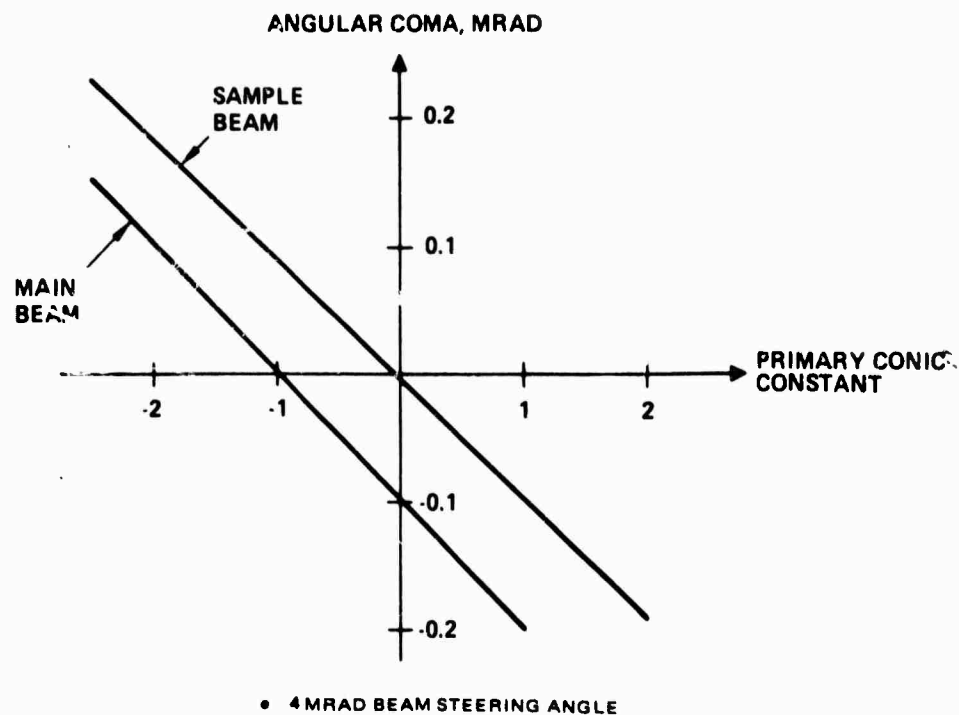


Figure 15. Variation of coma with primary mirror conic constant.

beam is steered. The aberration can only be corrected by integrated design of both the holographic optics and the error sensor optics.

Integrated Optical Design. Having established that the aberrations in the holographic grating are significantly different from those in the main beam, it was necessary to show that these aberrations can be balanced by proper design of the optics between the HG and the error sensor. For this stage of the design, it was assumed that the wavefront error sensor (which may, for example, be a shearing interferometer or a Hartman arrangement) is perfect, since the relevant issue is to provide the proper input to the error sensor, and not to design the error sensor itself. There were thus two requirements to be met. First, the aberrations in the sample beam must represent the aberrations in the main beam for all beam steering angles. Second, the exit pupil for the optics traversed by the sample beam must be accessible to the error sensor, so that no aperture wander can occur as a function of the beam steering angle on the sub-aperture

array of the wavefront error sensor. There are many possible optical arrangements for accomplishing this, some of which depend on a specific error sensor configuration. For purposes of the Holographic Grating Study, two of these concepts were pursued. Although the results are based on a telescope design of two co-focal parabolas (this design being essentially aberration-free for the main beam), the feasibility of modifying the designs for other telescopes (Dal Kirkham, etc.) was also established.

The two concepts investigated are shown in Figure 16. In the unfolded concept, the sample beam from the holographic grating is focused in the vicinity of the secondary mirror and is subsequently collimated by a two-mirror telescope. This telescope also images the primary mirror (which is the effective aperture stop) at a location which is accessible for

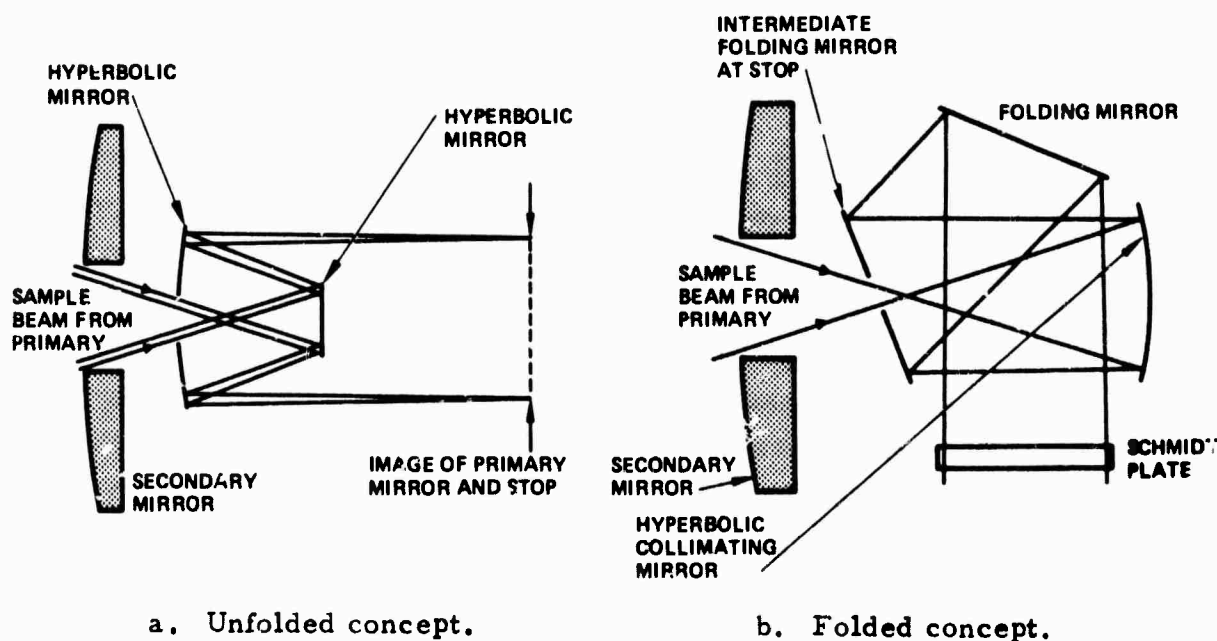


Figure 16. Two integrated design concepts.

mounting an error sensor. This sensor might consist of a Hartman array or a mirror that is servo-controlled to subsequently direct the sample beam in the same direction for all beam steering angles. In the folded concept (Figure 16b), the sample beam passing through a hole in the secondary mirror is collimated by a single mirror. The primary mirror (stop) is imaged on the intermediate folding mirror, which is servo controlled so that the collimated sample beam does not wander on the error sensor aperture array, as a function of the beam steering angle.

The design criterion for the aberrations can be achieved in the following ways. For each concept the residual spherical aberration (Figure 13) in the holographic grating can be corrected by a Schmidt plate, either in the playback optics (Figure 16b) or in the hologram construction optics (Figure 11). The field curvature can be corrected by varying the curvature of the mirrors in the error sensor optics. In the folded concept, however, there is only one mirror with power so that field curvature cannot be corrected without defocusing the beam. For both concepts, the coma is corrected by varying the conic constants on the mirrors in the error sensor optics.

The performance of five designs is summarized in Table 2. The designs are variations of the two concepts discussed above, depending on the mechanism used for correction of spherical aberration. Spherical aberration and coma are well corrected in all cases. The residual aberration in the folded design concepts is the peak error at the edge of the 6-mrad beam steering field-of-view for which they were designed. These residuals are at a level where they can readily be calibrated out as a function of the beam steering angle, assuming an appropriate wavefront correction algorithm is available. In the unfolded concept, the residual astigmatism and field curvature can also be corrected because of the

TABLE 2. PERFORMANCE FOR A TYPICAL LINEAR
OBSCURATION LESS THAN 40 PERCENT

Concept	Spherical Aberration Correction	Sample Beam Diameter, cm	Exit Pupil Location, cm	Aberration with ± 3 mr Beam Steering $f/\text{No.} = 2$
Folded	Hologram	10.6	20	Field curvature 8 μrad Astigmatism 2.2 μrad
Folded	Schmidt Plate	10.6	20	Field curvature 8 μrad Astigmatism 2.2 μrad
Unfolded	Hologram	10.6	25	No significant aberrations
Unfolded	First mirror in error sensor	10.6	25	Large, limited to approximately ± 1 μrad beam steering
Unfolded	Hologram	17	75	Can be made perfect. 1 μrad residuals

additional degrees of freedom available in the two-mirror collimating optics. The last design employs a different afocal magnification (6X as opposed to 10X) and the exit pupil is located far from the secondary mirror. This represents an attempt to design a system in which the sample beam could be folded so that the error sensor could be located to the side of the telescope, rather than behind the secondary mirror.

The foregoing designs demonstrate that the holographic grating can be designed in conjunction with the error sensing optics to ensure that aberrations in the sample beam match those in the main beam over a large range of beam steering angles. Once this point had been reached in the

program, the optical design was not carried further because to do so meaningfully would require a specific system and optical configuration.

Alignment Tolerances for Wavefront Control. The unfolded concept was investigated to determine alignment tolerances in the position of the error sensing optics relative to the primary mirror. This is an important task because in a practical system, the high vibrational environment makes these tolerances the most difficult to hold. The error sensing optics are relatively compact, and errors caused by static misalignments can be largely accommodated by calibrating the error sensor.

The dominant aberration produced by the misalignment of the error sensing optics is coma. As a crude tolerance criterion, the amount of misalignment producing a maximum angular error of $10 \mu\text{rad}$ referred to target space was computed. Since this corresponds to the extremes of a coma flare, it is roughly equivalent to maintaining a diffraction-limited system for a 1-meter aperture and the $3.8\text{-}\mu\text{m}$ wavelength assumed for the analysis. Results of the tolerancing are shown in Figures 17 and 18 which show the allowable tolerance as a function of the primary mirror f/number . For practical purposes, the allowable tolerance can be scaled linearly with the angular requirement. It is clear that decentration in the regime of tens of microns, and tilts in the regime of 0.5 to 2 mrad must be maintained for fairly fast optical systems. Although these tolerances are not loose, neither are they considered too stringent to be held in a practical system.

Tolerances on the alignment of other elements in the system were also investigated, but found to be less stringent than those given above for the error sensor relative to the primary mirror.

In laser applications the beam is generally not collimated (focused at infinity) but is focused instead at a finite distance. Variations in the focal distance can be accomplished by changing the distance between

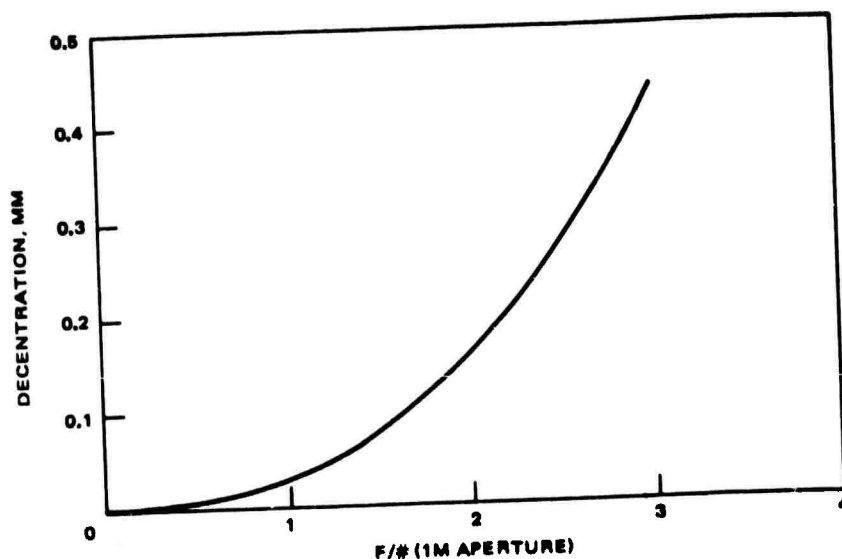


Figure 17. The maximum decentration of the primary which can be allowed while maintaining a diffraction-limited system ($10 \mu\text{rad}$) versus f/number .

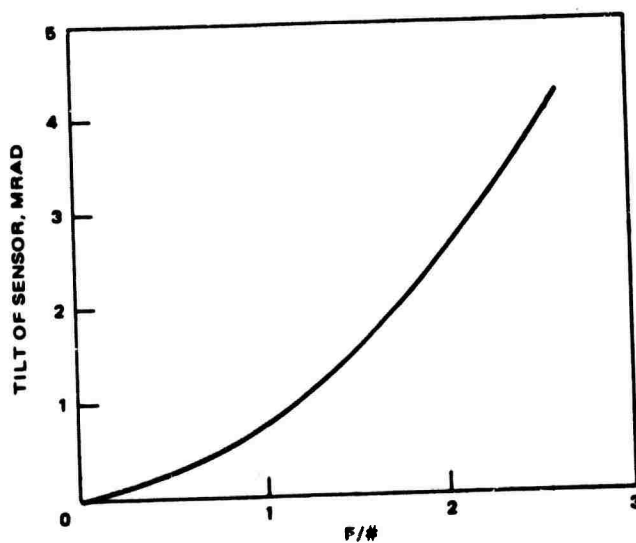


Figure 18. The maximum tilt of the error sensing optics which can be allowed while maintaining a diffraction-limited system ($10 \mu\text{rad}$ degradation).

the secondary and primary of the beam expander. In this study the beam sampler was designed to be aberration-free for a collimated beam. The effects of range variations on the sample beam were therefore investigated. The result of this investigation was that the angular errors in the sample beam are the same as those of the main beam scaled by the magnification, and optical path differences in both beams are the same. Two important implications of this are evident: (1) wavefront error sensing can be performed unambiguously regardless of range, and (2) range variation can, in principal, be accomplished by programmed control of the sample beam, though this may not necessarily be the best alternative from the point of view of HEL systems implementation.

Off-Axis Systems with Axi-Symmetric Sampling

Off-axis systems with axi-symmetric beam sampling, as in Figure 19, are extensions of the on-axis systems discussed above. They essentially

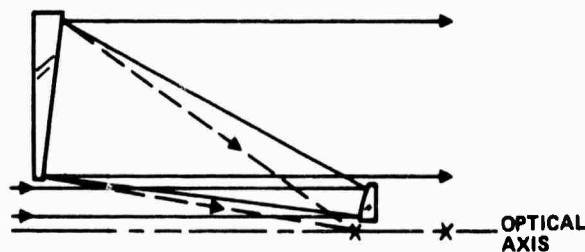


Figure 19. Off-axis system with axi-symmetric beam sampling.

involve extracting an off-axis portion of the on-axis system and scaling the desired dimensions to restore the original one-meter aperture. However, to maintain the same primary-to-secondary mirror separation as well, the parent f /number of the primary mirror must be decreased by a factor of about 2.5. For an $f/2$ system, the parent primary f /number therefore becomes 0.76. As a consequence, the amount of aberration correction required increases dramatically, and the tolerances that must be held are more stringent by about a factor of three, as shown in Figures 17 and 18.

An example of the typical aberrations observed in these systems is shown in Figure 20. These aberrations are mainly higher order spherical. (The very large peak at the aperture edge is caused by the rapid increase of high-order spherical aberration with aperture.) Such aberrations can be corrected readily by the use of high-order aspheric coefficients in

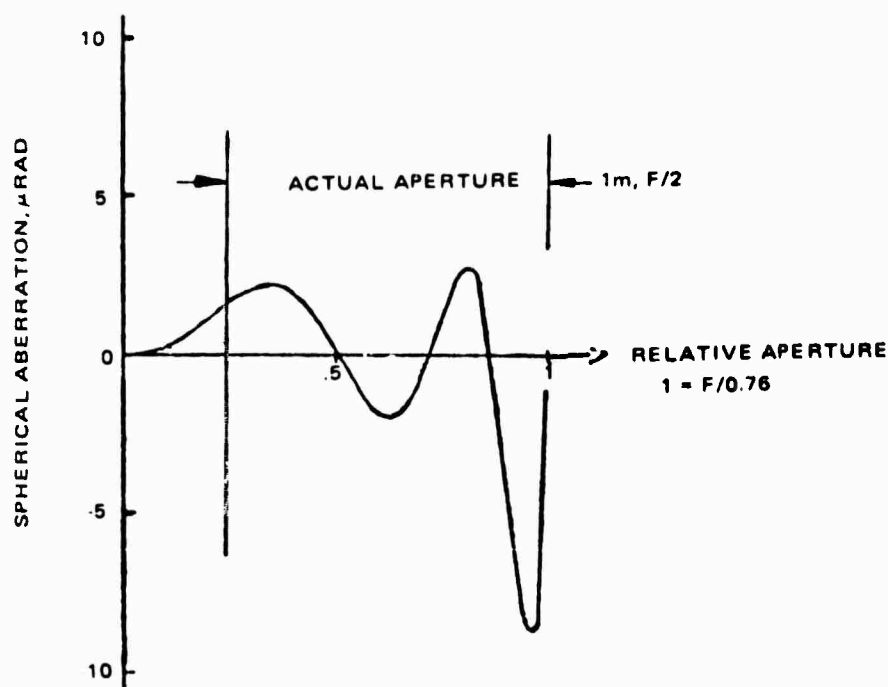


Figure 20. The on-axis aberrations of the parent telescope. The section to be used for the off-axis system is indicated.

the hologram construction optics; however, Figure 20 indicates that up to 11th order correction is required. In view of this and the tight tolerance constraints, only overriding systems requirements would justify an off-axis system in preference to the on-axis designs discussed previously. Having established the relative complexity of off-axis systems, no further design work was pursued. Nevertheless, there is no question that computer designs of these systems can be generated with well-corrected aberrations over a significant range of beam steering angles.

On-Axis Systems with Asymmetric Sampling

This concept involves constructing the holographic grating to focus the sample beam off-axis while the main telescope is an on-axis system as in Figure 21. An illustrative construction geometry for the concept is shown in Figure 22. In constructing the holographic grating with spherical wavefronts, there is a family of construction optics configurations for which

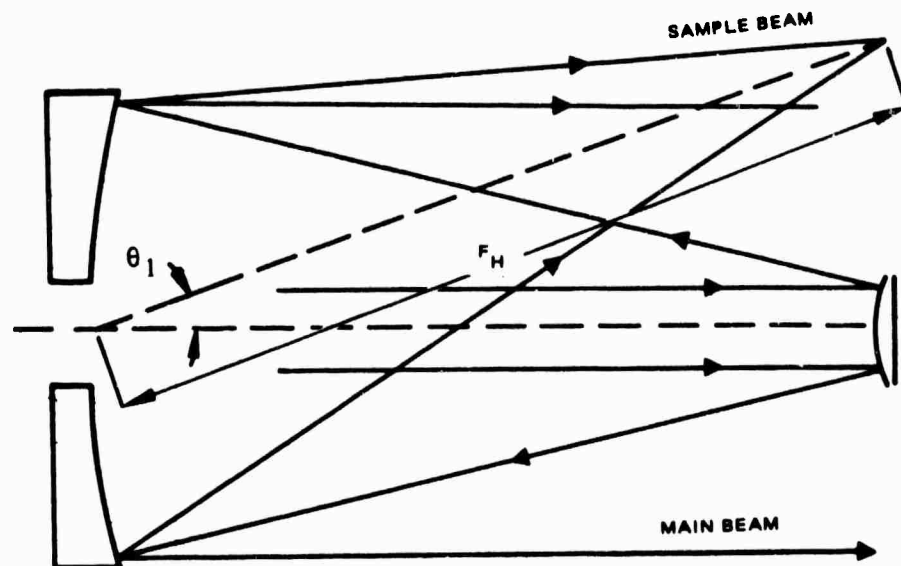


Figure 21. On-axis system with off-axis beam sampling.

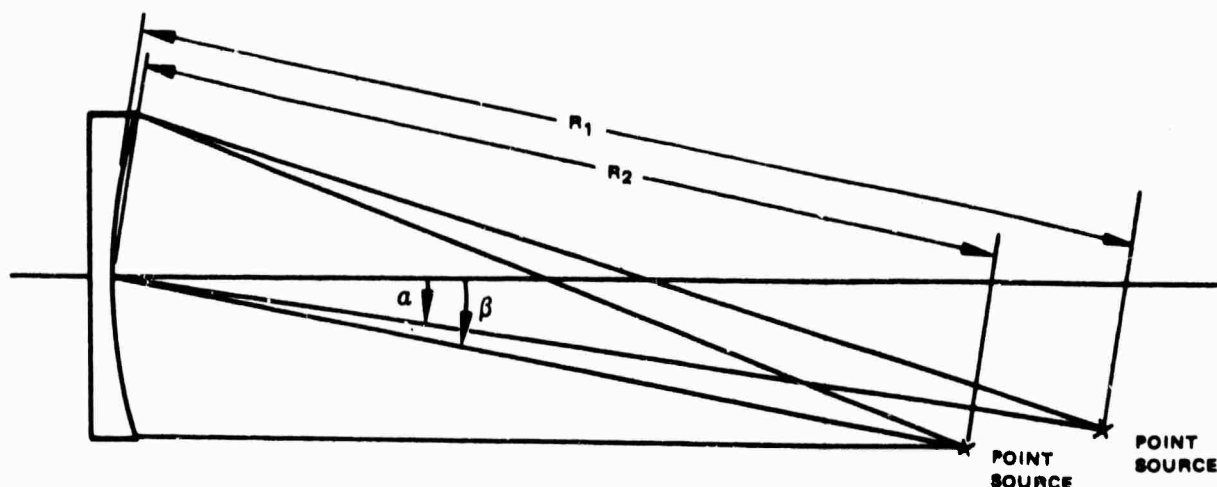


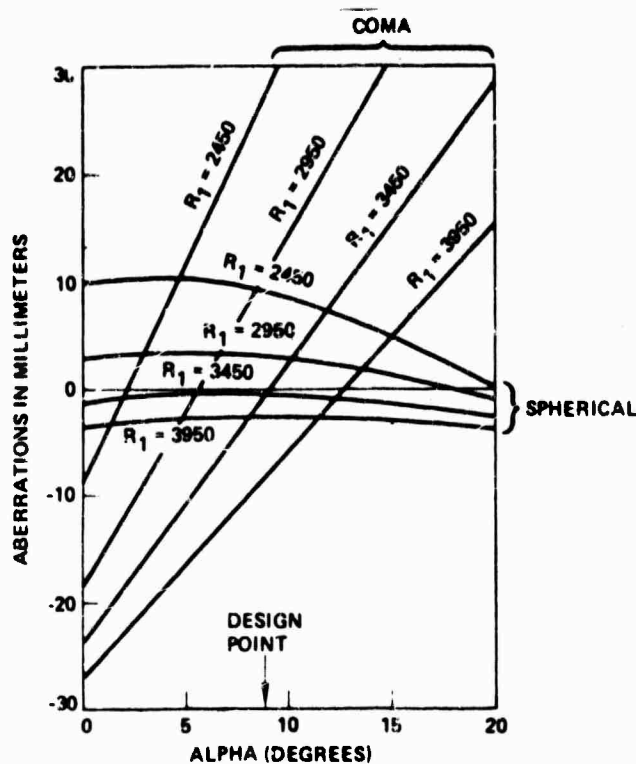
Figure 22. Hologram construction point source locations.

a) R_1 and R_2 can be selected to give the desired focal length, and b) α and β can be selected to give the desired off-axis angle, θ_1 , according to the grating equation. From this family of systems, it is desirable to select pairs of the parameters (R_1, R_2) and (α, β) that minimize the aberrations in the holographic gratings. With this as a starting point, the aberrations in the HG can then be further reduced by introducing appropriate aberrations into the two hologram construction wavefronts. Finally, the correction of aberrations throughout the field of view requires an integrated design of the HG and error sensing optics together.

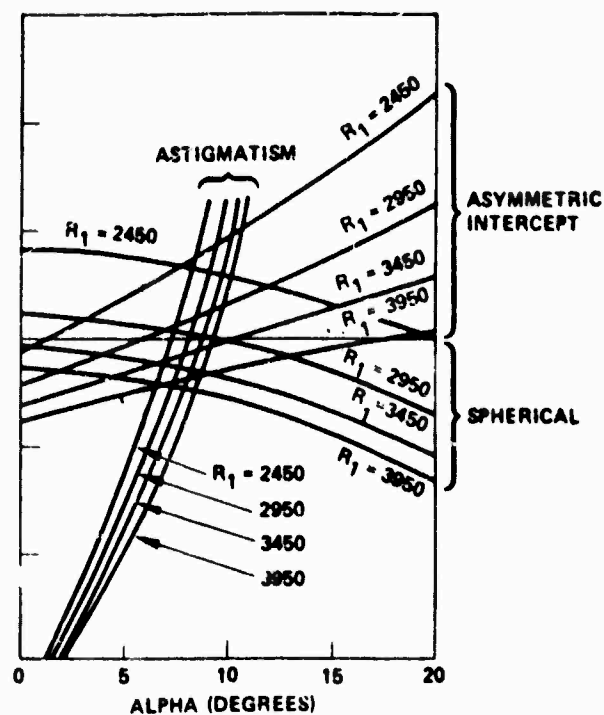
To assess the complexity of the design task, the aberrations in the holographic grating were investigated for a beam expander with an $f/2$ primary mirror and an HG focal length of 1770 mm. Because the sample beam optical system is no longer rotationally symmetric, asymmetrical aberrations arise for the central field point. The dominant aberrations are coma in the plane of asymmetry, spherical aberration in both planes, astigmatism, and a skew aberration (DY) which arises for fans

of rays traced out of the plane of asymmetry. These aberrations in the sample beam at the focus of the holographic element are shown in Figure 23 as a function of the angle α and the construction optics conjugate distance R_1 (see Figure 22). To convert the aberrations into angles, divide the linear aberration by the HG focal length, $f = 1770$ mm. There is no single pair of values of R_1 and α for which all the aberrations are zero. However, the aberrations in the plane of asymmetry go through a minimum around $R_1 = 3373$ mm and $\alpha = 8.75$ degrees. Since there is no equivalent position in the plane of symmetry, this presents itself as a natural starting point for an integrated design. Aberrations in the plane of symmetry can be minimized by introducing into the construction beams cylindrical lenses having optical power in the x-direction. This has the effect of changing the conjugates (R_1 and R_2) in the plane of symmetry while preserving α , β and the original conjugates in the y-z plane. The resulting construction optics are shown in Figure 24. The remaining aberrations at the central field point for an f/2 primary are shown in Figure 25.

At this stage, it is clear that significant aberrations are still present even at the central field point. To go further is a lengthy, complex optical design task involving other elements to aberrate the hologram construction beams and design together with some form of error sensing optics. However, the tolerance sensitivity of the concept to alignment errors of the error sensing optics with respect to the HG can also be assessed by computing the variation in the aberrations with field angle. The field aberrations shown in Figure 25 assume that the HG is so constructed that no aberration is present at the central field point. Since the beam steering angle is directly proportional to the image height in the HG focal surface, these curves can be used to estimate a decentration tolerance for the error sensing optics relative to the primary mirror. The results, shown in Figure 26, indicate that for decentration in the plane of symmetry, the tolerance is similar to that for on-axis systems. However, the tolerances are approximately three times tighter for a decentration in the plane of asymmetry.



a. Aberrations in the plane of asymmetry.



b. Aberration in the plane of symmetry.

Figure 23. Hologram aberrations versus the angle α and conjugate distances.

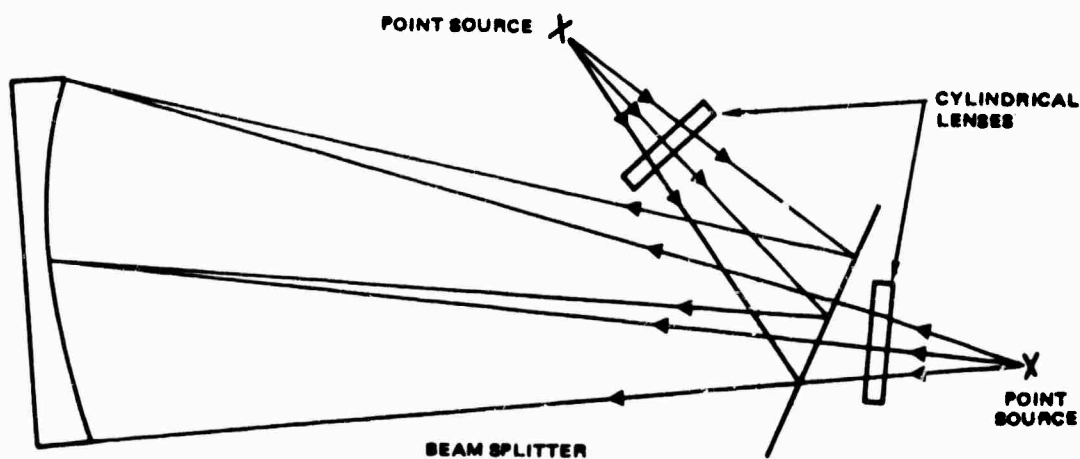


Figure 24. Hologram construction optics at the chosen design point.

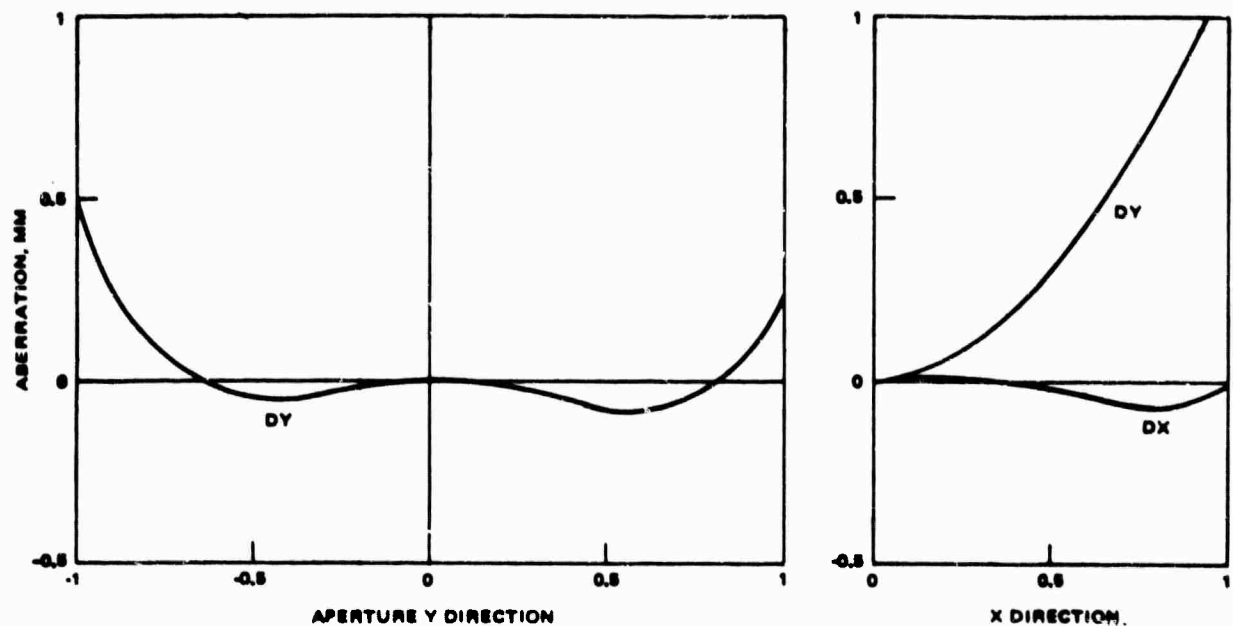


Figure 25. The resultant on-axis aberrations at the focal point of the hologram. The HOE focal length is 1770 mm.

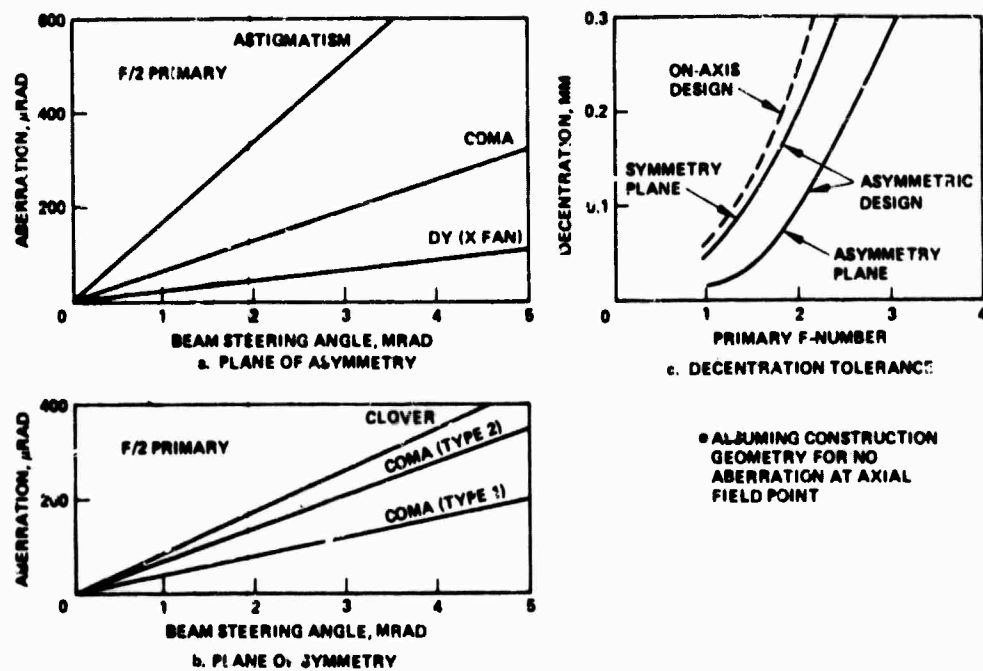


Figure 26. Off-axis aberrations and tolerance sensitivity for asymmetric beam sampling.

The aberrations to be corrected in an asymmetric beam sampling geometry have been shown to be large. With sufficient design effort, they can be corrected for at least a small range of beam steering angles. However, the design task is considerably more complex and correspondingly longer than for on-axis sampling. In addition, this approach has little advantage over the axisymmetric case; the sample beam is more conveniently located for packaging, but the design approach is more sensitive to misalignments and has other undesirable characteristics such as non-rotationally-symmetric distortions. The first order of distortion is rectangular (or anamorphic) and produces different values of magnification for the same field of view in each of the two perpendicular directions. For the intermediate image formed by the hologram this distortion is approximately 4 percent. This is not a negligible value for precision LOS control and would have a significant effect when such a system is used for beam steering. This effect will not be easy to eliminate in the integrated design of the error sensor optics.

2.3.3 Wavefront Errors Due to Surface Distortions

The effects of primary mirror distortions introduced a) preceding construction of the hologram, and b) following construction of the hologram, were investigated. In each case, both in-plane and out-of-plane distortions were studied. The results show that out-of-plane distortions (surface warping) affect both the main beam and the sample beam, and that the difference between the aberrations in the two beams can be very small so that correction of the sample beam is then commensurate with correction of the main beam. In-plane grating distortions, however, affect only the sample beam. Simulations performed for the Holographic Grating Study and another program indicate that the residual aberrations due to in-plane grating distortions are acceptably low for wavefront control.

The fact that out-of-plane distortions affect the main and sample beams to an almost equal degree in favorable geometries is an unexpected result which has far-reaching implications. The geometries of interest are those in which the sample beam is retro-diffracted, or nearly so (i. e., the diffracted beam returns along the optical path of the incident

beam). Systems that employ on-axis beam sampling from the primary mirror constitute an important class of design configurations in which the sample beam geometry is close to the condition of retro-diffraction. The practical significance of these systems is that correction of the sample beam by means of adaptive optics corrects for all errors in the HEL beam up to and including out-of-plane distortions on the primary mirror. A corollary to this is that the primary mirror need not be of high optical quality, provided that an ideal HG can be fabricated on it (see Figure 27).

Thus, correction of errors in the sample beam arising from errors in the primary mirror figure results in correction of the corresponding errors in the main beam. This conclusion suggests that significant potential exists for reducing the time and expense of fabricating large primary mirrors for HEL applications.

The extent to which out-of-plane distortions can be corrected depends on the holographic grating geometry, and is discussed below on a first-order analytical basis. This is followed by the results of a detailed computer modeling of playback with the primary mirror deformed

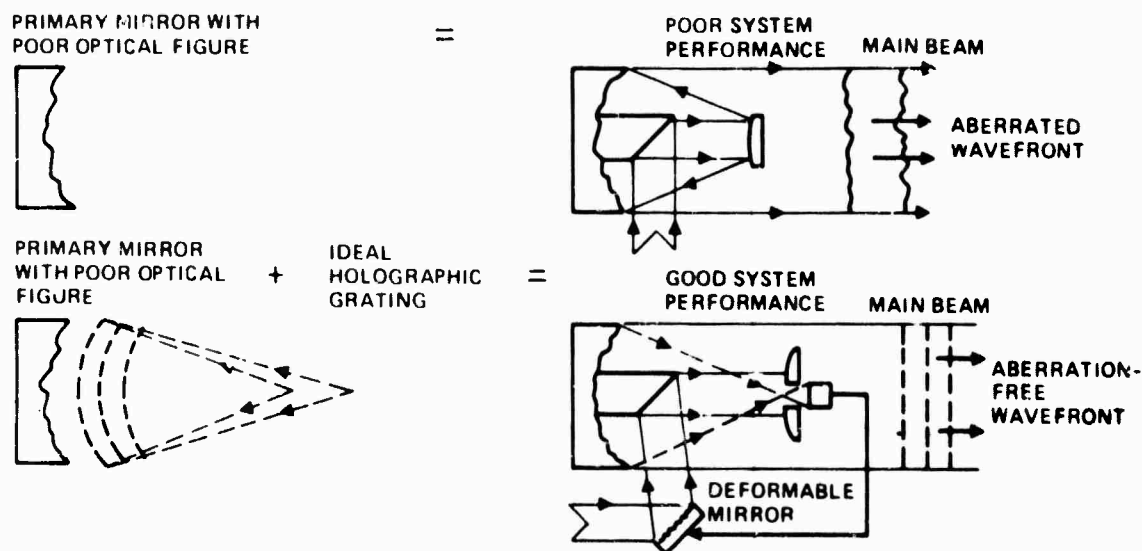


Figure 27. In certain classes of systems, good optical performance can be obtained with a poor primary mirror figure by correcting the sample wavefront obtained via an ideal HG on the primary.

a) before and b) after making the hologram. The detailed modeling requires the capability of tracing rays through a deformed holographic element. The technique used was developed at Hughes on company funds and is not detailed in this report. This technique is entirely different from and more precise than that indicated in the first-order analysis given below. However, the results obtained from the detailed model agree with the first-order predictions to a high degree of precision, lending credence to the statements made above. The technique used for ray tracing and computing OPDs through distorted holograms assumes that the coordinates (x_d, y_d, z_d) of a point on the distorted hologram are mathematically related to the coordinates (x_u, y_u, z_u) of a point on the undistorted hologram through the relationships

$$x_d = x_u + \Delta x(x_u, y_u)$$

$$y_d = y_u + \Delta y(x_u, y_u)$$

$$z_d = z_u + \Delta z(x_u, y_u)$$

The functions that are available for defining the distortion parameters Δx , Δy , and Δz are a 48-term Zernike polynomial, which contains both symmetric and asymmetric terms, a 24-term R^n polynomial, and an asymmetric Gaussian term. Note that the hologram is not considered to be distorted unless the surface has undergone a change in shape or size between hologram exposure and playback. This distortion may be due to changes in temperature, laser beam heating effects, or processing defects such as a non-uniform thickness of photoresist. The consequence of the latter effect is addressed at the end of this sub-section.

First-Order Effects of Out-of-Plane Distortion

The OPD error introduced by an out-of-plane distortion such as a bump of height h on the surface is readily seen by examining the projections of the bump in the directions of incidence and diffraction. Incident and diffracted wavefronts to be used for reference in OPD calculations are shown in Figure 28. Point A is directly above point C so that the phase

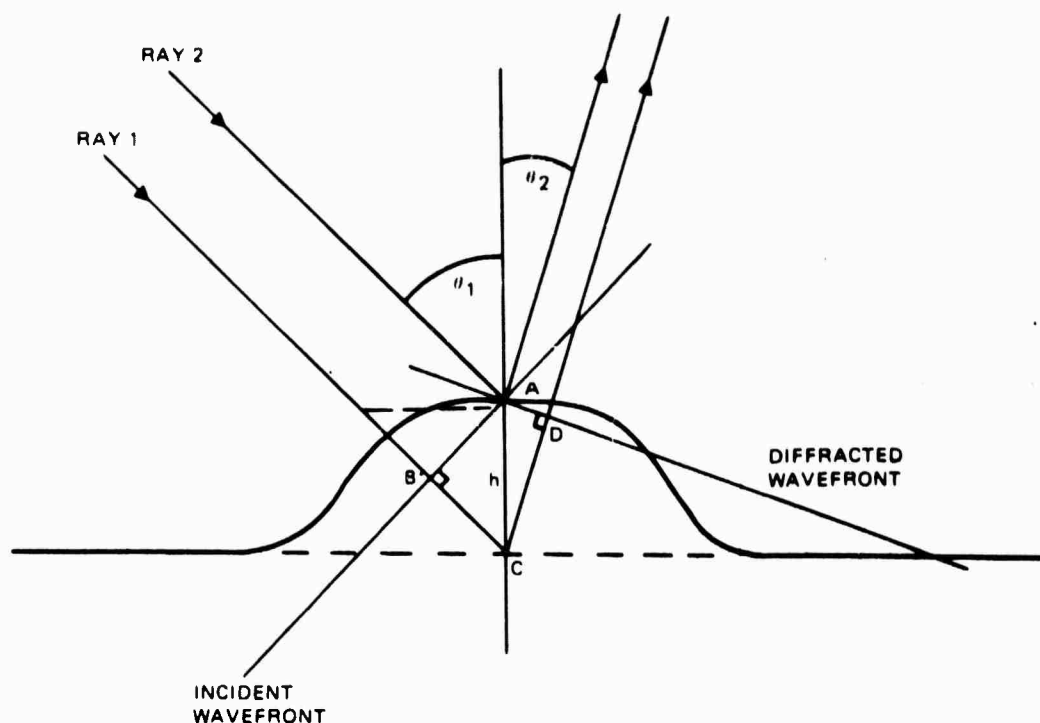


Figure 28. OPD error caused by out-of-plane distortion.

contribution due to the point of incidence on a given grating groove is the same for both A and C. The OPD error for ray 1, produced by the bump, and measured relative to ray 2 (diffracted from the undistorted grating), is thus:

$$\begin{aligned} \text{OPD} &= \text{BC} + \text{CD} \\ &= h (\cos \phi_1 + \cos \phi_2) \end{aligned}$$

This is simply the sum of the projections of the bump in the directions of incidence and diffraction, respectively. The following relations apply to reflection and retro-diffraction:

Reflection: $\text{OPD} = 2h \cos \phi_1 \quad (\phi_1 = \phi_2)$

Retro-diffraction: $\text{OPD} = 2h \cos \phi_1 \quad (\phi_1 = -\phi_2)$

This result leads naturally to the conclusion that, in the condition of retro-diffraction, out-of-plane distortions are mapped equally into

both the sample and main beams, as desired. Departure from this condition leads to a wavefront error difference between the main and sample beams which is determined by the magnitude of $h(\cos \phi_1 - \cos \phi_2)$. The error is small in on-axis beam-sampling systems where the sample beam is close to the condition of retro-diffraction. However, the error may become quite large in highly asymmetric systems such as on-axis telescopes with off-axis beam sampling.

A somewhat different line of argument must be used to understand the conditions under which a sample beam from an ideal HG fabricated on a poor quality mirror can be used to improve the quality of the main beam. In this case, special care is required to ensure that the grating grooves are placed in precisely the correct positions on the surface. The grating groove positions are determined by the interference fringes produced by the two construction wavefronts. In three-space, these fringes bisect the angles of incidence between the two construction wavefronts. When the two construction beams are incident at equal but opposite angles from the normal, the local fringe planes are perpendicular to the surface so that an out-of-plane surface error does not affect the location of the fringe on the surface (Figure 29). Conversely, if the fringe planes are oblique to the surface, an out-of-plane distortion gives rise to an error in the fringe location. Hence, it is desirable to work with construction geometries in which the fringe planes are approximately normal to the surface. This condition is a general feature of on-axis beam sampling systems and makes it possible to achieve a high degree of correction to compensate for primary mirror distortions in such systems. However, this condition is not necessarily true for highly asymmetric geometries, in which only a relatively small improvement is generally possible.

Computer Modeling with Deformed Construction

The aberrations in the main and sample beams have been modeled in computer simulations assuming that the primary mirror has been deformed before fabricating the hologram. The case modeled pertains to an $f/1$, 1-meter diameter parabolic mirror used in an on-axis

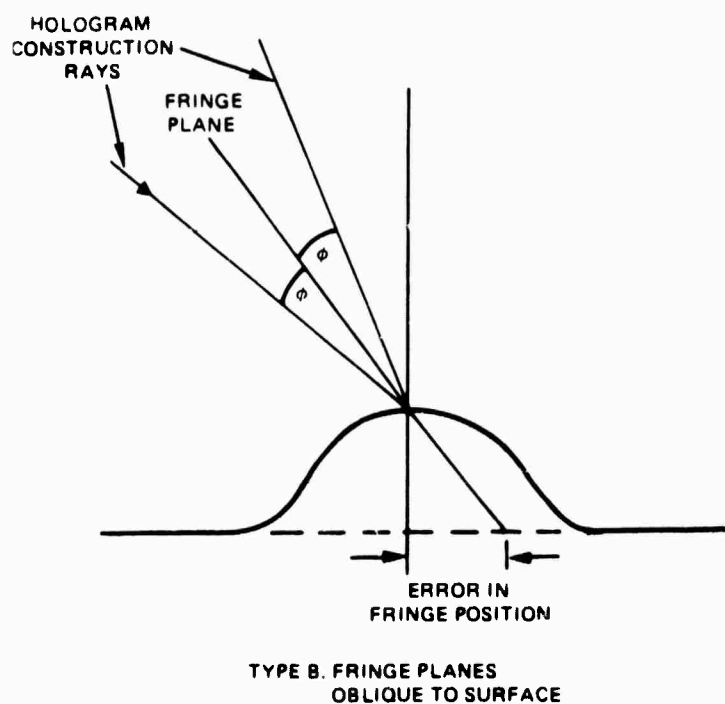
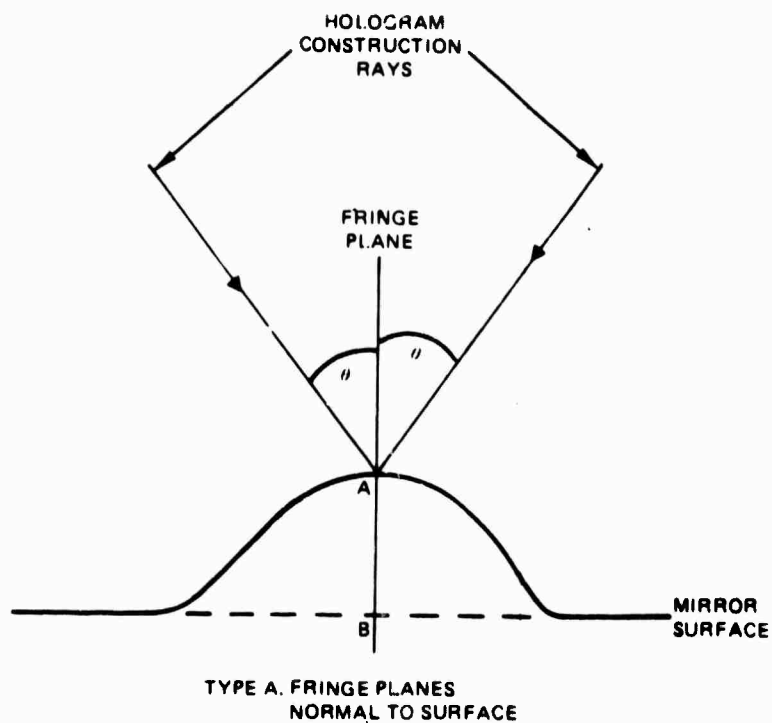


Figure 29. Effect of out-of-plane distortion prior to hologram fabrication.

configuration with on-axis beam sampling. The same deformation of the primary mirror is assumed to be present on playback, this being the case of a poor quality primary mirror. In general, the mirror figure error can have any form. However, for simplicity, the following Gaussian deformation was assumed:

$$\Delta z = 1.25 \times 10^{-7} \rho^2 \exp(-4 \times 10^{-6} \rho^2)$$

$$\rho = \sqrt{x^2 + y^2}$$

= mirror radial coordinate.

The deformation shown in Figure 30 is more than 15 μm . Without correction of the sample beam, the aberrations in the main beam exceed 70 μrad and are virtually identical to the aberrations in the sample beam, taking into account the afocal magnification, M , between the outgoing beam and the wavefront error sensor. In this example, the sample beam is collimated by the error sensing optics, with a magnification of about 5.6. After correcting the sample beam, the residual error is equal to the difference between the aberration in the sample beam, divided by M , and the aberration in the main beam. As shown in Figure 30, this residual has a maximum value of about 0.5 μrad .

This result demonstrates that the permissible tolerance in the primary mirror figure can be considerably relaxed if wavefront error sensing and correction are conducted in the manner described. The result also verifies the first-order theory discussed earlier, and shows that the relaxation in the tolerances can, in favorable geometries, be as large as two orders of magnitude (e.g., a 70 μrad error is reduced to 0.5 μrad).

- ABERRATIONS DUE TO DISTORTIONS ON THE PRIMARY MIRROR DURING HOLOGRAM CONSTRUCTION ARE SIGNIFICANTLY REDUCED BY CORRECTING THE SAMPLE WAVEFRONT

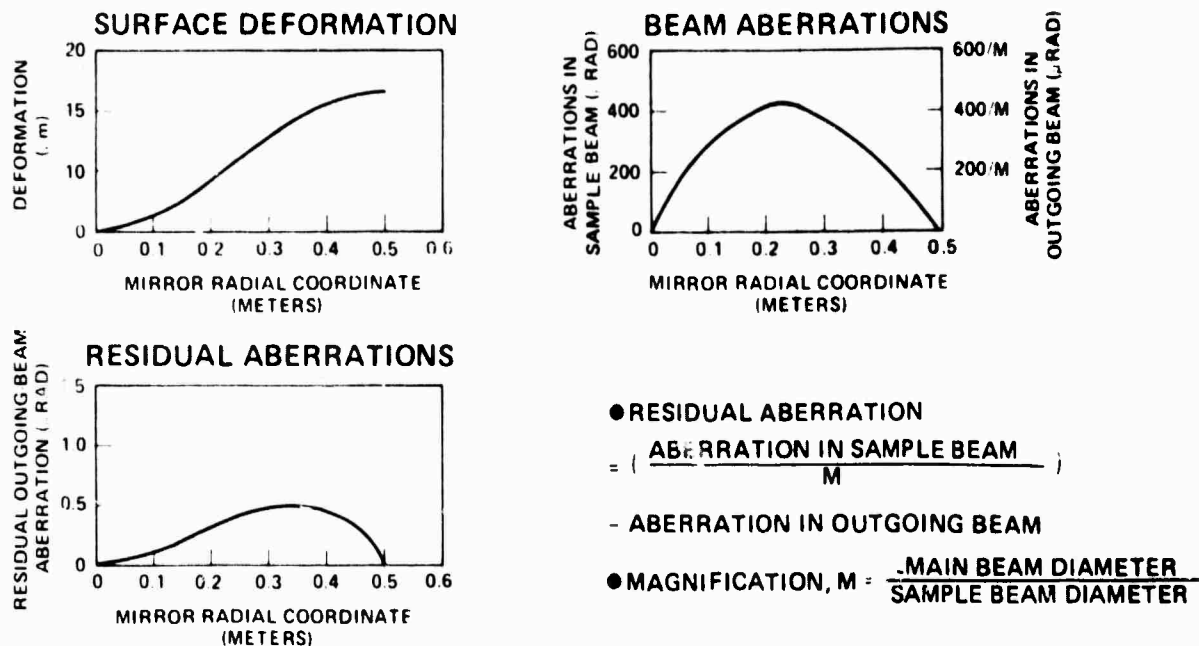


Figure 30. Playback with deformed construction.

Computer Modeling with Deformation on Playback

Outgoing-beam aberrations due to distortions introduced after construction of the hologram can be reduced to some extent, but not entirely eliminated, by correcting the sample beam. A limit exists to the distortions that can be tolerated. The distortion is modeled as follows:

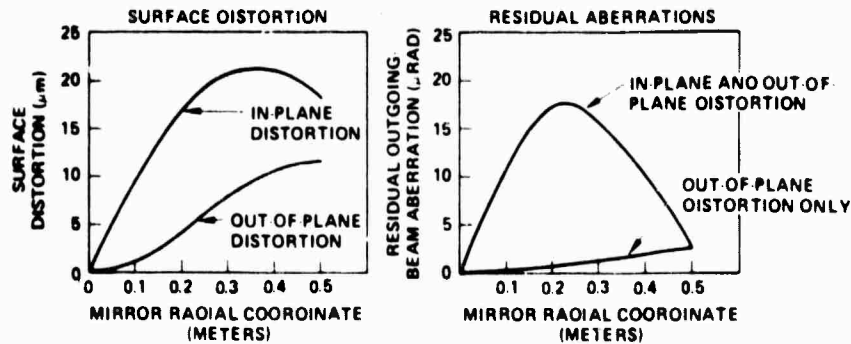
$$\Delta z = 1.25 \times 10^{-7} \rho^2 \exp(-4 \times 10^{-6} \rho^2)$$

$$\Delta x = 1.0 \times 10^{-4} x \exp(-4 \times 10^{-6} \rho^2)$$

$$\Delta y = 1.0 \times 10^{-4} y \exp(-4 \times 10^{-6} \rho^2)$$

The residual aberrations in the outgoing beam, after wavefront correction of the sample beam, are as shown in Figure 31. The aberrations depend on both the magnitude and slope of the surface deformation. The contribution due to out-of-plane distortion is small since the aberrations appear

• THERE IS A LIMIT TO THE DISTORTIONS THAT CAN BE TOLERATED AFTER HOLOGRAM CONSTRUCTION



- THE ABERRATIONS DEPEND ON BOTH THE MAGNITUDE AND SLOPE OF THE SURFACE DEFORMATION.
- THE ABERRATIONS DUE TO IN-PLANE DISTORTIONS ARE LARGER SINCE THERE IS NO COMPENSATING ABERRATION IN THE OUTGOING BEAM.

Figure 31. Deformed primary on playback.

in both beams and a favorable on-axis geometry was assumed. The residual aberrations due to the in-plane distortion are larger since there is no corresponding aberration in the outgoing beam. The in-plane and out-of-plane distortions can be considered independently and the resulting aberrations added together.

A second type of distortion considered was a curvature change of the primary mirror where the resulting in-plane distortions were assumed to be produced by simple bending of a flat plate.

This distortion can be represented by

$$\Delta z = \frac{\Delta c}{2} (x^2 + y^2)$$

$$\Delta x = -\frac{t \Delta c}{2} x$$

$$\Delta y = -\frac{t \Delta c}{2} y$$

where

Δc = curvature change

t = mirror thickness = $D/12$

D = mirror diameter

The effect of this distortion for a 0.1 percent curvature change is shown as a function of f-number in Figure 32. Increasing or decreasing the percentage curvature change varies the distortions linearly, with unity slope. The basic conclusions are

1. The aberrations increase with decreasing f-number
2. There is a significant correction at large f-numbers.
3. Degraded performance due to overcorrection will occur for f-numbers somewhat less than 1.

Correlation with NPT Primary Mirror Distortions

Although the foregoing simulations illustrate the mechanisms involved, they provide no information about the basic level of the residual aberrations that can be expected in an actual system. The magnitude of the residual depends on the type and magnitude of the distortion involved.

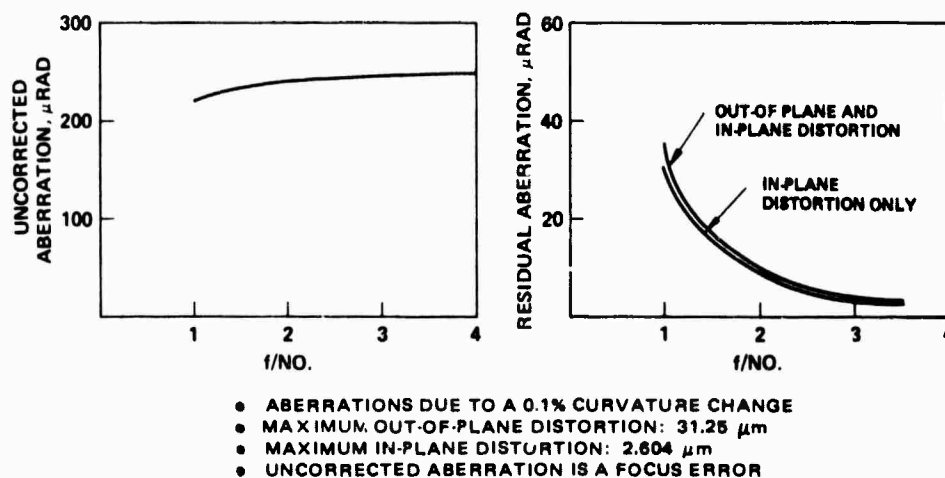


Figure 32. Aberrations due to curvature change.

Each of these parameters depends, in turn, on the HEL intensity distribution, and on the absorbed power, mirror design, mirror materials, and other factors. Hence, detailed modeling is required for each specific system to quantify the residual aberrations. Nevertheless, an attempt was made to correlate the effects of the distortions with laser power by making use of extensive data available from the Hughes Navy Pointer Tracker (NPT) system. The results of this effort are described in the following paragraphs.

In the Hughes computer simulation model of a pointing and tracking system for a high-energy laser, the distortion-induced optical path difference (OPD) for each laser mirror is the sum of OPDs due to temperature gradients in the mirror and to pressure differences associated with the flow of coolant fluid within the backup and supporting structures. The model describes out-of-plane distortions by means of empirically derived equations. However, little information is available concerning the in-plane distortions; the existing information has been used to deduce an expression for the in-plane primary mirror distortions for this study.

The cooled metal primary mirror is best characterized by backup distortions; that is, the pressure and beam-mapping distortions are quite small compared to the backup bending distortions. The out-of-plane distortion for the primary mirror is described by the following equation:

$$\Delta z = \Delta(x, y)_B = 3.356 \times 10^{-8} P \alpha \left(\frac{1262}{G} \right) \left(\frac{R}{35} \right)^2 \left[1 - \left(\frac{x}{R} \right)^2 - \left(\frac{y - k}{R + k} \right)^2 \right] f_1(t)$$

where:

$$f_1(t) = 3.67 \times 10^{-2} t \exp(1 - 3.66 \times 10^{-2} t)$$

and

$\Delta(x, y)_B$ = Optical path difference, cm

P = Input beam power, watts

α = Mirror absorptance = 0.01

G = Coolant flow = 1262 gm/sec

R = Beam radius = 50 cm

k = R/z for NACL and GDL input beams

k = 0 for Gaussian and uniform beams

It should be noted that for $k = 0$, this distortion corresponds to a change in curvature and hence can be represented by the distortion computations given in the previous subsection.

The only in-plane distortion investigation conducted in the NPT study was done for the secondary mirror. Following an examination of this data, it was concluded that the in-plane distortions of the primary mirror could be adequately represented by the equation for the out-of-plane distortions provided that the constant term were neglected. For the assumed values of α , G, and R this leads to

$$\Delta z = 6.868 \times 10^{-10} P \left[1 - \frac{x^2 + y^2}{(50)^2} \right]$$

$$\Delta x = 6.868 \times 10^{-10} P \left[\frac{x (x^2 + y^2)^{1/2}}{(50)^2} \right]$$

$$\Delta y = 6.868 \times 10^{-10} P \left[\frac{y (x^2 + y^2)^{1/2}}{(50)^2} \right]$$

(4)

An analysis was conducted using Equation 4 for various f-numbers at 5 megawatts of laser power and also as a function of power for an $f/2$ primary. The results of this analysis are shown in Figure 33.

For an uncooled ultra-low-expansion (ULE) glass primary mirror, the magnitude of the distortion is low compared to that of a cooled metal primary. As indicated in Figure 33 it is believed that the aberrations due to the ULE mirror will be at least one order of magnitude smaller than those associated with the cooled primary.

These results must not be taken too literally because they are very preliminary in nature and can be expected to vary greatly among different designs. The validity of the assumptions concerning the type and magnitude of the distortions (particularly the in-plane distortions) also remains to be fully established.

It should also be noted that the residual aberration in this model is comprised almost entirely of focus error. This arises naturally from the assumptions made concerning the nature of the distortion. However, the sample beam is not used for controlling focus errors since range information is not ordinarily utilized in a local-loop error sensing system. It may then be concluded that for the control of higher order aberrations, the residual errors due to grating distortions on the primary mirror are acceptably small.

More recently, additional simulations were performed for another program. These simulations are much more detailed in that they assume a typical HEL beam intensity profile incident on the primary mirror, and the in-plane distortions are obtained by superimposing the effects of each element of surface area on all other elements in the mirror surface. Full details of the simulations will not be given here. However, it may be noted that the results showed residual main beam errors of less than $1 \mu\text{rad}$ in a system having a diffraction limit of about $40 \mu\text{rad}$. It is therefore concluded, particularly for on-axis systems, that primary mirror distortions do not result in excessive residual wavefront errors when holographic beam sampling from the primary mirror is employed.

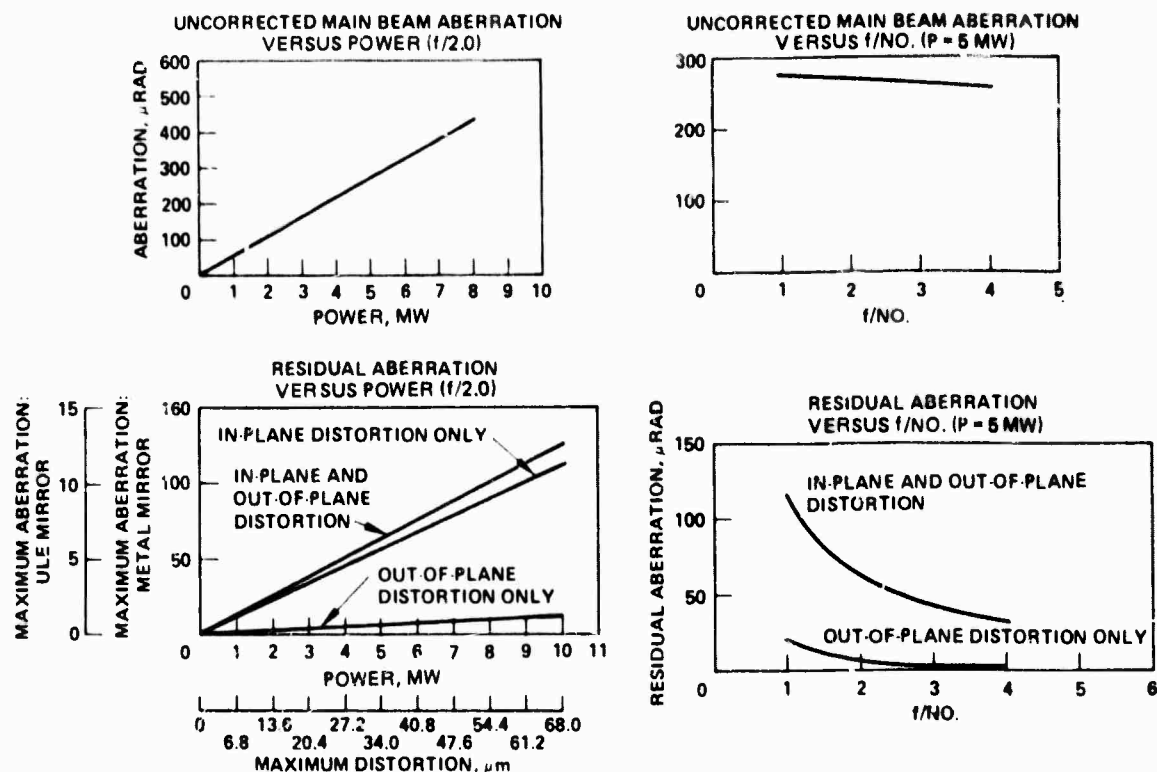


Figure 33. Aberration versus power due to distortion of cooled metal mirror.

Photoresist Thickness Variations

Another potential source of wavefront aberration in the sample beam is the photoresist thickness variation that is likely to occur during fabrication of a grating for a large primary mirror. A mathematical analysis of this problem leads to the conclusion that variations in the photoresist thickness as large as 0.5 μ m can be tolerated from the point of view of wavefront quality. From the point of view of efficiency and groove depth, a more stringent tolerance in resist thickness variations may be necessary. A first-order analytical approach estimating the effects of resist thickness variations on the aberrations that occur on playback is given below.

As seen from Figure 34, the change $\Delta\phi$ in the phase difference between the two incident wavefronts corresponding to a variation Δz in the photoresist thickness is given, to first order in Δz , by the expression

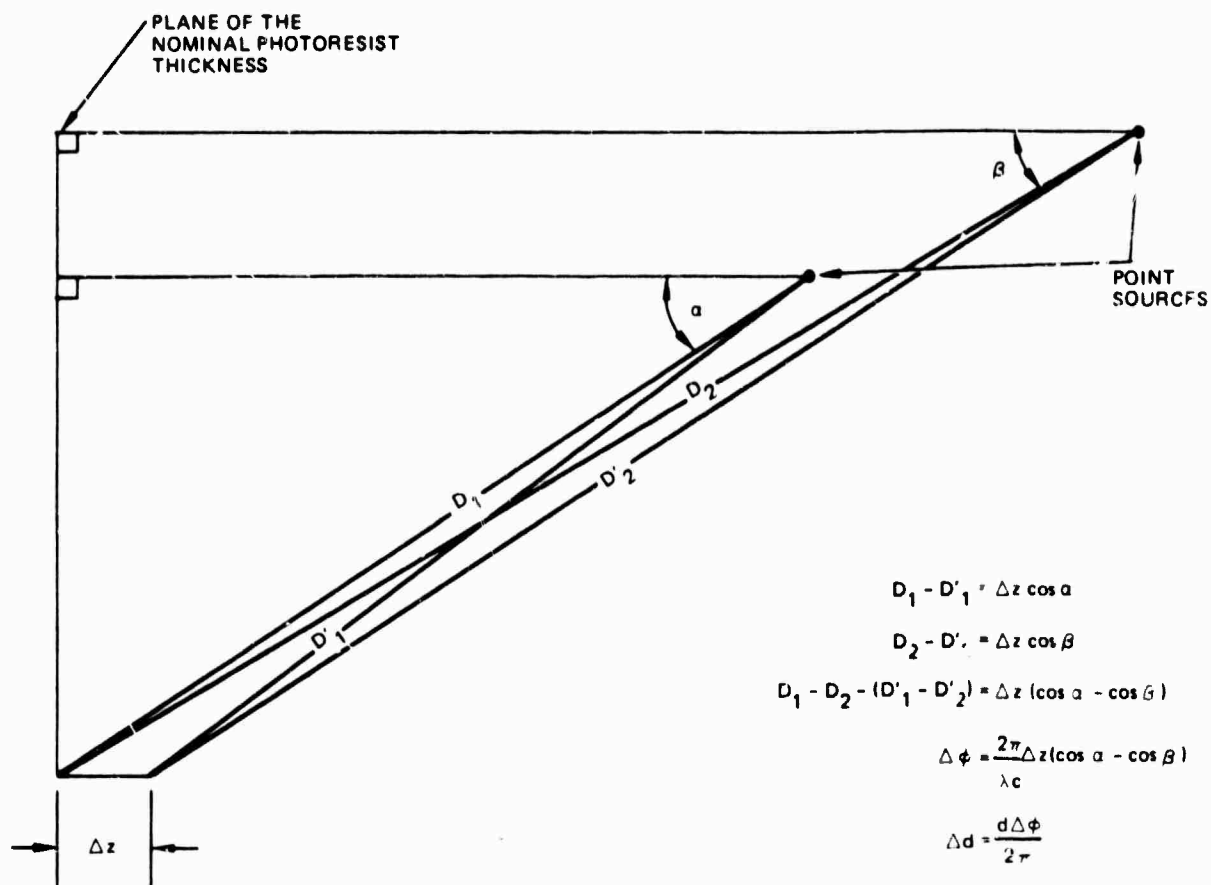


Figure 34. Geometry for photoresist variation calculation; Δz is assumed thickness change.

$$\Delta \phi = \frac{2\pi}{\lambda_c} \Delta z (\cos \alpha - \cos \beta)$$

where α and β are the angles from the point sources to the point in question on the mirror.

The corresponding fringe shift Δd is given by

$$\Delta d = \frac{d \Delta \phi}{2} = \frac{d}{\lambda_c} \Delta z (\cos \alpha - \cos \beta) \quad (5)$$

where d is the fringe spacing.

An expression for the ray angular aberration $\Delta \theta$ can be obtained by differentiating the diffraction equation to yield

$$\Delta\theta = \frac{\lambda_p}{d} \left(\frac{\delta d}{d} \right) \frac{1}{\cos \theta_d} \quad (6)$$

where $\delta d = (\Delta d_1 - \Delta d_2)$, θ_d is the diffraction angle, λ_p is the playback wavelength and Δd_1 and Δd_2 are the shifts of two adjacent fringes. By substituting Equation 5 in Equation 6, the aberration is found to be

$$\Delta\theta = \frac{\lambda_p}{\lambda_c} \frac{m}{\cos \theta_d} (\cos \alpha - \cos \beta) \quad (7)$$

where $m = (\Delta z_1 - \Delta z_2)/d$ is the local slope of the photoresist thickness variation. In the foregoing equations, second and higher order terms in the variables (Δz , etc.) have been neglected.

For a 1-meter diameter $f/2$ primary mirror with on-axis construction sources at distances of 2.93m and 2.44m, Equations 5 and 7 are given approximately by

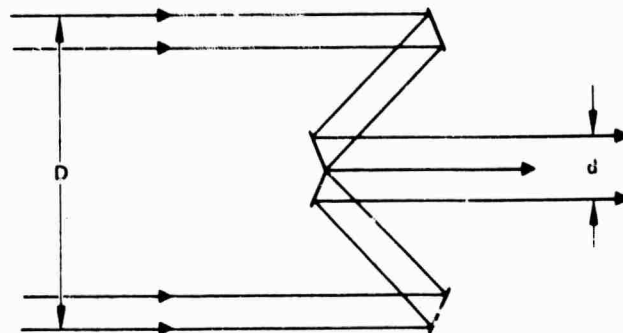
$$\Delta d = \frac{d}{\lambda_c} \Delta z (2.57 \times 10^{-8}) r^2 \quad (8)$$

$$\Delta\theta = \frac{\lambda_p}{\lambda_c} \frac{m}{\cos \theta_d} (2.57 \times 10^{-8}) r^2 \quad (9)$$

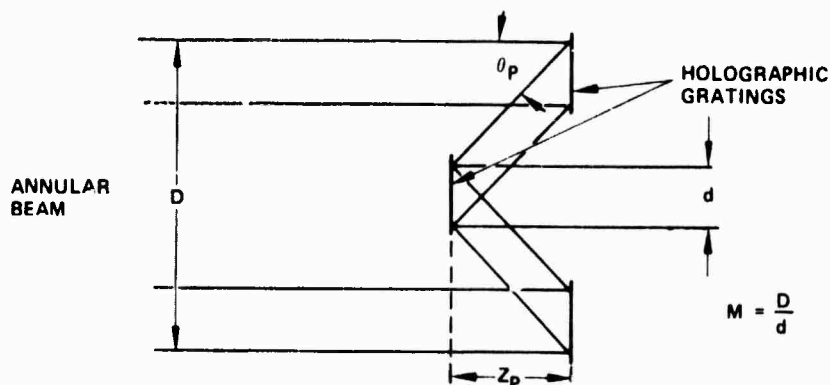
where r is the radial distance to the specified point on the mirror in millimeters. The appropriate parameter values are: $\lambda_p = 3.8 \mu\text{m}$, $\lambda_c = 0.4416 \mu\text{m}$, $r = 500 \text{ mm}$, $\Delta z = 0.5 \mu\text{m}$, $m = 0.5 \times 10^{-4}$ (i.e., a $0.5 \mu\text{m}$ change in Δz over a 10-mm radius), and $\theta_d = 45$ degrees. Substituting these values into Equations 8 and 9 gives $\Delta d = 0.0073d$ and $\Delta\theta = 3.9 \mu\text{rad}$. This value of $\Delta\theta$ is within the diffraction limit of the primary mirror. The $0.5\text{-}\mu\text{m}$ variation in Δz assumed is believed to be realizable experimentally; therefore, in terms of aberrations ($\Delta\theta$), the photoresist thickness variation should present little difficulty for wavefront sampling on mirrors up to 1 meter in diameter. Due to the r^2 dependence of $\Delta\theta$, a tighter tolerance on m will have to be established.

2.3.4 Holographic Grating Axicon

As discussed in Section 2.2.2, the holographic grating axicon (HGA) shown in Figure 35 offers two important potential advantages over a reflective axicon. First, since it has no tip, the HGA avoids the serious difficulties that arise in fabricating and cooling the tip of a high-power reflective axicon. Second, when used in an HEL resonator, the HGA, in principle, sustains full phase correlation around the cylindrical cross section of the gain medium. In contrast, a reflective axicon used for the same purpose can provide the desired mixing action only in a small region around its tip.



a. The conventional axicon



b. The holographic axicon

Figure 35. Illustrative holographic axicon playback geometries.

The analytical investigation of the holographic axicon concept covered the following aspects: (1) the first-order design relationships, (2) the permissible tolerances on alignment of a matched pair of HGA elements, (3) interference effects, and (4) high-efficiency requirements and computations. These topics are discussed in the following paragraphs.

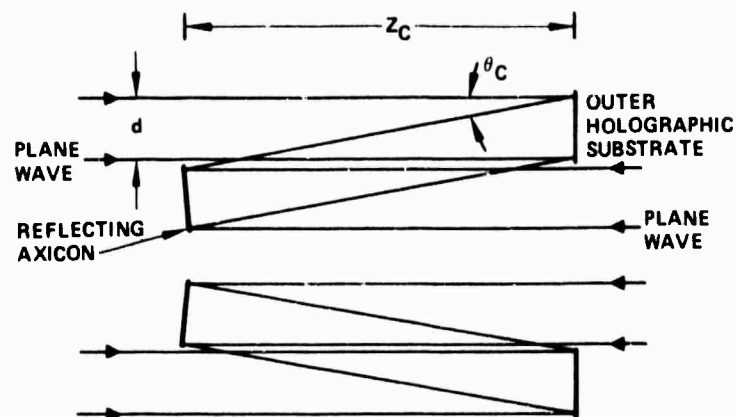
First-Order Design Relationships

Illustrative examples of the optics necessary to construct the outer and inner elements of a holographic grating axicon are shown in Figure 36. To record the desired interference pattern between the plane and conical wavefronts, it was assumed that conventional (reflective) axicons would be used in the path of one hologram construction beam. The construction geometries shown in Figure 36 are long in comparison with the playback geometries because of the large wavelength differences between the construction (0.4416 μm) and playback (3.8 μm) beams, representing a wavelength scaling ratio of 8.61. However, because the diameter of the inner element is equal to the width of one side of the outer element, its construction geometry can be half as long. Figure 36b also indicates that a recording at the very center of the inner element may not be feasible because of high intensity difficulties in this region. The appropriate equations relating the parameters shown in Figures 35 and 36 are:

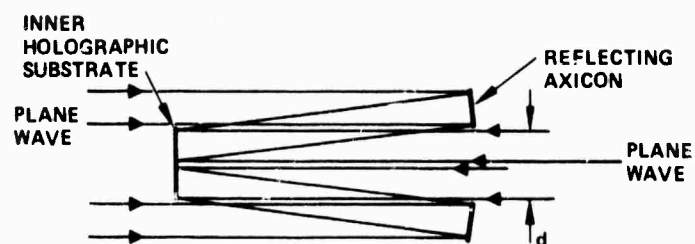
$$z_p = \frac{d}{2} (m - 1) \cot \theta_p$$

$$z_c \geq d \cot \theta_c$$

$$s = \frac{\lambda_p}{\sin \theta_p} = \frac{\lambda_c}{\sin \theta_c}$$



a. The outer element.



b. The inner element.

Figure 36. Illustrative holographic axicon construction geometries.

where the subscripts c and p refer to the construction and playback geometries respectively, s is the grating spacing and m is the beam magnification of the axicon. An illustrative set of axicon design parameters is given in Table 3. Due to the large wavelength difference between construction and playback, the construction optics for the outer element must be more than 6 times longer than the playback geometry. The computational data given below pertains to this design example.

In order to minimize radiation losses into higher orders of diffraction, it is desirable to construct the axicon in such a way that the grating spacing is beyond the cutoff for as many diffraction orders as possible outside those of interest. The grating equation is:

$$q \lambda = s (\sin \theta_1 - \sin \theta_2) \quad (10)$$

where q is the order and θ_1 , θ_2 are the angles of incidence and diffraction, respectively. In the axicon geometries, $\theta_2 = 0$ and $\theta_1 = \theta_p$ in the first order of diffraction. It is then clear that, provided θ_p is greater than 30 degrees, Equation 10 can be satisfied only for the -1, 0 and +1 orders of diffraction, for a wave incident normally to the first element. For the wave incident on the inner element from the outer element, only orders 0, 1 and 2 can exist. Thus, for $\theta_p > 30$ degrees, radiation can be diffracted into at most three orders, which should ease the problem of obtaining high diffraction efficiency in the orders of interest. This condition is satisfied in the design example given in Table 3, for which $\theta_p = 45$ degrees.

Alignment Sensitivity Analysis

Preliminary computer investigations of the sensitivity of the axicon design (Table 3) to tilts and decentrations of the two elements relative to one another were performed. The investigations were based on geometrical ray-tracing of the axicon in the reverse direction for ease of computer simulation (Figure 37). The aberrations are the same regardless

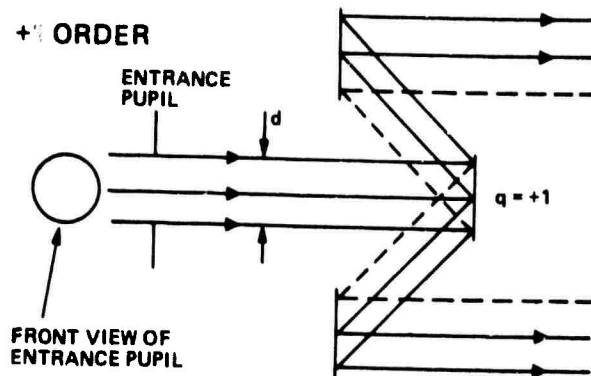
TABLE 3. HOLOGRAPHIC AXICON DESIGN EXAMPLE

Design Characteristic	Value
Beam magnification, $m = \frac{D}{d}$	5
Construction wavelength, μm	0.4416
Playback wavelength, μm	3.8
Construction cone angle, degrees	4.713
Playback one angle, degrees	45
Grating spacing, μm	5.374
Axicon length, ratio, z_p/d	2
Construction optics length ratio, z_c/d	12.13

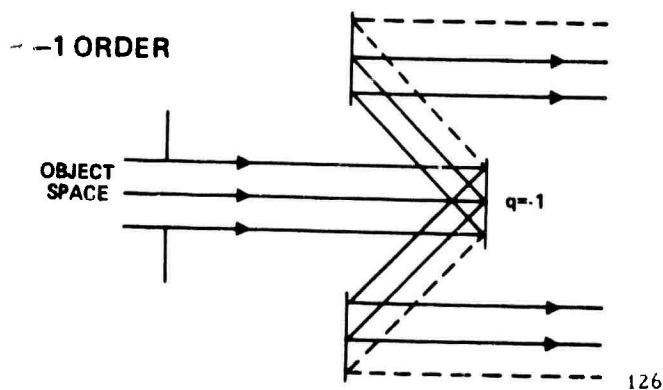
Note: d = Beam diameter at inner element
 D = Beam diameter at outer element

of direction because angular relationships are conserved through the axicon. In the simulation, the order $q = \pm 1$ on the inner grating was chosen to generate the outgoing beams, as shown in Figure 37. The $+1$ order forms the outer annulus of the outgoing wave and the -1 order forms the inner annulus. This is true because the grating vector must change continuously and therefore rotates around the center of the inner element in accordance with the circular fringe pattern. The results are presented for $d = 1$ meter and $m = 5$; the aberrations for any other value of d may be determined by scaling the distances linearly while maintaining all angular relationships.

The aberrations are all presented in terms of angular ray deviations in image space with respect to the reference ray. The latter is the ray from the specified object point through the center of the entrance pupil (Figure 37a). Unless otherwise noted, the object is an axial point at infinity.



a. Path of rays for $q = +1$ on inner grating.



b. Path of rays for $q = -1$ on inner grating.

Figure 37. Configuration used in holographic axicon aberration examination.

These aberrations are not readily identifiable according to the usual terminology; therefore, geometrical aberration curves are provided. These curves are determined by tracing ray fans as illustrated in Figure 38. A fan of rays is a group of rays starting at an object point and incident on the entrance pupil in a line as illustrated. The fan is referred to as a YFAN if the line on the entrance pupil is parallel to the y-axis, and similarly for an XFAN. For a given fan, the geometrical aberration curve is plotted with the pupil dimension as the abscissa and the aberrations as the ordinate.

The tilts and decentrations that produce angular aberrations in the beam are:

1. A rotation of the inner grating about any axis in the x-y plane.
2. A displacement or decentration of either grating in the x-y plane. The effect of displacing one is equivalent to displacing the other.

Since the gratings are rotationally symmetric, the rotations were taken about the x-axis and the decentrations were taken in the y-direction. Plots of the maximum aberration as a function of the relative tilt and decentration of the inner and outer grating are shown in Figures 39a and 39b, respectively, while plots of the angular aberrations with respect to the position of the ray on the entrance pupil are shown in Figures 40 and 41.

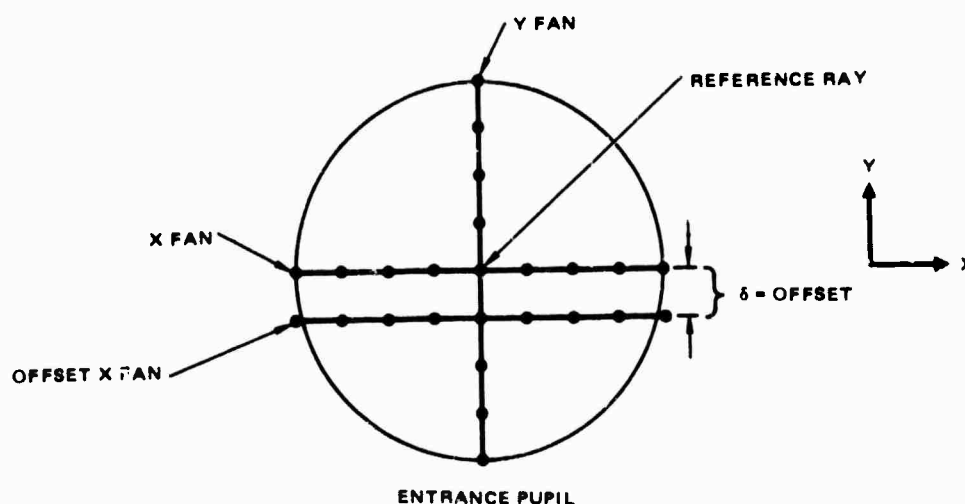
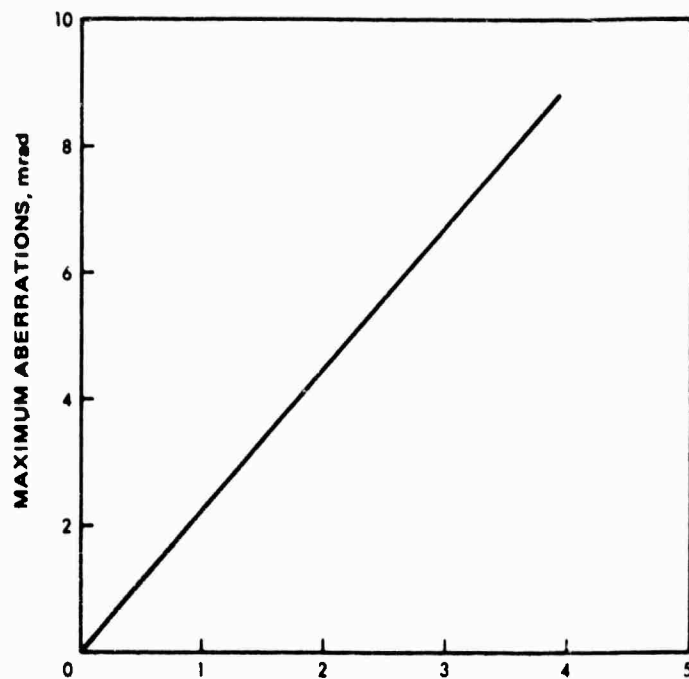
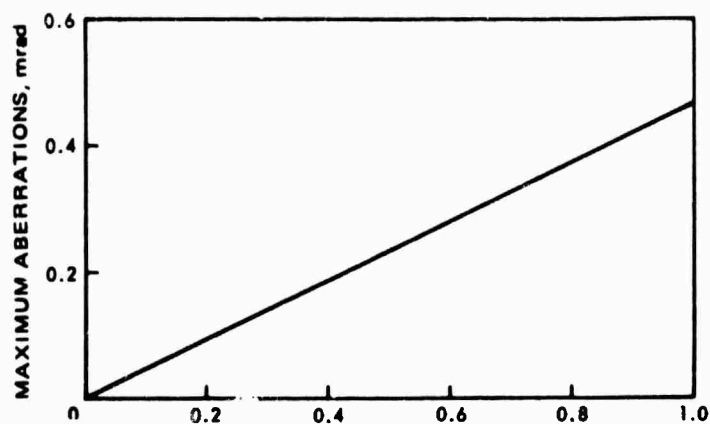


Figure 38. A fan of rays is a group of rays starting at an object point and incident on the entrance pupil in a line as illustrated.

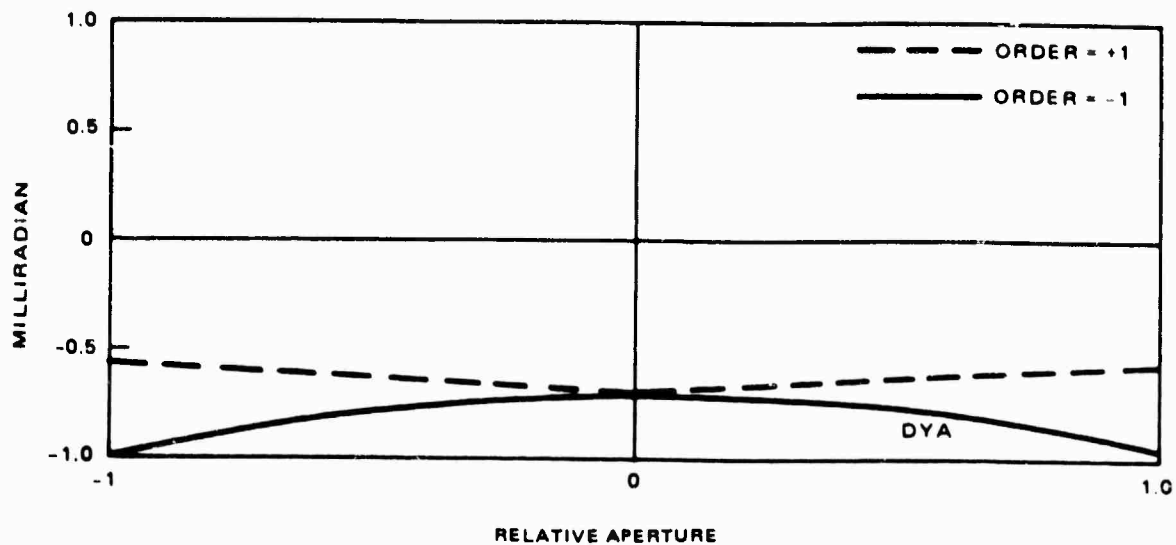


a. Tilt of inner grating, millirad.

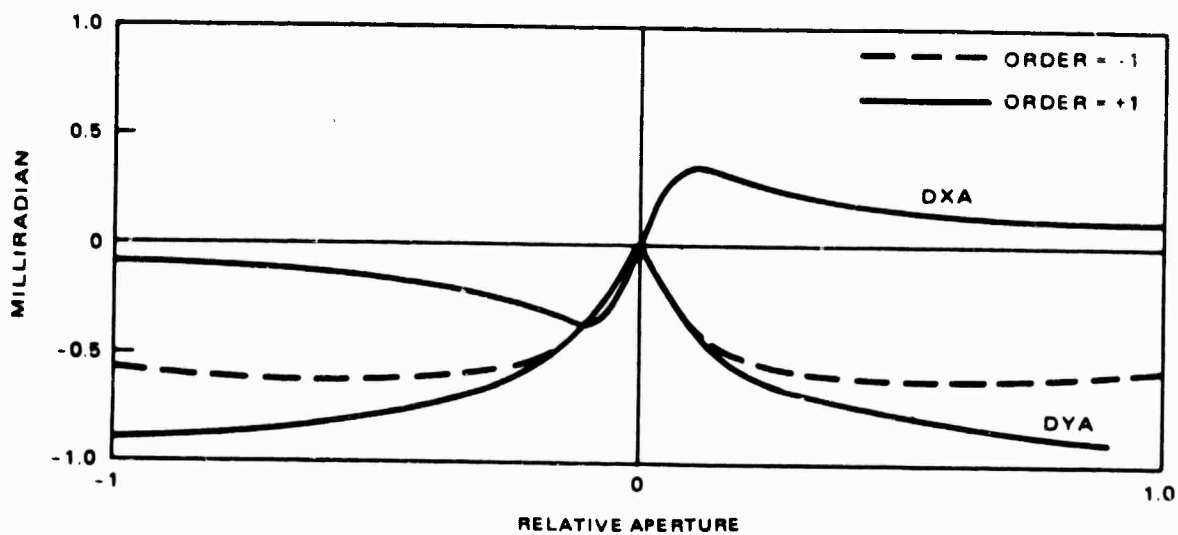


b. Decentration of either grating, mm.

Figure 39. Maximum angular aberration due to misalignment of inner or outer grating.

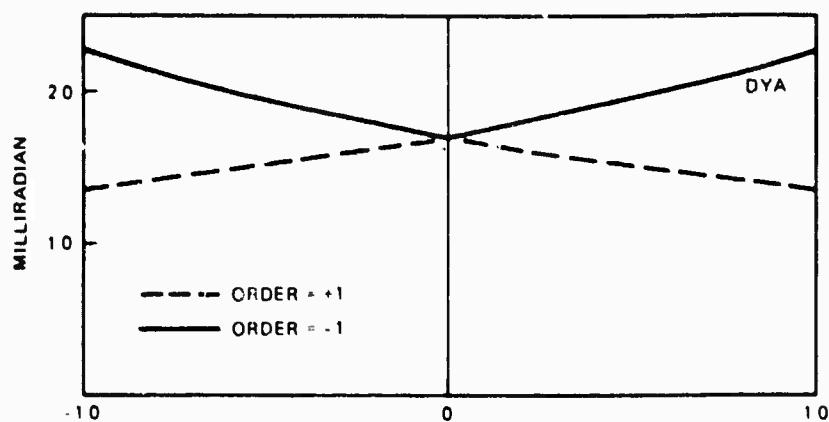


a. No offset.

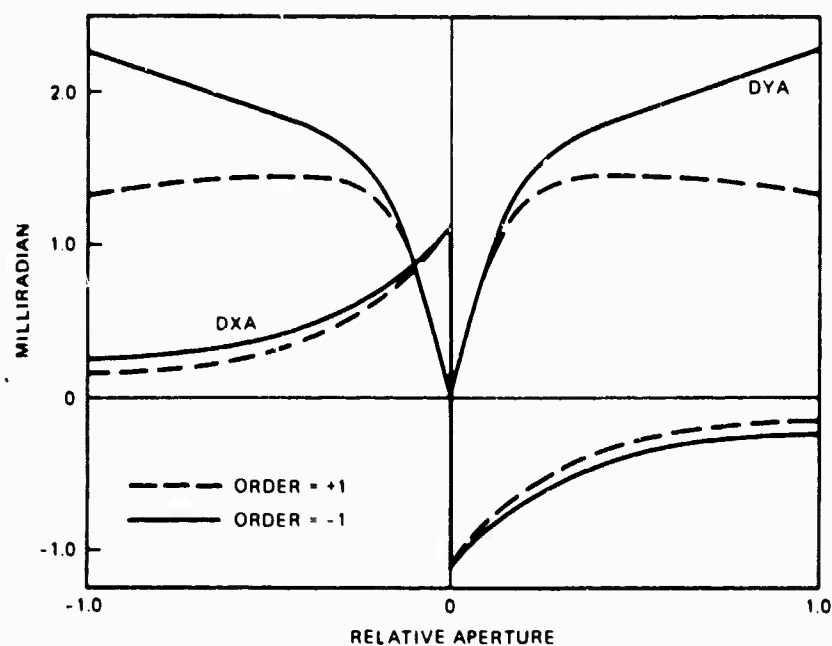


b. 5-cm Offset

Figure 40. XFAN aberrations introduced by a 2-mm decentration of either grating (DYA is angular aberration in the y-z plane, DXA is aberration in x-y plane).



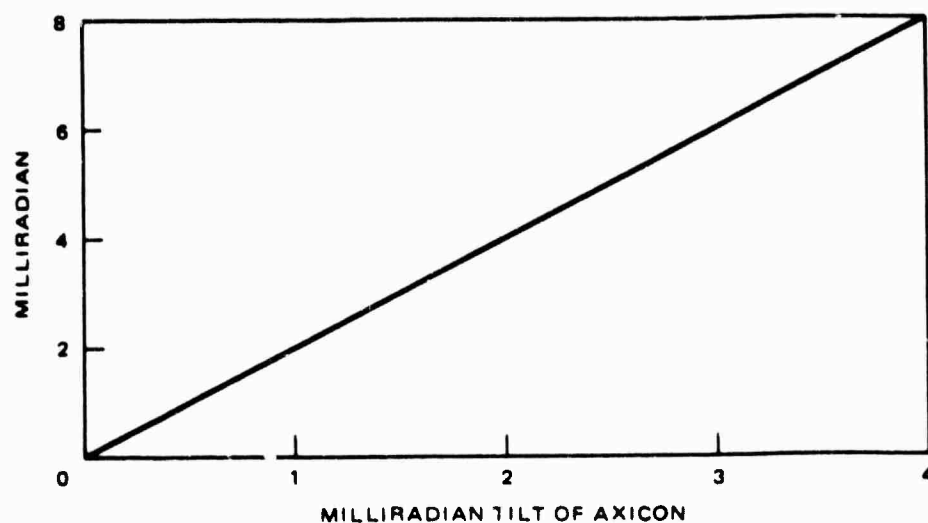
a. No offset.



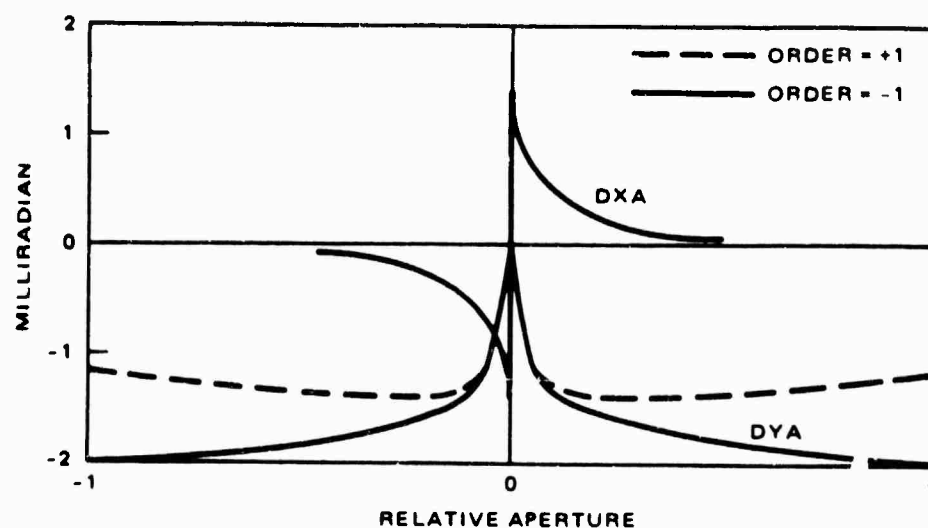
b. 5-cm offset.

Figure 41. XFAN aberrations introduced by 1 mrad tilt on inner grating (DYA is angular aberration in the y-z plane and DXA is aberration in the x-z plane). See Figure 38.

The aberrations introduced by tilting the entire axicon about any axis in the x-y plane are shown in Figure 42.



a. Maximum aberration versus tilt.



b. XFAN aberration at 1-mrad tilt (no offset).

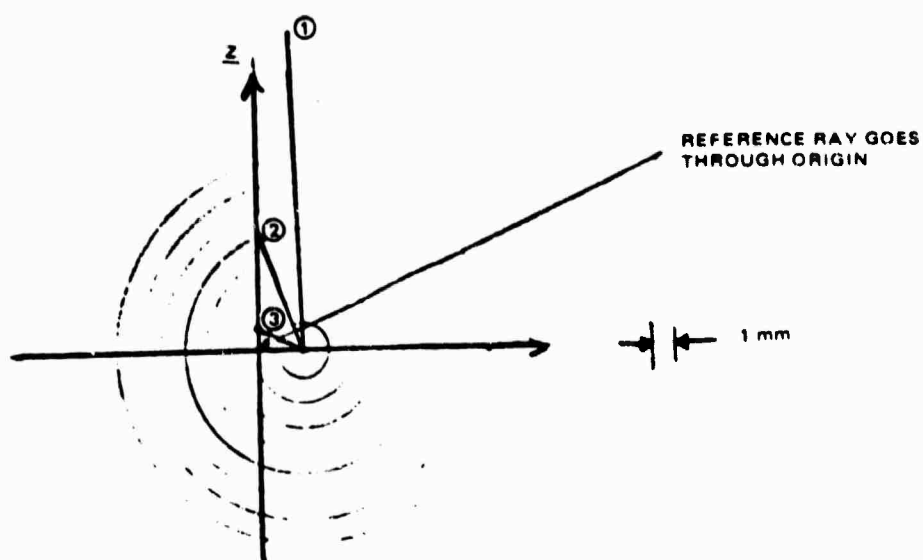
Figure 42. Aberrations introduced by tilting axicon (DYA is angular aberration in y-z plane and DXA is aberration in x-z plane).

The aberrations shown can be understood by close examination of the grating vector. Consider, for example, the case of a 2-mm decentration along the y-axis of the inner grating. The functional behavior of the grating vector, \vec{q} , for a fan of rays along the x-axis is shown in Figure 43a. Note the change in the direction of the grating vector for small and large x; this leads to an almost abrupt transition in the geometrical aberrations, as shown in Figure 40b for the case when $x = 0$. The ray entering at the full x-aperture leaves the inner grating ($q = 1$) at an angle of about 4 mrad in the y-z plane, since the angle between \vec{q} and the x-axis is also about 4 mrad. This angle is then reduced by a factor of 4.25 upon diffraction from the outer grating; hence, the full-aperture aberration is as shown in Figure 40a. Since \vec{q} has not changed from the original undeformed system along the y-axis, there are no aberrations for rays passing through the axis. The functional behavior of \vec{q} for the offset x-axis fan aberration curve is shown in Figure 43b. Note that \vec{q} changes direction much less rapidly with relative aperture; this leads to the curve in Figure 40b.

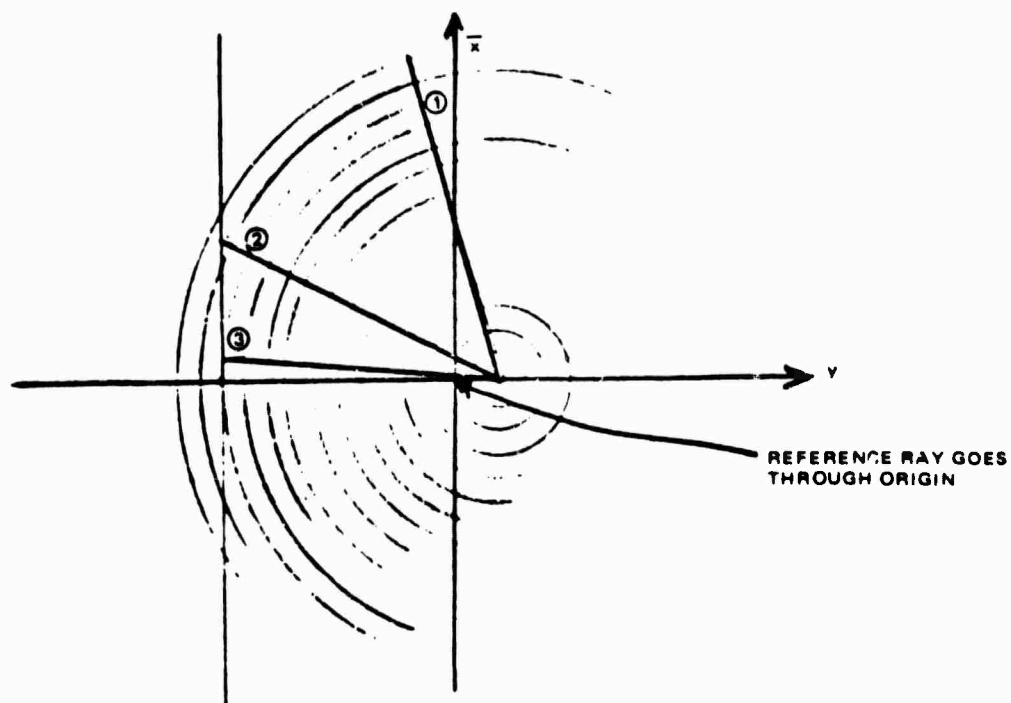
The aberrations produced by decentering the outer grating can be understood in a similar fashion. Such aberrations are given approximately by the change of the \vec{q} vector. For the plot in Figure 40a, this change is $0.002/d$ where d is the distance from the optical axis at which the ray intersects the outer grating. In this case the transition shown in Figure 40b is quite abrupt.

Except for a region very near the origin, the aberration curves resulting from decentrations of the inner and outer gratings are identical. This is to be expected since there is no meaningful way to distinguish the two cases. In the model, the distinguishing feature is the definition of the reference ray.

The other aberration curves are not interpreted here, but an understanding of them can be gained by examining the behavior of the grating vector, \vec{q} . The aberration curves and the interpretation given above are preliminary in nature. Further interpretations and computational results need to be examined to fully assess the behavior of the holographic grating axicon in relation to its potential application as an element of a laser resonator.



a. For a fan of rays traced on the x-axis ($y = 0$)



b. For an offset fan of rays.

Figure 43. Behavior of grating vector, \bar{q} , for 2-mm decentration of the inner element. ①, ②, and ③ represent direction of \bar{q} .

Interference Effects

When an HGA is used in conjunction with a laser beam (as part of a laser cavity, for example), a wave incident on the outer element may be combined in piecewise fashion, with diametrically opposite parts of itself at the inner element. Since both parts are mutually coherent, it is of interest to investigate the resultant wavefront combination from the standpoint of wavefront theory and interference. A discussion of some preliminary analysis along these lines is given below.

Considered from the standpoint of the wavefront theory of holography, the inner element at which the beams are mixed is a series of concentric rings corresponding to the interference pattern generated by the two construction beams in the plane of the element. Assuming a sinusoidal fringe pattern, the grating function recorded may be expressed as

$$G(r) \propto A + 2B \cos (k r \sin \theta_p)$$

where

A, B = constants

$r = (x^2 + y^2)^{1/2}$ is the radial coordinate in the plane of the grating.

$k = 2\pi/\lambda_p$

θ_p = angle of incidence of beam on playback

Expanding $G(r)$ into its exponential form,

$$g(r) = A + B [e^{ikr \sin \theta_p} + e^{-ikr \sin \theta_p}]$$

On playback, the grating is illuminated with a conical wavefront which can be represented mathematically by the expression

$$U = U(r') = e^{ikr' \sin \theta'} + e^{-ikr' \sin \theta'}$$

The wavefronts after diffraction are then given by

$$U_p = U(r') G(r)$$

Disregarding the zeroth and other orders which do not propagate in the direction of the axicon output leads to the result

$$U_p = B e^{ik(r \sin \theta_p - r' \sin \theta')} + B e^{-ik(r \sin \theta_p - r' \sin \theta')}$$

In the nominal design, $r' = r$ and $\theta' = \theta_p$ so the two waves that are mixed together in the direction of the axicon output add together to give a net amplitude of $2B$. These two waves are, however, complex conjugates of each other, so that wavefront errors arising from misalignments or distortions of the axicon elements are of opposite sign. If $r_p = r'$, $\theta_p = \theta'$ and residual wavefront errors of magnitude ϵ are present in each beam, the intensity distribution across the two waves of interest (which are propagating in the same direction) is

$$\begin{aligned} I(x, y) &= B^2 \left| e^{ik(r \sin \theta - r' \sin \theta' + \epsilon)} + e^{-ik(r \sin \theta - r' \sin \theta' + \epsilon)} \right|^2 \\ &= B^2 [2 + 2 \cos k\epsilon] = 4 B^2 \cos^2 (k\epsilon/2) \end{aligned}$$

The wavefront errors are thus mapped into an intensity distribution on the output beam. For example, if the inner element is decentered by an amount Δx ,

$$\begin{aligned} r' &= \left[(x + \Delta x)^2 + y^2 \right]^{1/2} \\ &= (r^2 + 2x \Delta x)^{1/2} \\ &= r + \frac{x \Delta x}{r} \end{aligned}$$

and

$$\epsilon = \frac{x \Delta x}{r} \sin \theta_p$$

$$I(x, y) = 4 B^2 \cos^2 \left(\frac{\pi}{\lambda} \frac{\Delta x}{r} \sin \theta_p \right)$$

This intensity distribution is zero along radial lines inclined at an angle ψ to the direction of decentration such that

$$\cos \psi = \frac{x}{r} = \frac{(n+1/2)\lambda}{\Delta x \sin \theta_p} \quad (n = 0, 1, 2, 3).$$

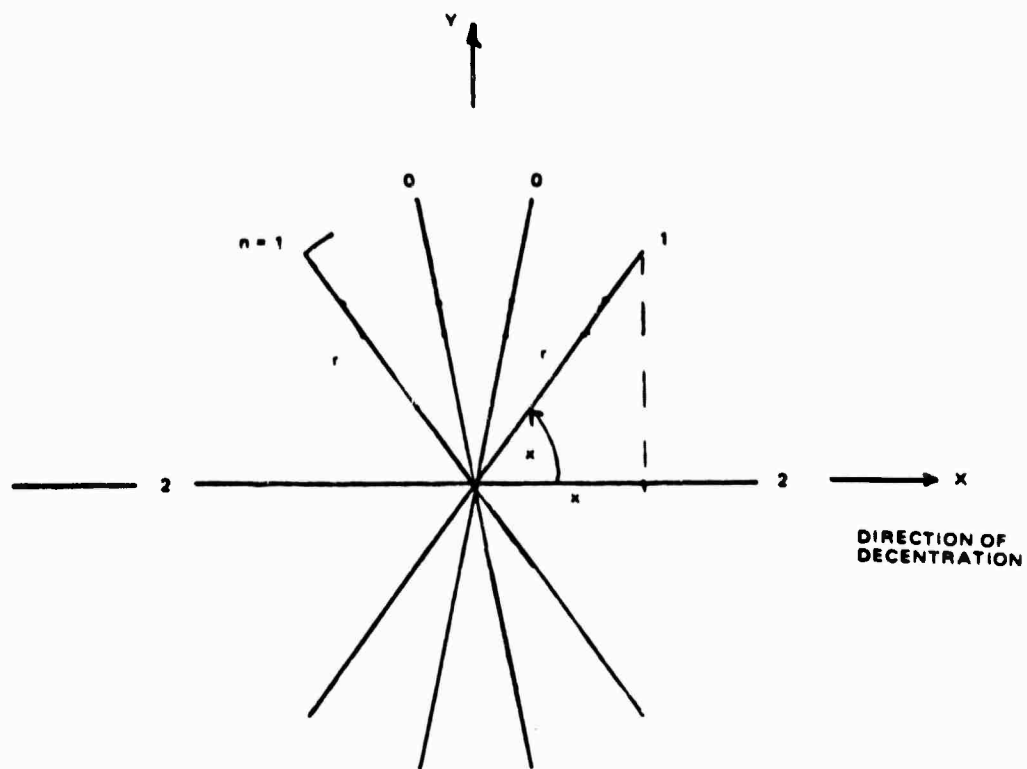
The resultant star pattern is illustrated in Figure 44.

Further conclusions may be drawn from the above and rationalized in a general way. First, x equals λ along the line $z = 0$, and $\epsilon = \Delta x \sin \theta_p$ is the OPD error along this line, the OPD being constant along radial lines. This result may be correlated with the grating equation for the axicon for the case in which one beam is normal to the axicon:

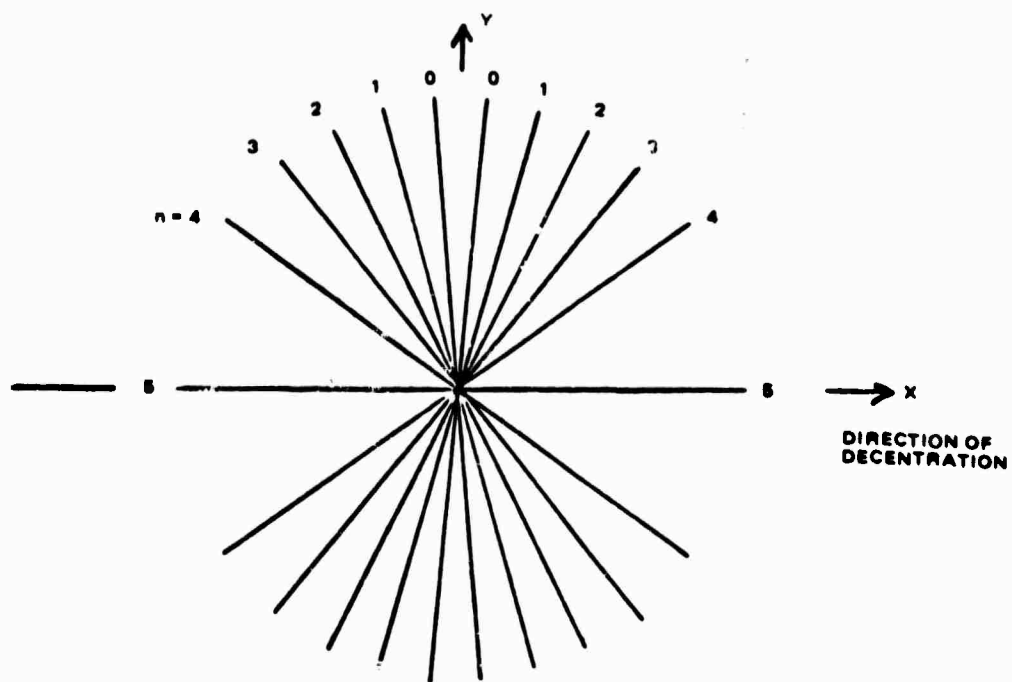
$$\text{Grating Equation:} \quad \lambda = d \sin \theta_p$$

$$\text{OPD Error:} \quad \epsilon = \Delta x \sin \theta_p$$

It is immediately evident that a decentration equal to the grating spacing, d , causes a full wave of OPD error. This is to be expected since each groove of the grating must correspond to an increment of one wave to obtain the first diffracted order. Furthermore, the OPD error due to decentration is independent of the scale or magnification ratio of the axicon; it depends only on the cone angle and wavelength and hence these two parameters alone determine the sensitivity of the axicon to decentration errors. Since the grating spacing is generally small,



a. $\Delta x \sin \theta_p = 2.5 \lambda.$



b. $\Delta x \sin \theta_p = 5.5 \lambda.$

Figure 44. Contours of zero intensity in output.

($5.4 \mu\text{m}$ for $\theta_p = 45$ degrees and $\lambda = 3.8 \mu\text{m}$) decentration tolerances of the order of a micrometer or less are implied. Although such tolerances are stringent, they are similar to those for a conventional reflective axicon. Furthermore, this sensitivity to decentration, coupled with the intensity mapping of the OPD errors offers a potential means of implementing adaptive control, and may, therefore be used to advantage. Although not analyzed here, it should be noted that similar results arise with respect to tilt errors in the axicon.

2.3.5 Off-Axis Virtual Mirror

To obtain uniformly high efficiency, the off-axis grating lens must be designed to exclude all diffracted orders but the first, at every point on the aperture. The angle, θ_D , at which the first order diffracts is varied to provide the optical power of the grating.

The range of diffracted angles can be determined from the geometry of the focus. A simple geometry in which the focal spot lies tangent to the inner edge of the incident beam is shown in Figure 45. Rays incident along this interface are retroflected by the grating; this is the Littrow condition in which

$$\sin \theta_i = \frac{\lambda}{2d}; \quad \theta_{D_{\max}} = \theta_i$$

A ray from the outer edge of the incident beam diffracts into an angle determined by the f -number ($f\#$) of the lens:

$$\theta_{D_{\min}} = \theta_i - 2 \tan^{-1} \left(\frac{1}{2f\#} \right).$$

The existence of no more than one diffracted order can be ensured through the use of the grating equation to locate the cutoff condition for the second order:

$$\sin \theta_i + 1 < 2(\sin \theta_i + \sin \theta_{D_{\min}}).$$

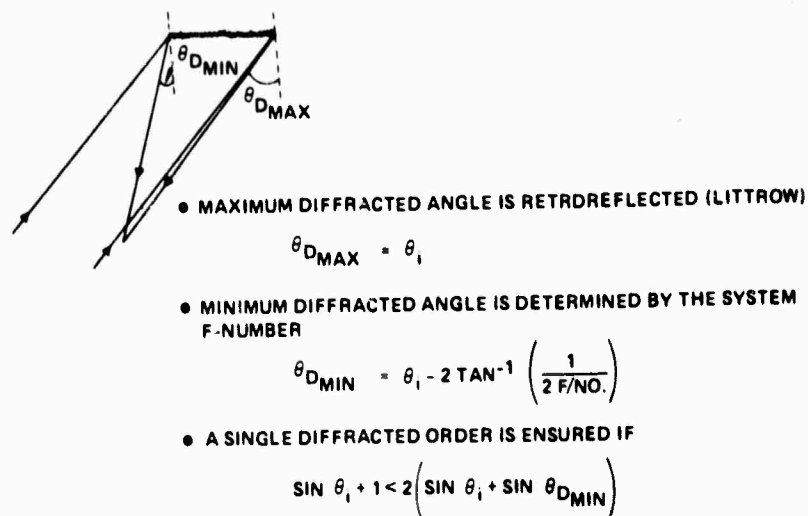


Figure 45. Virtual primary mirror: geometry used in efficiency analysis.

This condition is satisfied in the region above the solid curve in Figure 46; for any number above the curve, it was anticipated that high-efficiency virtual mirrors would be feasible.

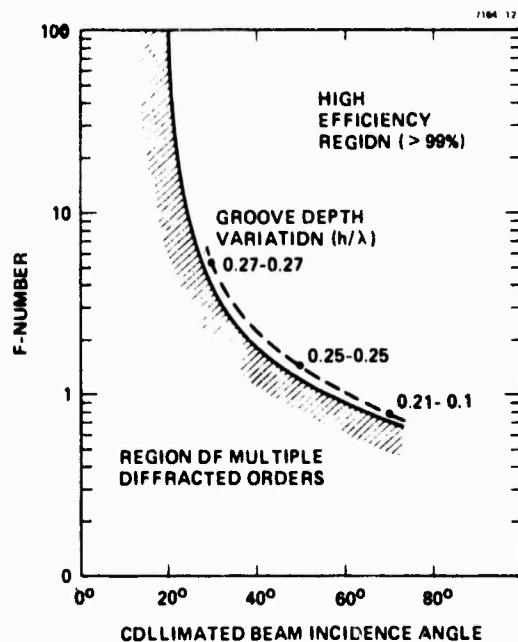


Figure 46. Virtual primary mirror design: efficiency guidelines for TM (E_{\perp}) polarization.

The diffraction efficiency code has confirmed this expectation in the following way. The first step was to see how close to the solid curve one could design a virtual lens with an ion-etched groove profile and still obtain 99 percent diffraction efficiency. It was found that one could come quite close to this curve; any design point above the dashed line of Figure 46 satisfied the requirement.

The next step was to see whether it would be necessary to tailor the groove depth across the surface in order to maintain uniformly high efficiency. The three points investigated are shown in Figure 46. The numbers listed under "groove depth variation" show the groove depths which will yield 99 percent efficiency at the outer and inner edges of the mirror. The groove depth could remain uniform for the shallower angles of incidence, but depth tailoring is required for the steeper ones.

3.0 FABRICATION INVESTIGATION

Task III of the Holographic Grating Study was an experimental investigation of techniques for fabricating low-efficiency and high-efficiency holographic gratings. The results of that effort, which extended throughout the study, are described in this section.

Section 3.1 contains an introductory discussion of potential fabrication methods, and of the reasons for selecting the aberrated-wavefront approach. This discussion is followed in Section 3.2 by an examination of the key fabrication issues, covering both low and high-efficiency gratings. The fabrication procedures that were used are described in Section 3.3, while the results of the investigation are detailed in Section 3.4 and in Section 3 of Volume II.

3.1 FABRICATION OVERVIEW

3.1.1 Fabrication Techniques

A holographic grating is defined in terms of its function as a holographic focusing element. The groove locations on the surface are the loci of the maxima of the interference fringes formed by the desired incident and diffracted beams. Therefore, fabrication of an HG requires the formation of grooves at these locations, and the various possible fabrication techniques can be evaluated in terms of the accuracy of the groove locations and the uniformity of the groove shape.

For low-efficiency holograms operating in the first order of diffraction, the optimum groove shape is probably a sinusoid, because this shape diffracts only into the first two orders of the grating (for low efficiency), and produces a minimum of scattered radiation.

In the case of high-efficiency HGs, the optimum groove shape depends on several parameters that differ for differing performance requirements, and substantially deeper grooves are required. Both of these requirements demand greater understanding and control of the fabrication process than is needed for low-efficiency gratings. For this reason, much of the fabrication

investigation was devoted to high-efficiency issues such as minimizing the effects of standing waves from reflecting substrates and achieving highly uniform coatings of photoresist.

The two major techniques of grating fabrication are briefly described in the following paragraphs.

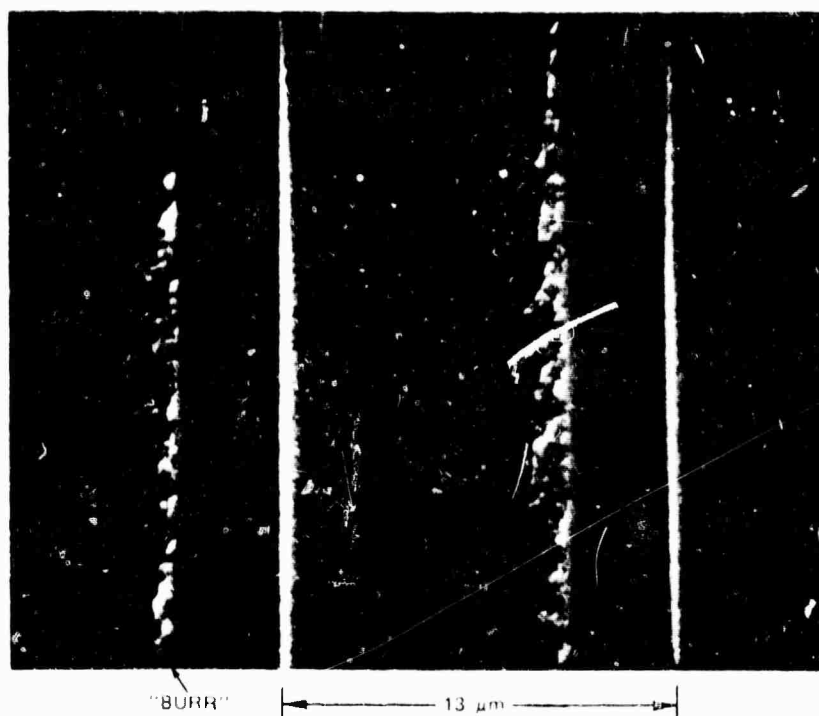
Mechanical Ruling

Mechanical ruling of the HG into the surface of the substrate requires that a complex positioning mechanism locate the cutting tool precisely at the calculated locations of a fringe maximum, and remove a very small amount of material as it is moved along the locus of this maximum. Figure 47 shows a magnified photograph of a portion of a typical ruled grating. Evidently, it is not reasonable to expect a sinusoidal groove profile by this method, and the presence of burrs indicates that the level of scattered light from such a grating is relatively high. Furthermore, ruling machines are quite expensive. If the fabrication of holographic gratings depended on mechanical ruling, they would not, in all likelihood, become practical devices. For comparison, Figure 48 shows a magnified photograph of a portion of a typical holographic grating; clearly, the holographic method permits much better control over the groove shape.

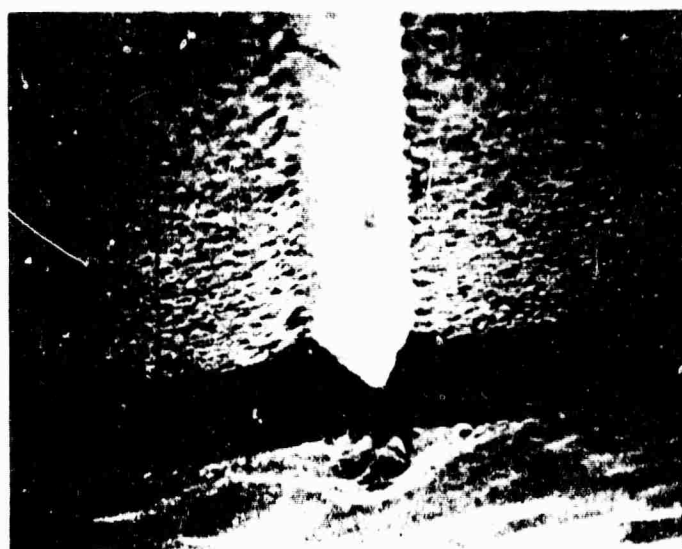
Ion-Beam Machining

Fortunately, an attractive alternative to mechanical ruling is available — that of ion-beam machining. In this technique, a beam of high-energy ions is used to ablate material from the surface through openings that must be provided to define the machining locations. These openings are produced by a layer of photoresist that is exposed and etched away prior to the machining process.

The spectral sensitivity of the photoresist is such that the exposing radiation must be in the blue or ultra-violet regions. Existing possibilities for providing this blue exposure include: (1) contact printing of a master; (2) projection of a previously-recorded pattern; and (3) direct exposure by a blue-light interference pattern. All of these techniques are potentially capable of producing a sinusoidal groove pattern, through a linear etch of the photoresist.



a. Top view.



b. Edge view.

Figure 47. Ruled grating.



Figure 48. Holographic grating.

Linear etching of several types of photoresist has been accomplished by holographers for the purpose of generating linear hologram recordings. This linear development process can be followed by ion-beam machining to obtain a desirable groove shape, since ion machining is also a linear process. To the extent that the etch rates for the photoresist and the underlying substrate are equal, the resulting groove shape will be sinusoidal. If the etch rates of the resist and substrate are different, the etched groove will be a distorted version of the shape existing in the resist, and its depth may be either greater or less than that in the resist. Nevertheless, even when the etch rates differ greatly, the process can be regulated to achieve good results.

3.1.2 Implementation Techniques

Several possible methods of providing the desired pattern of fringe locations on the resist-coated substrate are discussed in this subsection.

Ruled Master

If an appropriate ruling machine and conforming substrate are available, the desired pattern can be calculated from the operational requirements (conjugate points) of the system, ruled into a metal film on the conforming substrate, and used to contact-print the desired pattern into the

resist. The metal film can be completely removed, i.e., shallow grooves in the master are not required. The primary advantage of this method is that the groove positions are determined entirely by the master grating and not by the exposure/development/ion-beam-machining procedures. The major difficulty concerns the availability of an adequate ruling machine.

A possibly attractive alternative to a mechanically-ruled master is a photographically-recorded master. With this approach, a plotter or scanning recorder is used to provide the master. The principal difficulties lie in obtaining a suitable plotter and the necessity of providing the conforming substrate. The plotter is a generally useful tool, and so would tend to be more available than the ruling machine. A distinct advantage of this technique is that the groove shape could be tailored to meet various requirements.

Exact Holographic Grating

Conceptually, the most direct way to define the desired groove pattern is to expose the resist to the interference pattern produced by the two desired conjugate beams of the hologram. However, when infrared HGs are required, there are two major obstacles to this approach. First, the resist is not sensitive to the infrared radiation, nor are other recording materials available to be used on top of the resist or on a conforming substrate. This means that the desired fringes would have to be observed by a detector and transferred to the substrate by a blue light scanner, which is a difficult process.

The second obstacle to recording the desired hologram directly is in providing the necessary construction beams. Particularly when large reflecting substrates are involved (e.g., a primary mirror) clean, accurate optical systems of large aperture are required. For the reflection system, the converging beam must be supplied.

Magnification of a Visible-Light Original

According to holographic theory, if a hologram is recorded at a wavelength, λ_1 , it can be reconstructed at another wavelength, λ_2 , without aberration, provided that the hologram is enlarged (or reduced) by the

factor λ_2/λ_1 , the ratio of the playback to recording wavelengths. This means that a pattern could be recorded in the blue spectrum and then projected onto the substrate using incoherent blue light, with the required magnification. The advantage of this approach is that the aperture of the recorded hologram is much smaller than that of the final substrate, and the f/numbers of the blue recording beams are much larger than those of the playback beam. The major difficulties lie in producing a sufficiently accurate original hologram, in providing for curved substrates, and in achieving the extreme projection accuracies necessary for diffraction-limited sampling.

Blue Point-Source Construction Beams

As in the case of the magnified visible-light original, this technique employs blue construction beams to make an HG for use at a specified infrared wavelength. Instead of optically projecting an original hologram, however, the required fringe pattern is recorded directly on a photoresist-coated substrate at the correct scale for the IR playback wavelength, using blue point sources that most closely duplicate the prescribed wavefront. Aberrations can then be corrected on playback, using appropriate compensating optics in the diffracted beam. The advantage of this approach is that the construction point sources generate simple diverging beams that can be kept noise-free by spatial filtering. The principal disadvantage is that additional optical elements are required in the final system. Although small conventional elements might suffice to correct a low-power sample beam in this way, a high-efficiency HG would require specially designed high power components — a decidedly unattractive prospect.

Aberrated-Wavefront Construction Beams

Like the previous approach, the aberrated-wavefront technique employs blue construction beams to make a full-scale HG designed for use in the infrared. The two methods also share the ability to correct for aberrations arising from both the wavelength shift between construction and playback and the use of off-axis playback geometries. They differ, however,

in that the aberrated-wavefront approach introduces these wavefront corrections into one or both of the construction beams, rather than into the diffracted beam on playback. The correction is effected by using specially designed compensating optics to modify the spherical wavefronts emanating from optimally located point sources. The resulting fringe pattern describes an HG that is diffraction limited when played back at the specified IR wavelength and in the design geometry.

Besides making it possible to design HGs with "built-in" aberration corrections, the aberrated-wavefront method offers other significant advantages over alternative implementation techniques. These include the facts that the numerical apertures of the construction beams are much smaller (and therefore much easier to implement in the laboratory), that the construction wavelength can be selected to optimize the exposure process, and that only diverging beams are required. The small numerical apertures and diverging beams are both particularly important advantages. The principal difficulties stem from the need for stable, coherent construction beams and specially-designed, high quality correcting optics.

Because of the advantages noted above, and because the difficulties were considered to be quite manageable, the aberrated wavefront approach was implemented and used successfully throughout the HGS Program. Figure 49 shows a photograph of the recording setup that was used; it is described in the following subsections.

3.2 FABRICATION ISSUES

As noted above, the aberrated-wavefront method of generating holographic grating exposures requires special optical elements and stable, coherent blue (or UV) construction beams. Design and fabrication of the special optics are fairly routine tasks that were accomplished without undue difficulty (see Section 5). A serviceable coherent blue source was provided by the 4416 nm line from an available cw HeCd laser. Although some stability and reliability problems were experienced with this laser during the early part of the program, the manufacturer was able to solve them by rebuilding it to incorporate certain design modifications suggested by Hughes.



Figure 49. Holographic grating recording setup.

In future work, the HeCd laser will be replaced by a more suitable krypton laser fitted with an etalon to provide a highly coherent beam at 4131 nm. The higher power level available from this laser combined with the greater sensitivity of photoresist at the shorter wavelength results in more than a factor-of-ten improvement in the effective sensitivity relative to the HeCd laser. This improvement can be exploited to provide shorter exposure times and/or larger gratings.

Besides designing the correction optics and obtaining a laser suitable for making holographic exposures, a number of other issues relating to the experimental work were addressed in the course of the fabrication investigation; they are discussed in the following three subsections. The issues described in Section 3.2.1 deal with fabrication procedures applicable to both low-efficiency and high-efficiency HGs, while Section 3.2.2 covers issues of concern primarily for high-efficiency gratings. Modifications of procedures and facilities that will be needed for fabricating larger HGs up to one meter in diameter are discussed in Section 3.2.3.

3.2.1 General Issues (Low and High Efficiency)

A diagram of the HG recording setup that was used is shown in Figure 50. The construction beam optical system was designed to record the 45-degree HG beam sampler described in Section 5. This grating focuses a collimated 3.8 μm beam, incident at an angle of 45 degrees, to a point on the normal to the mirror. (See Figure 6, Section 2). The optical components consist of a beam splitter, dielectric mirrors and spatial filters, aberration-compensating lenses, and frequency stabilization optics.

Stability During Exposure

Stability is of great importance for accurately recording complex, interference patterns at high spatial frequencies. Because the interference is phase dependent, the optical path difference between the construction beams must be held constant while the pattern is being recorded. Therefore, the optical system was constructed on an optical table supported by pneumatic air mounts. The low natural frequency of these air mounts isolates the optical system from building vibrations. A plexiglass turbulence shield was

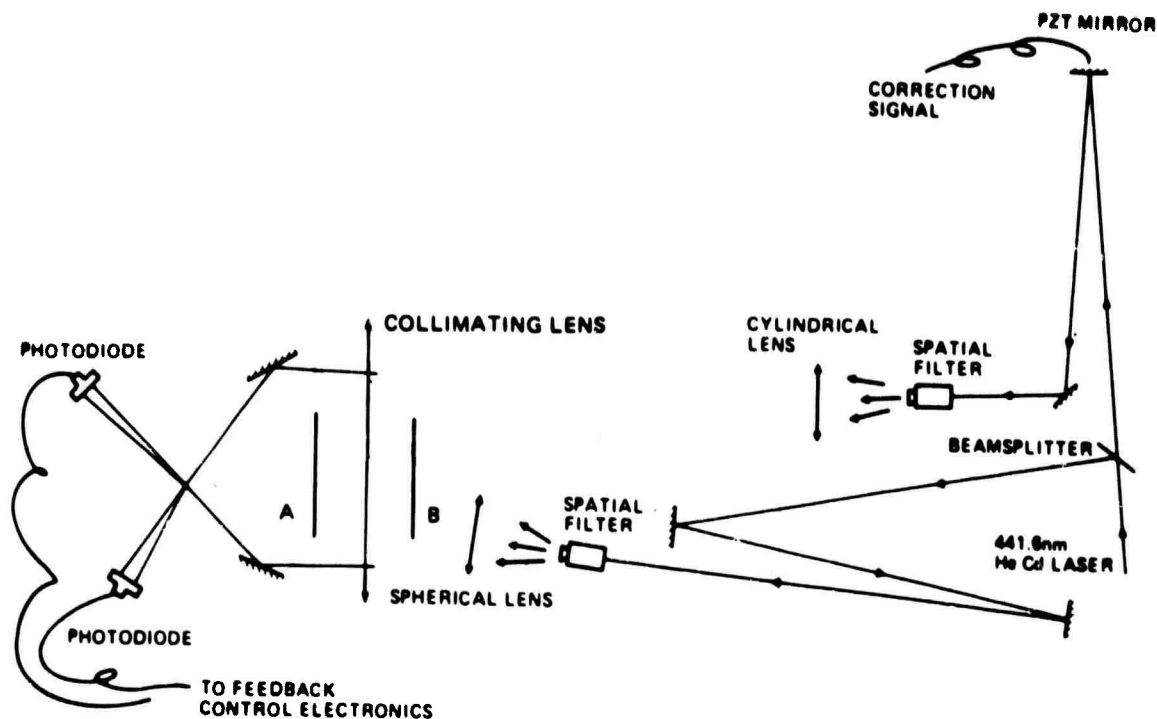


Figure 50. Exposure apparatus for exposing aberration-corrected holographic gratings.

fabricated on the optical table to minimize the effect of atmospheric disturbances and acoustic noise on the recording system. The laser source was located outside of the enclosure so as to isolate the construction beams from the thermal convection induced by the laser. In addition, the enclosure can be filled with a clean nitrogen atmosphere to prevent dust from settling on optical components. Interferometric techniques were used to study the stability of the construction optics and mounts, and the effectiveness of the isolation.

Since the optical path difference between the construction beams must be kept constant to a fraction of a wavelength, significant perturbations can be easily induced by thermal expansions of the optical components and

mounts. A feedback system was therefore designed to monitor and control this difference. Active correction with this system is accomplished through electronic processing of an error signal to drive a piezo-electric translator in one of the construction beams, achieving stability of better than $\lambda/20$.

Diffraction Effects

Dust particles on the construction optics are recorded in the photoresist as far-field diffraction patterns that appear at random positions over the area of the surface grating. On the other hand, aperture-limiting stops give rise to near-field diffraction that is distributed through the main beam that defines the grating. To investigate these aperture effects, a single-beam exposure system, consisting of a collimated beam and a 1-centimeter limiting aperture, was used. The setup is shown schematically in Figure 51, while Figure 52 shows a typical near-field pattern from this aperture, as recorded in a photoresist layer on a gold reflective substrate.

Because of the random-appearing nature of the pattern, it was initially thought to be a speckle effect due to a beam reflected from the gold. The experimental approach used to isolate the cause of this effect was to interrogate the intensity uniformity of the beam systematically after various components in the exposure system. The scans shown in Figure 53 were taken continuously across the beam through a 1-cm aperture, using a sampling aperture of $10\text{ }\mu\text{m}$ diameter on the photomultiplier tube. Strong Fresnel ringing is evident from the edge of the aperture but the central beam appears uniform. Therefore, various iterative exposures were employed on a variety of substrates using a simple diverging point source. This permitted the collimating lens to be eliminated, thereby minimizing the optical surfaces in the exposure setup. The substrates investigated were (1) simple microscope glass slides, (3) reflective gold evaporated on 2-inch silicon wafers, (4) reflective gold sputtered on 2-inch silicon wafers. Both spin-coating and dip-coating were used to coat the photoresist in these experiments. Exposures to the diverging point source exhibited no speckle. The next step was to add the collimating lens in the optical system and repeat the exposures on various substrates. Once again, no extraneous speckle was recorded in the photoresist.

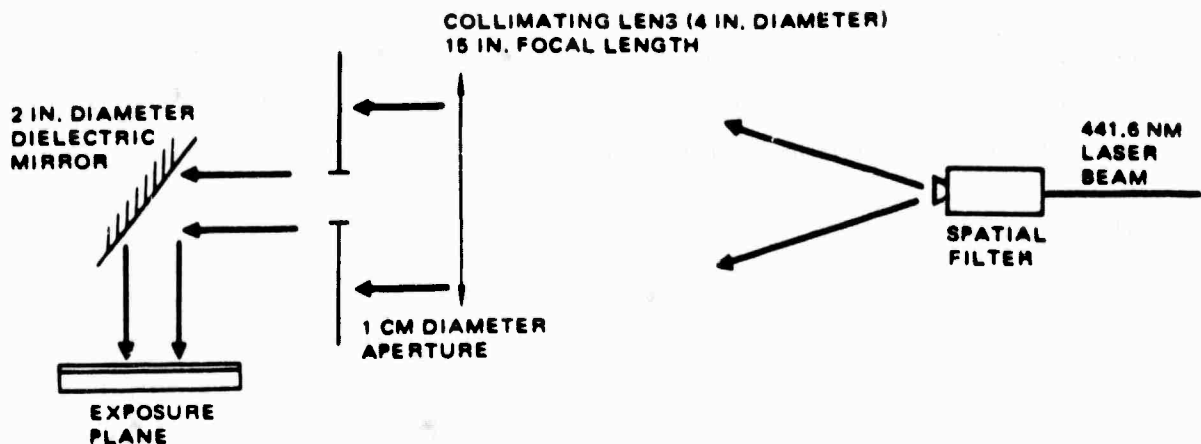
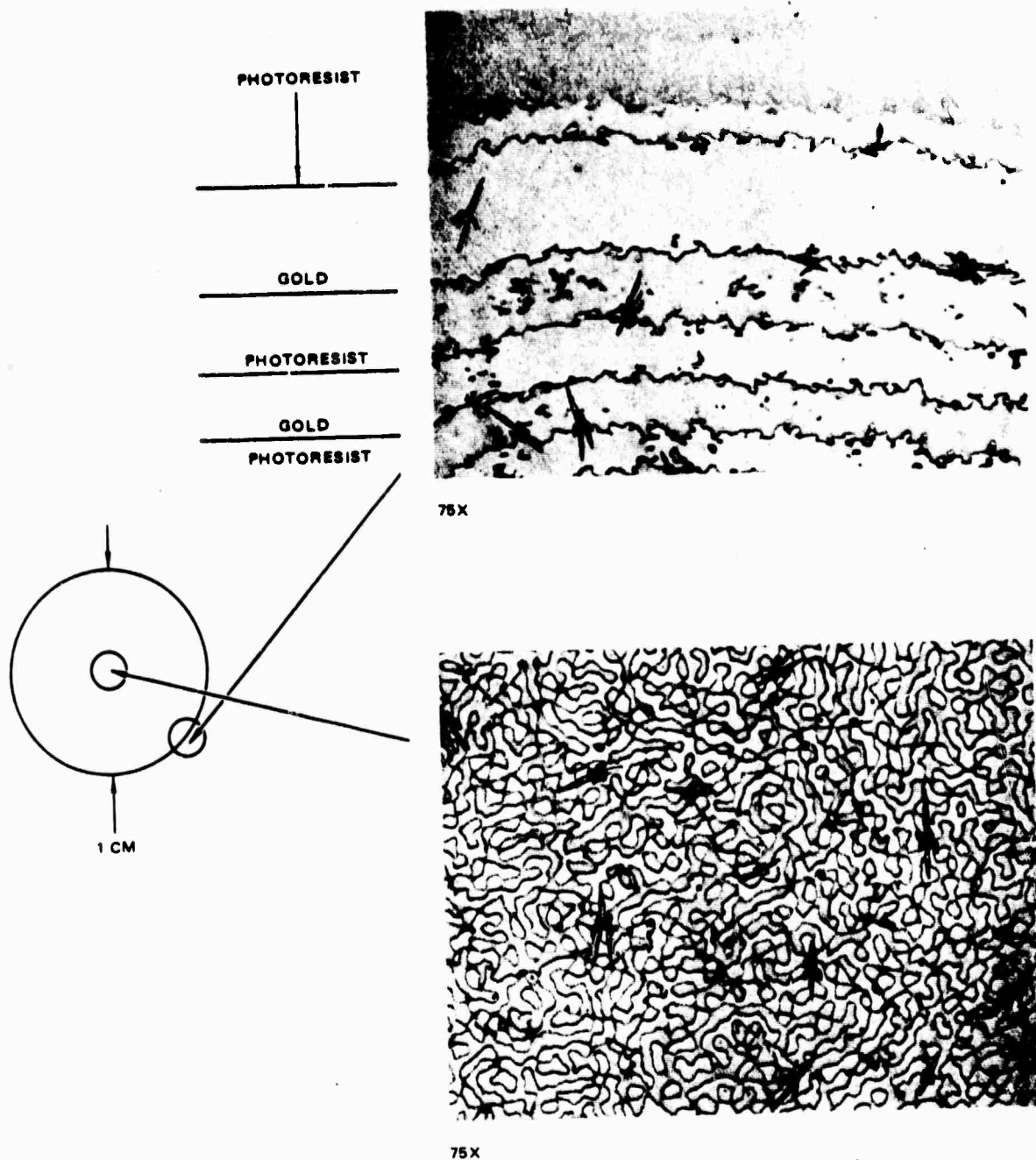


Figure 51. Single collimated-beam exposure system.

With the addition of the aperture in the optical system, patterns in the photoresist similar to those shown in Figure 52 were observed. The same effect was seen in exposures with the aperture at several locations in the construction beam. The far-field location of a 1-cm diameter aperture at 441.6 nm is $D^2/\lambda = 227$ meters (D = diameter of the aperture; λ = wavelength). Further experimentation has shown that even folding mirrors 1 to 2 inches in diameter can cause near-field diffraction problems if the incident beam over-fills the mirror aperture. The random appearance of the diffraction pattern is attributed to defects in the aperture. Imperfections in the aperture of the order of 25 μm can cause Fresnel rings less than 25 μm in diameter to break up into the random pattern seen in Figure 52.

Scattering From Reflective Substrates

In order to control the etch rate, etch depth, and the profile of the surface grating recording in Shipley 1350B photoresist, experimental data were collected for various exposures at fixed development times. Dip-coating and spin-coating techniques were used to apply photoresist to a gold reflective layer on glass substrates. After the photoresist was exposed and developed, the etch depth was measured with a Tallysurf instrument. Initial work using single-beam exposures at 441.6 nm showed effects of scattering from the reflective substrate, which resulted in a



NOTE: THE STAR SHAPED DEFECTS ARE DUE TO CONTAMINATION OF THE PHOTORESIST DURING THE COATING PROCESS.

Figure 52. Near-field diffraction of 1-cm diameter aperture recorded in Shipley 1350B photoresist layer on gold.

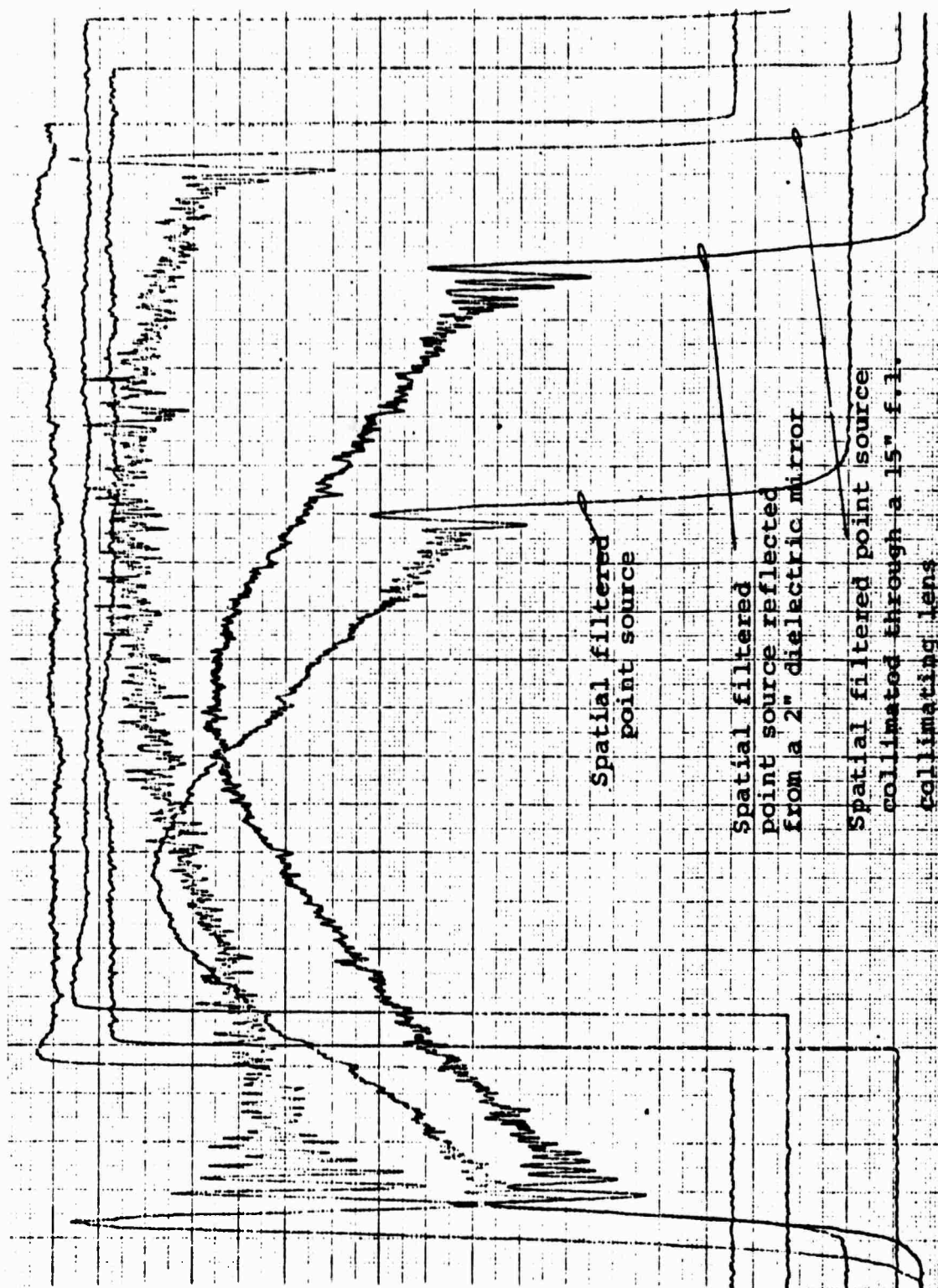


Figure 53. Intensity scans of beam uniformity across a 1-cm diameter aperture.

random relief on the photoresist rather than a smooth, etched surface. The sizes of the scatter reliefs were found to depend on the surface quality of the substrate. This does not pose a problem in the recording of surface gratings since the photoresist grating serves as a mask for ion-beam machining the final grating onto the mirror surface. The surface grating mask can be exposed until all the photoresist is removed in areas where the ion beam is to etch the reflective surface. However, the scattering does not allow accurate data to be obtained for exposures which do not completely etch down to the gold layer. To obtain etch rate data, the coherence of the 441.6-nm beam was intentionally reduced with a diffuser. Etch rate data were also obtained experimentally from exposures of linear gratings produced by interfering collimated wavefronts. It was found that the scattering problem is alleviated with interference exposures because the scattering from each single beam is dominated by interference effects.

During the course of the investigation, reflective optics were used whenever possible to minimize the effects of secondary reflections from the interfaces and surfaces of lenses.

3.2.2 High-Efficiency Grating Issues

Two key issues relating to the fabrication of high-efficiency HGs on metallic substrates were identified early in Task III: (1) obtaining highly uniform layers of photoresist and (2) minimizing or eliminating standing wave patterns in the photoresist grating caused by reflection from the substrate. The first issue is relevant to both low-efficiency and high-efficiency HGs, but is more critical in the latter case because of the deeper grooves required. The second issue is of concern only for high-efficiency gratings since standing waves appear only when the grooves are sufficiently deep.

Because of their critical importance to the successful fabrication of high-efficiency HGs, the foregoing issues were investigated at length during the study. They are described briefly in the following paragraphs, and at greater length in Section 3.3.

Photoresist Layer Uniformity

Variations in the thickness of a photoresist layer deposited on a substrate before exposure can lead to nonuniform diffraction efficiency in the developed grating. This effect can be understood with the aid of Figure 54. The sketch in the upper right-hand part of the figure represents a cross-sectional slice through an idealized holographic grating in a non-uniform layer of photoresist, following exposure and development. For illustrative purposes, only two well defined layer thicknesses are considered. It is also assumed that the depth of the groove after development is directly proportional to the exposure at each point. This linear exposure/development characteristic of both the "thick" and "thin" gratings is plotted in the upper left portion of the figure. A single characteristic describes both thicknesses up to the point where the photoresist in the thinner layer has been etched away down to the substrate. As the exposure increases beyond this point, the etching depth saturates in the thinner layer but continues to increase linearly in the thicker layer until the maximum exposure/depth is reached.

As a consequence of the difference in etching characteristics, the groove depth and duty cycle* will also vary with the thickness of the photoresist layer. The period, however, remains unchanged, since it is defined by the construction beam geometry. These effects can be seen by referring to the holographic exposure curve in the lower left part of Figure 54. Here, the ordinate of the curve is proportional to the exposure level at each point along a line perpendicular to the grooves. The sinusoidal shape of this curve characterizes the intensity distribution in the interference pattern of the two coherent construction beams. In the thicker layer, the grooves conform to this shape because of the linear photoresist characteristic.

In the thinner layer, however, saturation of the characteristic curve tends, in effect, to flatten the peaks of the cosine profile at the level indicated by the dashed line "A" corresponding to the layer thickness. As

*The duty cycle may be defined as the width of the groove wall, at a point half way to the bottom of the groove, divided by the period.

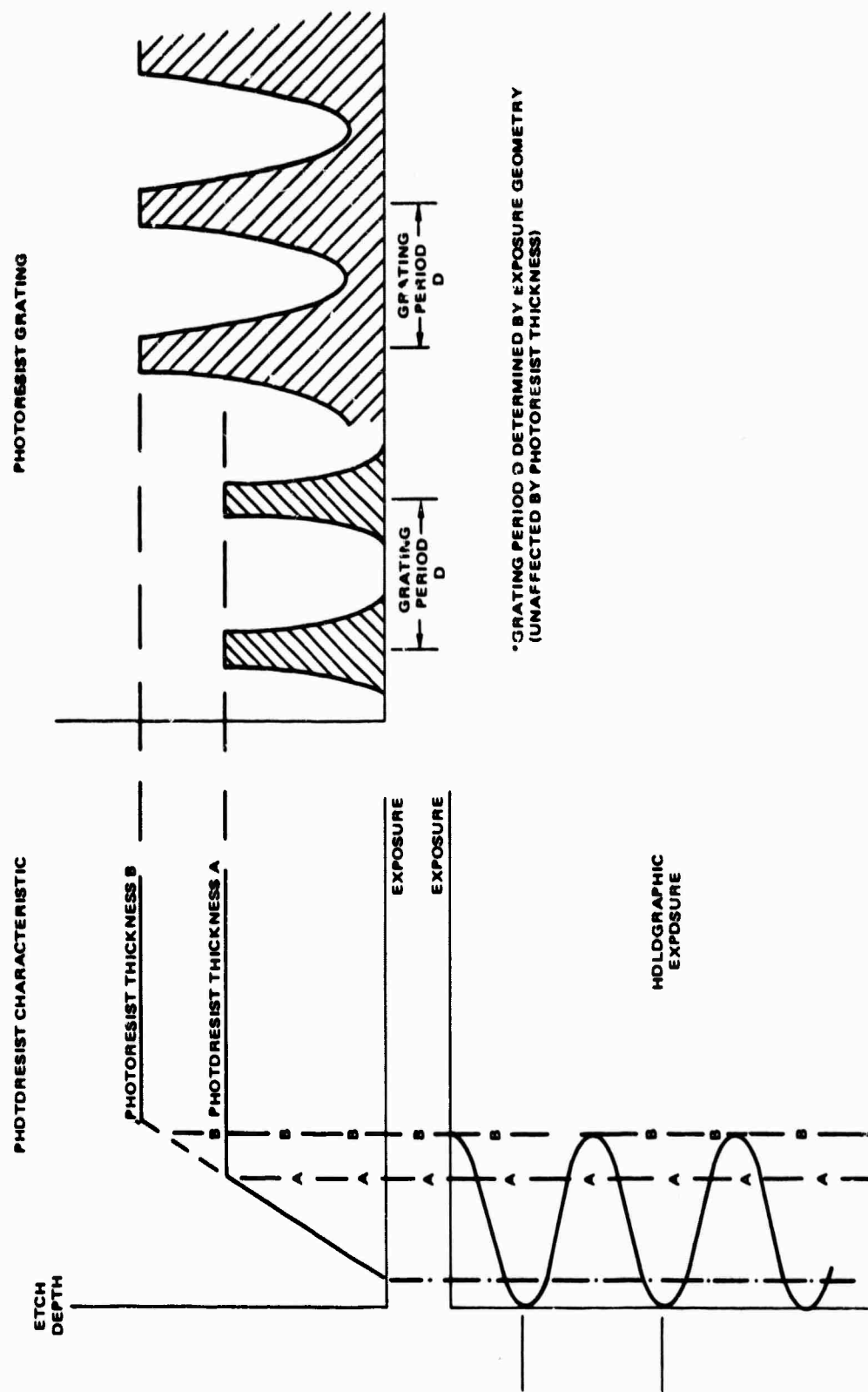


Figure 54. Groove shape dependence on photoresist thickness uniformity.

a result, the grooves in this part of the grating are not only shallower than in the thicker layer, but the duty cycle is also reduced.

Since the diffraction efficiency is a function of both the groove depth and duty cycle, it also varies with the thickness of the photoresist layer. (See Section 4.1.) Thus, obtaining uniform layers of photoresist is essential to achieving both maximum grating efficiency and good efficiency uniformity.

Standing Waves

Photoresist exposure to coherent illumination is characterized by the etching depth as a function of exposure energy for a fixed development time. Because of the reflective substrate on which the photoresist is coated, strong standing waves occur, causing intensity variations in the bulk of the photoresist along the normal to the substrate, even when the incident illumination is uniform. This phenomenon is illustrated in Figure 55 for a uniform exposure at normal incidence to the photoresist layer. In the bulk of the photoresist one must consider the attenuation of the exposing beam due to absorption as well as the intensity distribution resulting from interference between the incident and reflected waves. These standing waves have half-wave cycles with an intensity minimum at the reflective surface, where a 180-degree phase shift occurs. Their inherent stability is independent of the stability of the exposure setup.

The standing waves give rise to variations of exposure energy in the bulk of the photoresist layer. Because of such variations, the rate of development also varies as these sublayers of differently exposed photoresist are removed during development. The effect of this exposure nonuniformity due to standing waves, is shown in Figure 56. These curves were obtained experimentally by exposing the photoresist to uniform incident illumination at 441.6 nm. For a fixed development time of 1 minute in a one-to-one concentration of AZ developer in de-ionized water, the thickness removed by the developer at various exposure levels was measured using a Dektak instrument. Exposures were made on gold reflective substrates and microscope slides. The glass surface of the microscope slide was indexed with glycerol to a black absorbing surface to minimize reflections from the rear surface of the substrate. At similar exposure levels, a smaller amount

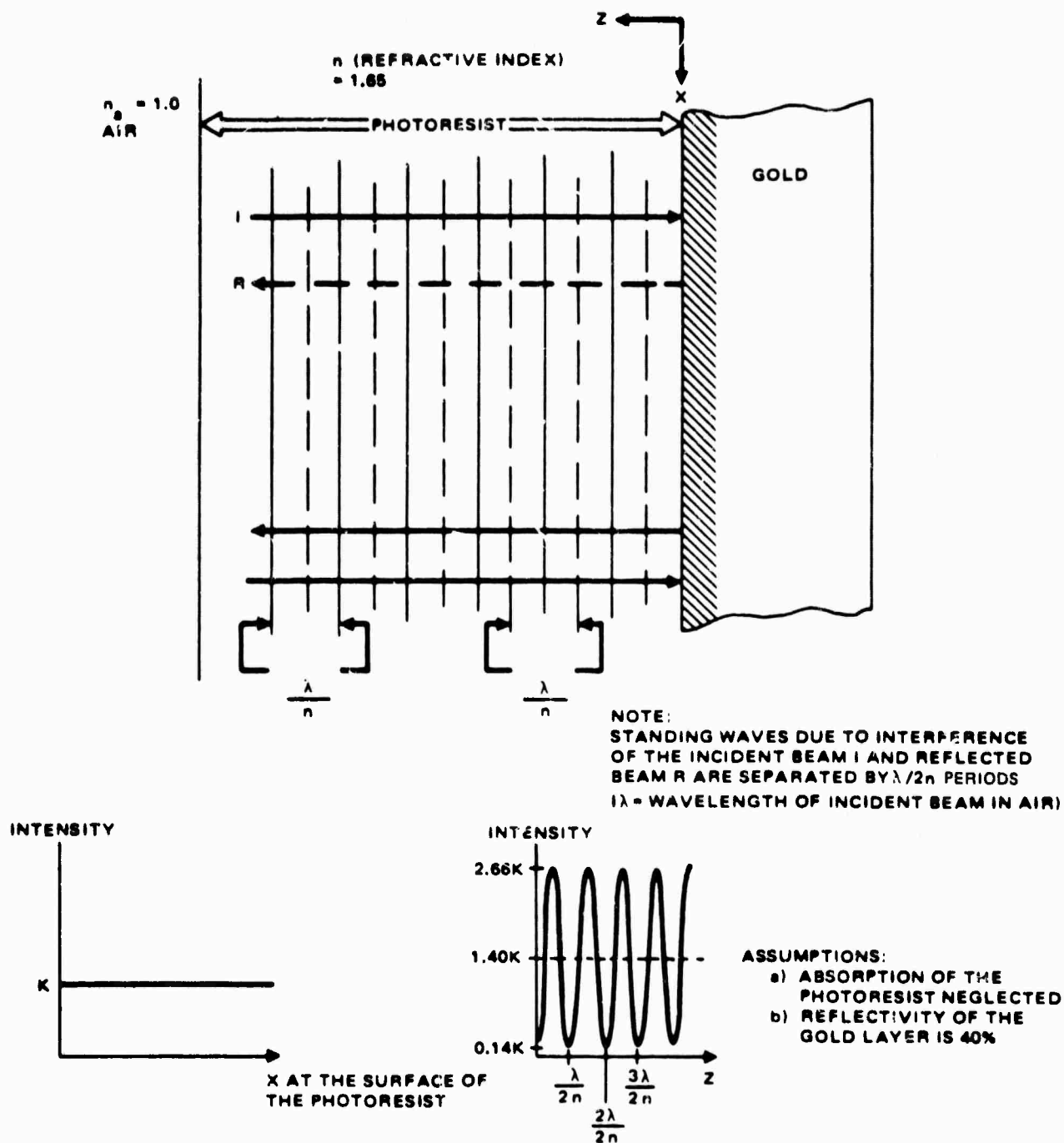


Figure 55. Standing waves in the photoresist layer due to interference of incident and reflected wavefronts.

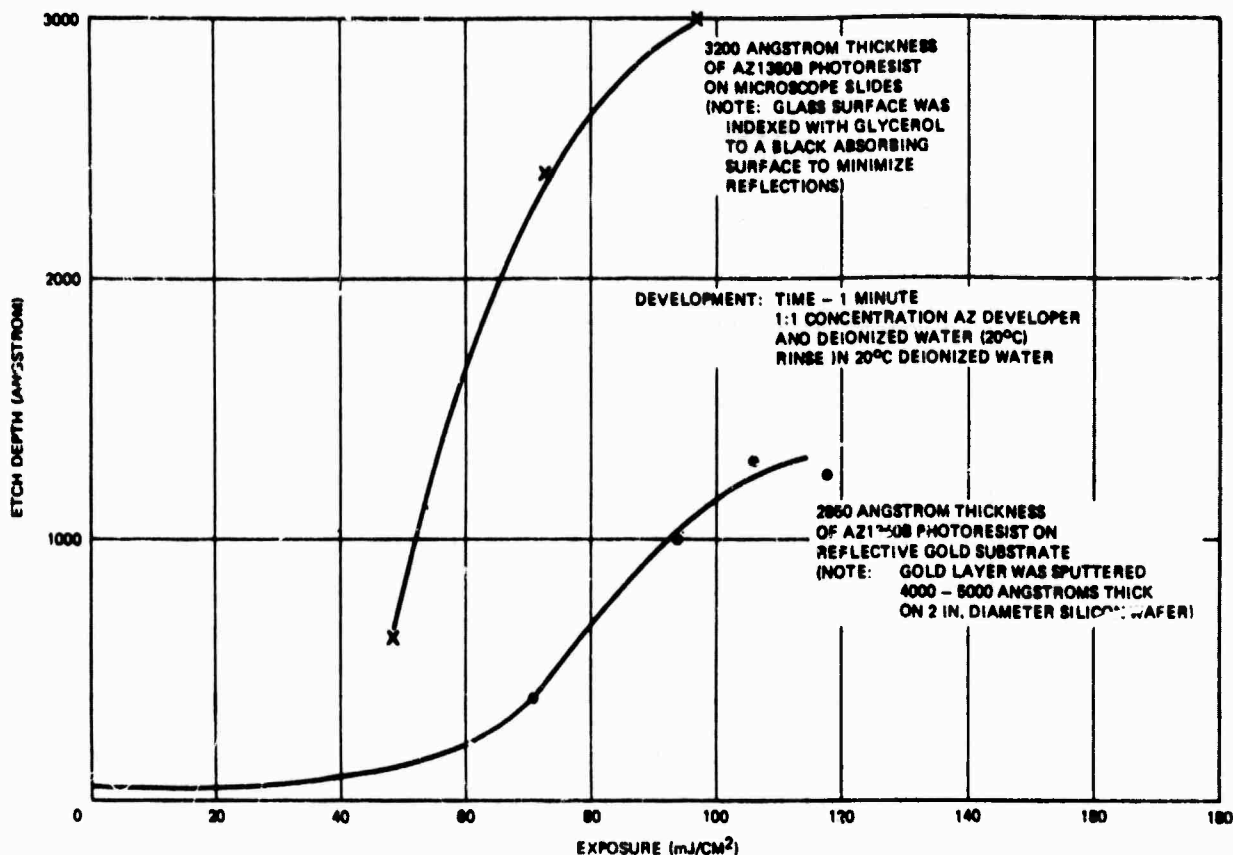


Figure 56. Etching depth versus exposure for AZ1350B photoresist developed for one minute in 1:1 AZ developer.

photoresist was removed from the gold-coated reflecting substrate than from the non-reflecting substrate. This shallower etching depth is attributed to the slower etching rate in the bulk of the photoresist where the exposure was reduced due to the presence of a minimum in the intensity of the standing wave.

3.2.3 Large-Area Grating Issues

With the single exception of a 9-cm diameter, water-cooled mirror, 2-inch diameter substrates were used exclusively for the HGs that were fabricated throughout the study. (The water-cooled mirror is discussed in Section 5.1.) This restriction was imposed so that the spin-coating

technique, which yields uniform layers of photoresist, could be used for the experimental investigation. Spin-coating is not feasible for large substrates because of the high mechanical stresses produced.

Nevertheless, it was evident from the beginning that the results of this task would be of limited value in HEL systems applications unless they could be extrapolated to much larger substrates. Because this issue is of central importance to the development of primary mirror HG beam samplers and other large-aperture concepts, a preliminary assessment was made of the problems involved in scaling up to 1-meter diameter curved substrates. The results of this assessment are summarized in the following paragraph.

Success in extending current fabrication techniques to 1-meter apertures hinges on three requirements: (1) obtaining a suitable laser source of higher power, (2) developing coating techniques for large-area curved substrates, and (3) designing and constructing ion-machining equipment that can accommodate the larger substrates.

The first requirement can be appreciated by noting that an exposure time of 71 hours would be needed to fabricate a 1-meter beam sampler grating using the HeCd laser that was available during the study. Although the fringe control system was designed to correct phase errors occurring during an indefinitely long exposure, it is difficult to ensure the necessary physical stability of the substrate itself over periods of several hours or more. This substrate stability requirement for large-area exposures is best met by providing higher laser output power in conjunction with single-longitudinal-mode operation to increase the coherence length.

Several laser manufacturers offer krypton and argon lasers capable of providing single-frequency output power levels of from 0.5 to 0.75 watts at 0.3638 μm and 0.5 to 2.5 watts at 0.4131 μm . These wavelengths are preferable to the high-gain argon lines at 0.4880 and 0.5145 μm (and to the 0.4416 μm HeCd line) because of the sharply higher photoresist sensitivity at the shorter wavelengths. Thus, for example, a previous change in the exposure wavelength from 0.4579 μm to 0.4416 μm resulted in a factor-of-five increase in sensitivity, and further improvements of from five to twenty times may be anticipated with the 0.4131 or 0.3638 μm krypton lines. As noted earlier, the 0.4131 μm krypton line will be used in future work.

Concerning the second requirement, two current techniques used to deposit photoresist on small-area substrates are spin-coating and dip-coating. The major difficulty with spin coating for 1-meter substrates is the high speed at which the substrates must be spun. Reducing the spinning speed leads to thickness non-uniformities caused by drying of the resist before full, uniform coverage can be achieved. Another factor contributing to non-uniformity is the increase in linear velocity with increasing distance from the center of rotation. Dip coating has been used at Hughes to coat 33-cm diameter mirrors with resist layers 0.5 μm thick, achieving a 10-percent thickness variation. This technique is suitable for coating large areas but needs refinement for application to 1-meter apertures and curved substrates.

Roller coating and spray coating are used by commercial vendors to deposit relatively thick layers of resist on substrates used in printed circuit board technology. However, the minimum thickness achieved with these techniques is 10 μm , which is excessive for HG applications. Further development of these techniques may make them viable for large-area, thin coatings.

The last major requirement for fabrication of surface gratings on 1-meter substrates is the design and construction of large ion-machining equipment. The area coverage attained by ion bombardment depends on the source size, the use of a "diverging lens" assembly, and the source-to-target distance. At the Hughes Research Laboratories, aperturing techniques have been developed and used with existing ion machining equipment to fabricate uniform machined gratings 25 cm by 30 cm in area. Section-by-section ion machining of large-area gratings has also been demonstrated. These techniques can be extended directly to 1-meter substrates.

3.3 FABRICATION PROCEDURES

3.3.1 Discussion of the Method

Holographic surface grating fabrication consists of a material preparation process and two exposure steps. First, a photoresist such as Shipley AZ1350B is coated on the desired substrate. For beam samplers,

the substrate consists of the reflective surface at which the surface grating will sample the incident beam. In the next step, a coherent exposure (at 441.6 nm, for example) records the required interference pattern in the photoresist layer. In the developing process, Shipley AZ developer is used to remove photoresist at a rate determined by the local exposure of the photoresist layer. The interference pattern is therefore recorded as a surface relief pattern in the developed photoresist. As a result, all the photoresist is etched away in heavily exposed areas and very little is removed in lightly-exposed areas. This photoresist pattern then serves as a mask for the second exposure step, in which an ion beam etches the surface grating into the underlying reflective layer.

The efficiency of the final grating is determined by the depth and profile of the ion-etched grooves in the substrate. This profile is, in turn, highly dependent on the profile of the photoresist grating mask. Because these gratings consist of lines comparable to wavelength dimensions, good process control of each step is essential.

Typical experimental parameters for layers of photoresist and substrate are shown in Table 4. In general, the photoresist can be either spin-coated or dip-coated onto the substrate. The volatile solvent in the photoresist solution liquifies the material for application to the substrate. After coating, the photoresist is dried at 70 to 80°C to remove all volatile solvents, which can cause variations in sensitivity.

TABLE 4. EXAMPLES OF PHOTORESIST AND SUBSTRATE LAYERS USED IN EXPERIMENTS

	Typical Material	Thickness, Å
Photoresist	Shipley 1350B	2500 - 3500
Reflective Substrate (Beam Sampling Surface)	Gold	4000 - 5000
Base	Glass	

Spin-coating is a method whereby the liquid photoresist is deposited on the substrate and the substrate is spun at a constant speed to produce a

uniform coating. The variables which determine the photoresist thickness are the initial photoresist concentration and the spin rate. With dip-coating, the substrate is extracted from a solution of photoresist at a constant rate ("dip-drawing") or the substrate is held stationary while the solution is drained away ("dip-draining"). The variables which determine the thickness in this case are the photoresist concentration and the pull rate or drain rate. Some typical thickness data are shown in Table 5. Although these results are repeatable under similar conditions, the thickness depends on the surface conditions as well as the size of the substrate. Therefore, representative films for each batch of material prepared were always measured by a Dektac machine to obtain accurate thickness information. For the most part, photoresist thicknesses in the range of 2500 to 3500 Å were used. This initial thickness determines the depth to which the reflective substrate can be etched in the ion-beam machining exposure.

TABLE 5. PHOTORESIST THICKNESS DATA

SPIN COATING	Concentrated Shipley 1350B Filtered
	Substrate-gold on 2 inch diameter silicon wafers 5,000 RPM — Photoresist thickness 2800 Å
DIP-DRAW COATING	Concentrated Shipley 1350B
	Substrate-glass 2 x 3 inches
	1 inch/20 seconds — Photoresist thickness 5600 Å
	1 inch/25 seconds — Photoresist thickness 4500 Å
	1 inch/30 seconds — Photoresist thickness 4000 Å

After being applied to the substrate, the photoresist is exposed to the interference of the construction beams. As discussed in Section 3.1.2, the Hughes approach employs aberrated wavefronts at the construction wavelength. This allows the grating to be constructed with diverging beams of small numerical aperture. Residual aberrations of the hologram can be corrected with small-aperture elements in these construction beams.

3.3.2 Grating Exposure

An exposure setup for recording linear gratings having a period of approximately $6\text{ }\mu\text{m}$ is shown in Figure 57. The fringe control interferometer behind the exposure plane maps one construction beam onto the other to produce broad fringes so that the intensity can be detected with the photodiodes. These detection fringes are 180° degrees out of phase with respect to each other due to a 90° degree phase shift of the reflected beams at the beam splitter. Intensity changes in these detected fringes correspond directly to phase changes in the construction beams. Phase errors due to mechanical vibrations of optical mounts, atmospheric disturbances of the construction wavefronts, etc., cause the intensity distribution of the interference pattern to drift. This motion of the construction wavefront interference pattern during an exposure results in a "blurred" recording of the grating. Therefore, feedback control electronics are used to modulate a piezo-electric translator in one of the construction beams. Intensity differences between the detected fringes are integrated to provide a correction signal to the

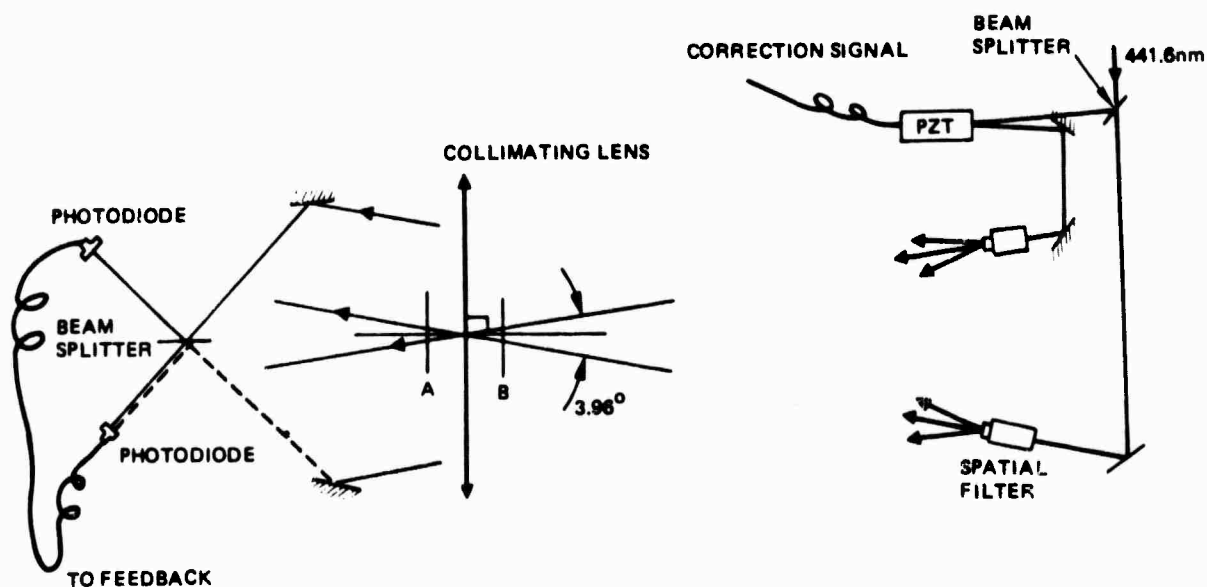


Figure 57. Exposure apparatus for recording linear grating ($6.38\text{ }\mu\text{m}/\text{angle}$) at location A and quasi-linear grating at location B.

translator. This active control system allows exposures to extend well beyond 1 hour by correcting phase errors to better than $\lambda/10$.

Due to the presence of the collimating lens in Figure 57, the diverging waves from the point sources are collimated at the exposure plane A so linear gratings can be recorded with plane wavefronts. The theoretical grating spacing s is:

$$s = \frac{\lambda_p}{2 \sin(\theta_p/2)} = \frac{0.4416 \mu\text{m}}{1.68 [2 \sin(1.18^\circ)]} = 6.38 \mu\text{m/cycle}.$$

where

$\lambda_p = \lambda_{\text{air}}/n$ = construction wavelength in photoresist

n = refractive index of photoresist

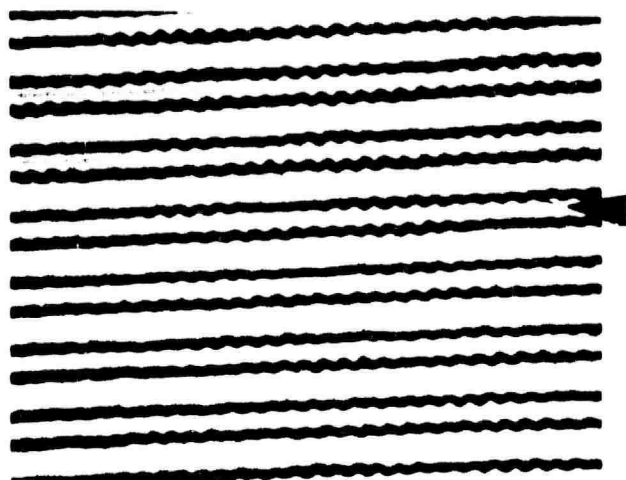
$\theta_p = \sin^{-1} [(\sin \theta_{\text{air}})/n]$ = included angle between construction beams in photoresist.

A typical grating period of the exposed photoresist gratings as measured with a microscope-stage micrometer, was $6.36 \mu\text{m/cycle}$, in agreement with this calculation. This grating spacing was chosen to be large enough so that a fair amount of detail can be seen through a conventional microscope at 1000-to-2000X magnification. Figure 58 shows an example of a photoresist grating recorded at location A in Figure 57.

Because of internal reflections between its front and back surfaces, the lens in Figure 57 refracts part of the incident beams at different angles, producing weak extraneous gratings. These extraneous gratings produce spurious diffracted orders which can be eliminated by using anti-reflection coated single-element lenses or reflective optics. Location B allows quasi-linear gratings to be recorded with spherical wavefronts and eliminates the extraneous reflections from the lens. The resultant grating is produced as expected with only the standing-wave effect as shown in Figure 59. Examination of the diffracted orders verifies the absence of other gratings.

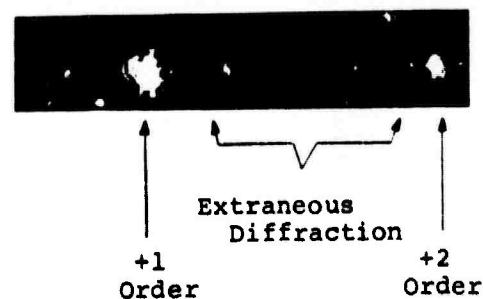
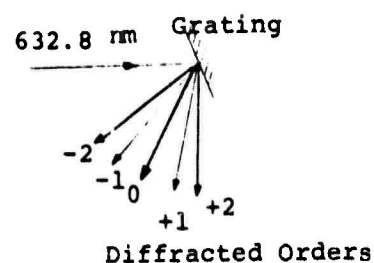


660x



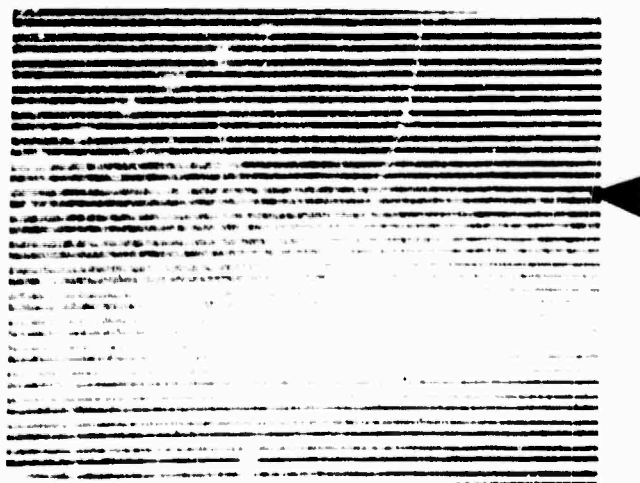
1650x

(a)

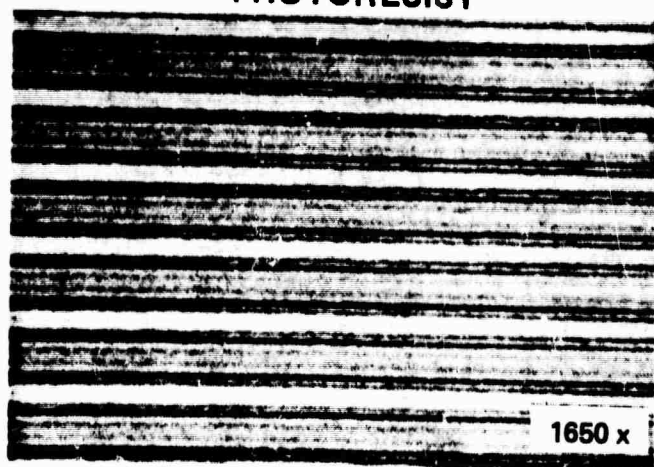


(b)

Figure 58. (a) Linear grating recorded in AZ1350B photoresist over gold on 2" x 3" microscope slide. Note extraneous grating structure along the edges due to spurious reflection from lens element. (b) extraneous diffraction caused by the extraneous grating structure. Note: Arrows in photograph denote the top of the grating step.

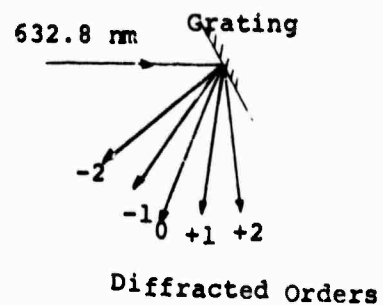


PHOTORESIST



1650x

(a)



+1
Order

+2
Order

(b)

Figure 59. (a) Quasi-linear grating recorded in AZ1350B photoresist over gold on 2" x 3" microscope slide. Note standing wave structure along the grating. (b) First and Second diffracted orders. Note: the secondary spot near the diffracted orders is due to reflections in the laser cavity; arrows in the photographs denote the top of the grating step.

3.3.3 Development of Photoresist Gratings

It can be shown that the relationship between etching depth, in photoresist, Δd , and exposure E (energy/unit area) is⁶:

$$\Delta d = T[r_1 - \Delta r \exp(-cE)] \quad (11)$$

where

T = development time (seconds)

c = exposure constant of the photoresist

r_1 = etching rate of exposed molecules

r_2 = etching rate of unexposed molecules

$\Delta r = r_1 - r_2$

If $cE \ll 1$ in Equation 11 (as is usually the case), then

$$\Delta d \approx \Delta r T c E + r_2 T \quad (12)$$

Equations 11 and 12 show that the etching depth in photoresist is strongly dependent on the etching rate of unexposed molecules. The characteristics of r_2 can be utilized to control the degree of linearity of the final etching rate of the material.

A survey of previous work done with AZ1350 photoresist is summarized in Figure 60. The wide dispersion of experimental data taken by various workers is evident. These experimental data are dependent on laboratory conditions and control of material preparation and processing. To obtain accurate data based on the preparation and processing employed in the Holographic Grating Study, the characteristics of r_2 were investigated using both AZ1350 developer and AZ303 developer. First, AZ1350B photoresist was spin-coated onto silicon wafers at 300 RPM to form a photoresist layer

⁶R. A. Bartolini, Appl. Opt. 13, 129 (1974)

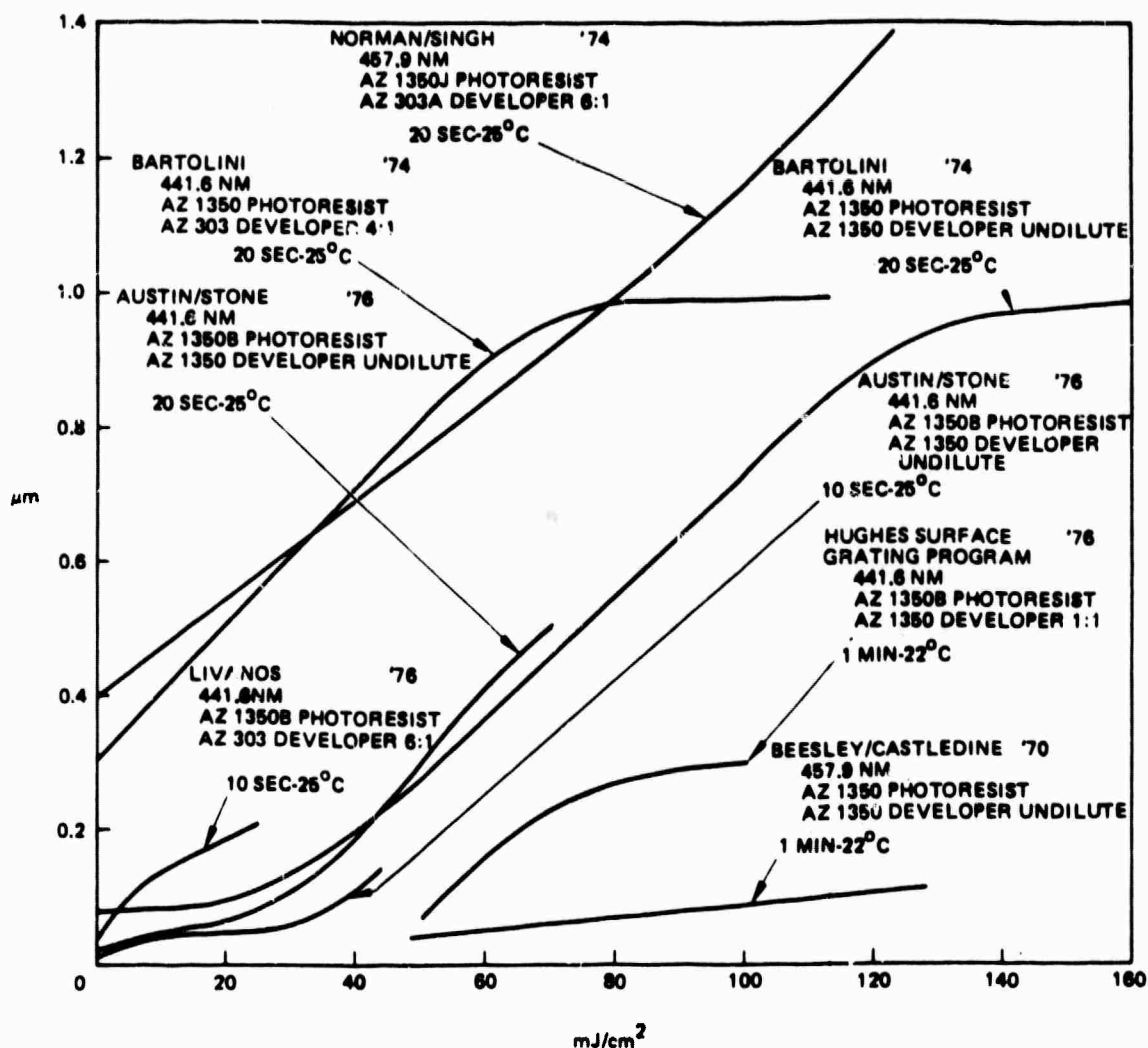


Figure 60. Summary of experimental data reported by various workers using AZ1350 photoresist.

approximately 4300 Å thick. The photoresist-coated wafers were then baked at 80°C for 20 minutes. Silicon wafers provide a convenient optical surface upon which photoresist layers of very uniform thickness can be applied by spin-coating techniques. The photoresist was then developed for various development times, rinsed with de-ionized water, and blown dry with nitrogen. During the experiment, variations in the etching depths occurred due to non-uniform agitation of the photoresist in the developer. Depletion of the developer occurs if agitation is not adequate to keep fresh developer at

the photoresist surface. Therefore, the developer was stirred at a constant rate during the development process to achieve consistency in the experiments. The developer temperature was held constant at 21 to 22°C.

Experimental data for r_2 corresponding to various dilutions of developer are shown in Figure 61. The etching depths were measured on a Dektac instrument. Referring to the experimental data, a very wide range of variation in the measurements was recorded for long development times with undiluted AZ1350 developer. This is attributed to a pronounced roughness of the etched surface resulting from extended development. At a one-to-one dilution ratio, r_2 is very small, which is desirable to prevent excessive removal of unexposed photoresist. The AZ303 developer was found to have a higher r_2 value. In addition to this increased r_2 value, other workers have found significant increases in development speed for r_1 using this developer. Hughes experience has verified this effect along with a smoother etched surface, as indicated by the relatively small spread in the experimental data. This is advantageous for exposing larger grating areas because the exposure energy density can be reduced.

3.4 EXPERIMENTAL RESULTS

In Section 3.2.2, two issues of major concern in the fabrication of high-efficiency HGs were described: (1) obtaining highly uniform photoresist coatings on the grating substrate, and (2) minimizing or eliminating standing wave patterns in the photoresist grating (which may be transferred into the final ion-etched grating). The first of these is a key element of a more basic issue underlying the development of such gratings: gaining sufficient understanding and control of photoresist and ion-machining processes to ensure that the desired groove depth and profile are accurately reproduced in the final grating. As noted earlier, control of groove properties is also needed to achieve good efficiency uniformity, which is important for low-efficiency, as well as high-efficiency HGs.

In contrast, standing waves are ordinarily of concern only in the fabrication of high-efficiency gratings. The reason for this is that standing waves occur only when the thickness of the photoresist layer exceeds a

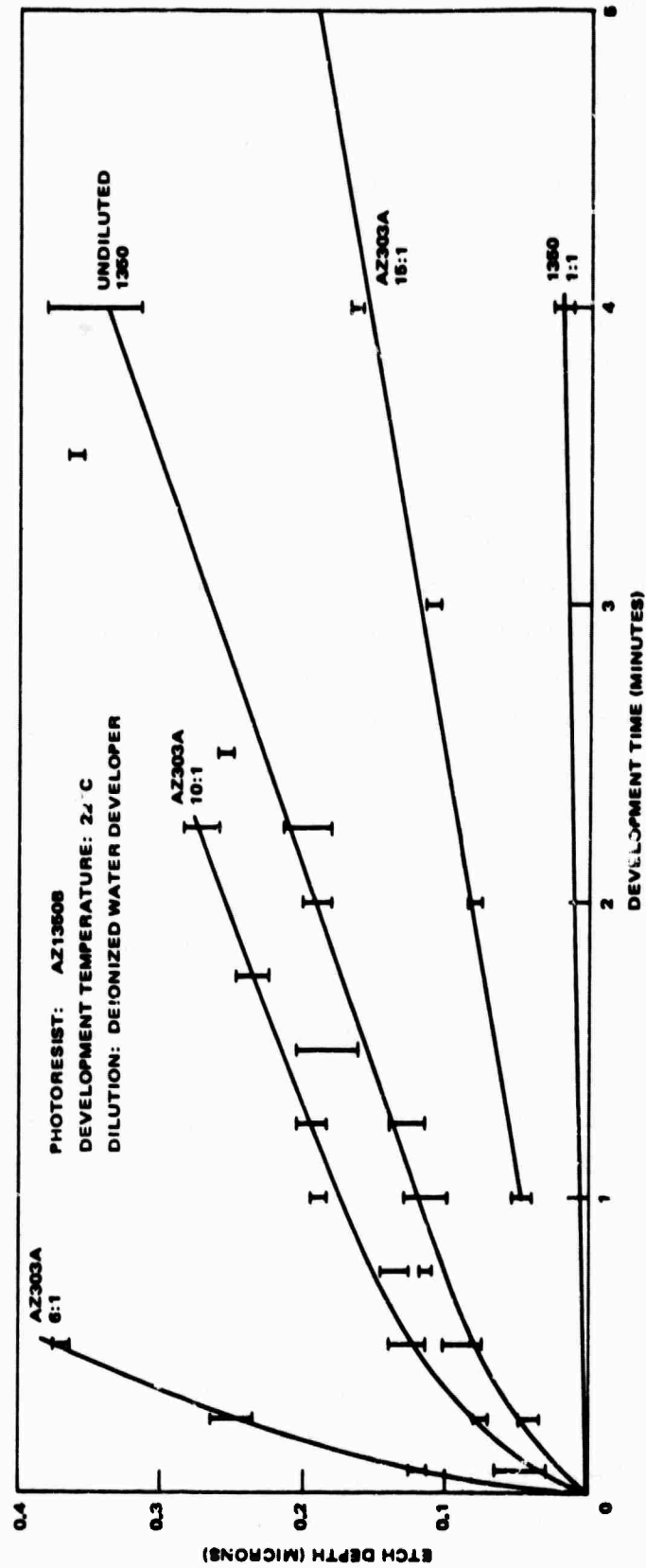


Figure 61. Experimental data of etching depth versus development time at various dilutions of AZ303A and AZ1350 developers.

half-wavelength of the exposing radiation (in the photoresist), and this limit is usually not reached with shallow, low-efficiency HGs. They do tend to appear in the thicker photoresist coatings that are required for producing high-efficiency gratings. When they occur, standing waves tend to reduce the attainable level of diffraction efficiency, and must therefore be suppressed whenever maximum efficiency is required.

The foregoing issues were examined systematically and in considerable detail under Task III. These investigations are described in the following subsections and in Section 3 of Volume II.

3.4.1 Investigation of Photoresist Properties

This subsection describes a series of experiments that led to a reproducible method of coating two-inch silicon substrates with layers of photoresist.

The following procedure was developed for cleaning the silicon substrates before depositing the gold layer:

1. Degrease with Trichloroethylene (15 minutes)
2. Wash in saturated solution of Alconox and water (20 minutes)
3. Wash in hot de-ionized water (2 hours)
4. Degrease with Transene (15 minutes)
5. Degrease with Transene (15 minutes)
6. Vacuum-bake at 115°C for 30 minutes in a half-closed jar.

In preliminary experiments, samples were stored under vacuum and were subsequently spin-coated at 7,200 rpm with AZ1350J resist. The quality of the resulting photoresist film was poor. Later experiments eliminated possible impurities in the photoresist and/or contamination of the substrate as causes of the layer nonuniformity. Finally, the cause was found to be the high speed of the spinner. At 7200 RPM the photoresist is subject to very high radial acceleration and velocity; consequently, it atomizes and strikes the inner surface of the spinner bowl, which reflects some of it back onto the substrate. In subsequent experiments, a lower spin speed (3600 RPM) was employed in conjunction with a lower-viscosity resist (AZ1370). This modification succeeded in eliminating the problem.

Following these initial investigations, 12 silicon wafers were cleaned according to the above procedures, and a 1.7- μm layer of gold was deposited on each of them, using vacuum evaporation techniques. Four of these 12 substrates, hereafter referred to as 69A, 69B, 69C and 69D, were coated in the following manner: 10 drops of filtered AZ1375 photoresist were deposited at the center of the wafer; a 30 second waiting time was allowed so that bubbles in the resist would rise to the surface, and the wafer was then spun at 3600 RPM for 30 seconds. The wafers were exposed to the interference pattern of the HeCd laser for 7 minutes, 13 seconds, resulting in an exposure energy density of 130 mJ/cm². The wafers were developed in AZ developer (1:1 dilution ratio) for 2 minutes and washed for 5 minutes in de-ionized water.

All wafers exhibited a textured pattern radiating outward from the center. Since repeatability and understanding of deposition processes were primary task goals, it was decided that an investigation into the causes of the texture, and means of eliminating it, was needed. For this purpose, a large number of experiments was performed; they are summarized below.

The cause of the textured pattern was determined to be irregular drying of the resist before and during the spinning process. The pattern was eliminated by applying either of two possible techniques: (1) adding acetone to the spinner bowl, or (2) employing a two-layer construction in the presence of photoresist thinner.

3.4.2 Evaluation of Techniques

Air Baking versus Vacuum Baking

The first experiment was designed to determine whether vacuum baking prior to exposure was causing the texture problem. For this purpose, the wafers 69A, 69B, 69C and 69D were cleaned using "Photrex" grade acetone and "Photrex" grade 2-propanol. After cleaning, they were re-numbered 25A, 25B, 25C and 25D, respectively. Low-viscosity 1350B resist and high-viscosity 1375 resist were used to obtain thin (0.3 to 0.4 μm) and thick (2-3 μm) layers, respectively. The different parameters that were varied during the experiment are summarized in Table 6.

TABLE 6. SUMMARY OF AIR AND VACUUM BAKING

Sample	Photoresist Type	Spin Speed, RPM	Baking Type/ Duration	Exposure Energy Density, mJ/cm ²	Miscellaneous Comments
25A	1350B	3600	Vacuum/2 hours	130	
25B	1350B	3600	Vacuum/2 hours	90	
25C	1350B	3600	Air/2 hours	130	
25D	1350B	3600	Air/2 hours	90	
25E	1375	2000	Air/2 hours	130	
25F	1375	2000	Vacuum/ 2 hours	130	
25G	1375	4000	Air/2 hours	130	
25H	1375	4000	Vacuum/ 2 hours	130	
25I	1375	6000	Air/2 hours	130	
25J	1375	6000	Vacuum/2 hours	130	
25K	1375	3600	Air/2 hours	130	Spinner bowl covered during waiting and spinning.
25L	1375	3600	Vacuum/2 hours	130	

Conditions: a. 20 drops photoresist
 b. 30 seconds waiting time
 c. 30 seconds spin duration

After exposure, the samples were developed in AZ developer (1:1) for 2 minutes and rinsed in de-ionized water for 5 minutes. No texture was observed on samples 25A, 25B, 25C, 25D, 25K and 25L. The texture problem was apparently caused by the high viscosity of the AZ1375 photoresist used (samples 25A, B, C, and D were made with very thin resist) and by partial drying of the resist while waiting, and while spinning the sample. Covering the spinner bowl (samples 25K and L) seemed to eliminate this problem.

In an attempt to confirm these conclusions, four substrates were cleaned with "Photrex" acetone and 2-propanol using procedures identical to those used in preparing samples 25K and 25L. However, after exposure and development, the new samples showed a textured pattern. At the time, the cause of this inconsistency was not known. Now it is believed that since samples K and L were the last ones prepared during the previous run, enough photoresist solvent remained in the spinner bowl to prevent localized

dring of the resist. The four wafers that were used the next day exhibited the textured pattern simply because there was then not enough resist and solvent in the spinner bowl to prevent the resist from dry...g. Samples A, B, C and D did not exhibit texture due to the high solvent content of the low-viscosity resist that was used.

Acetone in Spinner Bowl

To investigate the effect re-cleaning of the substrates would have on the success of Samples 25A, B, C and D in the previous experiment, previously exposed substrates were cleaned with "Photrex" acetone and 2-propanol on the spinner immediately before coating them with photoresist. The photoresist used was AZ1375; after applying it to the substrates, the samples were baked under vacuum for two hours. The other parameters are summarized in Table 7. Texture was absent from all samples. Because the cover of the spinner bowl isolated it from the exterior environment, the only real difference in the experimental conditions seemed to be in re-cleaning the old wafers. In the re-cleaning process, acetone and 2-propanol were used; these are retained as a vapor in the spinner bowl. The acetone environment seemed to aid the deposition process by preventing the thick resist from drying.

TABLE 7. EXTERNAL ENVIRONMENT VARIATIONS

Sample	Photoresist Quantity	Laminar Flow Bench	Cover
25G	10 drops	Off	On
25H	10 drops	Off	Off
25I	Flooded	On	On
25J	Flooded	Off	Off
25E	20 drops	Off	Off
25F	20 drops	Off	On
Conditions:	a. 30 seconds waiting time b. 30 seconds spin duration c. 3600 RPM spin speed d. 130 mJ/cm ² exposure		

To confirm these conclusions, the following experiment was performed. Three groups of substrates were cleaned and prepared in the following way:

Group 1. Samples 25G, 25H, 25I The samples in this group were spin-cleaned with "Photrex" acetone and 2-propanol at 10,000 RPM and the bowl was then dried. Afterward, ten drops of filtered resist were deposited on the substrates, and following a 30 second wait, the substrates were spin-coated at 3600 RPM for 30 seconds. The bowl cover was kept closed during the waiting period and while spinning the substrate.

Group 2. Samples 25L, 25K, 25E These samples were cleaned individually just before they were coated. In all other respects, the deposition was identical to that of the Group 1 samples.

Group 3. Samples 25F, 25J, 25A This group was prepared in identical fashion to Group 2 except for the fact that the laminar-flow bench was turned off and the spinner bowl cover was removed.

All of the samples were exposed and developed in the usual manner. As expected, only Group 1 showed the textured pattern. Following their development, samples from the three groups were measured with a Dektak instrument to determine the thickness of the photoresist. The results are summarized in Table 8.

TABLE 8. SUMMARY OF ACETONE MEASUREMENTS

Group	Samples	Atmosphere	Laminar Flow Bench	Spinner Cover	Thickness	Texture Present
1	25G, 25H, 25I	Dry	On	On	2.85 μ m	Yes
2	25L, 25K, 25E	Acetone	On	On	1.3 μ m	No
3	25F, 25J, 25A	Acetone	Off	Off	2.3 μ m	No

From this experiment it was concluded that the acetone in the spinner bowl prevents localized drying of the photoresist. However, the acetone also appears to attack the photoresist, changing its viscosity and sharply reducing the layer thickness. The thickness differences among the samples in Groups 2 and 3 indicate that the coating thickness is determined by the solvent content of the atmosphere in the spinner bowl.

Type of Resist, Waiting Time, and Spin Speed

Another experiment was performed to determine whether the photoresist viscosity or the acetone concentration is the important parameter, and to examine the extent to which the acetone atmosphere affects the resist thickness as a function of spin speed. The parameters that were varied are summarized in Table 9.

TABLE 9. RESIST TYPE, WAITING TIME, AND SPIN SPEED

Sample	Photoresist Used	Photoresist Quantity	Waiting Time Before Spinning, seconds	Spin Speed, RPM
26A	1370	Flooded	30	3600
26B	1370	Flooded	15	3600
26C	1370	10 drops	0	3600
25I	1370	Flooded	0	3600
25H	1350J	Flooded	30	2500
25H	1350J	Flooded	15	2500
25C	1350J	Flooded	0	2500
25B	1350J	10 drops	0	2500

Conditions: a. No acetone in bowl
b. 30 seconds spin duration
c. Laminar flow bench OFF
d. Cover OFF

All the samples were exposed and developed in the conventional way, and the textured pattern was evident in all of them. The conclusion, therefore, is that only an atmosphere of acetone (or equivalent solvent) can eliminate the texture problem, but this is achieved at the expense of a thinner coating of resist.

To improve the thickness of the resist coating using AZ1375 resist, glass slides were coated with AZ1375 resist in an acetone atmosphere at different spin speeds. The results are shown in Figure 62. It can be seen that the thickness improvement is minimal even for very low spin speeds (2000 RPM).

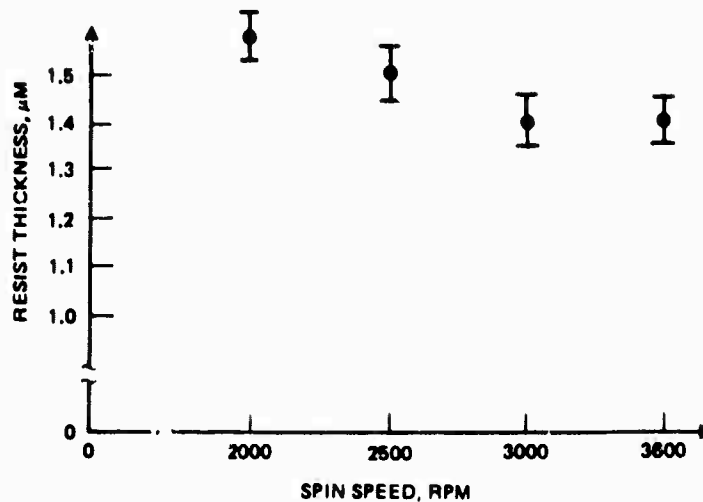


Figure 62. Resist thickness versus spin speed.

In conclusion, it appears that an acetone atmosphere is needed to eliminate the texture problem even for 1370 and 1350J resist. Only the 1350B resist yielded consistently acceptable coatings in the absence of an acetone atmosphere. However, only thicknesses up to 0.3 to 0.4 μm can be achieved. Furthermore, in the presence of the solvent atmosphere, the thickness of the resist layer does not vary significantly over the lower range of spin speeds.

Acetone Concentration

Since acetone is needed in the spinner bowl, it was decided that an improved resist thickness could be achieved by controlling the acetone dispensed in the bowl and/or the amount of time that the substrate is left on the spinning chuck. To assess these possibilities, nine 2-by-2 inch glass slides were pre-cleaned with acetone and 2-propanol. The substrate was placed on the vacuum chuck of the spinner with no acetone present. Then, 20 drops of filtered AZ1375 resist were dropped onto the center of the substrate, and a measured amount of acetone was dispensed with a pipette. Waiting times of 30 and 60 seconds were employed, and finally, the sample was spun at 3600 rpm for 30 seconds. The resulting thickness is shown in Table 10 as a function of the amount of acetone and waiting time.

TABLE 10. RESIST THICKNESS AS A FUNCTION OF ACETONE CONCENTRATION AND WAITING TIME

Sample	Amount of Acetone, ml	Waiting Time, seconds	Thickness, μm
A	0	30	2.7 (Reference)
B	2.5	30	2.2
C	2.5	30	2.25
D	2.5	60	2.1
E	5	30	2.05
F	5	30	2.1
G	5	60	1.95
H	10	30	1.95
I	10	60	1.85

Having achieved thicknesses on the order of 2 μm with measured amounts of acetone, four gold-coated wafers were prepared as follows:

<u>Wafer</u>	<u>Identical with Slide</u>
25B	B
25D	E
25C	H
25H	A

The substrates were exposed and developed according to the usual procedures. All of them exhibited textured patterns, although the ones made with acetone were not as strongly textured as the reference sample prepared without solvent. To improve the process, it was thought that allowing the acetone to saturate the spinner bowl (varying the waiting and spinning times) would prevent the photoresist from drying locally and generating the textured structure. All of the gold substrates were cleaned with acetone and Q-propanol. Twenty drops of AZ1375 resist were used on each substrate. Variable amounts of acetone were dispersed in the spinner bowl, and after a specified waiting time each sample was spin-coated at 2500 RPM. The different variations are summarized in Table 11.

TABLE 11. ACETONE CONCENTRATION, WAITING TIME AND SPIN DURATION

Sample	Amount of Acetone, ml	Waiting Time, seconds	Spin Duration, seconds
25A	0	0	30
25E	5	60	30
25F	5	120	30
25I	2.5	60	10
25J	5	60	10
25K	2.5	60	15
25L	5	60	15
26A	2.5	60	20
26B	5	60	20

After standard exposure and development, all the samples again exhibited texture. Sample 25A exhibited the least texture, probably as a result of the short time needed to complete the deposition. This motivated the next set of experiments, which was identical to the one just described except for reduced waiting and spin times. These variations are shown in Table 12. Again, the samples were exposed and developed following standard procedures. The textured structure was evident on all of them.

At this point, the only remaining alternatives were to (1) employ post-spin processing (using heat and saturated acetone) and (2) increase the amount of acetone dispensed in the spinner bowl.

Samples 26C, 25B, 33D and 33E were cleaned with "Photrex" acetone and 2-propanol. The wafer surface was flooded with AZ1375 resist, and after 30 seconds waiting time, was spun for 30 seconds at 3600 rpm. Sample 26C was baked in air at 120°C for 10 minutes and sample 25B was baked in air at 140°C for 5 minutes. Substrate 33D was placed in a saturated acetone atmosphere, whereupon the solvent attacked the photoresist after about 15 seconds, again causing large-scale surface nonuniformities. After sample 33E was placed in a saturated atmosphere of AZ thinner, a reaction similar to that seen in the acetone atmosphere was observed, with the exception that the reaction times were much longer. Upon exposure and development, none of these samples showed improvement.

TABLE 12. ACETONE CONCENTRATION, WAITING TIME AND SPIN DURATION FOR REDUCED WAITING AND SPIN TIMES

Sample	Amount of Acetone ml	Waiting Time, seconds	Spin Duration, seconds
25F	2.5	0	20
25K	2.5	10	20
25I	2.5	20	20
25A	2.5	0	10
33A	2.5	10	10
25H	2.5	20	10
33B	2.5	0	30
33D	2.5	10	30
SP3	2.5	20	30
25D	5	0	20
25L	5	10	20
25J	5	20	20
25E	5	0	10
25B	5	10	10
25C	5	20	10
33C	5	0	30
26C	5	10	30
26B	5	20	30

Finally, the amount of acetone dispensed into the spinner bowl was increased. In this experiment, 200 ml of acetone were poured into the spinner bowl. Sample 33B was mounted and flooded with AZ1375 resist, and after a 30 second wait, was spin-coated at 3600 RPM for 30 seconds. Subsequently, it was removed and an additional 200 ml of acetone were poured into the bowl, making a total of 400 ml. Sample 25C was mounted and processed identically to sample 33B. Subsequent exposure and development revealed no texture for either 33B or 25C. Unexposed photoresist was removed from the edges of the samples and the resist height of each was measured. Samples 33B and 25C were found to be 1.65 μm and 1.2 μm thick, respectively.

It was concluded that the texture problem could be eliminated by using acetone but the thickness of the resist layer could not also be preserved at the same time. Acetone atmosphere can be used to generate resist layers that are uniform to between 1.2 and 1.4 μm . The reason that the structure problem did not always appear in previous experiments was that some of the wafers were cleaned with acetone in the spinner bowl just before depositing the resist.

AZ Thinner

In an effort to improve the resist thickness and eliminate the textured structure, photoresist thinner was used instead of acetone. For this experiment, 350 ml of AZ thinner were dispensed in the spinner bowl, and 20 drops of AZ1375 resist were deposited on pre-cleaned wafers. The wafers were then spun at 3600 RPM. The laminar-flow bench was left on but the spinner area was kept closed. The variables involved here were the waiting time and the spinning time; they are summarized in Table 13.

TABLE 13. WAITING AND SPIN TIME VARIABLES

Sample	Waiting Time, seconds	Spin Duration, seconds
25L	0	10
25K	0	15
33A	0	30
25D	30	10
25A	30	15
25F	30	30

Following conventional exposure and development, samples 33A and 25F were examined and found to be good gratings with no visible texture. The measured thickness of the photoresist was 2.35 μm , an encouraging result. To determine the tolerances associated with this method, another experiment was performed in which the waiting and spin times were varied along with the spin speed, as shown in Table 14. The wafers were exposed to a laser energy density of 130J/cm², immersed in AZ developer (1:1) for 2 minutes, and rinsed in de-ionized water for 5 minutes following established

TABLE 14. WAITING TIME, SPIN DURATION AND SPIN SPEED VARIABLES

Sample	Waiting Time, seconds	Spin Duration, seconds	Spin Speed, RPM
25K	30	30	3600
33A	30	40	3600
25L	30	50	3600
25D	30	60	3600
25B	45	30	3600
26B	45	40	3600
33D	45	50	3600
25E	45	60	3600
SP3	30	30	2500
33C	30	40	2500
26C	30	50	2500
25A	30	60	2500

procedures. Only sample 25K did not exhibit the textured structure. Since the longer spin and waiting times did not eliminate the problem, it was decided to try reducing them instead. The results are summarized in Table 15.

Although in this experiment the conditions for preparing sample SP3 (30 seconds/30 seconds) were identical to successful previous runs, this sample still exhibited texture. For this reason, four more wafers were cleaned and processed for 30 seconds waiting and 30 seconds spin time. After development they showed no structure. Dektak measurements on all four wafers revealed thicknesses of $2.33 \pm 0.03 \mu\text{m}$. The thickness uniformity over a single test sample was better than 5 percent.

At this point, 27 more silicon wafers were cleaned and a $3.0 \mu\text{m}$ gold layer was deposited on each. Microscopic examination revealed that the gold surface had numerous defects resulting from the evaporation techniques employed. Nevertheless, it was decided to proceed with the preparation of these samples.

Six wafers were coated in an AZ-thinner environment, using 30 second waiting and 30 second spin times. These samples were exposed and

TABLE 15. REDUCED SPIN AND WAITING TIMES

Sample	Waiting Time	Spin Duration, seconds	Spin Speed, RPM
33D	25 seconds	25	3600
25B	25 seconds	30	3600
33C	25 seconds	35	3600
25K	30 seconds	25	3600
SP3	30 seconds	30	3600
25D	30 seconds	55	3600
25E	35 seconds	25	3600
26B	35 seconds	30	3600
25L	35 seconds	35	3600
26C	6 minutes	30	3600
25A	10 minutes	30	3600
26A	20 seconds	30	2500

developed conventionally, but unfortunately, they all gave evidence of texture. It appears that this technique is dependent on the external environment. Since the major parameters and factors had been investigated, this deposition procedure was abandoned because it was felt that an excessive amount of time would be needed to determine the proper conditions.

Dynamic Deposition

In an attempt to eliminate the textured structure, the photoresist was deposited while the substrate was spinning, thus reducing the drying time to a minimum. In place of the spinner cover, a 12-by-12 inch glass plate with a 1/32 inch hole was used and 900 ml of AZ thinner were introduced into the spinner bowl. The substrates were carefully mounted on the chuck, and after 30 seconds settling time were spun at 3600 RPM for 30 seconds while adding photoresist through the hole in the glass cover. The parameters varied were the settling time and the amount of photoresist added. The results are summarized in Table 16. Unfortunately, the texture results were not consistent. Therefore this method was also abandoned.

TABLE 16. THICKNESS VARIATIONS FOR DYNAMIC DEPOSITION

Sample	Waiting Time, seconds	Photoresist 1375	Thickness, μm
25D	30	20 drops	
25K	30	20 drops	
25E	30	20 drops	
25A	60	10 drops	1.85
SP3	60	10 drops	1.85
25L	60	10 drops	1.85

Double-Coating Procedure

The next step in the development of texture-free substrates was the incorporation of a sublayer of photoresist that would keep the final resist layer from drying prematurely. In all the experiments that follow, the textured structure was completely eliminated for all thicknesses. However, large-scale variations (2000-4000 Å) in resist thickness were observed over the substrate. Since double coating proved to be a reliable method of eliminating the textured structure, an investigation was initiated to solve the problem of thickness variations.

In the experiment described below, three techniques of photoresist deposition were compared. Curve A in Figure 63 represents the thickness variation as a function of spin speed for the following process: 900 ml of AZ thinner are introduced into the bowl. The substrate is positioned on the vacuum chuck and after 60 seconds, 20 drops of photoresist are deposited on the center of the wafer. The cover is then closed and the closed system is left undisturbed for 30 seconds, allowing bubbles in the resist to rise to the surface. After spinning, the substrate is removed immediately. From curve A (Figure 63), it can be seen that thick coatings can be achieved, but almost all of them exhibit the textured structure (the letter "T" after each experimental point denotes the textured structure).

Curve B in Figure 63 represents a procedure identical to that of Curve A except that, instead of closing the bowl with the

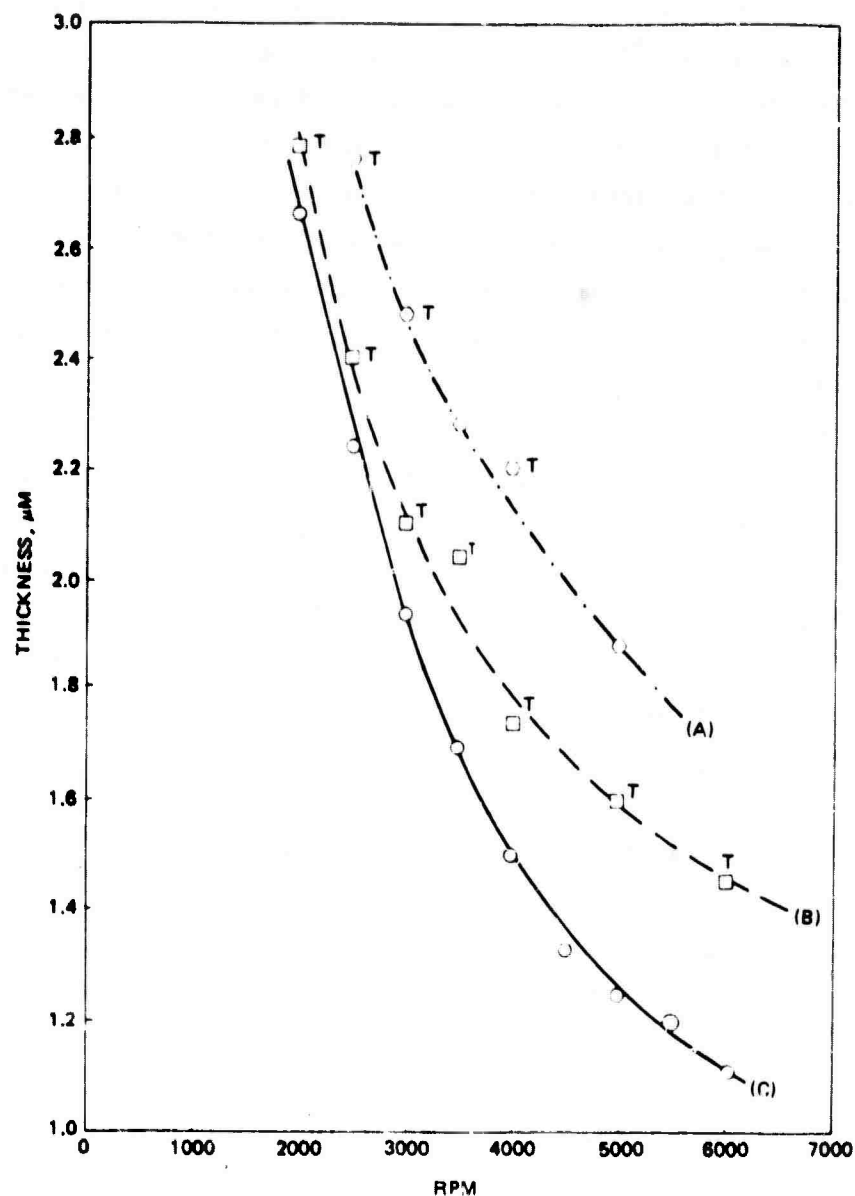


Figure 63. Thickness variations.

conventional cover, a 12-by-12 inch glass plate is used. This provides for a higher concentration of AZ vapor, thus reducing the thickness of the spin-coated substrate. Again, as can be seen from the number of T labels accompanying the data points, the textured structure remains.

Curve C exhibits no texture whatsoever. The coating procedure for this case is as follows: the substrate is positioned onto the spinner chuck and covered with the 12-by-12 inch glass. Following sixty seconds of settling time, the spinner is started. Ten drops of resist are dropped onto the spinner (while it is in motion) and the wafer is spun for 30 seconds. When the spinner stops, 20 drops are deposited in the center of the already-coated substrate, and after a 30-second waiting time it is spun again for 30 seconds. Although the textured structure was eliminated by this procedure, the coating exhibited large-scale nonuniformity. When viewed under bright light, concentric fringes appeared.

In an effort to improve the uniformity, the procedure for applying the resist sublayer was modified. Instead of dropping the resist while the wafer was spinning, 20 drops of photoresist were first applied, and after 30 seconds of waiting time it was spun for 30 seconds. Ten samples were prepared this way, resulting in improved uniformity. However, motion fringes were observed which made evaluation of the uniformity very difficult.

To determine the cause of the motion fringes, more substrates were cleaned, coated and exposed. Results were very inconsistent. After numerous trial-and-error runs (varying the settling time, holder pressure, etc.), it was concluded that the observed fringes were not caused by substrate motion during exposure, but were in fact the result of a materials problem. Again, after extensive experimentation it was discovered that the use of reagent-grade acetone with 0.003 percent residue after evaporation was staining the gold. A subsequent change to "Photrex" grade acetone with 0.0002 percent residue after evaporation succeeded in eliminating the "motion fringes."

To further improve the uniformity of the resist layer, a number of changes in the coating procedure were made. The waiting time before deposition of the sublayer was increased to 60 seconds, and the amount of photoresist used for the final coat was increased to 50 drops. Even with these changes, the coated layers were not as uniform as would be desirable. The final step was to increase the spin speed to 6,000 RPM. This solved the problem but produced layers 1.3 μm thick. It seems that with present technology this is the best that can be achieved by the spin-coating method.

Twenty-three new silicon wafers were cleaned according to the procedure described earlier and 2.4 μm of gold were deposited. The procedure for coating them was:

1. Fill the spinner bowl with 1000 ml of AZ thinner
2. Center the substrate on the vacuum chuck
3. Place 12-by-12 inch sheet of plate glass over the spinner bowl
4. Wait 60 seconds to allow equilibrium of liquid-vapor phase
5. Deposit 20 drops of 1375 resist in center of substrate
6. Wait 60 seconds
7. Spin at 6000 RPM for 30 seconds
8. Deposit 50 drops of photoresist at center of sublayer
9. Wait 60 seconds
10. Spin at 6000 RPM for 30 seconds
11. Remove substrate and vacuum bake at 60°C for 2 hours

All of the samples were exposed to 130 mJ/cm^2 energy density from the laser and were developed according to normal procedures. All were found to be uniform and no texture was observed.

3.4.3 Results of the Coating Technique Evaluation

With current technology, uniform and defect-free photoresist layers can be deposited in thicknesses up to about 1.4 μm using spin-coating techniques. Although it appears possible to produce thicker resist layers by other methods, investigation of such methods could not be undertaken within the time remaining in the program. However, thicker coatings may not be necessary, because gratings produced from 1.4 μm layers will contain at least 10 or 11 standing waves, which should average out in the ion machining process.

In summary, 20 substrates free of resist defects were prepared. Ten were photographed with a scanning electron microscope (SEM) and ten more were machined to various depths. Following the ion machining, SEM photos were made and the samples were measured. These results are described next.

3.4.4 Evaluation of Sample Gratings

For this investigation, 20 identical silicon wafers coated with a 0.5 μm gold layer were spin-coated with photoresist and used to prepare a control set of sample gratings. These substrates were subsequently exposed, developed, and ion machined to various depths to produce ten pairs of graded efficiency samples. The resulting gratings were then evaluated to provide a concise set of data on the transfer characteristics of the ion-machining process and to verify the diffraction efficiency code (see Section 4), as well as to gain improved understanding of photoresist properties.

For each sample, an SEM picture was taken of the photoresist grating, the ion-machined grating (before removing the photoresist), and the final grating in gold (with photoresist removed). The ion-machined gratings had peak-to-trough heights of 0.2 to 2.0 μm in steps of 0.2 μm . Figures 64 to 69 show some typical results obtained by varying the groove profile, period and duty cycle. Figure 70 is a summary of the photoresist-to-gold transfer characteristics for an initial grating with a 25-percent duty cycle.

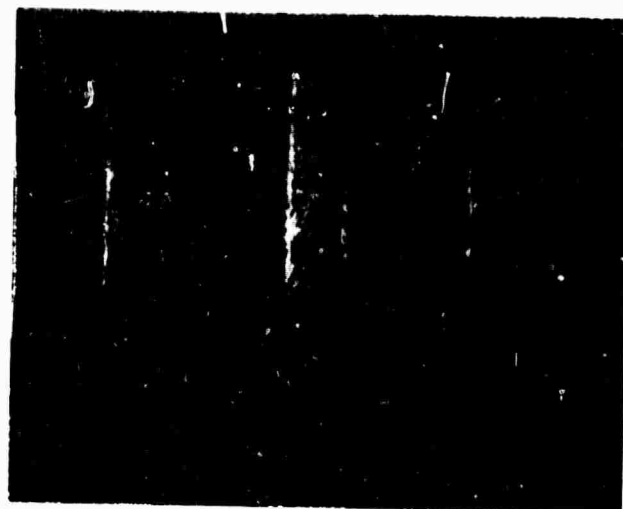
At the completion of these experiments, the holographic exposure setup was aligned according to the design specifications for the aberration-corrected grating construction described in Section 5. Four 2-inch $\lambda/20$ optical flats were coated and exposed. Two high-efficiency (≥ 40 percent) and two intermediate-efficiency (≥ 20 percent) samples were fabricated.

In conclusion, an investigation of the transfer characteristics of a photoresist mask on gold showed that trapezoidal gratings with a 60-degree base angle for various peak-to-trough heights of interest could be obtained consistently. In addition, sputter deposition of gold produced a more uniform surface than can be obtained by the e-beam vacuum evaporation method. Finally, the fabrication of both high-efficiency and low-efficiency aberration-corrected gratings was demonstrated.



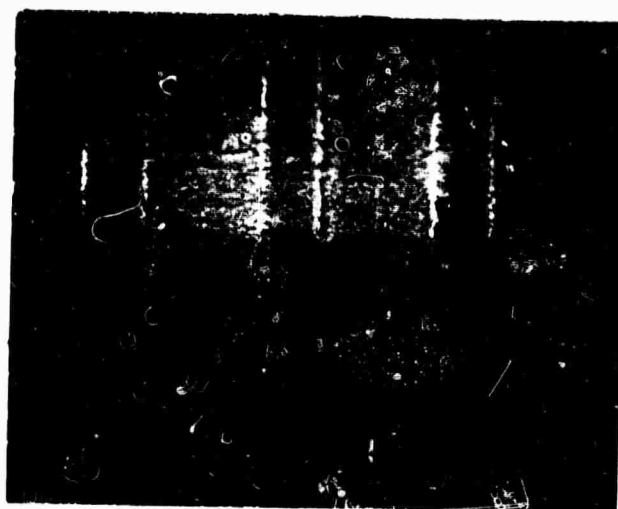
PHOTORESIST GRATING

1.4 μ M PEAK-TO-
TROUGH HEIGHT
25 PERCENT DUTY
CYCLE



ETCHED GRATINGS

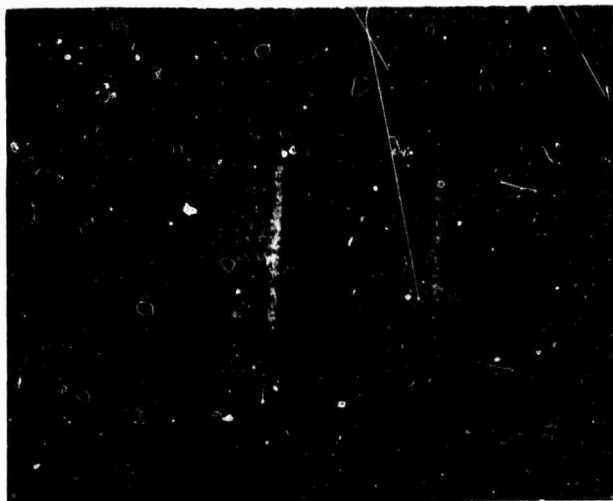
4.84 μ M PERIOD
RESIST TOP INTACT



ETCHED PHOTORESIST REMOVED

0.2 μ M PEAK-TO-
TROUGH HEIGHT
34 PERCENT DUTY
CYCLE
60 DEGREE ANGLE

Figure 64. Ion-etched gratings.



PHOTORESIST GRATING

1.34 μM PEAK TO
TROUGH HEIGHT
26 PERCENT DUTY CYCLE



ETCHED PHOTORESIST REMOVED

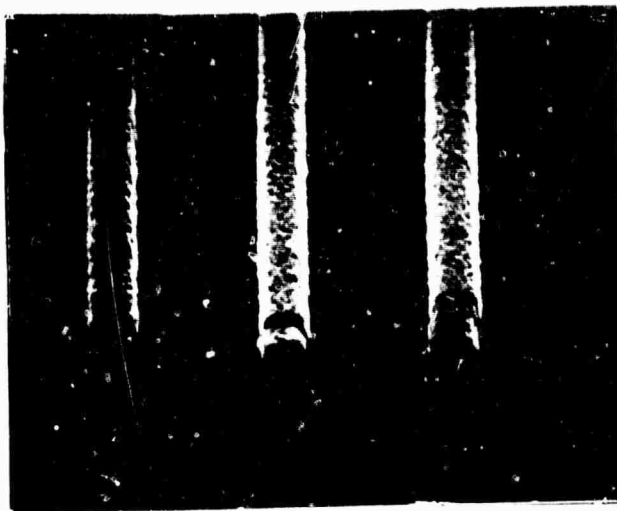
RESIST TOP
INTACT



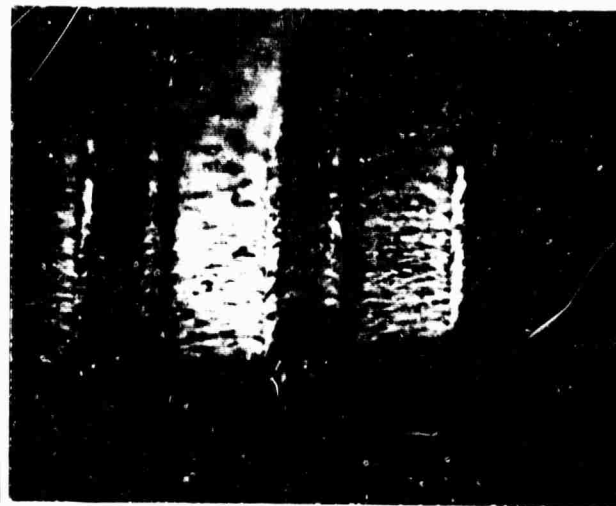
ETCHED GRATING

0.6 μM PEAK TO
TROUGH HEIGHT
41 PERCENT DUTY
CYCLE
60 DEGREE ANGLE

Figure 65. Ion-etched gratings.



1.31 μ M PEAK TO
TROUGH HEIGHT
22 PERCENT DUTY CYCLE



0.8 μ M PEAK TO
TROUGH HEIGHT
29 PERCENT DUTY
CYCLE
60 DEGREE ANGLE

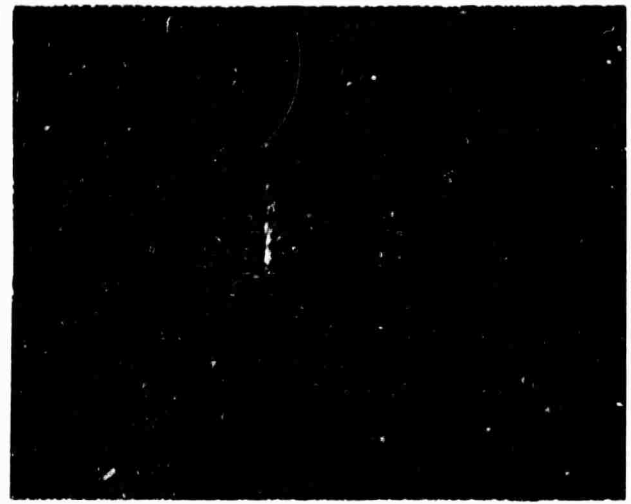


RESIST TOP
INTACT

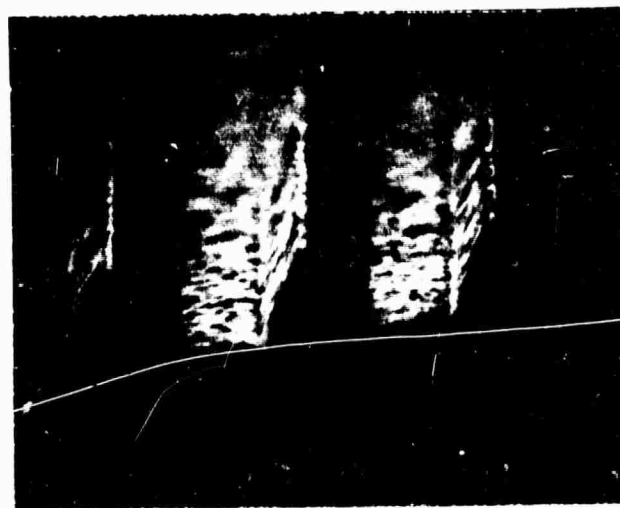
Figure 66. Ion-etched gratings.



130 μ M PEAK TO
TROUGH HEIGHT
20 PERCENT DUTY CYCLE



10 μ M PEAK TO
TROUGH HEIGHT
28 PERCENT DUTY CYCLE
60 DEGREE ANGLE

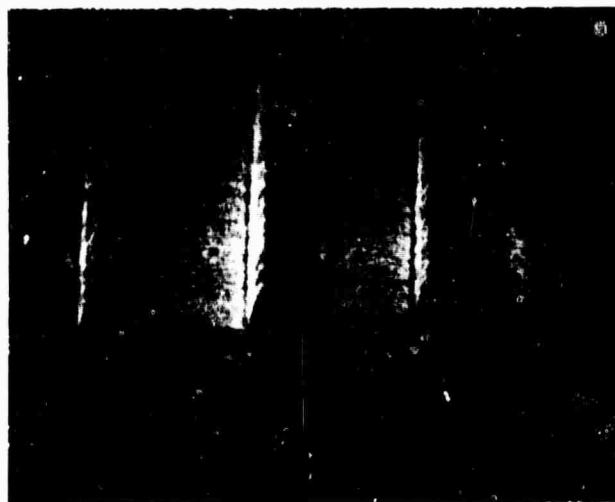


RESIST TOP
DEFORMS

Figure 67. Ion-etched gratings.



1.35 μ M PEAK TO
TROUGH HEIGHT
26 PERCENT DUTY CYCLE

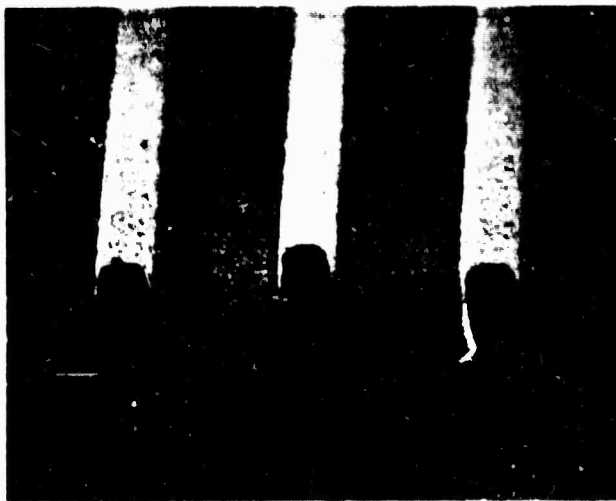


1.0 μ M PEAK TO-
TROUGH HEIGHT
28 PERCENT DUTY CYCLE
60 DEGREE ANGLE

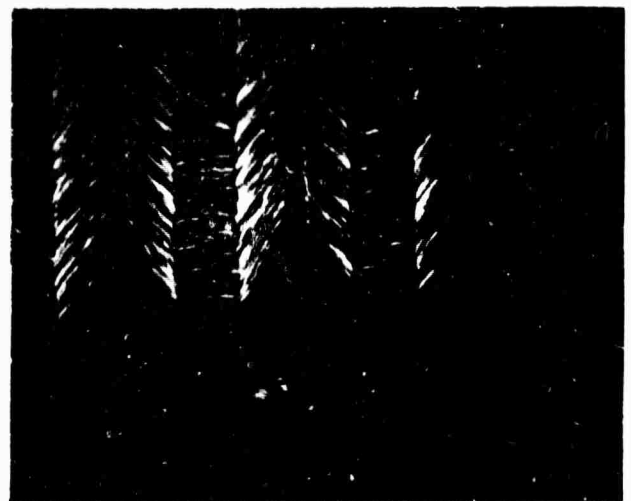


RESIST TOP
DEFORMS

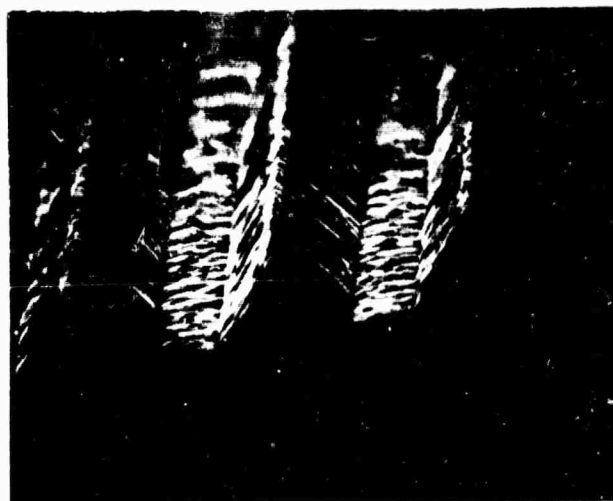
Figure 68. Ion-etched gratings.



1.28 μ m PEAK TO-
TROUGH HEIGHT
21 PERCENT DUTY
CYCLE



2.0 μ m PEAK TO-
TROUGH HEIGHT
0.09 PERCENT
DUTY CYCLE
50 DEGREE ANGLE



RESIST TOP
DEFORMED

Figure 69. Ion-etched gratings.

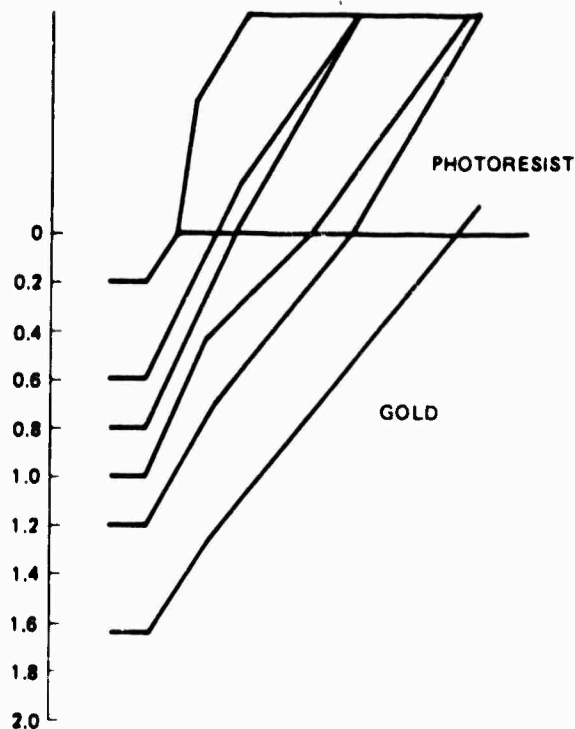


Figure 70. Photoresist-to-gold transfer characteristics (ion-etched gratings).

3.4.5 Standing Waves

When a photoresist grating is exposed on a reflecting substrate such as gold, standing wave patterns may develop in the photoresist as a result of interference between the incident exposing beams and wavefronts reflected from the substrate. An example of such standing waves in a linear photoresist grating over gold was shown in Figure 59.

In the absence of reflections, the interference intensity between construction wavefronts is

$$I_A + I_B + 2\sqrt{I_A I_B} \cos \theta_{AB}$$

where I_A and I_B are the wavefront intensities and θ_{AB} is the relative phase difference between the wavefronts. However, because of reflections, the

desired grating is modified by the superposition of standing wave gratings caused by the interference of reflected and incident wavefronts.

Figure 71a shows the four coherent fields within the photoresist bulk. For symmetrical construction beams (where $\theta_1 = \theta_2$), the general description of the intensity distribution due to the interference of these four coherent wavefronts is:

$$I = \left[1 + R + \underbrace{2 \sqrt{R} \cos \left(\frac{y 4 \pi n_p \cos \theta}{\lambda} - \phi \right)}_{\substack{\text{Thickness modulation} \\ \text{coefficient}}} \right] \left\{ I_A (1 + \gamma) \left[1 + K \cos \left(\frac{x 4 \pi n_p \sin \theta}{\lambda} \right) \right] \right\}$$

Desired exposure coefficient

where

$\gamma = I_A/I_B$ is the intensity ratio of the construction beams

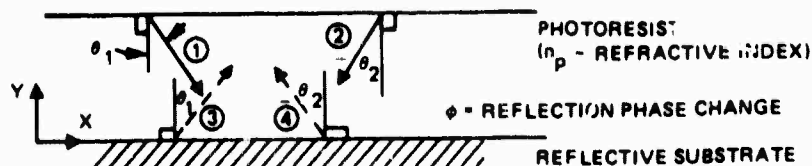
R = Reflection coefficient of the substrate

$K = \frac{2\sqrt{\gamma}}{(1+\gamma)}$ is the fringe contrast of the construction beam interference

θ = The included half angle between construction beams in the photoresist

ϕ = Phase shift due to reflection at the substrate

The desired grating formed by the two incident construction wavefronts has loci of constant-intensity fringes parallel to the bisector of the included angle between construction beams. For symmetrical construction beams, these fringes are perpendicular to the substrate surface. The distance between maximum-intensity fringe planes is the groove spacing, $d_x = \lambda/(2n_p \sin \theta)$. For construction beams with a small included angle, the standing wave pattern has loci of constant intensity lying nearly parallel to the substrate surface. The distance between maximum-intensity fringe planes is $d_y = \lambda/(2n_p \cos \theta)$. For small θ , these fringe planes are separated by $\lambda/2n_p$.



CONSTRUCTION FIELDS COMPLEX AMPLITUDE

$$\textcircled{1} \quad A e^{ik(X \sin \theta_1 + Y \sin \theta_1)}$$

$$\textcircled{2} \quad B e^{ik(-X \sin \theta_2 + Y \sin \theta_2)}$$

REFLECTED FIELDS COMPLEX AMPLITUDE

$$\textcircled{3} \quad A \sqrt{R} e^{i\phi} e^{ik(X \sin \theta_1 - Y \cos \theta_1)}$$

$$\textcircled{4} \quad B \sqrt{R} e^{i\phi} e^{ik(-X \sin \theta_2 - Y \cos \theta_2)}$$

$$k = \frac{2\pi n_p}{\lambda}$$

ψ = COMBINED WAVE MOTION OF CONSTRUCTION AND REFLECTED FIELDS

$$= (\textcircled{1} + \textcircled{2} + \textcircled{3} + \textcircled{4})$$

I = EXPOSURE INTENSITY

$$I = (\psi)(\psi^*)$$

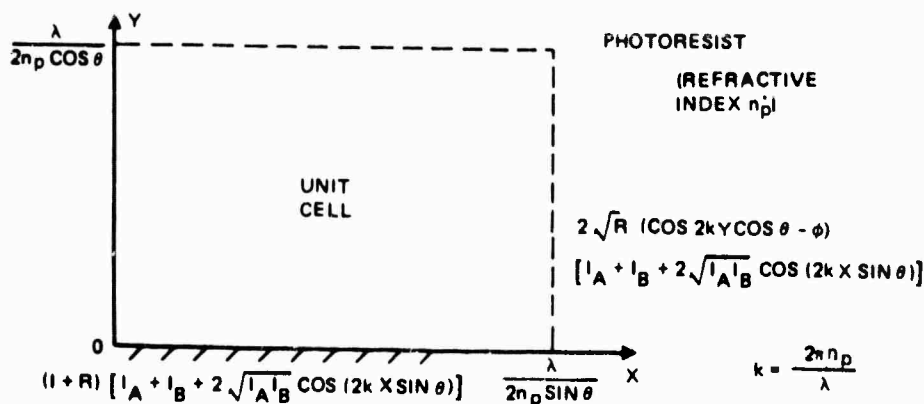
FOR $\theta_1 = \theta_2 = \theta$

$$I = I_A + I_B + 2\sqrt{I_A I_B} \cos(2kX \sin \theta) \quad \left. \begin{array}{l} \text{DESIRED EXPOSURE} \\ + R I_A + R I_B + 2R \sqrt{I_A I_B} \cos(2kX \sin \theta) \\ + [\cos(2kY \cos \theta - \phi)] [2\sqrt{I_A} + 2\sqrt{I_B} + 4\sqrt{I_A I_B} \cos(2kX \sin \theta)] \end{array} \right\} \text{THICKNESS MODULATION}$$

WHERE

$$\left. \begin{array}{l} I_A = |A|^2 \\ I_B = |B|^2 \end{array} \right\} \propto \text{INTENSITY OF CONSTRUCTION FIELDS}$$

a. Within photoresist bulk



b. Within unit cell of photoresist bulk

Figure 71. Interference intensity distribution of construction and reflected fields.

Neglecting absorption, these intensities are periodic within the bulk of the photoresist as shown in Figure 71b. Therefore, it is only necessary to consider a unit cell to see the intensity distribution caused by the summation of the desired interference with that caused by the standing waves. This intensity distribution is shown in Figure 72 for a one-to-one beam intensity ratio, assuming 30-percent reflectivity from a gold substrate. The varying intensity in the y-direction caused by the standing waves produces a corresponding variation in the development rate in the photoresist, resulting in a staircase structure such as that seen in Figure 59.

The intensity distribution for a 20-to-1 beam intensity ratio is shown in Figure 73. By increasing the intensity ratio of the construction beams, the fringe contrast of the standing-wave interference is reduced. However, the fringe contrast of the primary interference is also reduced. The net effect is a very slight intensity difference between areas of high exposure and low exposure. Ideally, the minimum exposure should be zero. With the one-to-one ratio the exposure at minimum is provided only by the standing waves, whereas with the 20-to-1 ratio the exposure at minimum is higher, although the contribution from standing waves is reduced. This is due to a large exposure at the minimum from the primary grating.

Effect of Beam Ratio

Exposures at these two beam ratios on a 2800 Å thickness of AZ1350B photoresist on gold were compared. The exposure times were adjusted to obtain equal exposure at the maximum value of $I(x, y)$. Standard development for one minute in one-to-one AZ1350 developer at 21°C was used. High-magnification photographs and SEM photographs in Figure 74 show the two gratings. Due to the size of the sample, maneuverability within the SEM was restricted and did not allow a scan of the profile of the standing wave structure to be made. However, a broadening of the standing wave steps is evident in the SEM photos when the beam intensity ratio was increased to 20 to 1.

Figure 75 is the SEM photo of the photoresist grating mask shown in Figure 59 after ion-beam machining into the gold layer to a depth of 3000 Å and removal of the remaining photoresist. A slight step in the ion-beam

1:1 BEAM RATIO

$$\gamma = 1$$

ASSUMPTIONS: SYMMETRIC CONSTRUCTION BEAMS

$$K = 1$$

$$\phi = \frac{\pi}{2}$$

$$R = .30$$

$$I(X,Y) = \left[1 + R + 2\sqrt{R} \cos\left(Y \frac{4\pi n_p \cos \theta}{\lambda} - \phi\right) \right] \left[I_A (1 + \gamma) \left(1 + K \cos X \frac{4\pi n_p \sin \theta}{\lambda} \right) \right]$$

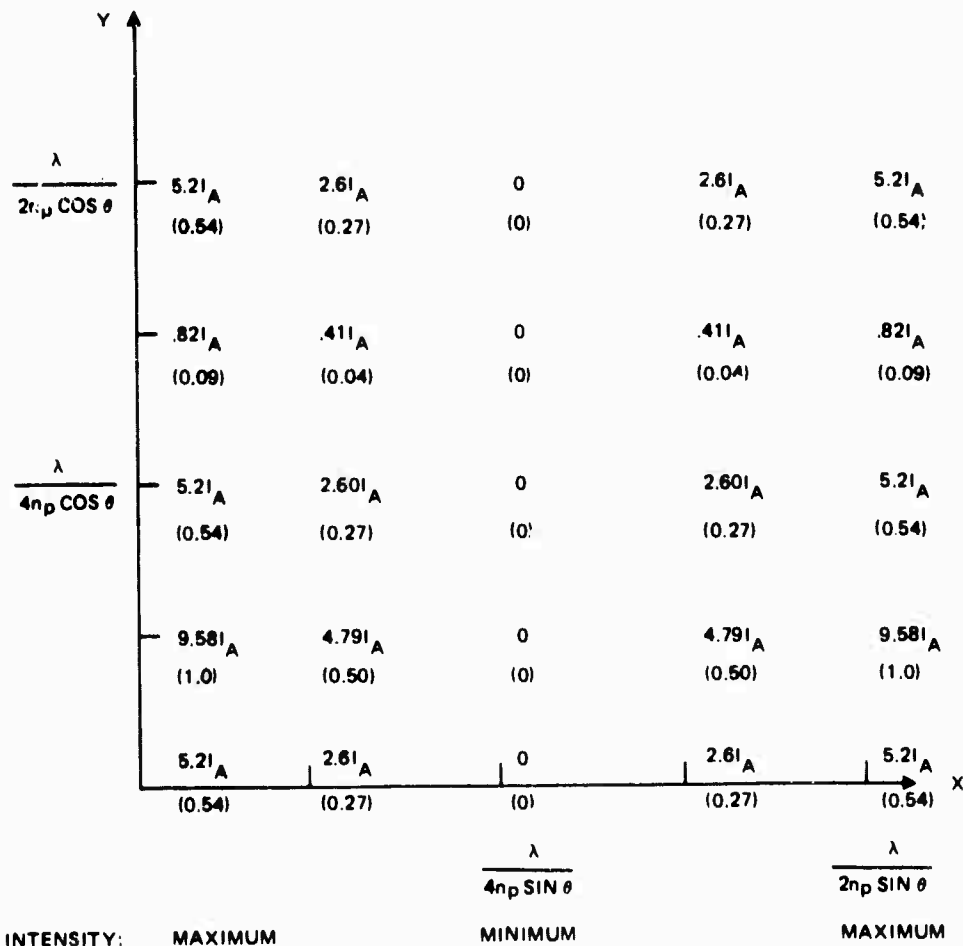


Figure 72. Intensity distribution within unit cell in bulk of photoresist with 1:1 construction beam ratio

(A 30-percent reflectivity from gold substrates is assumed. Quantities within the parenthesis are normalized to $I_{\max}(X,Y)$.)

20:1 BEAM RATIO

$$\gamma = 0.05$$

$$K = 0.43$$

$$R = 0.30$$

ASSUMPTIONS: SYMMETRIC CONSTRUCTION BEAMS

$$\phi = \frac{\pi}{2}$$

$$I(X,Y) = \left[1 + R + 2\sqrt{R} \cos \left(\gamma \frac{4\pi n_p C^2 \theta}{\lambda} - \phi \right) \right] \left[I_A (1 + \gamma) \left(1 + K \cos X \frac{4\pi n_p S_1 Y \theta}{\lambda} \right) \right]$$

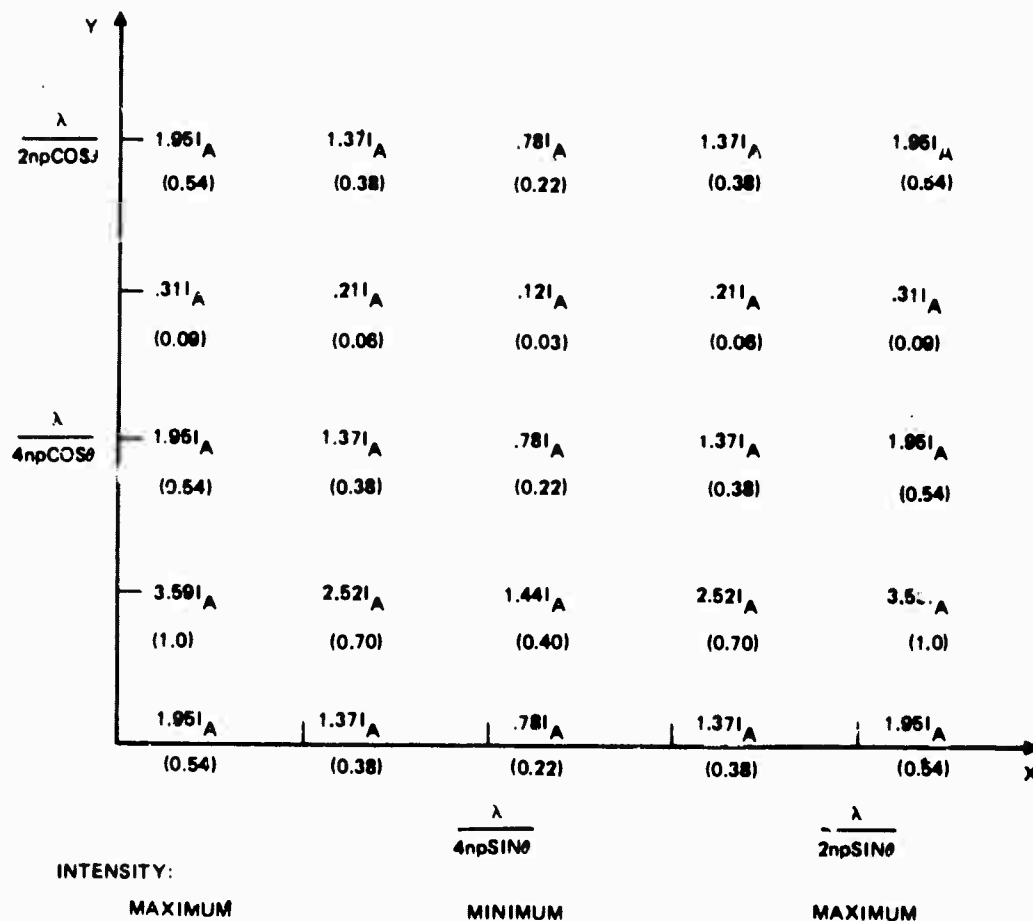
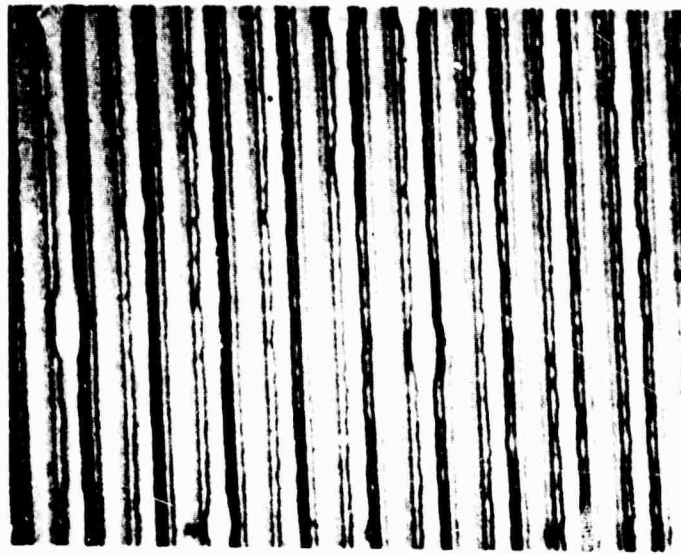


Figure 73. Intensity distribution within unit cell in bulk of the photoresist with 20:1 construction beam ratio (A 30-percent reflectivity from gold substrates is assumed. Quantities within the parenthesis are normalized to $I_{max}(X,Y)$).



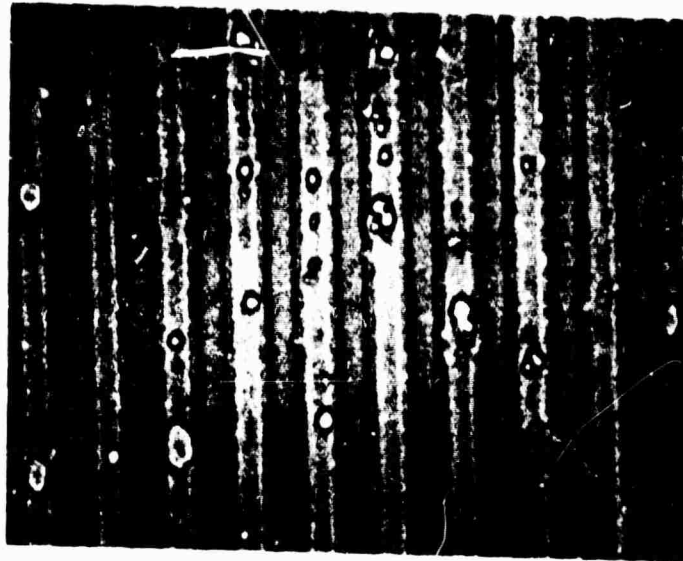
1650x



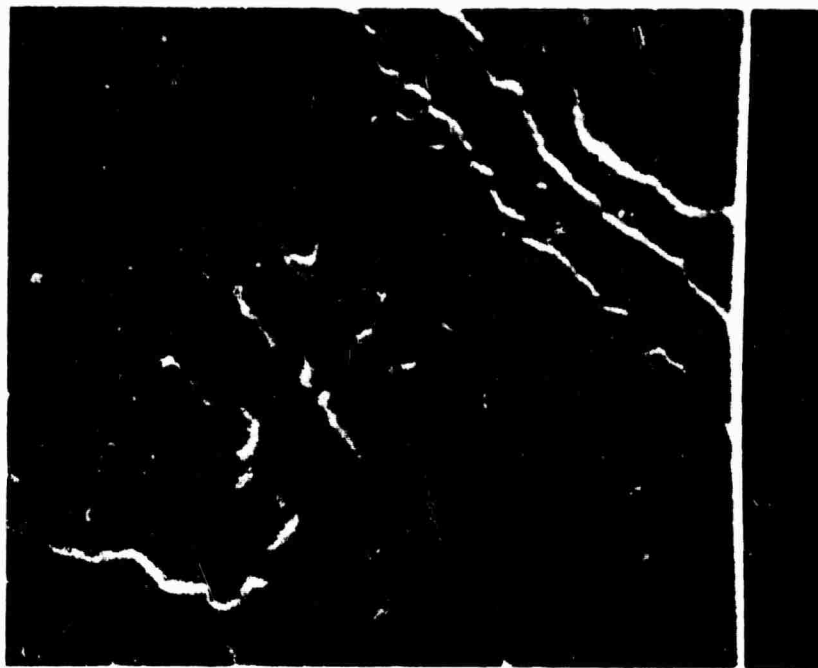
12,600x

a. 1:1 beam ratio

Figure 74. Exposures of AZ1350B photoresist on gold.



1650x



12,600x

Note small areas in the 1650x photo where the
gold substrate is showing through.

b. 20:1 beam ratio

Figure 74. Exposures of AZ 1350B photoresist on gold. (Continued)

SEM. ION-MACHINED GROOVES



2000x



Figure 75. SEM photograph of 3000 Å ion-beam machined grating in gold.

machined (gold) grating is evident, caused by the standing waves in the photoresist mask. However, a comparison of the photoresist grating mask and the final ion-beam machined (gold) grating shows a large reduction of standing wave structure due to the ion-beam machining process. Further experimental work is needed to compare the ion machined grating profile with the photoresist grating mask profile.

Effect of Substrate Reflectivity

Gratings were fabricated on various substrates in order to investigate the effect of standing waves experimentally as a function of substrate reflectivity. Photoresist was spin coated on (1) gold (39 percent reflectivity) (2) chromium oxide sputtered over gold (6 percent reflectivity) and (3) glass substrate coated with absorbing black paint (less than 0.5 percent reflectivity). Exposures were made with 0.4416 μm construction wavelength beams and a grating period of 4.8 μm . After standard development, the grating profiles were examined with a scanning electron microscope (SEM).

In Figures 76 and 77, photoresist grating profiles 4000 Å high on uncoated gold are shown as a function of exposure energy. At large exposure energies (200 to 400 mJ/cm^2) the standing waves are almost eliminated and the duty cycle is small, ranging from 10 to 15 percent. At lower exposures (100 mJ/cm^2) the duty cycle (40 percent) is improved but the standing wave pattern predominates. At still lower exposure energies (Figure 77) the duty cycle improves further (70 to 80 percent), but the standing waves in turn exhibit the strong characteristic staircase pattern. Gratings produced with exposures of 50 mJ/cm^2 or less are not suitable for ion machining due to the presence of excess photoresist in the grating 'valley'. The separation between the "staircase" levels was calculated to be 1300 Å and was verified by examining the pictures. Since the photoresist-to-gold etching rate is about 1 to 3, this limits the peak-to-trough height machined into gold to about 4000 Å, for a duty cycle of approximately 50 percent. This is adequate for low-efficiency grating applications such as beam sampling. Deeper grooves can only be achieved by using higher exposure energies to minimize standing waves in the master resist grating at the expense of a reduced duty cycle.

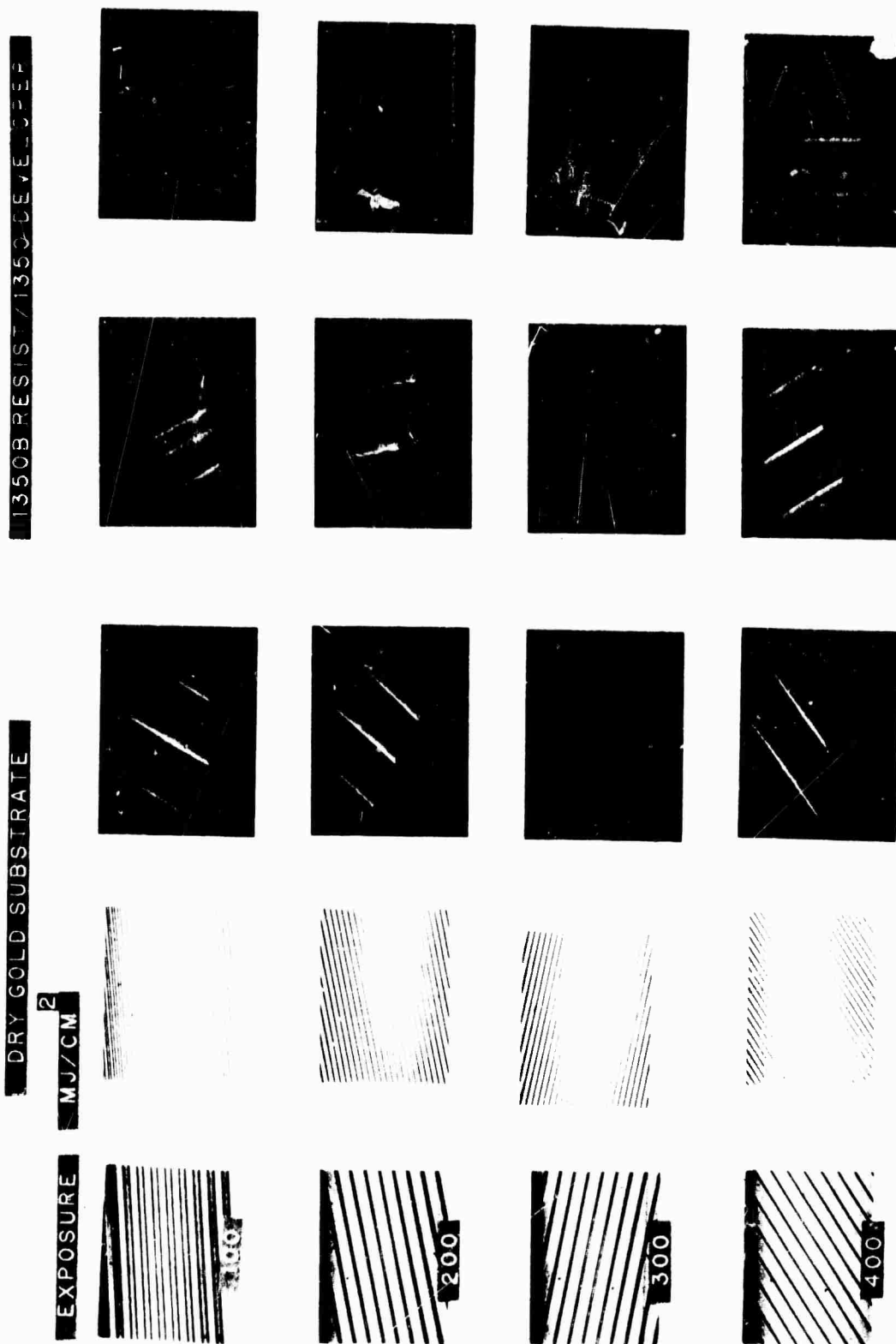


Figure 76. Dry gold substrate - 1350B resist/1350 developer, beam ratio 0.72, developing time - 1 minute, dilution 1:1.

1350B RESIST/1350 DEVELOPER

DRY GOLD SUBSTRATE

2
MJ/CM

EXPOSURE

25

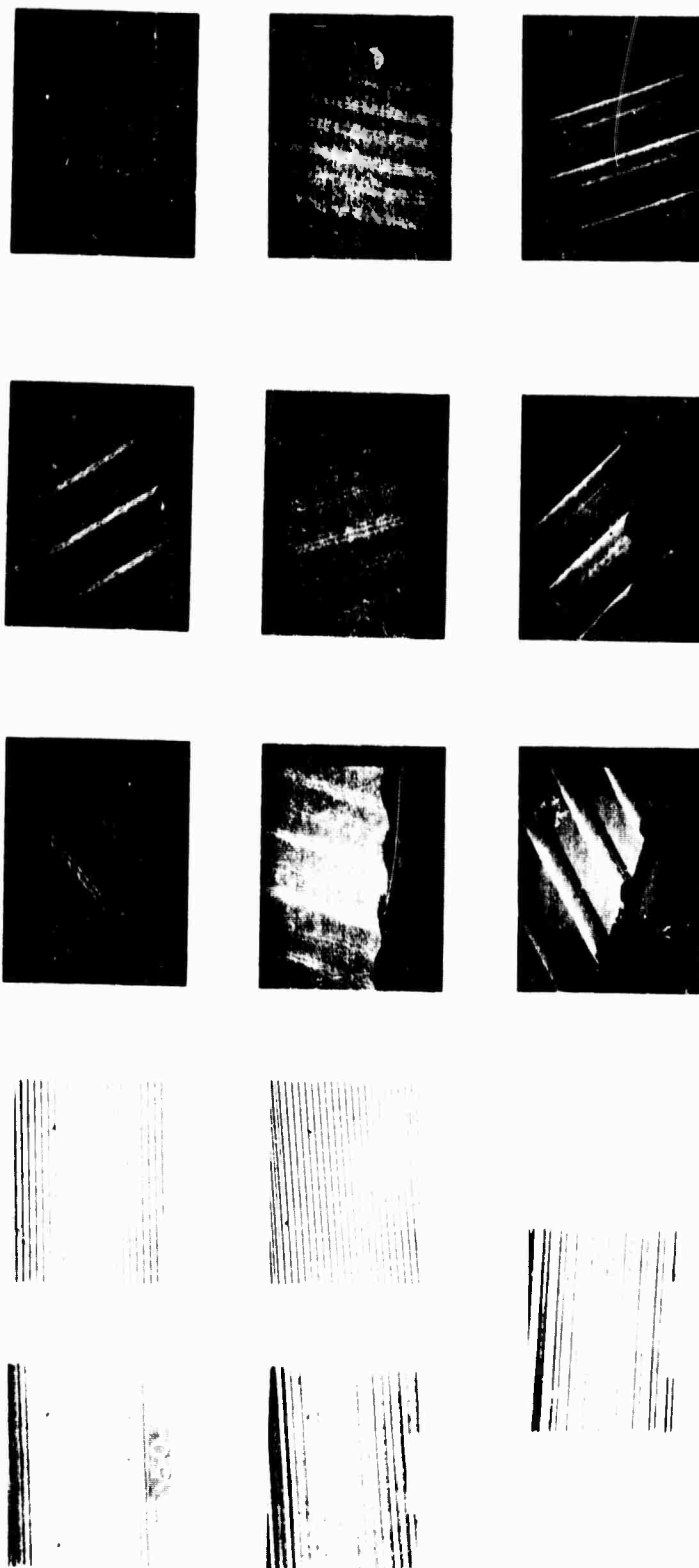


Figure 77. Dry gold substrate - 1350B resist/1350 developer, beam ratio 0.80, developing time - 1 minute, dilution 1:1.

In Figures 78 and 79, photoresist gratings on dark chromium oxide are depicted as a function of exposure energy. A substrate reflectivity of 6 percent was measured at the 0.4416- μm laser wavelength. However, even at this low reflectivity value, the desired grating exposure intensity is modulated 63 percent in the bulk of the resist. As expected from the theory and verified by the SEM pictures, the standing waves have been partially eliminated and the duty cycle improved.

To fabricate gratings with large peak-to-trough heights, a 2- μm layer of photoresist was used on glass substrates coated with flat black paint. The reflectivity of these substrates is less than 0.25 percent. The method used to process these samples was described in the May report. Resultant grating profiles are shown in Figure 80 as a function of exposure energy. A marked improvement in the efficiency (peak-to-trough height) and duty cycle is evident, and the standing wave pattern has been completely eliminated. The duty cycle (rms width divided by one period) ranges from 25 to 40 percent while the peak-to-trough height is about 2 μm . These master photoresist gratings are suitable for high-efficiency grating applications such as virtual axicons. The 2- μm peak-to-trough height achieved is well in excess of that required in most applications.

The grating profile is a function of the etch-exposure characteristic of the photoresist/developer combination. To obtain a square-wave shaped grating from a sinusoidal holographic exposure, nonlinear photoresist characteristics are desirable. The profiles shown in Figure 80 for 1350J photoresist and 1350 developer are typically trapezoidal. The slope angle between the side of the grating and the substrate is 75 to 80 degrees. This is a consequence of the linear region that lies between threshold exposure, below which little or no photoresist is removed by the developer, and saturation exposure, above which all the photoresist is removed.

In Figure 81 a different photoresist (1375) was used with 1350 developer to see if there was marked difference in the grating profiles. The duty cycle here ranges from 30 to 50 percent. The profiles are basically similar to those obtained with 1350J photoresist and the slope angles range from 65 to 70 degrees.

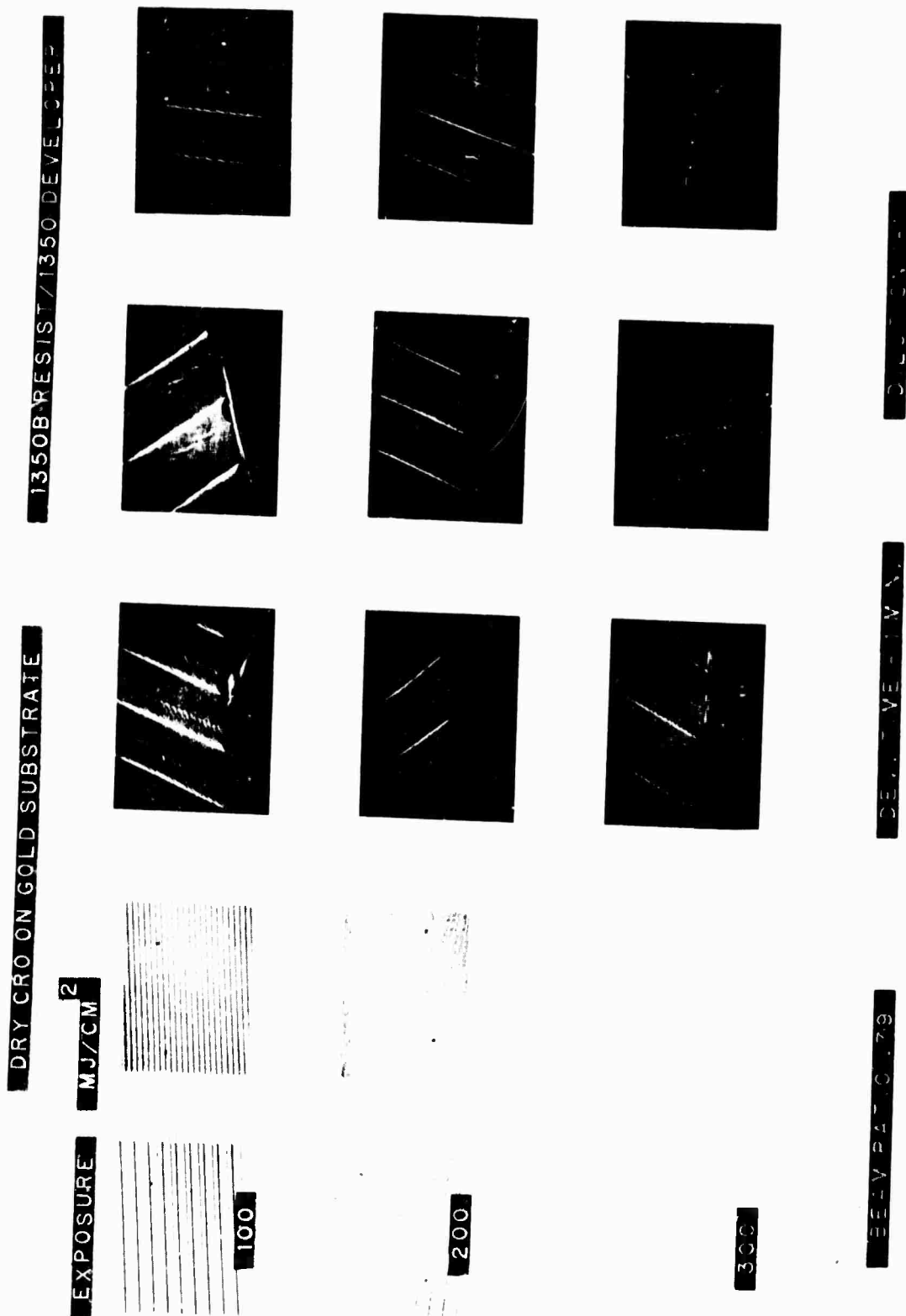
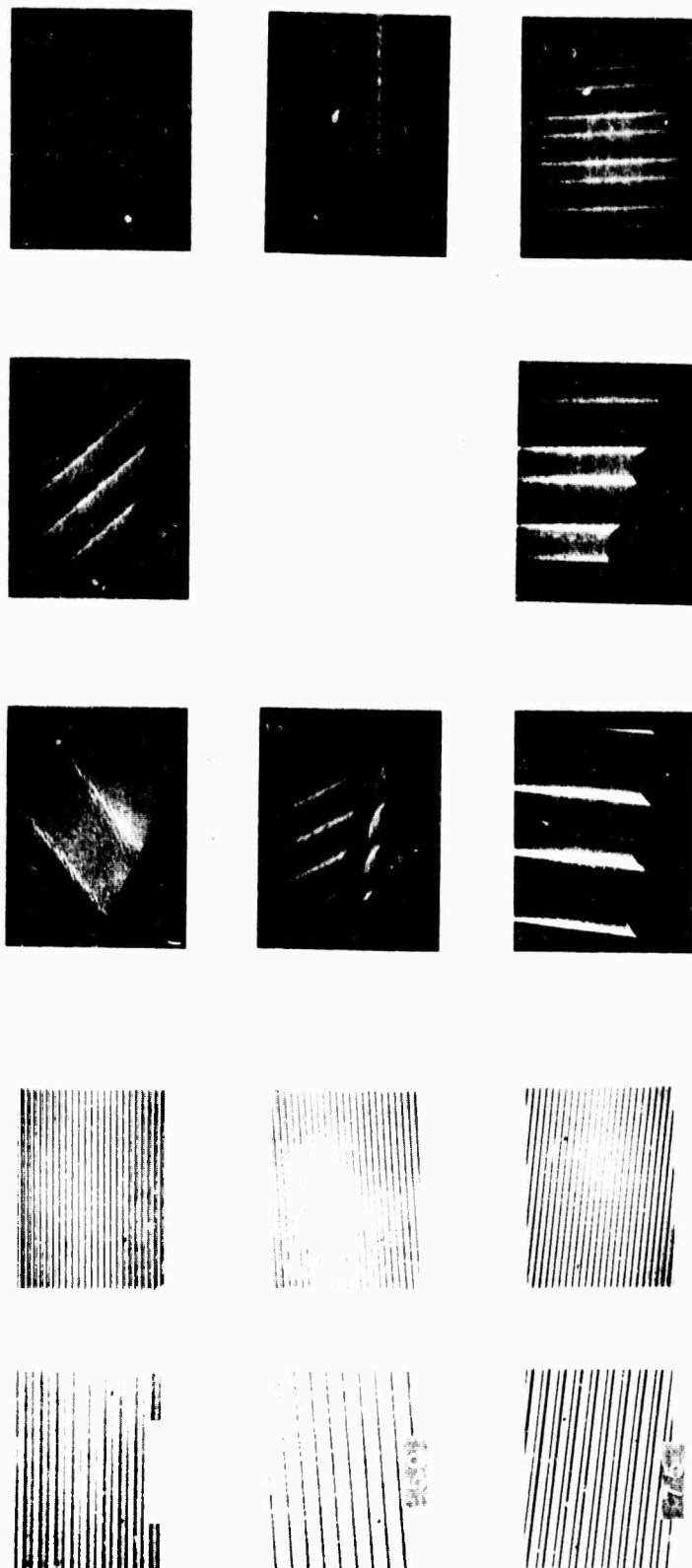


Figure 78. Dry CrO on gold substrate - 1350 resist/1350 developer, beam ratio 0.79, developing time - 1 minute, dilution 1:1.

1350B RESIST / 1350 DEVELOPER



DILUTION 1:1

DEV. TIME - 1 MIN.

BEAM RATIO 0.78

Figure 79. Dry CrO on gold substrate - 1350B resist/1350 developer, beam ratio 0.78, developing time - 1 minute, dilution 1:1.

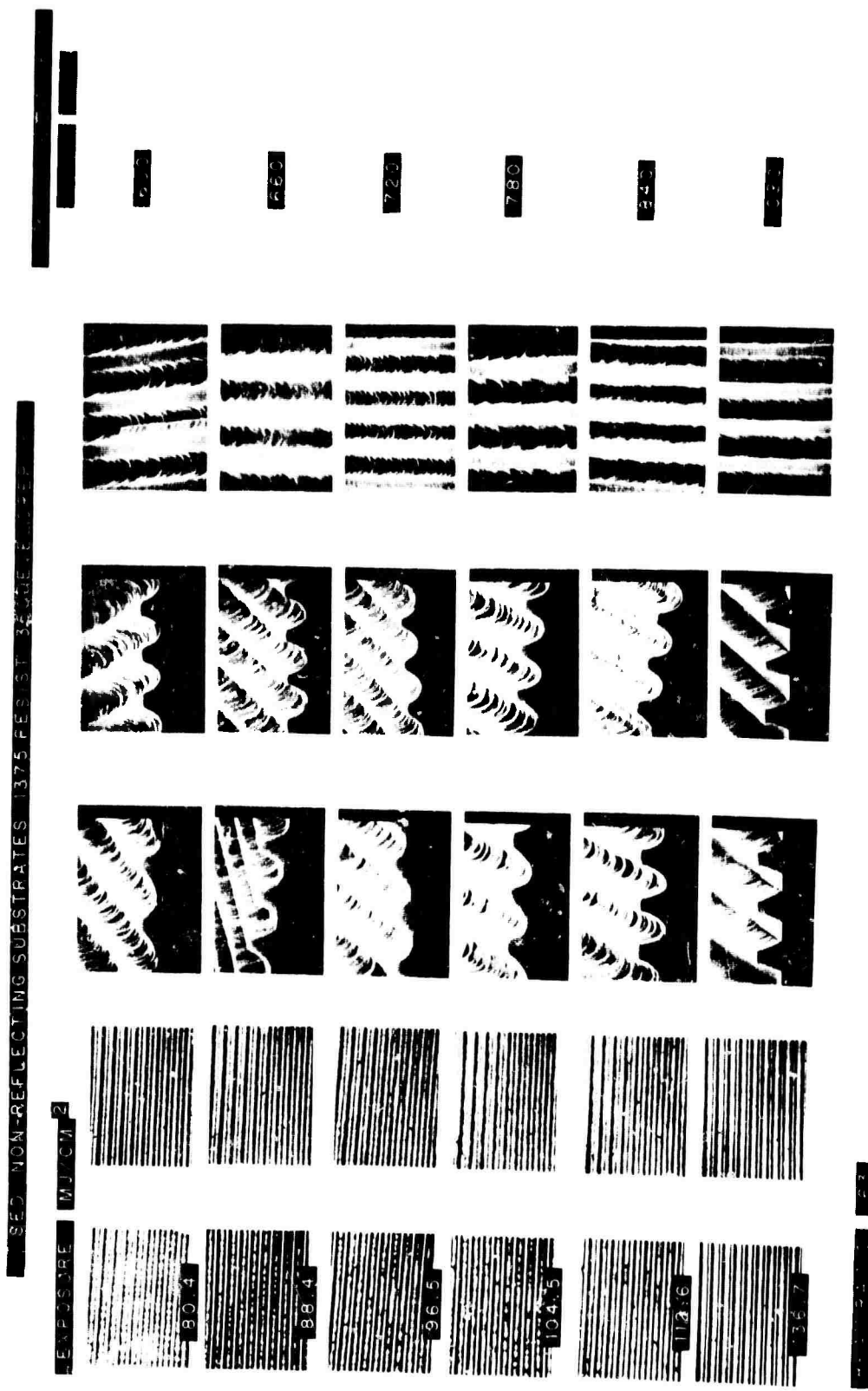
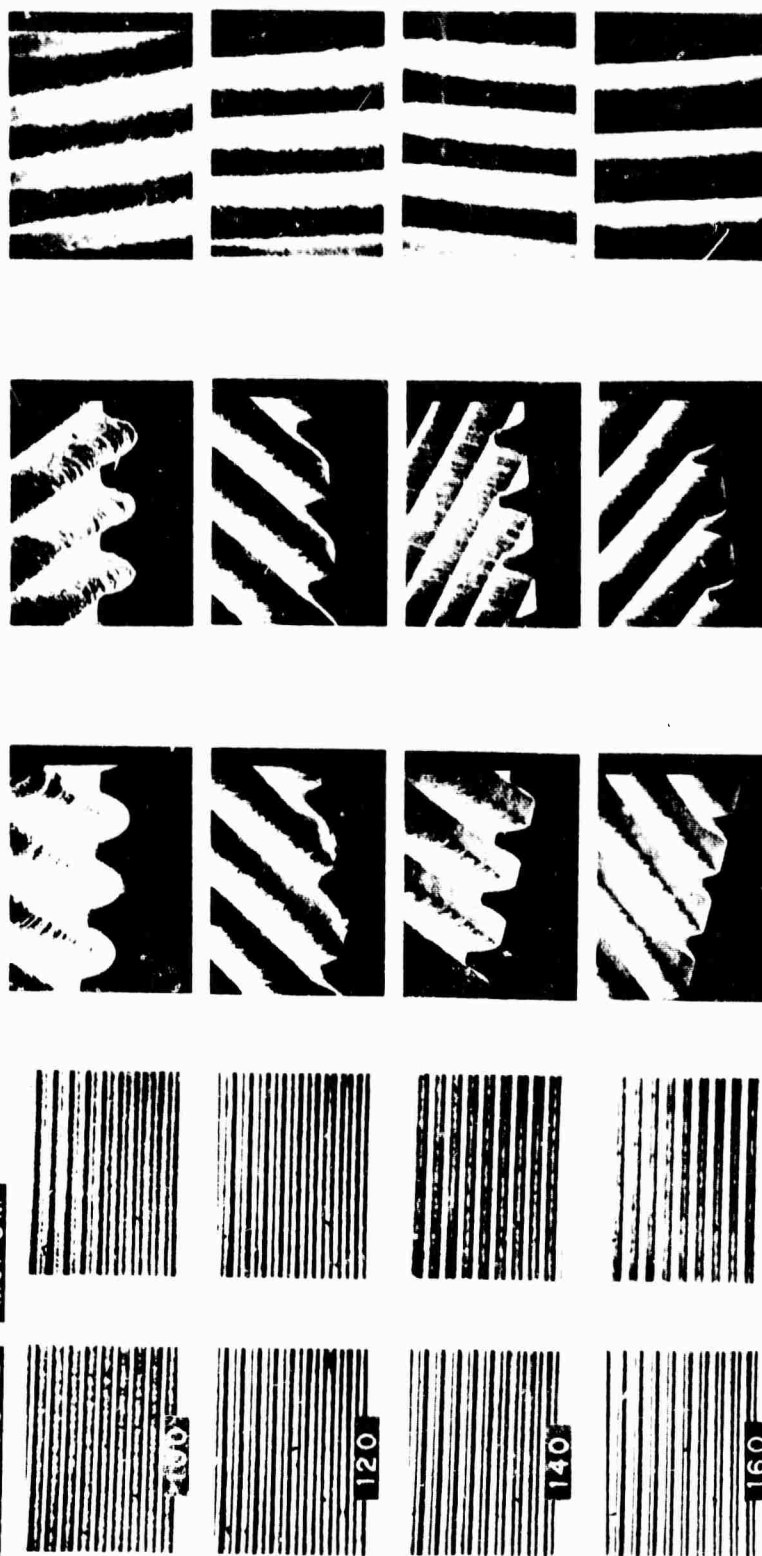


Figure 80. Dry/non-reflecting substrate - 1350J resist/1350 developer, beam ratio 0.63, developing time - 2 minutes, dilution 1:1.

DRY/NON-REFLECTING SUBSTRATE 1375 RESIST 1350 DEVELOPER

EXPOSURE MJ/CM²



BEAM RATIO .64

DEV. TIME - 2 MIN.

DILUTION - 1-1

Figure 81. Dry/non-reflecting substrate - 1375 resist/1350 developer, beam ratio 0.64, developing time - 2 minutes, dilution 1:1.

Finally, simultaneous-exposure-and-development (SED) techniques were used with 1375 photoresist/1350 developer, as outlined in the May report. The results are shown in Figure 82. Again, the profile characteristics are similar, with slope angles of approximately 75 degrees, but the duty cycle has improved to from 40 to 60 percent.

Standing Waves in Thick Photoresist Layers

In Section 3.4.5 an experiment to apply anti-reflection (AR) coating techniques to the fabrication of high-efficiency gratings was outlined. The composition of these coatings was varied to evaluate their effectiveness in eliminating standing waves. Photoresist layers 2.6 μm deep made with an exposure energy density of 130 mJ/cm^2 were used to achieve ion-machined depths of up to 2 μm . A grating period of 5.15 $\mu\text{m}/\text{cycle}$ was chosen to match the axial period of the aberration-corrected design grating.

Scanning-electron-microscope interrogation of the samples (Figures 83 and 84) showed little or no evidence of standing waves. It will be shown later that the slight structure remaining is "smoothed" out by the ion machining process and does not transfer into the final gold grating. Because the AR coatings were selected to have reflectivities ranging from less than 0.1 percent up to 10 percent, the absence of a dominant staircase structure at the high reflectivities did not correlate with previous theoretical and experimental work with thin ($<0.5 \mu\text{m}$) photoresist layers used for fabrication of low-efficiency gratings. To further investigate this effect, similar gratings were fabricated on gold substrates without AR coatings. The results in Figure 85 show gratings of a quality comparable to those using AR coatings. Because gold has a reflectivity of about 40 percent at the exposure wavelength (0.4416 μm), the absence of standing waves is attributed to the thickness of the photoresist layer. Photoresist gratings fabricated with 1.3- μm layers on gold (Figure 86) exhibited a more definite staircase structure than those on 2.6 μm photoresist layers. At present, the exact mechanism by which thick photoresist layers suppress standing waves is not known. However, these experiments demonstrate the feasibility of fabricating suitable photoresist gratings holographically for producing ion machined high-efficiency gratings in gold.

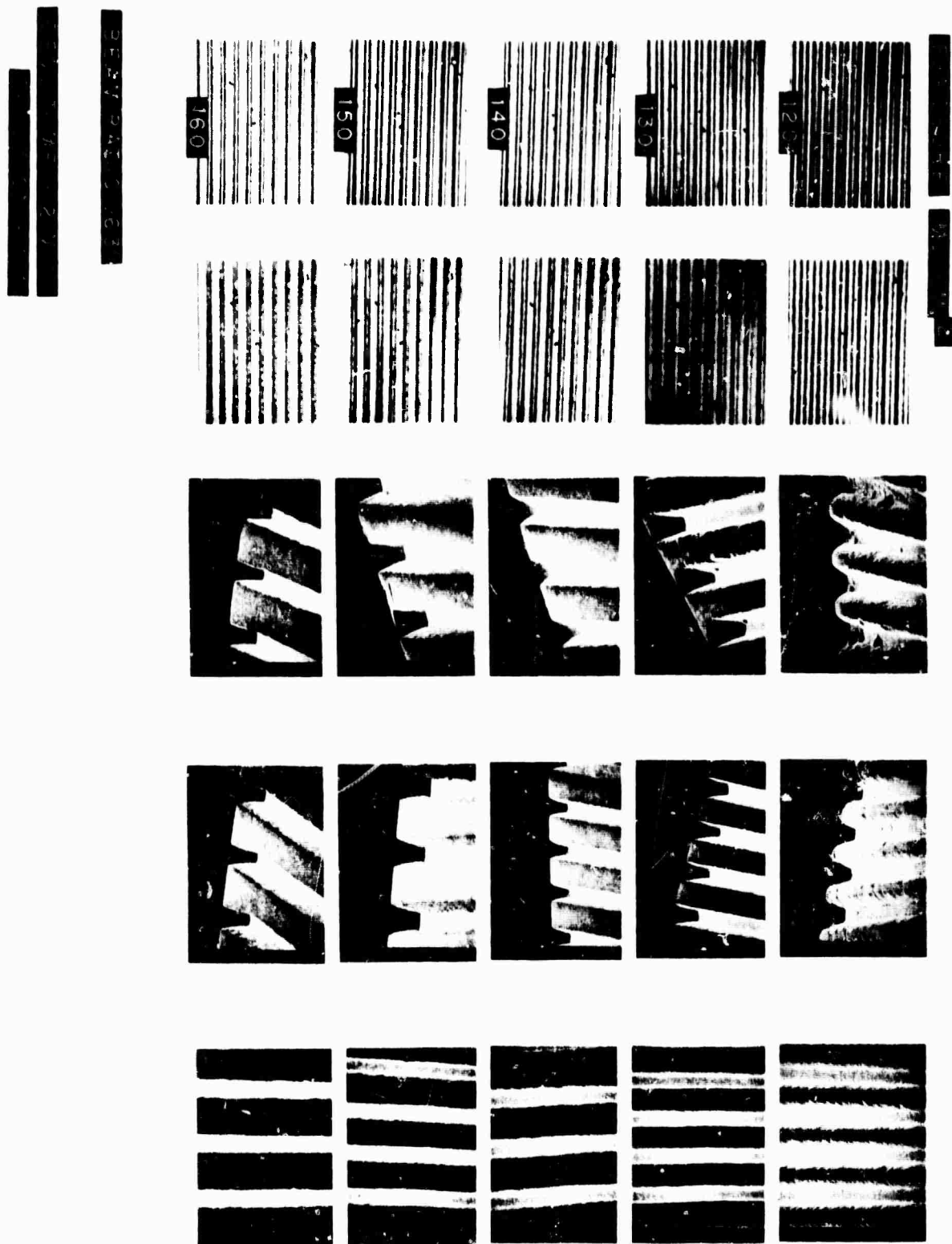
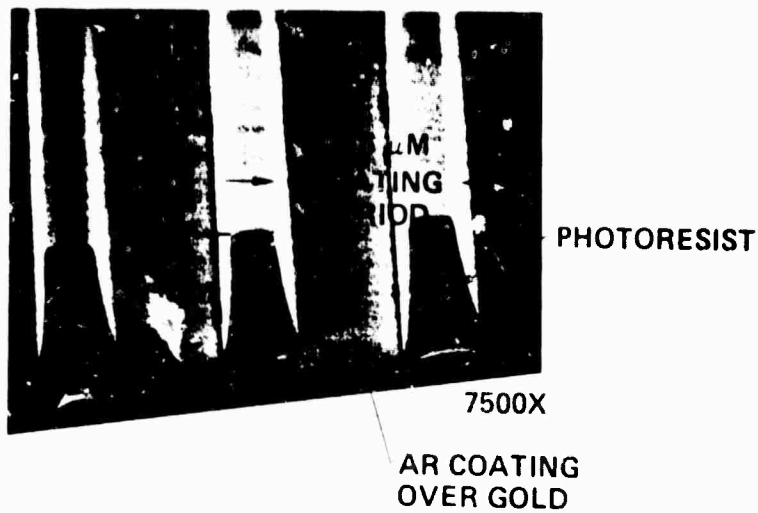


Figure 82. SED non-reflecting substrates-1375 resist/3500 developer, beam ratio 0.63, developer dilution 5:1.



a. Substrate reflectivity = 11 percent



b. Substrate reflectivity = 2 percent



c. Substrate reflectivity = 0.2 percent

Figure 83. SEM photographs of holographic gratings in photoresist on gold with AR coatings of varying reflectivity.

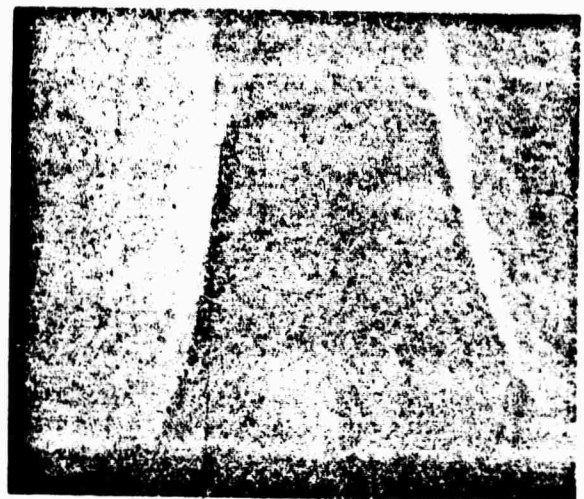
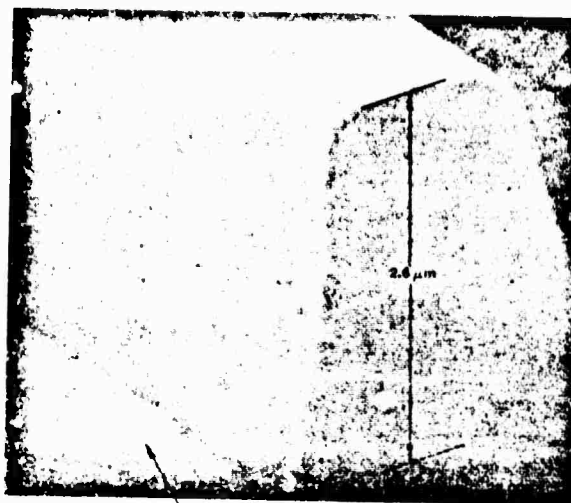


Figure 84. High-magnification SEM of typical grating profile on gold with AR coating showing minimal standing wave structure (20 steps, $\lambda/4$ (1300 Å) separation).

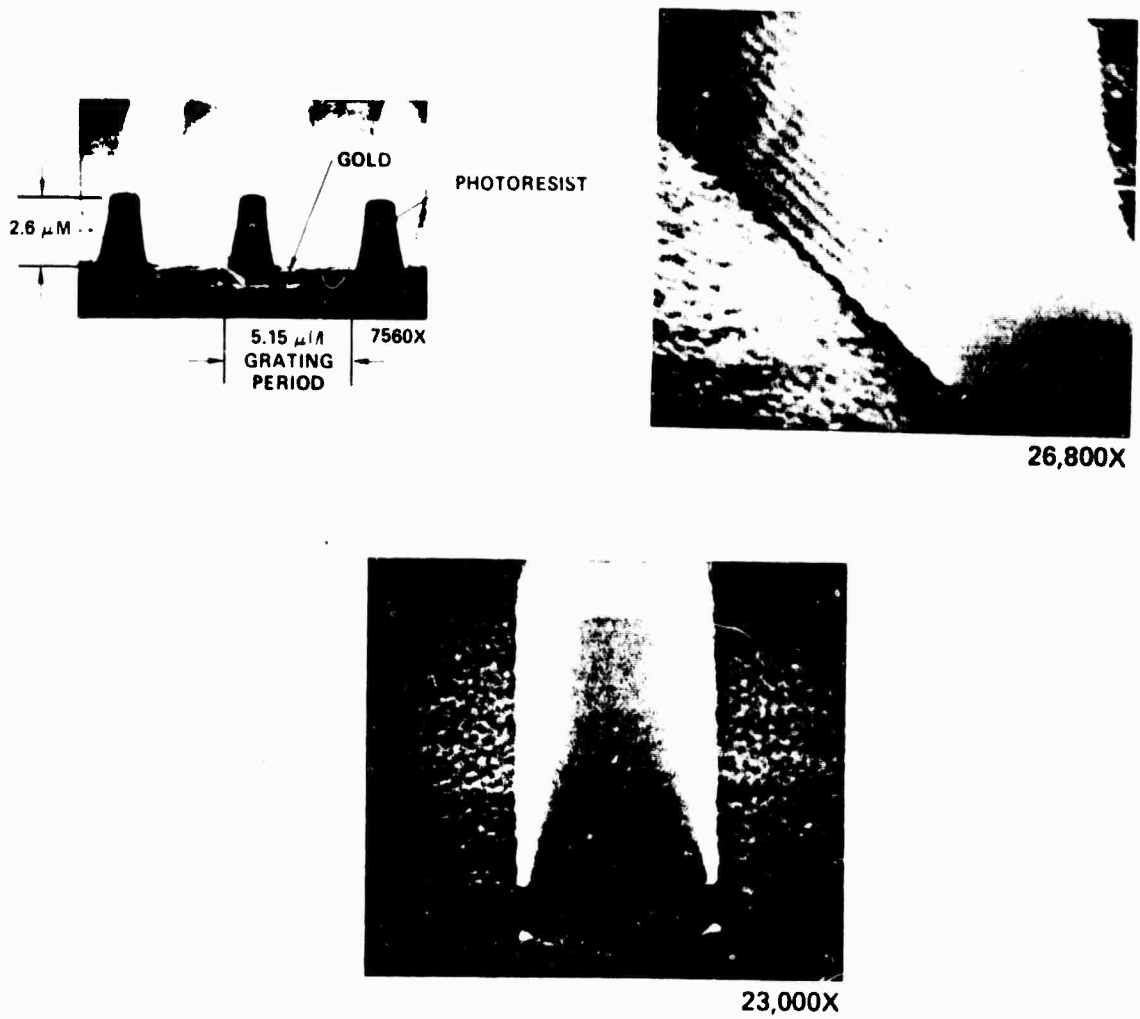


Figure 85. SEM photographs of (2.6 μ m relief height) holographic gratings in photoresist on gold with minimal standing wave structure.

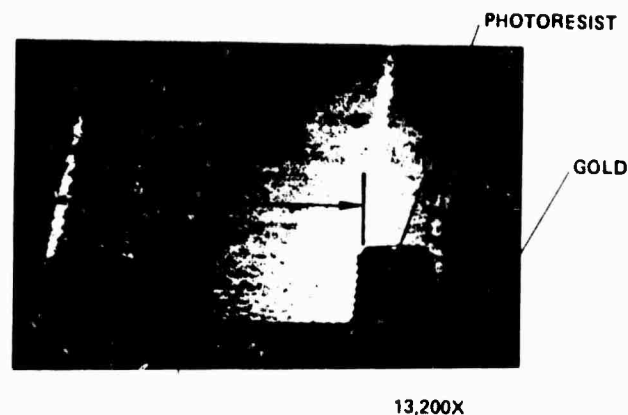
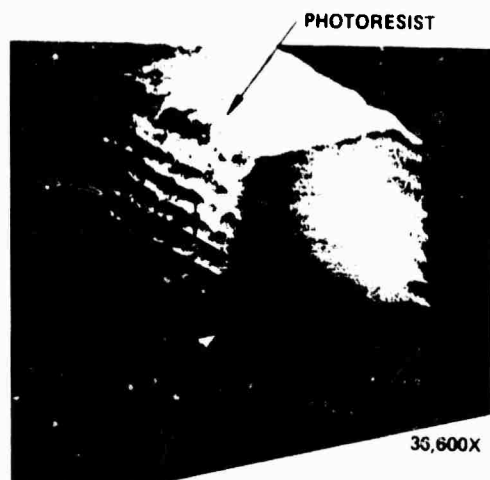
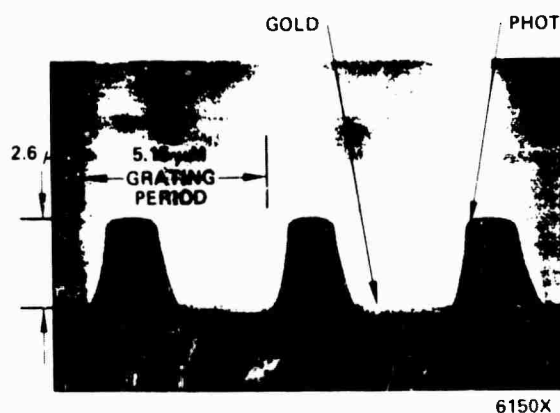
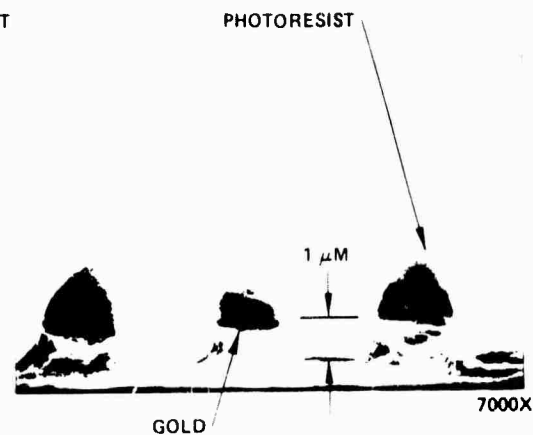


Figure 86. SEM photographs of holographic gratings on gold using $1.4\text{ }\mu\text{m}$ thick resist. (Standing wave structures are more dominant compared to gratings fabricated with $2.6\text{ }\mu\text{m}$ photoresist thickness: see Figures 84 and 85).

Having achieved suitable photoresist gratings with $2.6\text{ }\mu\text{m}$ peak-to-trough heights on gold (Figures 85, 87 and 88) four samples were ion machined in pairs to grating depths of 1 and $2\text{ }\mu\text{m}$ in gold (Figures 87 and 88. One sample of each pair was used for SEM interrogation. Comparison of Figures 87 and 88



a. Before ion machining.



b. After ion machining.

Figure 87. High-efficiency $1\text{-}\mu\text{m}$ deep grating ion machined in gold using photoresist grating mask with $2.6\text{ }\mu\text{m}$ relief height (minimal standing wave structure in photoresist mask is not transferred into gold grating.)



ION MACHINING EXCEEDED THICKNESS
OF THE GOLD LAYER CAUSING EXCESSIVE
ROUGHNESS AT GROOVES OF GRATING
AND EXPOSING SILICON SUBSTRATE

a. Before ion machining

b. After ion machining

Figure 88. 2- μ m deep grating ion machined in gold using photoresist grating mask with 2.5 μ m relief height. (Ion machining exceeded thickness of gold layer causing excessive roughness of grating grooves and exposing silicon substrate.)

shows the deformation of the photoresist grating mask caused by high-energy ion bombardment as the grating is transferred into gold. The photoresist grating becomes more triangular as the machining depth of 2 μ m is approached. The grooves of the gold grating also approach a triangular shape for increased depth. However, the top width of the grating which is shielded by the photoresist during the ion machining remains unchanged.

With the two remaining samples, the deformed photoresist grating mask was cleaned off, leaving the final gold grating. Efficiency measurements were taken with TE and TM polarization and compared with the predicted data of the Berkeley diffraction efficiency code based on the grating shape, depth and duty cycle. Quantitative data from these measurements are presented in Section 4 of this report.

4.0 HIGH-EFFICIENCY GRATING ANALYSIS AND MEASUREMENT

The material presented in this section includes the major portion of the work that was carried out under Task IV (High-Efficiency Grating Investigation). The balance of this effort, dealing with identification and analysis of high-efficiency holographic grating concepts, was covered in Section 2. While the earlier optical design analyses were concerned primarily with the wavefront quality of the diffracted beams, the computer analysis described in Section 4.2 was directed toward achieving high efficiency in practical holographic grating designs. The presentation begins with a discussion of high-efficiency design issues.

4.1 HIGH-EFFICIENCY HOLOGRAPHIC GRATING DESIGN ISSUES

Although high-efficiency linear gratings have been successfully produced by a variety of methods, this fact does not automatically ensure that comparable results can be achieved with nonlinear holographic gratings, which have neither straight grooves nor uniform groove spacing. To make high-efficiency holographic gratings, it is necessary to take into account the fact that the angle of incidence and the groove orientation (relative to the plane of incidence), as well as the spacing, may vary as a function of position on the grating.

The necessity of controlling all of these variables simultaneously might appear to preclude the possibility of producing high-efficiency holographic gratings. However, the geometry of the grating groove (shape, width, depth) is also a very important factor affecting the diffraction efficiency. Small changes in groove geometry can cause relatively large changes in the grating efficiency. For example, a grating with a sinusoidal groove profile theoretically can have an efficiency of 100 percent for either polarization (electric vector perpendicular to the grooves, E_{\perp} , or parallel to the grooves, E_{\parallel}). The variation of diffraction efficiency as a function of

groove depth for a sinusoidal linear grating is shown in Figure 89^{7,8}, for a particular groove period and angle of incidence. Note that very high efficiency can be achieved in both polarizations for the same set of conditions. This does require rather deep grooves, however. Achieving the necessary groove depth with a controlled groove shape is the major issue in the fabrication of high-efficiency holographic gratings.

The calculated efficiencies for both polarizations as a function of relative groove period for a particular groove depth and angle of incidence

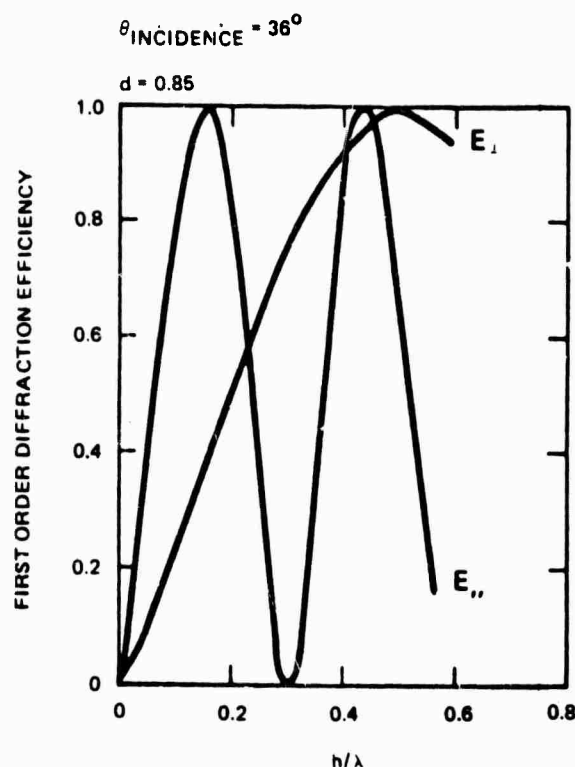


Figure 89. Efficiency versus groove depth.

7. K. A. Zaki and A. R. Neureuther, "Scattering from a Perfectly Conducting Surface with a Sinusoidal Height Profile: TM Polarization," *IEEE Trans. Ant. and Prop.*, AP19, 747 (1971).
8. K. A. Zaki and A. R. Neureuther, "Scattering from a Perfectly Conducting Surface with a Sinusoidal Height Profile: TE Polarization," *IEEE Trans. Ant. and Prop.*, AP19, 208 (1971).

are given in Figure 90. These calculations were made for a rectangular linear grating.⁹ Here it is not possible to get peak efficiency for both polarizations with the same groove period, for these particular parameters. Similar plots can be made as a function of the angle of incidence and for other groove shapes (triangular, trapezoidal, flattened sinusoids, etc.). Numerous calculations such as these have been described in the literature and the computed efficiencies agree quite well with measured values, especially in the infrared region of the spectrum.

The dependence of the diffraction efficiency on the groove depth and profile applies equally to holographic gratings and was verified during the study. Since the efficiency of these gratings is also a function of position,

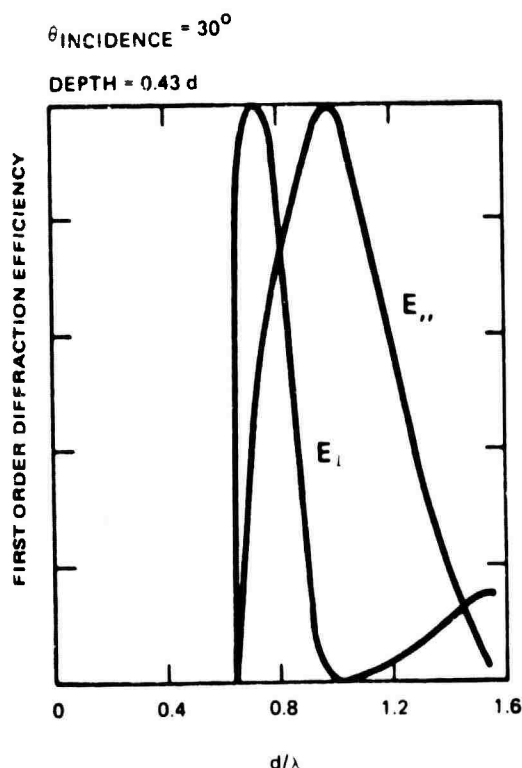


Figure 90. Efficiency versus groove period.

9. A. Wirgin and R. Deulil, "Theoretical and Experimental Investigation of a New Type of Blazed Grating," J. Opt. Soc. Am. 59, 1348 (1969).

because of the factors noted above, it should be possible, in principle, to vary the groove geometry in a simple way (e.g., the groove depth) to optimize the efficiency at every point. In particular, both high efficiency and good efficiency uniformity can be realized in this way.

The optimization approach just described was pursued in conjunction with the fabrication investigation of Task III and yielded excellent results. Thus, the feasibility of producing holographic gratings having uniform high efficiency hinges on the ability to control the groove shape and depth. These fabrication issues were discussed in Section 3.

4.2 COMPUTER MODELING OF HIGH-EFFICIENCY GRATINGS

4.2.1 Description of the Berkeley Code

To calculate the holographic grating diffraction efficiencies, a computer code developed at the University of California at Berkeley by H. Kalhor, K. Zaki, and A. Neureuther was used. The code models a perfectly-conducting metal grating whose cross-sectional groove profile is composed of up to 50 contiguous line segments per period. A periodic Green's function is chosen for use in an integral representation of the total field. A numerical solution to the integral equation can then be generated, yielding both the near and far fields.

The code has been arranged in the form of two subroutines, TESTTE and TESTTM, which calculate the diffraction efficiencies for the TE($E_{||}$) and TM(E_{\perp}) incident beam polarizations. The subroutines are used in conjunction with a calling program that translates the groove profile parameters of interest (such as the groove depth and duty cycle of rectangular grooves) into the lengths and angles of the contiguous line segments. For most applications a small number of segments is adequate — two for triangular blazed gratings and four for the trapezoidal grooves produced by ion-machining. Other required inputs are the groove period, the incident

beam angle (measured to the surface normal), and parameters that govern the number of sample points and the degree of convergence of the numerical solution.

The subroutines compute the distribution of diffracted power into all orders. Other readily available information includes the field magnitudes and phases of all the diffracted orders, and the fields existing at the grating surface. A check on the accuracy of the numerical solution is obtained by invoking conservation of the incident and diffracted energies; by this criterion the TM solutions are typically accurate to within 0.5 percent and the TE solutions to within 0.1 percent.

Following is a discussion of the mathematical formulation used to determine the groove period and orientation.

The groove period and orientation at each point are determined from the construction geometry shown in Figure 91. To compute the fringe (groove) pattern the two converging fields are summed, i. e.,

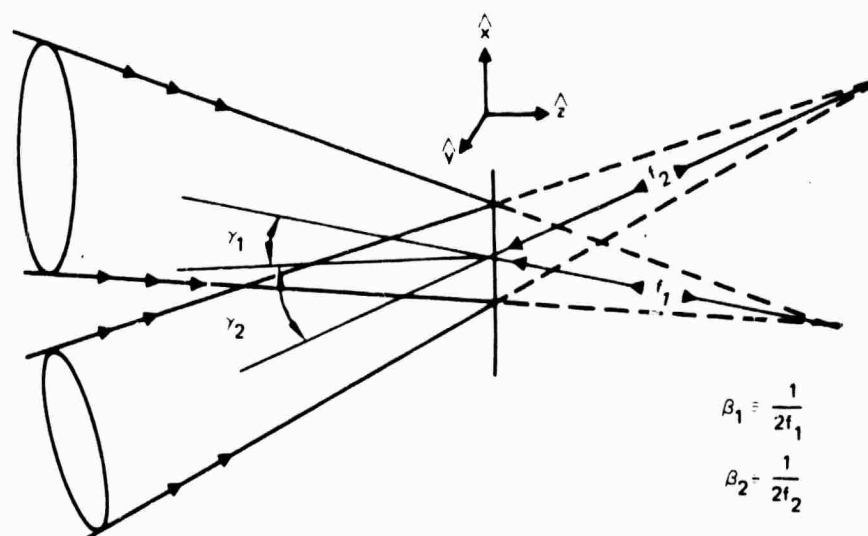


Figure 91. Construction geometry for the hologram.

$$U \sim \exp \left[jk (\beta_1 r^2 + x \sin \gamma_1 - z \cos \gamma_1) \right] \\ + \exp \left[jk (\beta_2 r^2 - x \sin \gamma_2 - z \cos \gamma_2) \right]$$

The symbols are defined in Figure 91. The resultant intensity on the holographic plate ($z = 0$) is

$$I \approx 2 + 2 \cos \left\{ k \left[(x^2 + y^2)(\beta_1 - \beta_2) + x (\sin \gamma_1 + \sin \gamma_2) \right] \right\}$$

The fringe maxima describe an off-center region of a concentric circular pattern, as shown in Figure 92. The equation for these circular fringes is:

$$\left[x + \frac{\sin \gamma_1 + \sin \gamma_2}{2 (\beta_1 - \beta_2)} \right]^2 + y^2 = \frac{\eta \lambda}{(\beta_1 - \beta_2)} + f(\gamma_1, \gamma_2, \beta_1, \beta_2)$$

or,

$$\left| \frac{r}{r_0} - 1 \right|^2 = \frac{\eta \lambda}{(\beta_1 - \beta_2)} + f(\gamma_1, \gamma_2, \beta_1, \beta_2), \quad n = 0, 1, 2, \dots$$

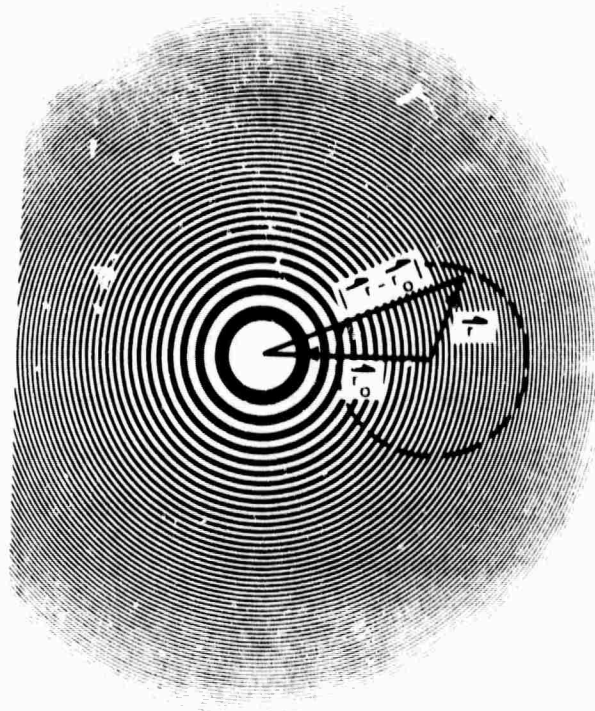


Figure 92. Fringe pattern of a holographic lens; the region enclosed by the dashed circle is an example of the pattern for non-normal incidence.

The grating period d/λ is equal to the distance from the m^{th} to the $(m + 1)^{\text{st}}$ groove, measured along a radius perpendicular to the grooves. Since this direction is given by the vector $\vec{r} - \vec{r}_0$, the period is, approximately,

$$\frac{d}{\lambda} = \frac{1}{\lambda} \frac{\partial |\vec{r} - \vec{r}_0|}{\partial m} \cdot \frac{1}{2|\beta_1 - \beta_2| |\vec{r} - \vec{r}_0|} \quad (13)$$

where:

$$|\vec{r} - \vec{r}_0| = \sqrt{\left[x + \frac{\sin \gamma_1 + \sin \gamma_2}{2(\beta_1 - \beta_2)} \right]^2 + y^2} \quad (14)$$

To illustrate the use of this expression, consider a hologram made by interfering an on-axis converging beam ($\beta_1 = \beta$; $\gamma_1 = 0$) with a 45-degree off-axis collimated beam ($\beta_2 = 0$; $\gamma = \gamma_2 = 45^\circ$). We wish to determine how the change in period affects the diffraction efficiency. The maximum change in d/λ occurs between the two edges of the grating on the x-axis (along the $-\vec{r}_0$ direction in Figure 92). Denoting these points by $x = \pm x_0$, $y = 0$, the f-number of the grating is given by

$$f/\text{no.} = \frac{f_1}{2x_0} = \frac{1}{4\beta x_0}$$

Hence, the two points in question are defined by

$$x_0 = \pm \frac{1}{4\beta f/\text{no.}}$$

$$y = 0$$

By substituting these values into Equations 13 and 14, the periods at the two points are found to be

$$\frac{d}{\lambda} = \frac{1}{\sin \gamma \pm 1/(2f/\text{no.})}$$

For an $f/2$ system with $\gamma = 45$ degrees, the period varies across the grating within the range $1 < d/\lambda < 2.2$.

As an example of how the code can be used to guide the design of a high-efficiency holographic grating, a typical set of efficiency design curves (shown in Figure 93) was plotted. These groove designs were chosen to yield diffraction efficiency values close to the theoretical limit of 50 percent for a holographic grating axicon with the trapezoidal groove profile indicated in the figure. They also apply to the design of the aberration-corrected beam sampler (see Section 5) which has almost the same beam geometry as a small region of the axicon — a 45-degree angle of incidence and two diffracted orders. From Figure 93, the best efficiencies for both polarizations were obtained when the ridge width (T) was between 30 and 50 percent of the groove period (D).

4.2.2 The Need for a Complex Model

It is a widely held misconception that diffraction grating efficiency has been satisfactorily modeled for many years. In fact, adequate efficiency prediction has only become feasible with the development of computer codes that could approximate the full electromagnetic boundary problem posed by the periodic structure, with a high degree of accuracy.

To understand the need for a complex diffraction efficiency model, it is helpful to envision the incident beam exciting and interacting with standing wave modes within the grooves. Low-order modes will be real, and the rest will be evanescent.

When the grating period is large ($d/\lambda \gg 1$), the groove can support a large number of real modes. The evanescent modes contribute relatively little to the matching of fields at the grating surface. Under these conditions, it is valid to approximate the effect of the grating as a simple surface phase modulation of the incident wave, and to use Fourier components to weight the diffraction efficiencies of the resulting orders. Polarization dependence need not be considered.

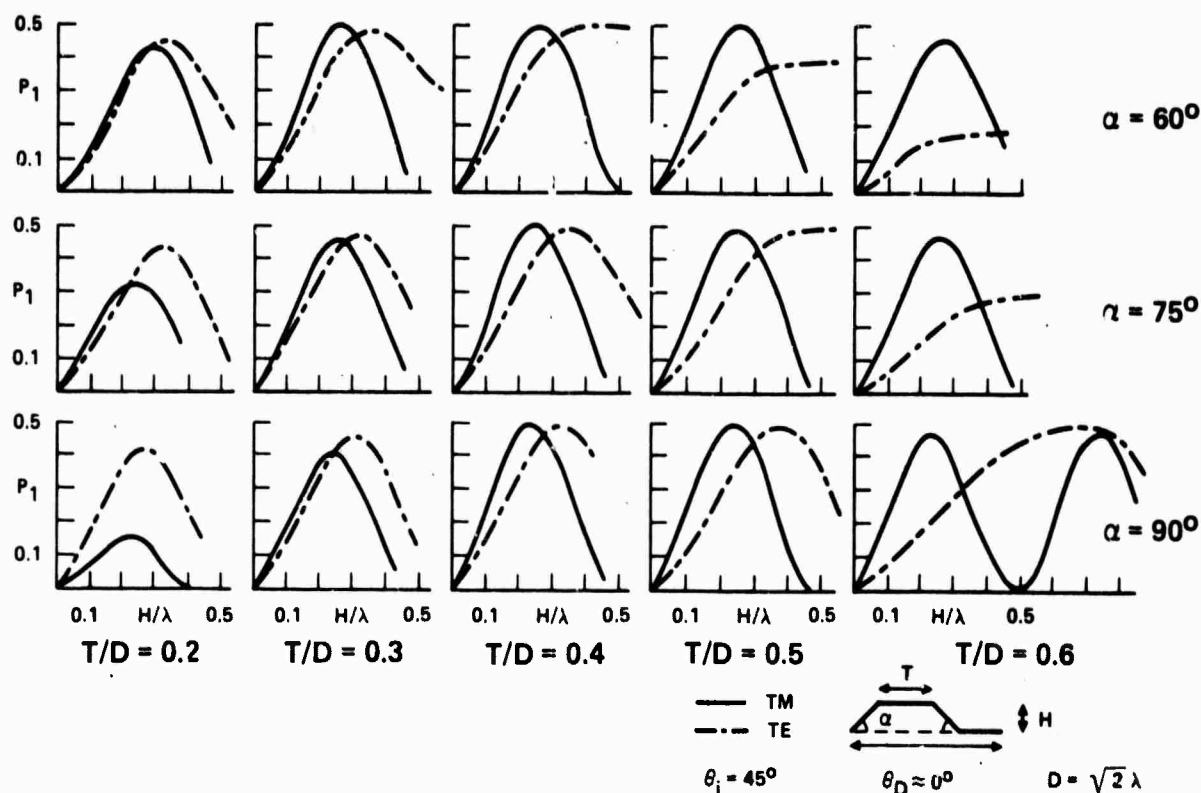


Figure 93. Diffraction efficiency design curves:
beam sampler or mixing axicon.

As the grating period becomes comparable to the wavelength, the boundary matching condition will depend more and more on evanescent fields. Very high diffraction efficiency may occur when the incident wave couples strongly into one of the real modes. Some types of anomalies will occur when a similar resonance enhances an evanescent field. To characterize the efficiency of a particular grating, the modes which the groove can support must be known in detail as a function of the incident polarization, groove shape, substrate conductivity, etc. Unfortunately, this sort of analysis is nearly impossible to carry out except in the special cases of rectangular and 90 degree blazed grooves. For most practical applications, an approximate or numerical solution is required.

Two suitable numerical codes have been developed to date. The first is the Berkeley code, which was used in this study. The code assumes that the surface fields on the grating can be fitted to a simple polynomial within a small enough cell. Within such cells, the wave equations can be integrated exactly, and the resultant matrix can be inverted to determine the coefficients of the polynomial-approximated fields.

The second code, which was developed at the Faculté des Sciences et Techniques de Saint-Jerome in France, manipulates the integral equations into a form in which they are amenable to an asymptotic expansion.

Theoretically, both codes can handle finite conductivity regimes; however, the version of the Berkeley code that was used in the Holographic Grating Study does not do this.

4.2.3 Verification of the Code

Comparison of predicted efficiencies with experimental data has yielded a high degree of confidence in the accuracy of the Berkeley code at wavelengths of 3 μm and above. The results of one code verification effort are presented in Figure 94. Loewin, et al¹⁰ have published data which indicate excellent agreement between their measurements and the Saint-Jerome code. Calculations from the Berkeley code for the same grating configuration have been added to these curves. In the TM polarization the curves are very well matched; in the TE polarization the shape of the curve is identical, but the curve appears to be shifted to slightly shorter wavelengths.

10. E. G. Loewin, et al., "Correlation Between Efficiency of Diffraction Gratings and Theoretical Calculation Over a Wide Range," Japanese J. Appl. Phys., 14 (1975) Suppl. 14-1.

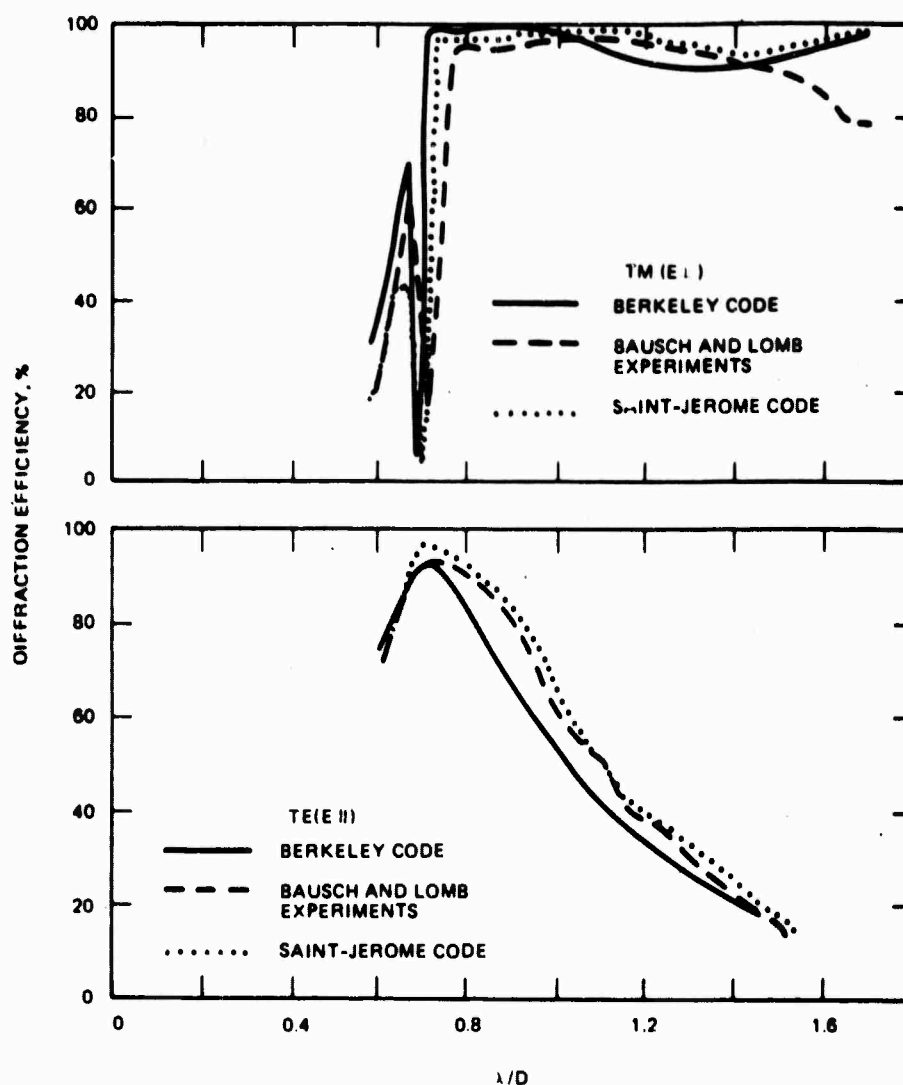


Figure 94. Code verification; Bausch and Lomb blazed gratings.

Another code verification is shown in Figure 95. The University of Dayton Research Institute compared the unpolarized reflectivity of a trapezoidal ion-etched grating to predictions of the Saint-Jerome theory: again, values computed with the Berkeley code have been added to the plot. The two curves compare very favorably.

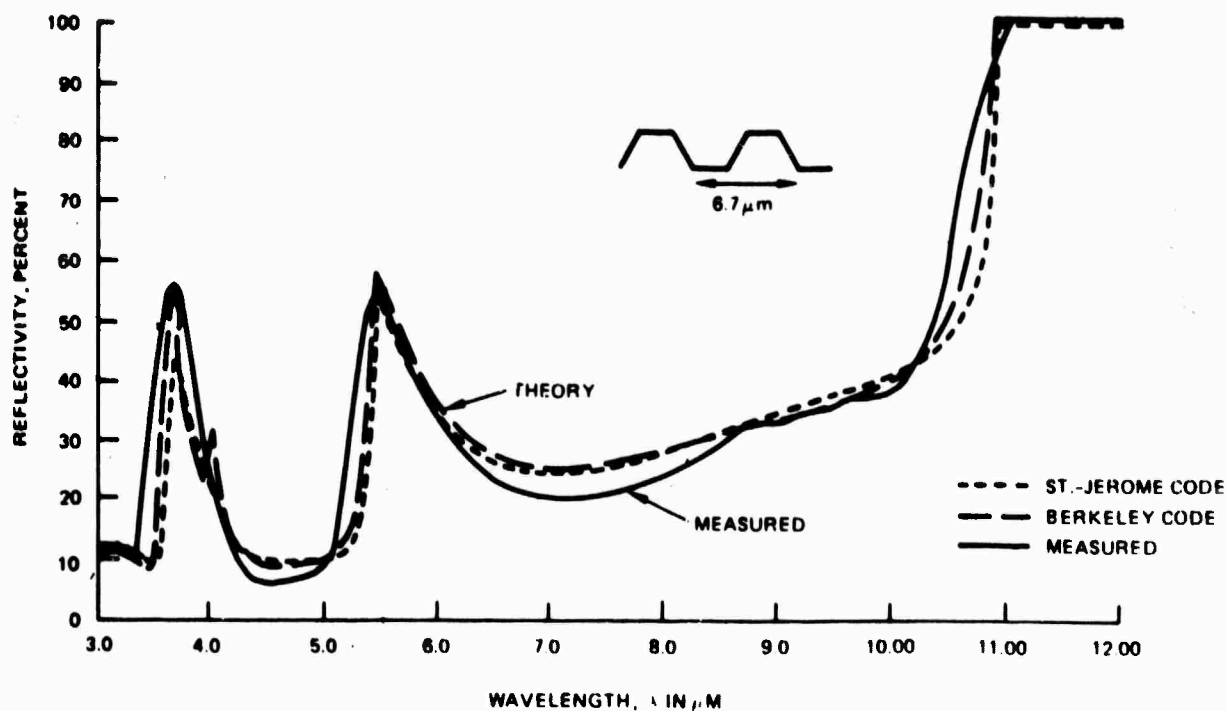


Figure 95. Code verification: Hughes ion-etched grating. Reflectivity in unpolarized light.

4.3 HIGH-EFFICIENCY HOLOGRAPHIC GRATING MEASUREMENTS

A set of ten holographic grating samples was fabricated as described in Section 3.4.4. These gratings are of the type modeled in Section 4.2.2 (see Figure 93). The theoretical diffraction efficiency limit for these gratings is 50 percent for an incident angle of 45 degrees. Figures 96 and 97 show the measured efficiency values for both polarizations. Gratings with groove geometrics of this type are suitable for use as high-efficiency grating axicons. In the axicon case (normal incidence), approximately 50 percent of the incident beam would be diffracted into each order ($n = \pm 1$). These samples confirm the high diffraction efficiency characteristics of ion machined holographic reflection gratings.

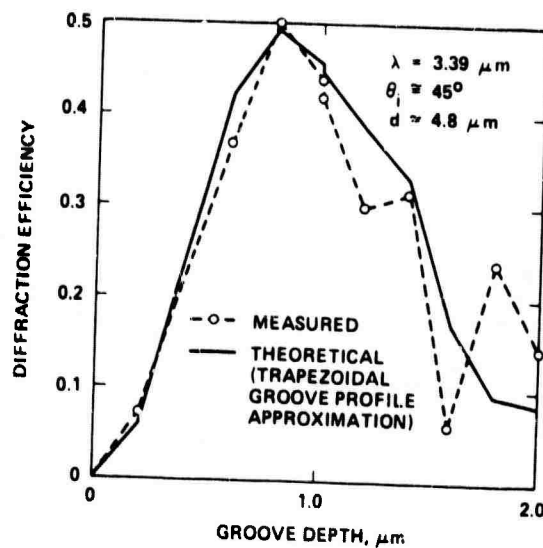


Figure 96. Ten high-efficiency samples: calculations for TM (E_{\perp}) polarization.

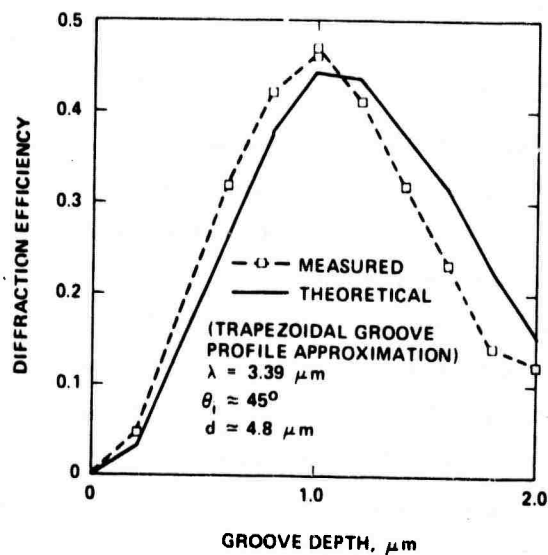


Figure 97. Ten high-efficiency samples: calculations for TE (E_{\parallel}) polarization.

5.0 ABERRATION-CORRECTED HOLOGRAPHIC GRATINGS

This section of the report documents the work accomplished under Task VI (Aberration-Free Beam Sampler Feasibility Demonstration). * Section 5.1 contains a discussion of the task objective and the design and fabrication issues involved, while the detailed design of the demonstration grating is presented in Section 5.2. Results of the spot profile and diffraction efficiency measurements that were performed are described in Section 5.3.

5.1 OBJECTIVE AND DESIGN ISSUES

The advantages of using aberration-corrected holographic gratings in HEL systems applications and the possibility of fabricating them by means of the "aberrated-wavefront" exposure technique were discussed in preceding sections of the report. The objective of Task VI was to demonstrate that such gratings could in fact be designed and fabricated by existing methods. For this purpose, a design configuration was chosen that would be representative of a beam sampler for an infrared HEL beam. First, aberration-corrected designs of the grating and construction optics were performed with

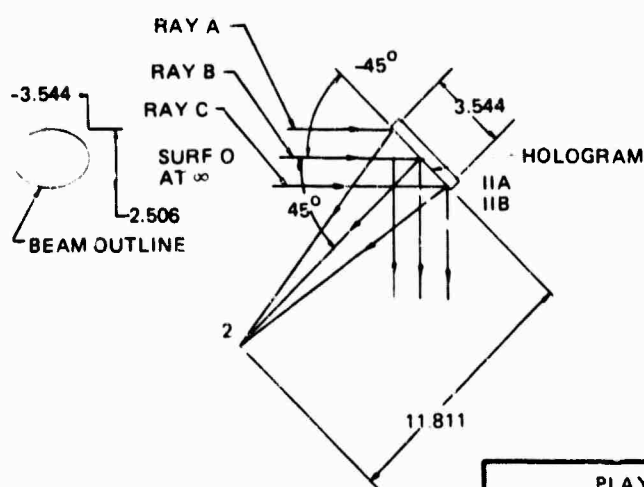
*The gratings developed under this task were originally called "aberration free," but this designation was subsequently dropped in favor of the more accurate term "aberration corrected". The two descriptions are used synonymously in this report.

the aid of existing optical design computer programs. Then the holographic grating was fabricated using the specially designed compensating optics in the construction beams. Following completion of the fabrication process, ion machined samples were played back in the design geometry and wavelength, and the intensity distributions of their focal spots were measured to assess the residual aberrations.

The sampling geometry selected for the demonstration was a flat mirror oriented at 45 degrees to an incident parallel beam. The holographic grating was designed to focus the first diffracted order at a point on the normal through the center of the mirror, as shown in Figure 98. This choice was influenced by two major considerations:

1. The aberrations associated with this highly off-axis configuration are relatively severe compared to those of other designs and therefore constitute a convincing test of the aberration-correction technique. Furthermore, the degree of compensation achieved is more easily evaluated when the corrected aberrations are large relative to the diffraction limit.
2. Since the spin-coating technique used throughout most of the fabrication investigation is not well suited for curved substrates, a flat grating design was chosen for demonstration purposes.

PLAYBACK OPTICS							
SURF	ELEM	DWG	RAD	MATERIAL	THK	LIMIT RAY HEIGHTS	
						RAY A	RAY C
0	SOURCE			AIR	∞	1.772	-1.772
1	IIA, IIB		∞	AIR (HOLOGRAM)	-11.811	1.772	-1.722
2	FOCUS					0	0



PLAYBACK OPTICS
SCALE: 1/3

PLAYBACK OPTICAL CHARACTERISTICS	
EQUIVALENT FOCAL LENGTH	11.811 INCHES
F-NUMBER	3.33
CONSTRUCTION WAVELENGTH	0.4416 μ M
PLAYBACK WAVELENGTH	3.39 μ M

Figure 98. 45-degree mirror beam sampler. Mirror sample point distance 11.81 inches (30 cm).

An important practical consequence of the 45-degree configuration employed was that the alignment tolerances for both construction and playback turned out to be especially stringent. (The tolerances are specified in Section 5.2 in connection with the design description.) In fact, the alignment tolerances for playback would probably preclude the use of this design in a real HEL system, at least with a fixed mirror. Because of these tolerances, the alignment procedures required for exposure and measurement of the demonstration grating were unusually delicate and time consuming. Nevertheless, the aberrations were successfully reduced to a level approaching the diffraction limit, thereby confirming the feasibility of the method. The focal-spot and efficiency measurements are described in Section 5.3.

A second issue of concern relating to the design of aberration-corrected gratings was the optical quality of the substrate. Since the grating design is predicated on the assumption that the substrate is perfectly flat, any distortions of the substrate (which also distort the grating) will tend to introduce spurious aberrations and confuse the grating evaluation.* For this reason, the demonstration grating samples were fabricated on $\lambda/20$ optical flats, as described in Section 3. Both high-efficiency and intermediate-efficiency samples were made by machining the gratings to different depths in the substrate. The latter were used in place of low-efficiency samples which would be difficult to measure accurately with a low-power laboratory laser.

Even though the requirements of Task VI were satisfied by the aberration-corrected gratings on optical flats, it was of interest to see if similar results could be obtained with a larger and more realistic substrate.

*Refer to the discussion of grating distortions in Section 2.3.1.

For this purpose, a molybdenum water-cooled high-power mirror approximately 9 cm in diameter was loaned to Hughes by the Air Force Weapons Laboratory. Because of its size and weight, this mirror could not be spin coated, as were the flats. Instead, after being polished flat, it was coated with photoresist using an experimental dip-draining technique.

After initial experimentation with the new technique, the demonstration grating was fabricated on the "GFE" mirror and its residual aberrations and efficiency uniformity were measured over an aperture of about 3 inches. The measurements showed that the larger grating also achieved nearly diffraction-limited performance, although some peaking of the diffraction efficiency was observed near the edges of the mirror. These results were achieved in spite of the fact that the mirror had been polished, but not coated under pressurized conditions and was therefore somewhat distorted.

(Experimental difficulties prevented it from being coated under pressure.)

An interferogram of the unpressurized mirror before coating is shown in Figure 99.

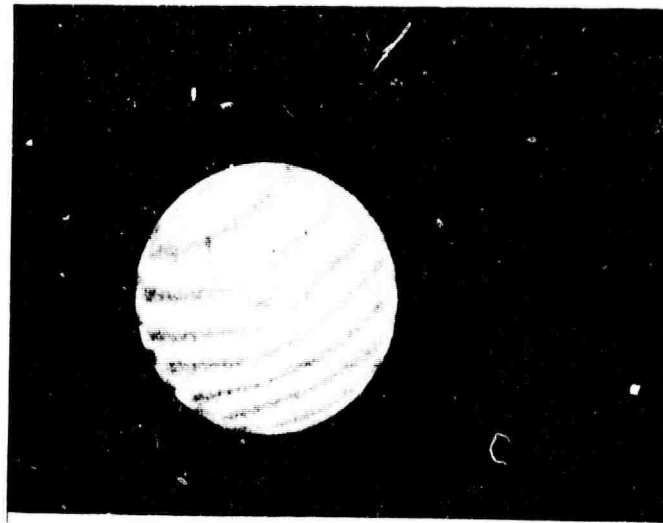
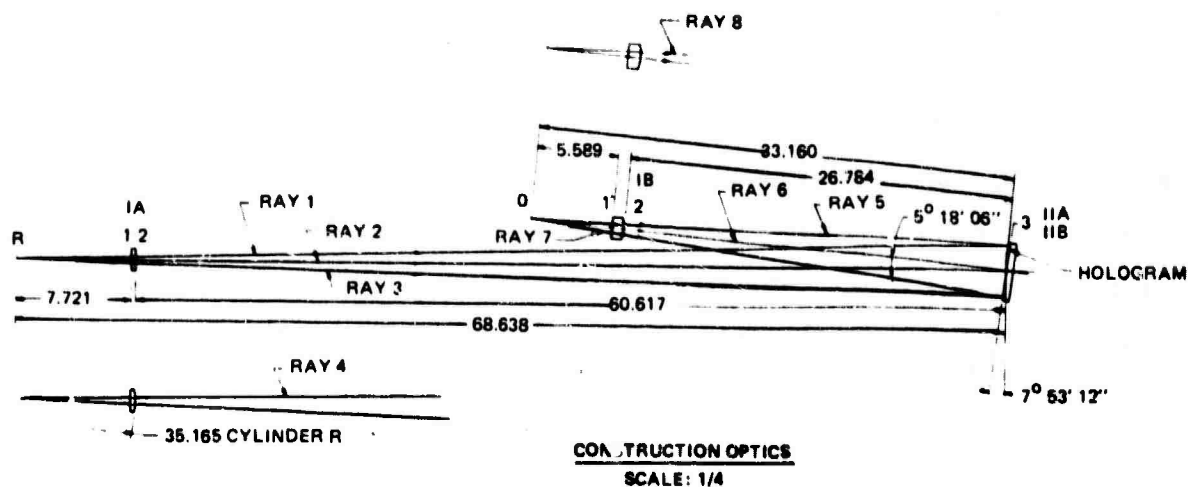


Figure 99. Interferogram of GFE mirror.

5.2 ABERRATION-CORRECTED BEAM SAMPLER DESIGN

The aberration-corrected 45-degree beam sampler, shown in Figure 98, consists of a nonlinear holographic grating on a plane mirror. The grating was designed to diffract a collimated 3.39- μm beam incident at 45 degrees in such a way that an aberration-free wavefront converging to a point 30 cm from the mirror is obtained in the first order. The grating on the mirror is 9 cm in diameter, with a nominal speed of $f/3.3$. The axial ray, which passes through the center of the grating, is diffracted along the normal to the mirror.

The holographic grating fringe pattern was recorded in photoresist using interference between two coherent wavefronts at a wavelength of 0.4416 μm . The hologram construction optics necessary to record the correct grating pattern are shown in Figure 100. To correct aberrations on playback in the infrared ($\lambda = 3.39 \mu\text{m}$), the hologram was constructed with aberrated wavefronts by means of a cylindrical lens in one beam and a spherical lens in the other. These construction optics are advantageous in that the f -numbers of the construction beams are much smaller than that of the final beam, and both are diverging beams. The conventional optical elements required in this case are of small aperture and can be easily manufactured and cleaned. However, the alignment tolerances of these elements on the optical bench are stringent. The steps taken to obtain the



REFERENCE BEAM SYSTEM								
SURF	ELEMENT	DRAWING	RADIUS	MATERIAL	THICKNESS**	LIMIT RAY HEIGHTS		
						RAY 1	RAY 3	RAY 4
R	SOURCE			AIR	7.721	0	0	0
1	IA	SK 2325	∞	517 - 642	0.300	0.197	-0.198	0.199
2			-35.165*	AIR	60.817	0.204	-0.206	0.207
3	IIA		∞	HOLOGRAM		1.772	-1.772	1.772

* CYLINDER RADIUS
** THICKNESS IS ALONG RAY 2

OBJECT BEAM SYSTEM								
SURF	ELEMENT	DRAWING	RADIUS	MATERIAL	THICKNESS***	LIMIT RAY HEIGHTS		
						RAY 5	RAY 7	RAY 8
0	SOURCE			AIR	5.589	0	0	0
1	IB	SK 2326	12.615	517 - 642	0.787	0.298	-0.299	0.299
2			-10.800	AIR	26.784	0.339	-0.341	0.340
3	IIB		∞	HOLOGRAM		1.7222	-1.722	1.772

*** THICKNESS IS ALONG RAY 6
HOLOGRAM CONSTRUCTION WAVELENGTH = 441.6 NM

Figure 100. Construction optics for aberration-corrected 45-degree mirror beam sampler.

final construction optics design for the aberration-corrected, 45-degree beam sampler are summarized below.

First, the distances and angles of the construction point sources that satisfy the paraxial equations were investigated in a tradeoff mode. This showed that coma and astigmatism in the beam on playback both decrease with an increase in the conjugate distances of the construction optics. Coma can also be minimized by properly selecting the angles of the two construction beams relative to the mirror. The conjugate distances of the construction optics were therefore selected so that the longer distance would conveniently fit on the available optical bench in the laboratory, and the angles were selected to minimize the coma. Residual astigmatism was corrected by inserting a cylindrical lens in the beam corresponding to the long conjugate distance. This effectively changes the focal distance along one axis of the mirror. Spherical aberration was then corrected by adjusting the power and bending of the lens in the short-conjugate beam (Figure 100) along with the distance of the short conjugate point from the mirror. The final stage of the design was to vary all of the construction optics parameters simultaneously using the Hughes optical design optimization program, to minimize the residual aberrations and obtain the smallest possible geometrical blur.

The geometrical aberrations of the design are shown in Figure 101; they are well below the diffraction limit for the design geometry, which is a spot of 13.8 μm radius. The dominant residual aberration is high-order spherical aberration, which is of opposite sign in the planes of symmetry and asymmetry. This aberration can be most effectively reduced by the addition of complex higher-order aspherics to the construction optics.

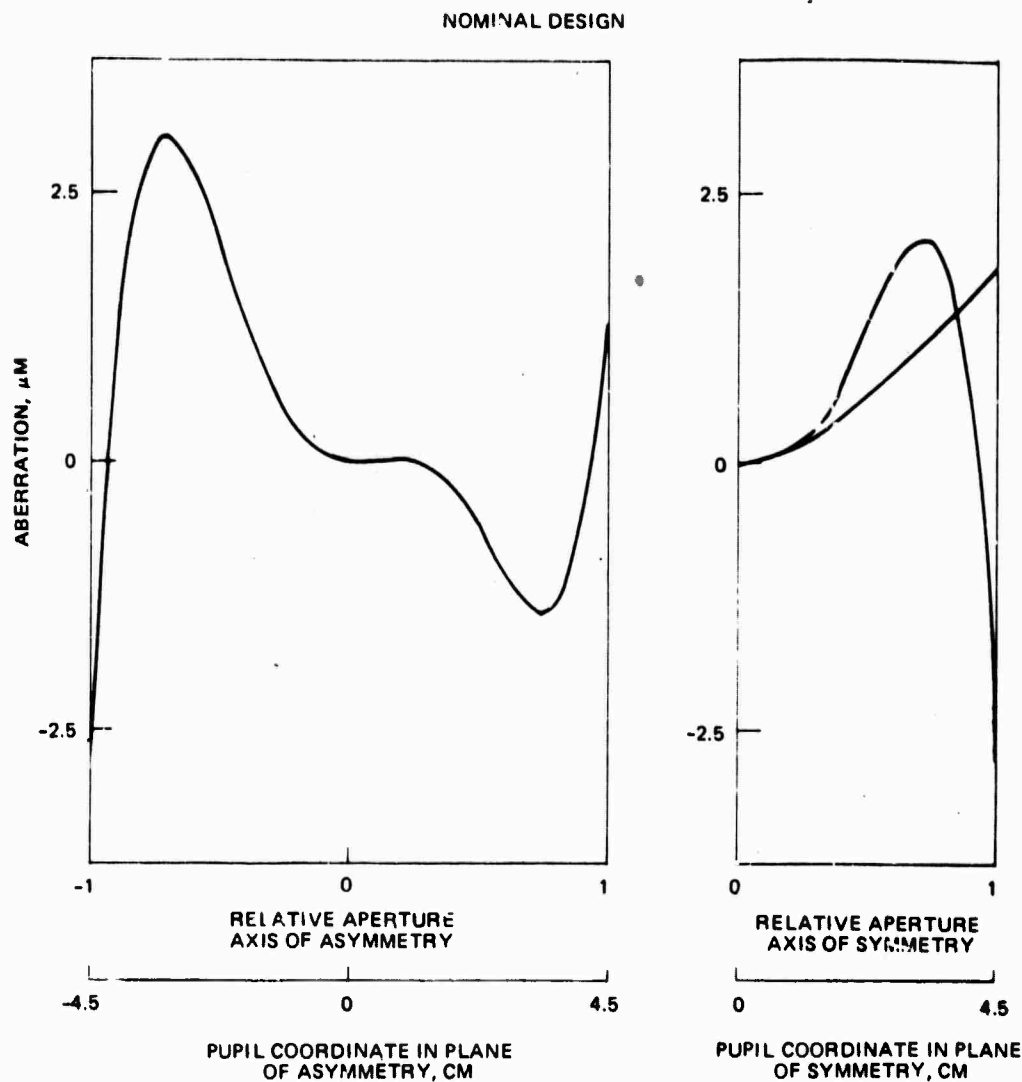


Figure 101. Departure of the rays from a perfect geometrical focus versus the relative aperture. The diffraction limit is $13.8 \mu\text{m}$.

However, the added cost is not warranted in view of the already low aberration level and the nature of the overall program objectives. Because of the rapid increase in the aberration near the edge of the pupil, care must be taken not to utilize this design with a larger aperture. The geometrical aberrations over the full aperture are further represented by the spot diagram and knife edge traces shown in Figure 102. Finally, recent

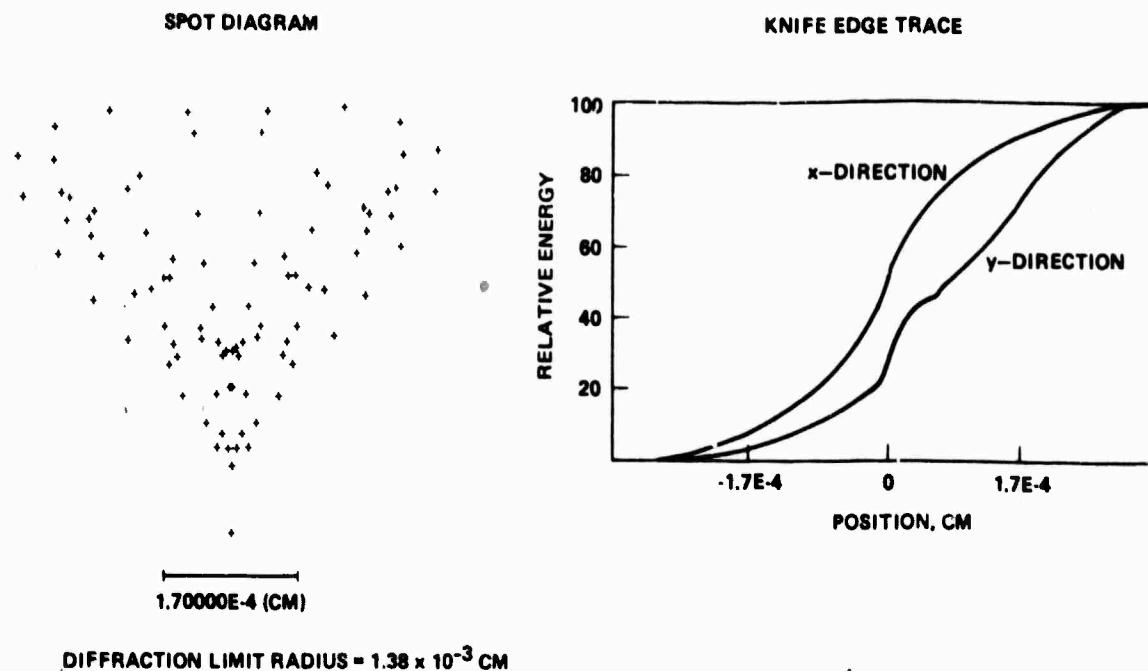


Figure 102. Geometrical spot diagram and knife edge trace for nominal design of the aberration-corrected 45-degree beam sampler.

modifications of the Hughes optics codes permit computation of waveforms passing through holographic optical elements. In this design, the maximum wavefront aberration is about $\lambda/14$.

The design was evaluated to establish the opto-mechanical tolerances that would have to be maintained during construction. The tolerance criterion employed was that the root-sum square of the geometrical performance degradations associated with the tolerances given in Table 17 should be less than the difference between the diffraction limit and the maximum aberration in the nominal design. These tolerances are based on the assumption that on playback, both the focus and angle of incidence of the beam on the mirror are adjustable over a small range of values to obtain the minimum spot size. If this is not done, the tolerances become excessively severe, particularly for the angles of the two construction beams relative to the mirror. The tolerances given in Table 17 are stringent, but can be held in the laboratory.

TABLE 17. CONSTRUCTION OPTICS TOLERANCES ASSUMING ADJUSTMENT OF THE INCIDENT BEAM AND FOCUS ON PLAYBACK

Design Parameter	Value	Tolerance
<u>Short Conjugate</u>		
Distance between point source and lens, inches	5.589	± 0.003
Distance between lens and mirror, inches	26.784	± 0.045
*Angle of incidence of beam on mirror, degrees/minutes/seconds	2°35'06"	$\pm 1'$
<u>Long Conjugate</u>		
Distance between point source and lens, inches	7.721	± 0.015
Distance between lens and mirror, inch	60.617	± 0.053
*Angle of incidence of beam on mirror, degrees, minutes, seconds	7°53'12"	$\pm 1'$
<p>*A variation of one or both of the construction angles can be compensated by a variation of the playback beam angle of incidence. However, the difference between the two construction beam angles must be held to a tolerance of less than $\pm 1'30''$.</p> <p>NOTE: The lens drawing tolerances are given in Figures 103 and 104.</p>		

The drawings for the lenses used in the construction optics are shown in Figures 103 and 104. These lenses were designed to fit existing test plates.

5.3 EVALUATION OF DEMONSTRATION GRATING DESIGN

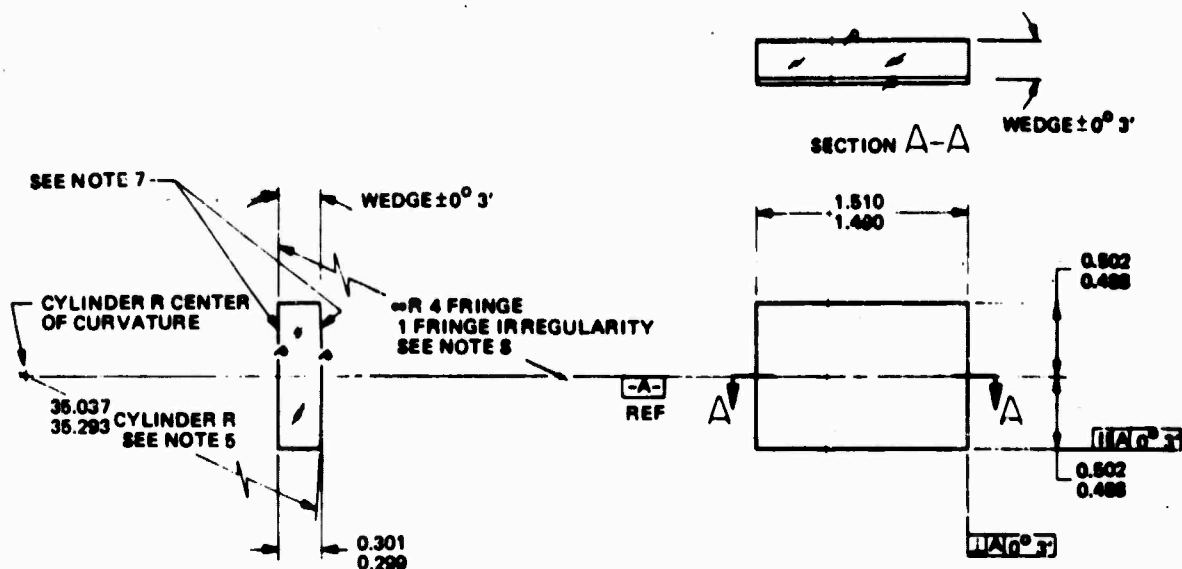
5.3.1 Focal Spot Profile Measurement

The measurement of aberrations in holographic gratings designed for use in the 3- μ m wavelength region is constrained by the following considerations:

1. Holographic gratings can be corrected for aberrations only for a single reconstruction geometry and a single wavelength. Thus, testing must be done at the design wavelength in the design geometry.

2. The availability of lasers operating near $3\text{ }\mu\text{m}$ and having good phase characteristics is very limited. At the Hughes Research Laboratories, a $3.39\text{-}\mu\text{m}$ laser with an output power of about 15 mW was the only available source. The non-visible wavelength and low power make the use of interferometry to measure the diffracted wavefront unwieldy and impractical.

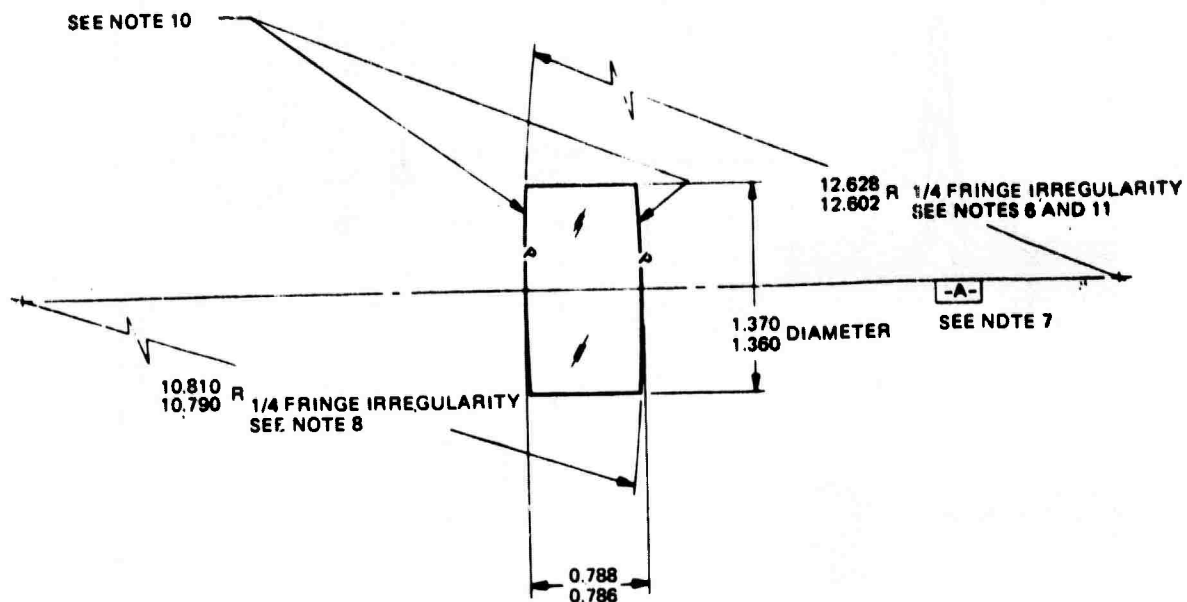
Fortunately, the holographic gratings of interest are designed for use with point-source or collimated beams; hence, evaluation of the focal spot produced by the grating is sufficient to determine its focusing properties and the degree of aberration correction achieved.



NOTES: UNLESS OTHERWISE SPECIFIED

1. MATERIAL: GLASS, OPTICAL, TYPE 517-642 CLASS 1, GRADE B, FINE ANNEALED
2. SURFACES MARKED "P" POLISHED. ALL OTHERS GROUND WITH 220 GRIT SIZE OR EQUIVALENT
3. CLEAR APERTURE:
ENTRANCE: WITHIN 0.050 OF ALL EDGES
EXIT: WITHIN 0.050 OF ALL EDGES
4. SURFACE QUALITY: 80 - 50
5. SURFACE TO FIT TEST PLATE TO WITHIN 1 FRINGE, 1/4 FRINGE IRREGULARITY
6. CHAMFER EDGES 0.005/0.025 FACEWIDTH \times 45/90 DEGREE
7. COAT POLISHED SURFACES TO CLEAR APERTURE FOR A REFLECTANCE OF LESS THAN 0.5 PERCENT AT WAVELENGTH OF 441.8 NM
8. PLACE IDENTIFYING MARK ON EDGE OF LENS TO INDICATE PLANO SURFACE

Figure 103. Lens, cylinder 1A.



NOTES: UNLESS OTHERWISE SPECIFIED

1. MATERIAL: GLASS, OPTICAL, TYPE 517-642 CLASS 1 GRADE B, FINE ANNEALED
2. REF ONLY: AT $\lambda = 546.1$ NM, NOMINAL, EFL = 11.347, BFL = 11.106, FFL = 11.065
3. SURFACES MARKED "P" POLISHED. ALL OTHERS GRIND WITH 220 GRIT SIZE OR EQUIVALENT
4. CLEAR APERTURE:
ENTRANCE: WITHIN 0.050 OF ALL EDGES
EXIT: WITHIN 0.050 OF ALL EDGES
5. SURFACE QUALITY: 80 - 50
6. SURFACE TO FIT TEST GLASS WITHIN FOUR TIMES THE IRREGULARITY CALLOUT TEST WAVELENGTH 546.1 NM NOMINAL
7. DATUM -A- IS THE OPTICAL AXIS (THE LINE CONNECTING THE TWO CENTERS OF CURVATURE)
8. CENTERING ERROR: 1 MINUTE DEVIATION MAX (REF ONLY: 0.007 DIA TIR)
9. CHAMFER EDGES 0.005/0.020 FACEWIDTH x 40/50 DEGREE
10. COAT POLISH SURFACES TO CLEAR APERTURE FOR A REFLECTANCE OF LESS THAN 0.5 PERCENT AT A WAVELENGTH OF 441.8 NM
11. PLACE IDENTIFYING MARK ON EDGE OF LENS TO INDICATE LONGEST RADIUS

Figure 104. Lens, IB.

The grating samples were mounted in the reconstruction geometry for which they were designed. They were illuminated at an angle of 45 degrees with a well-collimated beam of 3.39- μ m radiation 15 cm in diameter. The intensity distribution in the focused spot was measured by scanning the focused beam over an InSb detector with a pinhole aperture which was small compared with the diffraction-limited spot size.

Details of the testing setup are shown in Figure 105. The horizontal scanner swept the 3.39- μ m focal spot in a slow linear scan past the pinhole.

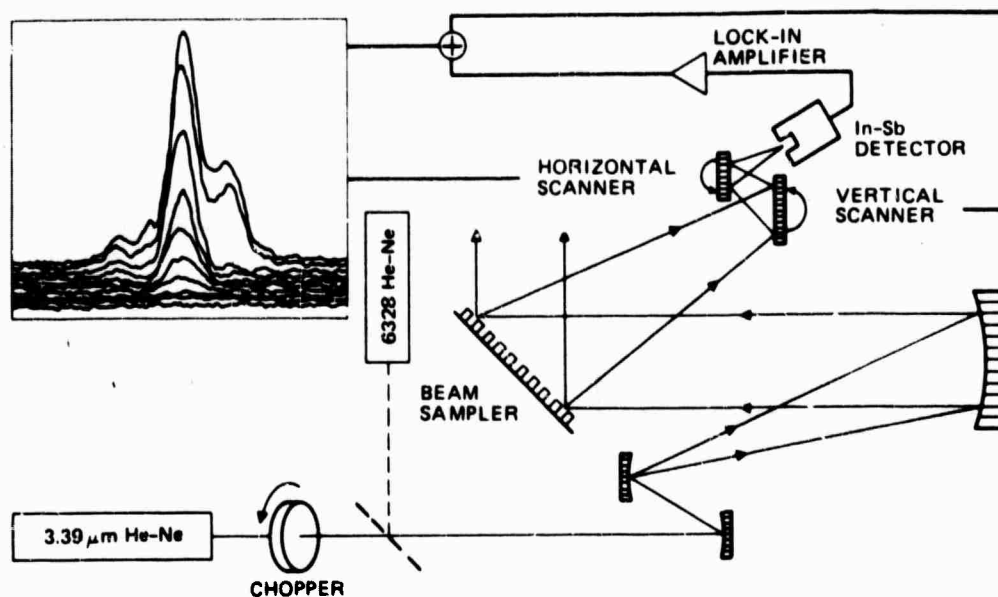


Figure 105. Focal spot profile measurement.

The vertical scan signal was DC and was varied in small increments. It was advantageous to amplify the detector output with a lock-in amplifier and chopper. By combining the amplified detector output with the DC vertical signal, the signals for a three-dimensional scan profile were obtained on an x-y recorder. Some sample scans are also shown in Figure 105.

The size of the focal spot was calibrated by comparing the width of the plotted sweep trace to the measured angular mirror deflection. The given experimental errors ($\pm 5 \mu\text{m}$) are a result of possible errors in measuring the small (~ 10 minute) mirror deflections. Correction was made for the finite size of the pinhole by subtracting the pinhole size from the calculated spot size.

Alignment and interferometric testing of the collimator optics were accomplished with a 6328 \AA HeNe beam which was introduced co-linearly with the $3.39\text{-}\mu\text{m}$ beam. Collimation testing was performed by shearing the beam alternately in the horizontal and vertical directions with a 4-inch

Fabry-Perot plate. The residual aberration remaining after collimation was difficult to measure with the shearing plate. A conventional interferogram of the HeNe wavefront was then made (Figure 106) which showed several waves of aberration at 6328 Å. Fortunately, this corresponds to only a fraction of a wave at 3.39 μm .

Measurements were made in the TE(E_{\parallel}) polarization because the diffraction efficiency of the gratings was found to be more uniform in this polarization. (Diffraction efficiency measurements are discussed in Section 5.3.2.)

Results

The focal spot profile of a 2-inch high-efficiency sample grating was obtained. This sample was chosen because its high efficiency compensated somewhat for the small fraction of the incident beam area being used. Since the small samples were processed identically up to the point of ion machining, it was not necessary to measure the beam quality of more than one. However, the grating etched into the water-cooled GFE mirror was processed differently (the photoresist was dip-drained rather than spin-coated, and the aperture was larger), so additional time was devoted to measuring this grating. The results of the two tests are shown in Figure 107 and 108. The diffraction-limited spot size of the 2-inch sample is 49 μm ; the spot was passed through a 12.5- μm pinhole. The 3-inch grating on the watercooled substrate had a theoretical spot size of 33 μm , and a 7- μm pinhole was used in this case. Both plots show that within the limits of experimental accuracy the central spots are of the predicted width. This represents a dramatic reduction in spot size relative to the spot from an uncorrected focusing beam sampler. However, by the amount of energy scattered into the sidebands it was evident that some residual aberration



a.



b.

Figure 106. Interferograms of collimated incident beam at 6328 \AA .

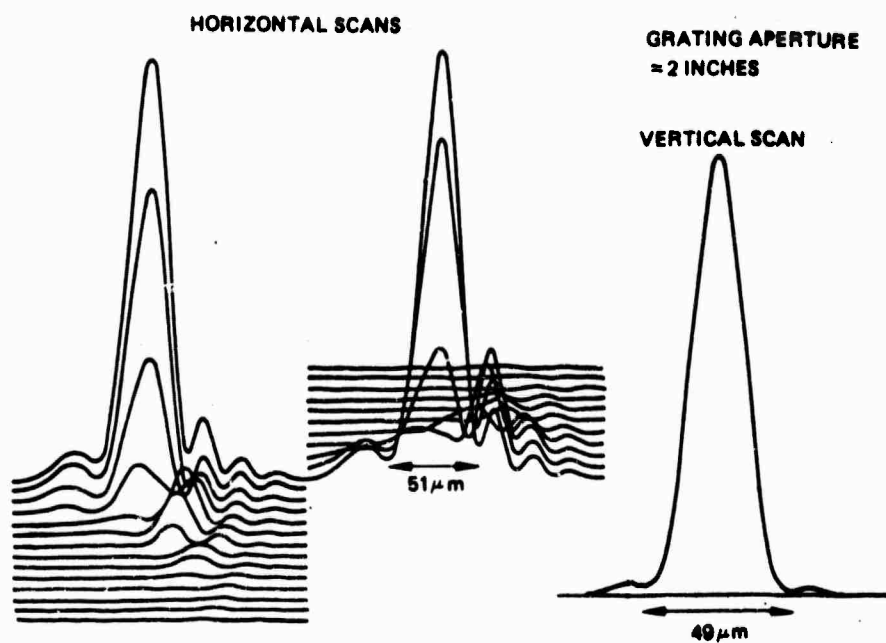


Figure 107. Focal spot profile of aberration-corrected beam sample: High-efficiency sampler.

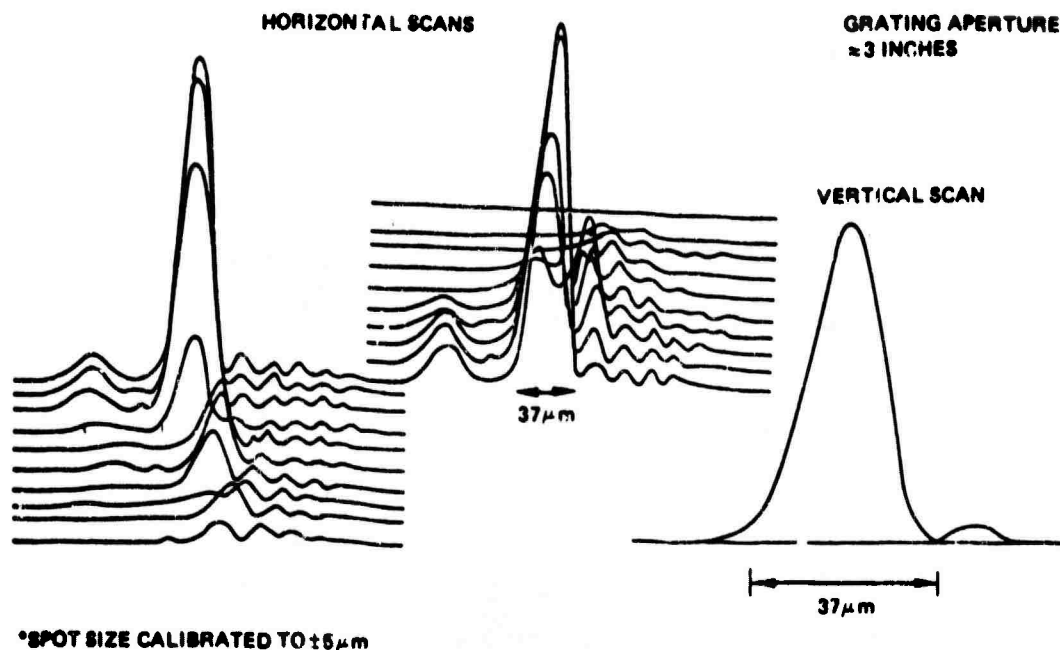
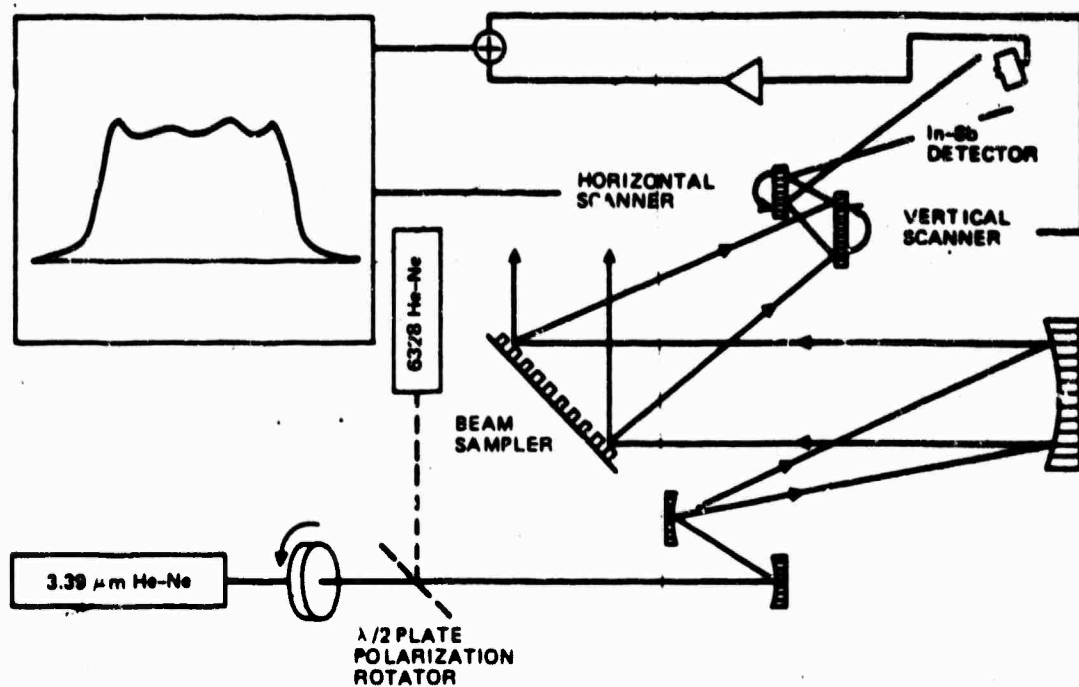


Figure 108. Focal spot profile of aberration-corrected beam sampler on water-cooled mirror.

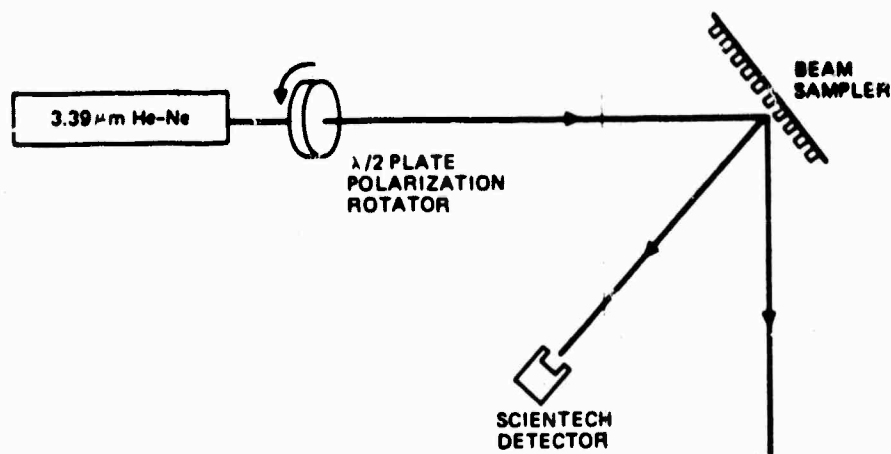
was still present. In the time available, it could not be determined whether this was caused by high order aberrations in the beam sampler itself, or the residual aberrations in the collimated incident beam. To answer this question, additional measurements would be required.

5.3.2 Diffraction-Efficiency Measurements

A measurement of diffraction efficiency uniformity was obtained by scanning an image of the diffracted beam past the detector (Figure 109a).



a. Uniformity measurements



b. Spot calibration measurements

Figure 109. Diffraction efficiency measurements.

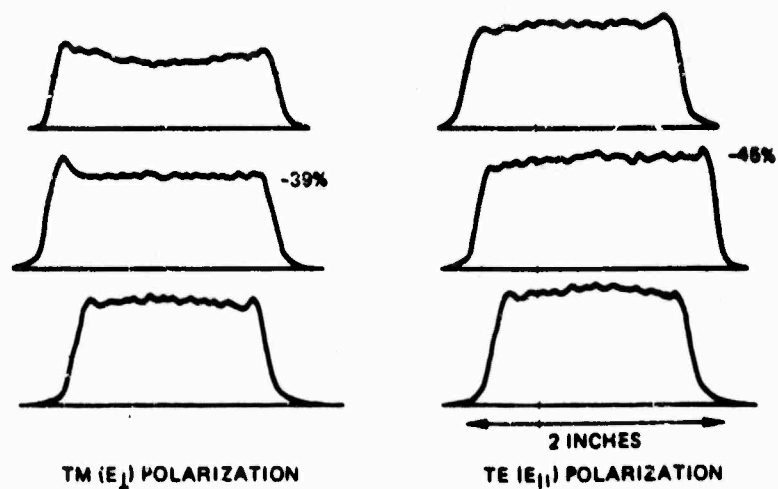
Some horizontal scans at different heights for the measured gratings are shown in Figure 110. The small, sputter-coated samples exhibit excellent uniformity in both polarizations. The larger grating shows excellent uniformity in the TE polarizations, while some peaking occurs near one edge of the mirror in the TM polarization. One note of interest concerning this grating is that the upper and lower scans reveal a small amount of coupling between the two polarizations. Peaks and dips occur in the same places even though the magnitudes remain quite different. This is probably caused by the curvature of the grooves; at the centerline where the grooves are vertical, no such coupling is observed.

To calibrate the magnitudes of these curves, spot checks were made at half-inch intervals along the horizontal centerline scan, using the unexpanded 3.39 μm beam and a Scientech thermopile detector (Figure 109b). The center efficiency was measured as follows:*

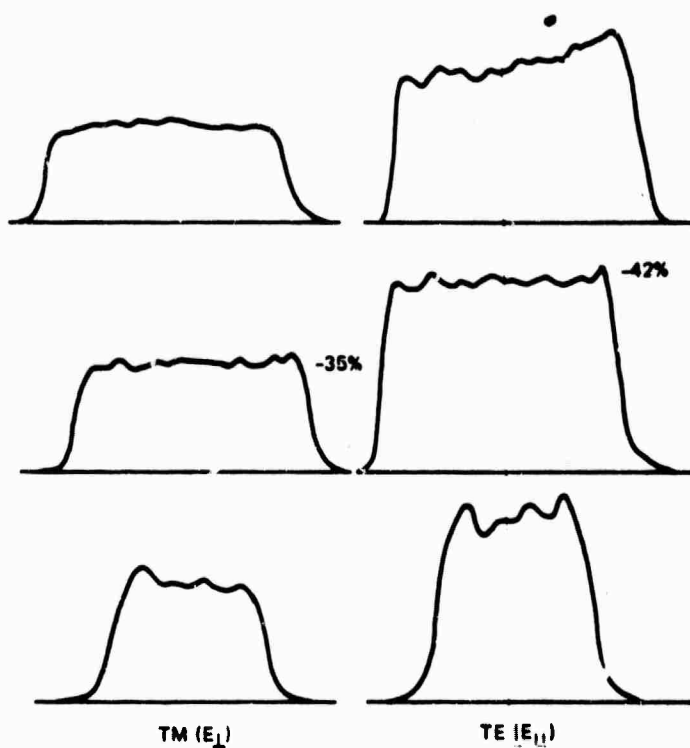
39 percent TM (E_{\perp})	Small high-efficiency sample No. 1
45 percent TE (E_{\parallel})	
35 percent TM (E_{\perp})	Small high-efficiency sample No. 2
42 percent TE (E_{\parallel})	
20 percent TM (E_{\perp})	Small intermediate-efficiency sample
13 percent TE (E_{\parallel})	
9.5 percent TM (E_{\perp})	Water-cooled substrate sample
6.7 percent TE (E_{\parallel})	

The spot measurements also corroborated the shape of the scanned diffraction efficiency curves.

*These gratings were not designed to have equal efficiency values.

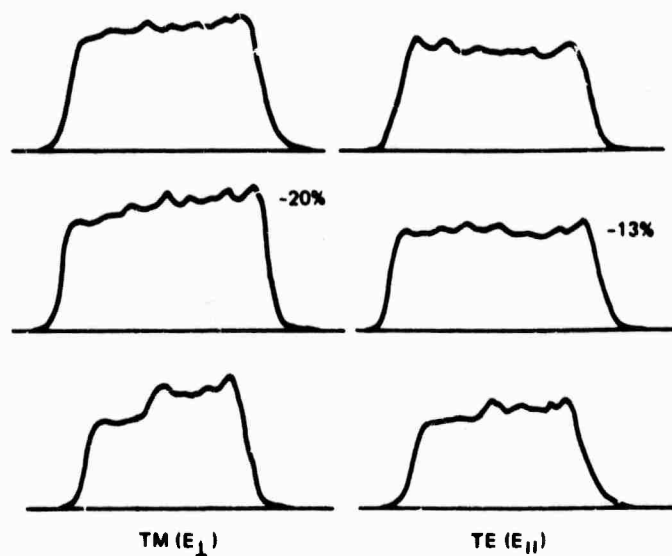


a. High-efficiency sample No. 1

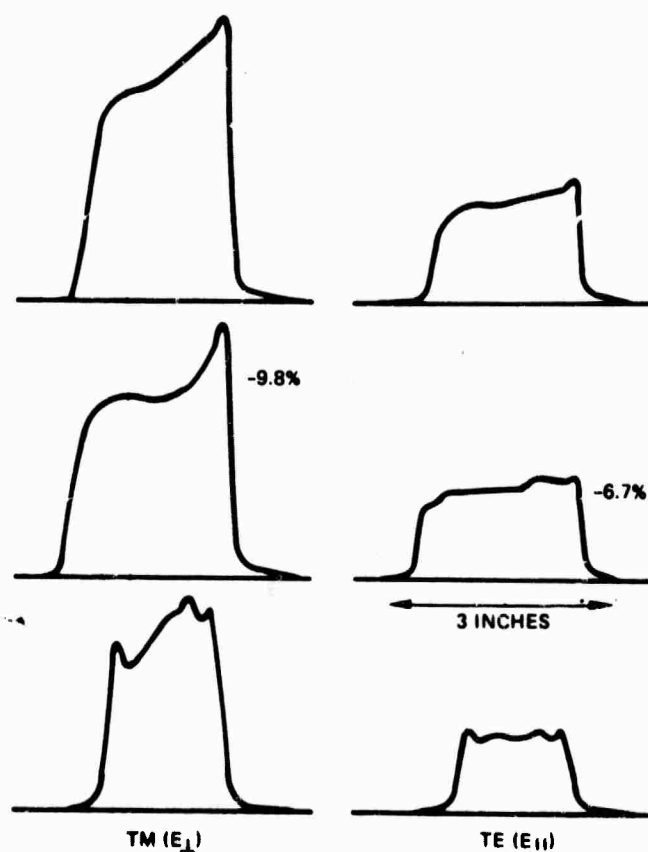


b. High-efficiency sample No. 2

Figure 110. Diffraction efficiency uniformity. Horizontal scan recorded at three heights; calibration varies from sample to sample, and between polarizations; efficiency at grating center is noted for each.



c. Intermediate-efficiency sample



d. Grating on the water-cooled mirror

Figure 110. (Continued)

6.0 CONCLUSIONS OF THE STUDY

The two primary goals of the Holographic Grating Study were to demonstrate the feasibility of fabricating low and high-efficiency ion-etched holographic gratings (HGs) and, by means of optical analysis, to establish their suitability for use in practical HEL systems. Although prospects for complete success were uncertain in the beginning (hence, the reason for the study), both goals were in fact fully achieved. In this concluding section of the report, the results of the study are summarized and their implications for the continued development of holographic grating technology are discussed.

6.1 SUMMARY OF RESULTS

The most tangible outcome of the experimental investigation was the successful fabrication of several low-efficiency and high-efficiency sample gratings ion-machined on gold-coated optical flats, and a low-efficiency beam sampling grating in gold on a water-cooled, high-power mirror approximately 9 cm in diameter. The measured diffraction efficiency of the spin-coated sample gratings exhibited excellent uniformity in both polarizations, while the efficiency of the mirror grating, which was dip-coated, was only slightly less uniform. These results serve to demonstrate the efficacy of the fabrication techniques employed, including the measures taken to obtain uniform photoresist coatings, spatial stability of the interference fringes during exposure of the grating, and control of the ion-machining process to ensure accurate transfer of the photoresist grating into the gold. Effective methods of suppressing standing wave patterns in the photoresist gratings were also demonstrated.

The optical analysis effort yielded several important results. Foremost among these was the conclusion that sampling of an HEL beam for purposes of line-of-sight or wavefront control by means of a holographic grating on the primary mirror is feasible for certain sampling geometries. This concept was analyzed in considerable detail and led to the definition of an

implementation approach for a primary mirror HG beam-sampling LOS control subsystem. A holographic grating axicon concept was also examined in sufficient depth to establish it as a promising candidate for use in an annular ring resonator of a high-energy laser. Another concept found to have significant potential for HEL systems was a holographic grating rhomb.

The design, fabrication and evaluation of aberration-corrected holographic gratings were also addressed during the study. For this task, a corrected 45-degree beam sampling grating was designed and fabricated on the water-cooled mirror and four of the optical flats. In each case, the focal spot was found to be the same size (within experimental accuracy) as that of a diffraction-limited beam; this represents a dramatic improvement over the performance of an uncorrected grating with the same design geometry. Thus, the results of this effort verified the aberration-corrected design and also demonstrated that the optical performance inherent in this design is preserved in the fabrication process.

The remaining investigation was directed toward establishing the feasibility of designing and fabricating high-efficiency holographic gratings. This effort was also successful, as evidenced by the high-efficiency gratings that were produced under the fabrication task. As an example of the results obtained, an HG designed for 50 percent diffraction efficiency yielded measured values of 50 and 46.5 percent for two orthogonal polarizations of the incident beam. These results were achieved with the aid of a computer code to determine the optimum grating parameters for a specific design. The success of this effort was especially gratifying since the development of practical high-efficiency HGs was regarded as perhaps the most difficult technical challenge of the Holographic Grating Study, and paves the way for a number of important high-efficiency applications, notably the HG axicon and the HG rhomb.

6.2 IMPLICATIONS FOR FUTURE DEVELOPMENT

Due in large measure to the successful outcome of the Holographic Grating Study, the development of ion-machined holographic gratings has

progressed from R&D status to the threshold of becoming a generally accepted engineering technology. Since the viability of several HG concepts for HEL systems has been shown analytically, while the requisite design and fabrication techniques for both low-efficiency and high-efficiency gratings have been demonstrated with optical flats and a 9-cm water-cooled mirror, the results of the study would appear to leave only one major issue unresolved - the scalability of the fabrication methods to much larger substrates, e.g., primary mirrors exceeding one meter in diameter.

Before addressing this question, it should be noted that neither the optical design techniques used to analyze the grating concepts and configurations, nor the computer-aided design of the grating itself are in any way limited to small apertures. Hence the results of the study are sufficient to establish confidence in the analytical tools presently available. It is also evident that the basic understanding of photoresist deposition, exposure, and ion-machining processes acquired in the course of the experimental investigation is entirely applicable (and in fact essential) to the fabrication of larger gratings.

The scalability of the fabrication methods hinges on developing a scalable substitute for the spin-coating photoresist deposition process that was used for most of the experimental work. (Spin coating is inherently limited to small substrates because of the mechanical forces involved.) On the basis of preliminary investigation during the Holographic Grating Study and subsequent additional development, Hughes believes that the dip-coating method is a suitable replacement for spin coating, and is fully scalable to any desired size.

The other two requirements for scaling up the fabrication process involve only straightforward, low-risk engineering modifications. As discussed in Section 3.2.3, the additional laser power needed for making large-area holographic gratings with reasonable exposure times has already been provided by upgrading the source with a new laser of higher power and shorter wavelength (for improved photoresist sensitivity). Scaling up the ion-machining and substrate-handling facilities is also a straightforward engineering task.

Thus, although further work is needed to assess absorption and scattering effects, the most critical issues relating to the development of large ion-machined holographic gratings have been successfully resolved. In conclusion, the HGS Program has shown that holographic gratings constitute a viable technology for high-energy laser systems applications. As the versatility and unique properties of these devices become more widely appreciated, they will inevitably assume an increasingly important role in the development of HEL systems.



MISSION of Rome Air Development Center

RADC plans and executes research, development, test and selected acquisition programs in support of Command, Control Communications and Intelligence (C³I) activities. Technical and engineering support within areas of technical competence is provided to ESD Program Offices (POs) and other ESD elements. The principal technical mission areas are communications, electromagnetic guidance and control, surveillance of ground and aerospace objects, intelligence data collection and handling, information system technology, ionospheric propagation, solid state sciences, microwave physics and electronic reliability, maintainability and compatibility.